Effects of Dwell Fatigue, Temperature, Frequency and Environment in a Titanium Alloy

Georgia Mills

A thesis submitted to The University of Birmingham
for the degree of

Doctor of Philosophy

School of Metallurgy and Materials College

of Engineering and Physical Sciences

The University of Birmingham

September 2019

Abstract

This project concentrates on dwell fatigue crack growth, together with a detailed study on fatigue thresholds, fatigue crack growth resistance curves and the influence of environment in a titanium alloy Ti 6246.

When a dwell period is introduced crack growth rates increase by a small but significant amount compared to baseline with the crack growth mechanism remaining transgranular. Striations are observed on the fracture surfaces of some tests, particularly at high ΔK values. When present, striation spacings match crack growth rates obtained experimentally. Conditions influencing the effect of the dwell period included dwell time, environment and temperature. When the dwell time was one hour, the crack growth rate saw an increase of up to 3.5 times compared to baseline crack growth. However, when the dwell time was reduced to two minutes, the maximum increase in dwell crack growth rate over baseline crack growth was only 1.5 times. Furthermore, the environment also influenced the effect of dwell on the fatigue crack growth rate. For example, a test carried out in air conditions had a maximum increase in crack growth rate of 3.5 times when the dwell period was introduced whereas a vacuum test saw an increase of 4.5 times in crack growth rate when the dwell period was introduced.

A one hour dwell test carried out at 575°C experienced a rapid increase in crack growth rate, as shown by the significant elevated "m" value obtained of 6.1. The maximum increase in crack growth rate compared to baseline loading experienced for this test was approximately by a factor of 15 times. Even at this increased temperature, the crack growth mechanism remained transgranular, however, creep damage becomes much more dominant.

Near threshold crack growth rates and ΔK_{th} values were assessed for a range of extrinsic operating parameters. Despite differences in near threshold crack growth rates, altering the temperature from room temperature to 500°C, R ratio from 0.1 to 0.5 and frequency from 10 to 0.25 Hz was found to have only very modest effects on ΔK_{th} values, which were all found to be very similar, approximately between 3 and 4 MPa√m. However, when R ratio was significantly increased to 0.87, ΔK_{th} was reduced significantly to 1.5 MPa√m.

Acknowledgments

Thanks to both my supervisors Prof Paul Bowen and Dr Hang Yue Li for making this research project possible and enabling me to develop my personal research skills. I am very grateful for their extensive support and expertise, encouraging me when needed and helping me to set both results and research into perspective when necessary.

Thanks also to Mr David Price and Dr Tim Doel without whose expert knowledge and support this study would not have been possible. Thank you to all my fellow doctoral researchers and friends who helped me to keep a level head when needed and made these past years incredibly enjoyable

Table of Contents

List of Figures

quarter circle. b + c) Show SEM images taken at a low ΔK value. d + e) Show SEM images taken at high ΔK values.

Figure 7.7: Results for the R ratio 0.1 constant load range mechanical tests at 500°C in both air and vacuum conditions. Results show both 0.25 and 10 Hz frequenices.

Figure 7.8: Results for the R ratio 0.1 constant load range mechanical tests at room temperature in both air and vacuum conditions. Results show both 0.25 and 10 Hz frequenices.

Figure 7.9: Images captured of specimen CX 037 tested at 500°C, 0.25 Hz, R ratio 0.1, vacuum. The crack growth direction is diagonal from bottom left to top right. a) Shows optical image of the crack showing an even quarter circle. b + c) Show SEM images taken at a low ΔK value. d + e) Show SEM images taken at high ΔK values. All crack growth shows a transgranular mechanism.

Figure 7.10: Images captured of specimen CX 033 tested at room temperature, 0.25 Hz, R ratio 0.1, air. The crack growth direction is diagonal from bottom left to top right. a) Shows optical image of the crack showing an even quarter circle. b + c) Show SEM images taken at a low ΔK value. d + e) Show SEM images taken at high ΔK values.

Figure 7.11: Images captured of specimen CR 068 tested at room temperature, 0.25 Hz, R ratio 0.1, vacuum. The crack growth direction is diagonal from bottom left to top right. a) Shows optical image of the crack showing an even quarter circle. b + c) Show SEM images taken at a low ΔK value. d + e) Show SEM images taken at high ΔK values. Shows less secondary cracking at high ΔK values than tests carried out in air at otherwise similar conditions.

Figure 7.12: Results for the R ratio 0.5 constant load range mechanical tests at 500°C in both air and vacuum conditions. Results are from 0.25 and 10 Hz frequencies.

Figure 7.13: Results for the R ratio 0.5 constant load range mechanical tests at room temperature in both air and vacuum conditions. Results are from both 0.25 and 10 Hz frequencies.

magnified image of the transition period from baseline to dwell loading with striations on the fracture surface highlighted. C) Shows striation spacing from the baseline crack growth period at a ΔK of 16 MPa√m. D) Shows the striation spacing from the dwell crack growth period at a ΔK of 17 MPa√m. E) Shows the transition from dwell loading to the final baseline loading. The crack growth mechanism remains transgranular.

Figure 8.12: Results comparing the two minute maximum hold dwell tests in air and vacuum at 500^{o}C.

Figure 8.13: Results from CX 030, the one hour maximum hold dwell test in air at 575^{o}C. Showing three periods of baseline crack growth and two periods of dwell crack growth. Data from a 575^{o}C baseline Paris regime test is also included to show the similar rates obtained.

Figure 8.14: Optical Image of CX 030, the one hour dwell at 575^{o}C in air at maximum hold. Some anisotropic crack growth is seen on the fracture surface as well as secondary sights of oxidation on the surface, away from the primary crack.

Figure 8.15: SEM images of CX 030, the one hour dwell at 575^{o}C in air at maximum hold. The crack growth direction is straight form bottom to top. Image A + B) Show the first baseline crack growth period with transgranular crack growth. C+D) Show the first dwell period, despite the much accelerated rate the mechanism remains transgranular. E+F) Show the final dwell period, again with a transgranular crack growth mechanism.

Figure 8.16: Optical image of the 575^{o}C one hour dwell test that failed prematurely away from the notch. Lots of secondary cracking is visible on the specimen surface.

Figure 8.17: Results comparing the two minute dwell test and one hour dwell test at 500^{o}C in air.

Figure 8.18: Results comparing the two minute dwell test and one hour dwell test at 500^{o}C under vacuum conditions.

List of Tables

Chapter 1 - Introduction

The project aims to understand and explore the effects of dwell on fatigue crack growth resistance in a titanium alloy Ti 6246 as well as understanding the effect that environment, creep and frequency has on crack growth. Ti 6246 is currently used for the compressor discs located in both the intermediate pressure and towards the front end of the high pressure compressor section of an aeroengine. The compressor is located between the fan at the front of the engine and the combustor located towards the back of the engine. Ti 6246 is used for this application due to its characteristic of having a high strength to weight ratio. Useful creep resistance is also maintained at higher temperatures when compared with other titanium alloys such as Ti 64[19]. The use of Ti 64 applications is limited to approximately 350^{o}C whereas Ti 6246 can be used to temperatures exceeding 500^{o}C [5].

It is understood that dwell fatigue in an aeroengine occurs not only during the initial take off of the aircraft but also during the aircrafts climb to full height typically lasting between 15 and 20 minutes. Therefore, long dwell periods of up to 3600 seconds are tested in this project to gain an understanding of actual life application. The crack growth mechanisms as a result of long dwell periods are examined in various conditions including in air or under vacuum alongside varying temperatures and dwell periods. R ratios are also varied between 0.1 and 0.5 throughout the project.

Chapter 2 summarises gas turbine engines and where and why titanium alloys are used. Chapter 3 summarises the basic metallurgy of titanium alloys and gives a review of the titanium alloy Ti 6246. Chapter 4 details fatigue and fracture within metals. Chapter 5 describes experimental procedures and analytical technique. The results for microstructural characterisation of Ti 6246 and near threshold tests are given in Chapter 6. Constant load range tests and dwell tests are presented in chapters 7 and 8 respectively. Chapter 9 gives a discussion and Chapter 10 states conclusions and addresses future work.

Chapter 2 - Gas Turbine Engines

2.1 Gas Turbine Engines

The gas turbine jet engine enables accessible air travel around the world. The turbo jet engine was first patented by Frank Whittle in 1930 with a prototype of the engine running in 1937 [20, 21]. In 1941, the Gloster E28/39 successfully flew with Whittle's W1A engine [22-24]. Since then, aviation has progressed significantly with understanding of materials and technologies evolving constantly. Each new engine that is proposed and built aims to be better than the previous in terms of efficiency.

The gas turbine aeroengine works on the principle of Newton's third law of motion which states; for every action, there is an equal and opposite reaction. This therefore allows for a propulsive jet to be formed as a result of the exhaust from the turbine being accelerated [25]. The engine can be simplified into three main sections which all play a vital role in ensuring the engine works correctly. These sections are; the compressor, the combustor and the turbine; although there are several other sections involved in the working of the engine [26]. For example, the fan is located at the front of the gas turbine engine and is responsible for 85% of the thrust created [27]. A vast amount of air is sucked in through the fan which is rotating. The air in the fan is then accelerated as a result of the rotating blades and separated to be sent in two directions. One direction sends the air through to the core of the engine where it enters the compressor section. The other direction leads the air directly through to the surrounding area of the core via ducts therefore bypassing the core of the engine. This air travels to the back of the engine remaining cooler than the air in the core of the engine and reduces the noise of the engine. It is this air that helps to produce force needed to propel the aeroplane forward and hence improves thrust and efficiency [28,29]. The bypass ratio can be defined by;

$$\text{Bypass Ratio} = \frac{\text{Bypass Air Flow}}{\text{Core Inlet Air Flow}}$$

It is the bypass ratio which has a particularly dominating effect on the performance of the engine. For example, having a high bypass ratio of between 4 to 8 will improve the specific fuel consumption when cruising but causes decreased specific thrust at take-off. Low bypass ratio of between 1 and 3 are used for military fighters as this provides improved thrust [30].

The compressor section is located behind the fan and is considered the first component in the core of the engine. In the compressor, there are rows of bladed disks known as either rotors or stators depending on their function. The rotors and stators are repeated in an alternating sequence. The rotors rotate at high speeds and are connected to a central shaft. The stators are held stationary in order to increase the pressure of the air coming through by making sure the air remains flowing in a straight line after it passes through each of the rotors. The stators are often attached to the outer casing [1] as demonstrated in Figure 2.1. The flowing air is then forced through the compressor. As the fan blades get smaller in size along with the cavity the compressor is in, the pressure of the air rises. Therefore a greater potential energy of the air is achieved. This high pressure, high energy air is then fed through to the combustor [20, 30].

The compressed air is added to the fuel in the combustor. Here, a spark ignites the fuel causing it to burn. High temperature exhaust gas is formed as a result. This causes the power turbine to turn and thrust is achieved by the high temperature gas expanding as it passes through the turbine section. The temperatures of the combustor inlet are dependent on the engine pressure ratio, load, engine type and whether the turbine is regenerative or not. Regenerative gas turbine engines see combustor inlet temperatures reach up to 600°C with exit temperatures exceeding 1600°C. Normal combustion temperatures range from 1800 to 1950° C [31]. The turbine is similar to the compressor in that they both have alternating rows of rotating rotors and stationary stators. Blades located in the turbine rotate due to the stream of high pressure gas. The rows of airfoil cascades that make up the turbine are able to extract energy from the air flow and decrease pressure along the turbine. This then drives the fan and the compressor whilst blowing out of the exhaust nozzle to create thrust [26]. Efficiency of the jet engine is influenced by many aspects. Some of the key factors which need to be addressed include the pressure rise achieved in the compressor section, the combustor efficiency and the temperature of the gases as they enter the turbine.

Figures 2.2 and 2.3 demonstrate both the principles of the gas turbine in operation and also, exactly what materials are located where in the engine making it very clear to see where exactly titanium alloys are situated [2].

Development of aeroengines is an ongoing process and is divided into two streams. The first is improving efficiency of the engine and the second is improving performance. Both efficiency and performance are related to weight savings which is often achieved by using different materials with higher specific strength and stiffness than those currently in use. This is why the use of titanium alloys in aircrafts has been increasing as shown in Figure 2.4 which depicts commercial Boeing aircrafts from 1960’s to the year 2000 [3].

Chapter 3 - Titanium Alloys

3.1 The Production of Titanium

Titanium is the fourth most abundant metal, with only iron, aluminium and magnesium being more copious [32]. However, despite being so abundant, titanium is notably more expensive. This is why its use tends to be for high cost applications such as aerospace[32]. Figure 3.1 demonstrates the areas titanium alloys are used in [4].

The reason behind titanium being an expensive element is due to the extraction process. Unlike cheaper metals such as iron, carbon cannot be used to reduce titanium from its oxides as this causes titanium carbides (TiC) to form leading to the metal becoming too brittle. Instead, a more expensive process is used whereby many stages must be performed requiring a lot of energy. The main ores for titanium are rutile $Ti0_2$ and ilmenite $FeTi0_3$. Despite rutile $Ti0_2$ being more costly and less common than ilmenite $FeTi0_3$, it is more frequently used due to the fact that ilmenite contains iron compounds which makes processing more challenging [5, 32].

3.2 The Metallurgy of Titanium and its Alloys

Titanium is around 60% less dense than steel and nickel-base superalloys and capable of being used to temperatures reaching 600^{o}C dependent on composition. The melting temperature of titanium exceeds 1660^{o}C [5]. On the metal surface of commercially pure titanium, oxide films form that allow for the metal to be extremely corrosion resistant. These films are stable, continuous and highly adherent. The protective films form instantaneously whenever a fresh surface is exposed to either air or moisture [35].

3.2.1 Phase Transformations

Titanium is an allotropic element meaning there are two fundamental crystal structures that it can exist in. One structure has a hexagonal close packed (hcp) arrangement, known as the α phase, whereas the second structure has a body centred cubic (bcc) arrangement, known as the β phase. Compared to the β phase, the α phase has lower diffusion rates and ductility and higher resistance to plastic deformation and creep resistance. Furthermore, the α phase is anisotropic in its response to stress meaning the properties displayed are directionally dependant. For example, if the stress is applied parallel to the c axis, Young's modulus (E) is found to be approximately 145 GPa but when the stress is applied perpendicular to the c axis, E is found to be greatly reduced to approximately 100 GPa. A similar relationship is found for the shear modulus (G). Therefore, the properties of the alloy depend on the intensity of the texture and orientation of the aligned α grains [36]. In general, the β phase has a lower Young's modulus (E) than the α phase [36].

Along with the two crystal structures of hcp α and bcc β there are four common classifications of titanium alloys. These are;

I. α
II. Near-α
III. α / β
IV. β

At room temperature, titanium has a hcp crystal structure so exists in α phase formation. Upon heating, the crystal allotropically transforms from α phase hcp structure to β phase bcc structure as shown in Figure 3.4 [5]. The temperature at which the structure is 100% bcc β phase is known as the β transus temperature and is reached at 882.5°C [37]. On cooling from this temperature, the α phase will occur at room temperature. The β phase will transform on cooling to the α phase in one of two ways; either martensitic transformation or Widmänstatten transformation. Generally, a martensitic transformation occurs from fast cooling rates whereas Widmänstatten occurs from slower cooling rates and is based on diffusion. As well as the rate of cooling, additional alloying elements also influence the transformation. The specific alloy composition can also alter the β transus temperature. For example, it is possible to obtain β phase at room temperature. This will be discussed in more depth in the titanium alloys section, 3.2.2. When cooling from the β phase field, it is theoretically possibly for 12 different orientations of the α phase to form from one single β crystal [38, 39]. The crystallographic relationship between β and α alloys for both the martensitic and Widmänstatten transformations obeys Burgers relationship [7, 40, 41] as shown in Figure 3.5 [6].

3.2.1.1 α and Near α Alloys

α alloys are titanium alloys consisting entirely of the α phase and near α alloys contain majority α phase with a small amount of β phase. Aluminium is used in both of these alloys as an additional alloying element due to the fact it is a major α stabilising element. In near α alloys there is a small percentage (<2%) of β stabilising alloying elements which could include molybdenum or silicon. The additional alloying elements, particularly aluminium, found in α and near α alloys provide solution strengthening to the alloy. They have higher creep resistance and resistance to plastic deformation over β alloys. However, in comparison to β alloys, they have poorer levels of ductility [42, 43]. It is thought that these alloys can maintain mechanical strength up to temperatures of 600°C which is why they are often used for applications such as autoclaves, high pressure cryogenic vessels and missile fuel tanks.

3.2.1.2 α/β Alloys

α/β alloys are the most commonly used type of titanium alloys. Ti 64 is particularly common with over 50% of all titanium alloys used today being of this composition. α/β alloys are alloys which consist of a mixture of both α and β phases. They contain 4-6% of β phase stabilising elements. These elements include molybdenum and vanadium to name a few. They are known for having a good balance of properties, many exhibiting high strength and high toughness as well as high temperature capabilities. α/β alloys are used heavily in the aerospace industry for manufacturing steam turbine blades, compressor discs and other critical components. They are capable of being used at temperatures exceeding 450°C [44].

3.2.1.3 β Alloys

β alloys are titanium alloys rich in β phase stabilising elements and low in α phase stabilising elements. Precipitation hardening is often used in order to significantly strengthen β alloys resulting in a complex microstructure and increased levels of toughness. However, the use of β alloys is limited due to high specific weight, poor oxidation behaviour and challenging weldability [44].

3.2.2 Titanium Alloys

Figure 3.6 [7] demonstrates the effects alloying elements have on whether α or β phases are present at different temperatures. When looking at the neutral graph shown in Figure 3.6, without any influence of alloying elements, α alloys appear at lower temperatures and β alloys form at higher temperatures. Neutral additional alloying elements consist of tin and zirconium as these have no effect on the β transus temperature. Neutral elements have an electron to atom ratio of 4 [45].

There are ways of altering the β transus temperature through the addition of different elements. For example, α stabilisers include aluminium, oxygen, nitrogen and carbon. The addition of these elements will increase the β transus temperature meaning the α phase is stable at higher temperatures compared to when these additional elements are not present. For near α alloys, the β transus temperature can be raised to as high as 1050°C [5]. It also allows for α and β to exist together in forming α/β alloys. All α stabilising elements have an electron to atom ratio of less than 4 [45].

β stabilising elements are able to lower the temperature at which the β phase is stable and therefore reduce the β transus temperature [46]. It is possible for the β transus temperature to be as low at 700°C [36]. These β stabilising elements are divided into two subgroups. These are the isomorphous β stabilisers and the eutectoid β stabilisers. All β stabilising elements have an electron to atom ratio of more than 4 [45].

Isomorphous β stabilisers are elements which are entirely soluble in the β phase and include vanadium, molybdenum, niobium and tantalum. With isomorphous β stabilisers, β can be present at room temperature and hence α and β can exist together to create an α/β alloy.

Eutectoid β stabilisers include elements such as iron, chromium and silicon. Eutectoid β stabilisers are elements which have limited solubility, display sluggish reactions due to substitutional atoms being involved and are able to impose an eutectoid system on titanium [8]. Eutectoid β stabilisers are used in conjunction with one or more isomorphous β stabilising elements to increase the β phase stability and to minimise the likelihood of intermetallic compounds forming at elevated temperatures. The risk of intermetallic compounds forming as a result of using eutectoid stabilisers is the main reason that isomorphous β stabilisers are more commonly used; however, eutectoid elements do increase the hardenability and the response to heat treatment of the alloys.

As well as additional alloying elements, thermal history such as cooling rates also affect both microstructure and properties of the alloy. Due to the fact that the α phase is insensitive to heat treatment, only α/β and β alloys have a response to different heat treatments. On quenching, a diffusionless martensite transformation of the β phase to the α phase will occur. However, if cooling rate is slower, the transformation will occur by diffusion-controlled nucleation and growth of the α phase. This is shown schematically in Figure 3.7 [8, 47]. Rapid cooling from above the β transus temperature can lead to five different transformations. These are;

$\beta \rightarrow \alpha'$ (HCP martensite) β

$\rightarrow \alpha''$(Ortho. Martensite)

$\beta \rightarrow \alpha'' + \beta + \omega$

$\beta \rightarrow \beta + \omega$

β (retained β)

When titanium alloys with low concentrations of β stabilisers are quenched, α' forms. This happens via a diffusionless transformation which results in laths, packets or acicular morphologies. α′ is hexagonal in crystal structure and appears as an acicular phase. α′′ forms in more solute-rich alloys as a result of supersaturation and therefore upon quenching the hexagonal structure is distorted. α′′ is an orthorhombic phase[5]. If there are more β stabilising elements, ω phase will form as a result of rapid cooling in β stabilised alloys. The α phase can then nucleate from the ω phase as they act as pre-cursers for α phase nucleation[8].

3.2.2.1 Ti 6246

The material this project is focused on is Ti-6Al-2Sn-4Zr-6Mo (wt pct) which is more commonly known as Ti 6246. Ti 6246 is most commonly a solid solution strengthened α/β alloy with high levels of β stabilising elements. It offers an attractive combination of high strength, fracture toughness, creep resistance and low cycle fatigue properties which is why it is replacing alternative titanium alloys such as Ti 6242 and Ti 64 [5]. The microstructure of Ti 6246 used for this project was Widmänstatten which produces coarse, needle like α laths within a β matrix as shown in Figure 3.8 [9]. This type of microstructure is produced firstly via a high temperature homogenisation β phase step to ensure the material consists entirely of bcc matrix. Subsequently, the material is then cooled to room temperature and it is this cooling rate which determines the width of the α lamellae and the quantity of α at the β grain boundaries. Following on, the material is then plastically deformed in the β phase field often via a forging technique. This encourages a high density of dislocations whilst keeping the lamellar structure together[36, 48].

There are different processing routes for Ti 6246 which result in different microstructures and hence different mechanical properties being achieved. For example, α-β processed Ti 6246 develops a bi-modal/fully equiaxed microstructure as shown in Figure 3.9 whereas β processed titanium alloys comprise a basket weave/Widmänstatten microstructure such as shown in Figure 3.8 [9]. Bi-modal microstructures display higher ductility, formability and strength, improved hydrogen tolerance and better low cycle fatigue (initiation) properties. Widmänstatten microstructures exhibit superior fracture toughness, creep properties and improved fatigue resistance [49]. For compressor disc applications, a β processing route is used as this gives optimum properties required for this application. This includes annealing above the β transus temperature which for Ti 6246 is found to be between 935 and 945°C [15, 50]. This processing route results in high aspect ratio Widmänstatten primary α laths forming within a deformed coarse-grained fully transformed β matrix. The high aspect ratio encourages higher fracture toughness, increased fatigue crack propagation resistance and improved creep strength [51, 52]. Contained within the β matrix are fine secondary α laths.

Ti 6246 has more β phase when comparing the alloy to more traditional titanium alloys such as Ti 64. This allows for an improved heat treatment response and creep performance as well as being able to operate at higher temperatures [53]. When looking at the microstructure of Ti 6246 under SEM using back scattered electrons, the α and β phases are easily recognisable. Primary α appears dark in contrast compared to the retained β which appears light. The primary α can be seen in two kinds of morphology. One type of morphology shows the primary α growing in colonies along original β grain boundaries. This type of morphology is known as grain boundary α. The second type of morphology seen is inside the original β grain. Here, the appearance is of a basket weave plate [54].

Each of the additional alloying elements in the alloy plays a specific role in ensuring the alloy achieves the most desirable properties for particular applications [55]. For example, aluminium, tin and zirconium are all substitutional alloying elements. Tin and zirconium are soluble in both the α and β phase and are classed as neutral as they do not influence the β transus temperature. However, the addition of aluminium leads to an increase in β transus temperature since it is an α stabiliser. Molybdenum is a β-isomorphous element and therefore has complete solubility in β titanium. This encourages lower resistance to deformation compared to α modification meaning there tends to be improved fabrication of the alloy under both hot and cold working operations [56].

Chapter 4 - Fatigue and Fracture

4.1 Introduction

Fatigue is a damage process whereby overtime through the process of cyclic loading a component experiences a reduction in life span as a result of localised, time-independent deformation leading to permanent damage. Cyclic stresses applied below the yield stress of the material cause the initiation and propagation of cracks which, in turn, reduces the structural integrity of a component [57].

Compressor disks, along with many other aeroengine components are likely to experience cyclic stresses during service which may cause initiation and propagation of cracks [58]. Therefore, to ensure all components remain within safe limits a full understanding of fatigue and the mechanisms is essential. Material fatigue data can be used to ensure all components that have a limited fatigue life are subject to design against fatigue failure. A defect tolerance approach can be applied to ensure components are designed against fatigue failure.

4.1.1 Defect Tolerance Approach

When materials are manufactured, processed, machined and formed to become useful components it is likely flaws and defects may form. In order to establish whether these flaws may become safety critical, fracture mechanics is used to analyse them. For example, it is possible a defect will not grow and therefore is safe. However, a defect may propagate as a crack which could lead to a catastrophic failure. Therefore a defect tolerance approach using fracture mechanics is used to answer some important questions such as what is the maximum flaw size which can be tolerated and if a flaw is present, what is the maximum service life of the component [59].

Non-Destructive Examination (NDE) techniques are used to size any defects contained within the material. If no defects are picked up it is still assumed they are present and therefore the resolution limit of the NDE technique is used as the initial defect size. Fracture mechanics is then used to establish how many fatigue cycles it would take to propagate the initial defect (a_0) to a critical crack length (a_{crit}) resulting in failure. By always assuming an initial defect is present, it allows for a worst case scenario to be calculated. This leads to all estimates on fatigue life being conservative and as components are safety critical, it is paramount to minimise the likelihood of catastrophic failures.

4.1.2 Linear Elastic Fracture Mechanics

In a linear elastic material, three basic cracking modes have been derived as shown in Figure 4.1 [60]. Mode one refers to tensile opening. Here the tensile stress is applied normal to the plane of the crack. Mode two refers to sliding or in shear plane which means a shear stress acts parallel to the plane of the crack and perpendicular to the crack front. Mode three refers to tearing or anti-plane shear whereby a shear stress acts parallel to the plane of the crack and also parallel to the crack front. Mode one is the most common mode that leads to brittle fracture [17, 61]. This mode is also the most commonly used for research of understanding and developing fatigue resistance. The research within this thesis used mode one tensile opening at the crack tip for all mechanical tests.

4.1.2.1 The Stress Intensity Factor

Based on linear elastic fracture mechanics (LEFM), Irwin developed a failure criterion which accounted for crack tip plasticity and was based on the crack tip stress field. Unlike Griffith who focused on the entire body of material, Irwin focused on a localised region [62].

By drawing a relationship between asymptotic stress and displacement fields around the crack front, Irwin was able to show that:

$$\sigma_{ij} = \left(\frac{K_i}{\sqrt{2\pi r}}\right) f_{ij}(\theta) \qquad \textit{Equation } 4.1$$

where σ_{ij} refers to the Cauchy stresses [63], r is the distance from the crack tip, θ is the angle in respect to the plane of the crack and f_{ij} is a dimensionless function dependant on the crack geometry and loading conditions. Finally, K is the stress intensity factor for which the units are MPa√m. The stress intensity factor, K, describes the severity of the elastic stress field surrounding a crack. Depending on loading configuration and crack geometry, the way K is computed varies. However, a common form for K to exist in is given by:

$$= \sigma \;\; \pi\sqrt{a\;x}\, f\left(\frac{a}{W}\right) \qquad \textit{Equation } 4.2$$

where f is a dimensionless function dependant on the crack length (a) and the width of the test specimen (W). This shows how K is linearly related to the applied stress and square root of the crack length. The function $f\left(\frac{\_}{W}\right)$ can be replaced by Y which is specific compliance function. In an infinite plate with a central crack Y = 1 [64].

Fracture toughness, K_{1C}, is a critical value of K at failure. Fast fracture would occur if K_{1c} is met and is independent of specimen size and thickness as well as defect size [59]. The '1' in K_{1c} refers to mode one crack opening which is tensile crack opening. A value of K_{1c} can be obtained experimentally by applying a load to a fatigue pre-cracked specimen and measuring the crack length at which failure occurred. This would be known as the critical crack length. The equation for K_{1c} is based on equation 4.2 and given as:

$$K_{1c} = \sigma\sqrt{\pi a_{crit}}\; f\left(\frac{a}{W}\right) \qquad (Equation\ 4.3)$$

K_{1c}, is only dependant on the temperature and hence when a defect is present it is used to characterise material property and predict failure [59].

4.2 Fatigue

Fatigue is a damage process which includes both crack initiation and crack propagation as a result of cyclic stress. A cyclic stress is applied and this results in a maximum stress (σ_{max}) and minimum stress (σ_{min}). The mean stress (σ_{mean}) is given by:

$$\sigma_{mean} = \frac{\sigma_{max} + \sigma_{min}}{2} \qquad (Equation\ 4.4)$$

The range of the applied stress ($\Delta\sigma$) is given by:

$$\Delta = \sigma_{max} - \sigma_{min} \qquad (Equation\ 4.5)$$

Furthermore, stress ratio, R, is the ratio between minimum and maximum stress throughout the fatigue cycle. R is given by:

$$R = \frac{\sigma_{min}}{\sigma_{max}} \qquad (Equation\ 4.6)$$

Under cyclic loading conditions, crack initiation and propagation can occur at a stress intensity far below the fracture toughness value. Crack growth can be correlated to the stress intensity factor range ΔK, for instances of small scale yielding, using the following equation:

$$\Delta = K_{max} - K_{min} = Y\Delta\sigma\sqrt{\pi a} \qquad (Equation\ 4.7)$$

Fatigue life is usually described in three different stages: crack initiation, crack propagation and final fracture. The final fracture stage happens very rapidly, hence total fatigue life is made up predominately of the time for crack initiation and the time for propagation until catastrophic failure occurs.

4.2.1 Fatigue Crack Propagation

Fatigue cracks may form and propagate as a result of an initiation event which may occur either on the surface or at an internal site within the material. Initiation events may include defects, surface flaws or inclusions which ultimately act as stress concentrations within the material and gives a favoured position for cracks to initiate.

Fatigue crack propagation is often described in terms of a relationship between the sub-critical fatigue crack growth rate (da/dN) and the stress intensity factor range (ΔK). A sigmoidal shaped curve is often used with the relationship between da/dN and ΔK plotted on a log-log scale.

When plotting the fatigue crack propagation on a log-log scale, three distinct regimes of crack growth transpire which is shown in Figure 4.2 [65]. Regime A is the threshold fatigue crack growth, regime B is the Paris regime and regime C is the catastrophic failure regime.

4.2.1.1 Threshold Region

In the threshold region, a crack growth threshold value is found (ΔK_{th}). Below this value, fatigue cracks are thought not to grow. There are many factors which influence ΔK_{th} but some of the most important factors include: stress ratio (R), microstructure, load history, strength or yield stress and environment [66]. For example, by increasing the R ratio, the ΔK_{th} may decrease due to reduced closure effect [67]. Above values of ΔK_{th}, there is a rapid increase in crack growth rate as the ΔK is increased until it enters the Paris regime whereby the crack growth rate evens out to become linear with ΔK. Understanding threshold behaviour and ΔK_{th} is useful to ensure that fatigue cracks will not propagate when a component is in service.

4.2.1.2 Paris Region

In the Paris regime there is often a linear log-log relationship between ΔK and da/dN crack growth rate. The relationship between fatigue crack growth and the stress intensity factor, K, was proposed by Paris and Erdogen [12] and given by the following equation:

$$\frac{d}{dN} = C(\Delta K)^{m} \qquad (Equation\ 4.8)$$

Where C and m are material constants, da/dN is the change in crack length per cycle and ΔK is the stress intensity factor range. The constants C and m are established using the linear regime of the fatigue crack resistance curve [68].

Within the Paris regime, the crack growth occurs perpendicularly to the applied load range due to the fact the plastic deformation is no longer limited to a few grain diameters. When the crack propagates in this manner, it is common for ripples known as striations to form on the fracture surface, although they tend to be much more visible on the fracture surfaces of FCC metals and alloys. Striations are essentially a result of the crack tip blunting (plastic deformation) and resharpening (slip) throughout each fatigue cycle from a plastic process as shown in Figure 4.3 [69]. Therefore these striations represent each individual fatigue cycle [70, 71]. Striations can be used to work out the average crack growth rate per cycle using the spacing between them. In this regime a continuum mechanism with striation crack growth dominates with crack growth rate being determined mainly by the stress intensity factor range ΔK [59].

Due to the fact there is a linear relationship between da/dN and ΔK, the Paris regime can be used to predict number of cycles to failure for a given stress range and crack shape using a defect tolerant approach. The number of cycles it would take to reach the critical crack length from the current crack length at a given stress range can be identified [68]. This is done by integrating the following equation:

$$\frac{d}{dN} = C(Y\Delta\sigma\sqrt{\pi a})^m \qquad (Equation\ 4.9)$$

Which leads to the equation:

$$\int_{a_0}^{a_f} \frac{da}{a^{m/2}} = CY^m\,\Delta\sigma^m\pi^{m/2}\int_0^{N_f} dN \qquad (Equation\ 4.10)$$

The final crack length, a_f, is calculated using the critical stress intensity factor (K_c) and the Paris constants m and C are calculated from the fatigue crack growth curve. For the final crack length, a_f, to be worked out using K_c, the following rearrangement of the critical stress intensity factor equation is used:

$$a_f = \frac{K_c^2}{Y^2\sigma^2\pi} \qquad (Equation\ 4.11)$$

4.2.1.3 Catastrophic Failure Region

In this region, crack growth propagation is unstable and occurs rapidly therefore making it very difficult to predict. For this reason, this region is largely unimportant in terms of design. The number of cycles and time spent in this region are discounted from any lifing calculations.

4.3 Fatigue Crack Growth in Titanium Alloys

Over the last few decades, a substantial amount of research has been carried out into the fatigue crack propagation behaviour of titanium alloys. Fatigue in titanium alloys in terms of initiation and propagation will be reviewed in the following sections.

4.3.1 Fatigue Crack Initiation and Crack Growth

In titanium alloys crack initiation and the growth of short cracks has been found to represent approximately >85 % of total life [72, 73] and hence shows the importance and significance of crack initiation on fatigue life. Factors within titanium alloys which influence crack initiation include microstructure and the associated crystallographic texture as this affects nucleation of cracks and the propagation of these into long cracks [73]. Fatigue crack initiation within titanium alloys is closely associated with occurrence of heterogeneous slip bands in the α phase. During fatigue cycles, intense slip bands are created and cracking occurs either on or parallel to these slip bands. This forms cracks as the slip bands interact with phase boundaries and deformation debris [74, 75]. Fatigue cracks can also initiate at the interface between the α phase and the transformed β phase if the applied stress is low, large planar α/β grain boundaries exist or there is large slip occurring at the interface [76, 77]. To inhibit fatigue crack initiation, the number of slip bands can be reduced which limits the size of shear [13]. This is done by altering the microstructure of the alloy. For example, by reducing the colony size, with the best example being Widmänstatten, the amount of slip is reduced.

In α/β titanium alloys the desired microstructure would be fine, small grains with short interfaces between the α and β and as little texture as possible as this limits both slip length and the formation of large interfaces between α and β[73].

4.3.2 Fatigue Crack Propagation

Once a crack has been initiated, the rate of crack growth propagation can be predicted with the use of linear elastic fracture mechanics (LEFM). On the fatigue crack growth resistance curve, when the fatigue crack growth rate is linear with the ΔK, it is known as the Paris regime. The crack propagates via transgranular crack growth perpendicularly to the applied stress cycles. In this regime for titanium alloys microstructure has been found to influence crack growth rates, particularly at low ΔK values. For example, crack propagation resistance in a β processed alloy is much greater than in an α or α + β processed alloy [5]. Liang et al (2016) [78] investigated the effect of microstructure on fatigue crack growth behaviour in the titanium alloy Ti 17. A β processed lamellar microstructure was compared to an α + β processed bi- model microstructure. Results found that for the lamellar microstructure, the crack growth rates were consistently lower compared to the bi-modal microstructure, therefore showing superior resistance to crack growth. The reason for this superiority was found to be a result of a largely deflected crack path. The deflected crack path was likely a result of the lamellar microstructure having large colonies of α acting as an effective slip barrier. This meant that the transmission of slip to neighbouring colonies was prevented. Hence, the crack would change direction when it reached a boundary between colonies. Crack paths in titanium alloys have been found to be strongly influenced by neighbouring colonies or grains [79].

The crack path for the bi-modal microstructure, whereby no obvious colonies had formed, was found to be much straighter, cutting through grains rather than going around them, resulting in a higher fatigue crack growth rate.

If fatigue crack growth rate is reduced, so that the rate is no longer linear to ΔK, it is no longer part of the Paris regime of the fatigue crack growth resistance curve. It is instead classed as the threshold region. Dubey et al (1996) investigated the effects of stress ratio and crack closure on threshold values in titanium alloys [80]. Results found that the fracture surface for all near threshold fatigue crack propagation tests of α/β titanium alloys appeared very flat and featureless with transgranular crack growth being the mechanism of crack propagation [80]. The stress intensity ratio, R, influenced the threshold value, ΔK_{th}, with higher R ratios resulting in lower threshold values usually attributed to reduced crack closure effects. The crack growth rates for ΔK values slightly above ΔK_{th} value were also higher in tests with higher R ratios [80, 81].

4.3.2.1 Effect of Dwell on Fatigue Crack Propagation

Dwell fatigue is a process whereby the fatigue life of the component is reduced due to presence of a dwell period during cyclic loading. Dwell refers to the section of the loading cycle in which a load is maintained for an extended period of time before the fatigue cycle begins again. It has been found that by introducing a period of dwell at the maximum tensile load, the fatigue crack propagation rate is usually increased when compared to normal fatigue crack growth without a dwell period present [82].

Cold Dwell Fatigue Mechanisms

Bache (2003) [82] conducted an investigation the cold dwell phenomenon in relation to titanium alloys. Theories regarding the cause of the dwell phenomenon included the effect of bulk constraint, the formation of brittle hydrides and the effect of quasi-cleavage facets. Component failures attributed to dwell fatigue were found to have cracks which had initiated sub-surface (away from where a maximum stress had been predicted to have been applied). Therefore dwell fatigue not only affects crack propagation but also crack initiation. As a result of cyclic stress redistribution, the formation of quasi-cleavage facets was found to be the reason behind sub-surface sites being the preferred location for cracks to initiate [82, 83]. The stress redistribution between neighbouring grains causes slip to occur on the basal plane. The initial facet size was a result of the common alignment of the basal plane between neighbouring α grains [15, 82, 84].

With regards to bulk constraint, initially, due to the components having large cross-sectional dimensions, the dwell phenomenon was thought to be a consequence of constraint and plain strain [82]. However a study using small geometry specimens [85] found that sub-surface cracks and failures still occurred. Further studies [86, 87] looking into the effect of bulk constraints found that quasi-cleavage facets and sub-surface cracks still were present. This therefore led to the conclusion that bulk constraint does not play a role in promoting dwell behaviour.

Dislocation pile ups in neighbouring grains result in the formation of quasi-cleavage facets as shown in Figure 4.4 [82]. This model proposed by Stroh [88] suggests that there are weak grains which are favourably orientated with the basal planes inclined to the principal stress. Slip occurs in the weak grains which leads to a pile up at the neighbouring grain boundary. Strong grains are grains that have a basal plane perpendicular to the principal stress. The pile up from the weak grains causes shear stress in the strong grains and leads to basal slip, perpendicular to the principal stress. This eventually produces facets which act as nucleation sites for fatigue cracks [82]. Due to the fact that basal slip planes are a result of the α phase, dwell sensitivity may be improved by controlling both the α phase content and the α colony size [15].

Furthermore, ample research has been conducted into the effects of interstitial elements on stress-strain behaviour in titanium alloys [42, 89]. Despite the addition of hydrogen, nitrogen and oxygen all improving yield and ultimate strength they cause a reduction in ductility. The addition of these interstitial elements can consequently result in brittle hydrides being formed. These brittle hydrides have been suggested to play a role in causing the dwell phenomenon [90]. However, they are very difficult to detect in titanium alloys and hence the exact role they play in terms of effect on dwell fatigue is vague.

An alternative reason for the cause of the dwell phenomenon is due to the effects of creep (time dependant deformation). Traditionally, creep was thought to occur at elevated temperatures. In titanium alloys though there have been numerous reports of cold dwell occurring meaning strain is accumulated under both static and cyclic loads at ambient temperatures due to planar slip damage [82, 91, 92].

The dwell phenomenon is relevant in gas turbine engines as in the 1970's two titanium alloy fan disks in Rolls-Royce RB 211 engine experienced unexpected and uncontained failures [93, 94]. These in-service failures were attributed to be the consequence of dwell fatigue. During a flight cycle, it is thought dwell fatigue would be most significant during take-off and the aeroplanes climb to maximum height. As a result of the incident in the 1970's, it was known that fatigue in titanium alloys could no longer be characterised by simple low cycle fatigue behaviour. Dwell periods during the flight cycle had dramatically affected the fatigue lifing behaviour [82].

Cold Dwell in Ti 6246

Ti 6246 has been found to be largely insensitive to the effects of dwell fatigue on crack growth rates at ambient temperatures[14]. Dwell at ambient temperature in Ti 6246 has previously been studied by Spence et al (1997) [14]. The study looked at the effects of two minute dwell holds with regards to both total cyclic life and crack growth rate. Temperatures investigated ranged between 20 and 150°C. Both notched and plain sided Ti 6246 specimens were involved in the study.

The plain sided test pieces were used to construct S-N curves, as shown in Figure 4.5, comparing both cyclic baseline loading and dwell loading whereby the dwell period was a 2 minute hold at peak load. All tests were carried out at 80^{o}C. Results showed that dwell lives did experience a slight reduction at high stress levels compared to baseline 15 cycles per minute trapezoidal loading. However, the reduction in life was only subtle being typically only a factor of between 1.5 and 2.2 times. At low stress levels, the regression lines appear to slightly converge together suggesting that as the stress was decreased so was the effect of dwell, with the lowest stress levels experiencing no dwell effect at all.

The effect temperature had on dwell sensitivity was also investigated. SN curves were created comparing tests carried out at 20, 80 and 150^{o}C under both dwell and cyclic conditions. Results were similar to the first SN curve produced at 80^{o}C, confirming that dwell loading had very limited effect on total life across a range of relatively low temperatures.

Furthermore, corner crack specimens with double edge notches were used in order to investigate the effect of dwell on fatigue crack growth rates by comparing dwell crack growth tests to cyclic crack growth. Results plotted on a da/dN vs ΔK curve showed how the crack growth rates for both dwell and cyclic loading were indistinguishable, again suggesting that at ambient temperatures, Ti 6246 is insensitive to dwell fatigue loading.

When comparing the fracture surfaces of both the dwell and cyclic tests, there were a number of common features. These included featureless quasi-cleavage facets which were most common at short crack lengths and near surface locations. In addition, large flat regions were common which displayed the underlying microstructure as shown in Figure 4.6. Finally, secondary cracking was apparent which was seen to mostly follow the interface between the α and β.

It has been suggested that the reason Ti 6246 is insensitive to effects of dwell is due to the processing route. For example, for a material to be dwell sensitive, within the microstructure, there must be stress redistribution between weak and strong sites. There must also be the possibility for separation to occur as a result of suitably orientated basal plane. With Ti 6246 having a high content of β stabilising element molybdenum and a very fine Widmänstatten microstructure, large regions of commonly orientated basal planes do not form[82, 95]. The dwell phenomenon at ambient temperature in other titanium alloys is found to be mainly due to regions of microtexture within the microstructure. Ti 6246 has a Widmänstatten microstructure which ensures microtexture is eliminated from the final microstructure and therefore reduces any dwell sensitivity.

Further research has been carried out into the effect of cold dwell fatigue (CDF) behaviour in a Ti 6246 alloy by Whittaker (2011) [96]. Results indicated that there was no effect of enduring long periods of CDF loading on the alloy with regards to cycles to failure. This conclusion was obtained based on the fact that not only was there no real reduction in cyclic life at high stresses when a dwell period was introduced but also the fact that there was an absence of load normal fatigue facets present on the fracture surface. These factors would be anticipated if material was sensitive to cold dwell fatigue. On the occasion cycles to failure were reduced when subject to a 2 minute cold dwell fatigue the premature failures were attributed to other factors. These included general yielding of the test specimens and also due to exhaustion of ductility as the stresses used for the test were close to the tensile strength. For these tests, a ductile microvoid coalescence failure mechanism was observed on the fracture surface again suggesting the alloy was not cold dwell sensitive.

Zheng et al (2017) [97] investigated mechanistic basis of temperature dependent dwell fatigue in the titanium alloys Ti 6246 and Ti 6242. An explanation was provided as to why Ti 6242 was dwell sensitive at ambient temperatures whereas Ti 6246 was not. It was argued that at lower temperatures load shedding occurred within in Ti 6242 with stress from soft grains being redistributed to neighbouring hard grains whereas this same load shedding did not occur at these temperatures in Ti 6246. Strongly linked with dwell sensitivity in these alloys is rate sensitivity for low strain rate regimes. This is controlled by dislocations escaping from pinned obstacles via thermal activation. The thermal activation energy resulting in dislocation escape for Ti 6246 is higher than it is for Ti 6242 due to the fine Widmänstatten microstructure. Therefore, in order to develop dwell sensitivity, higher operating temperatures are needed for Ti 6246 in order to achieve thermal activation which in turn would cause dislocations to escape from pinned obstacles. This suggests that at elevated temperatures, Ti 6246 may become dwell sensitive. Although it is noted that load shedding causing the dwell phenomenon as a result of thermal activation may become superseded in replacement for environmental factors at the elevated temperatures needed [97].

Elevated Temperature Dwell in Ti 6246

There has been a limited amount of research focusing on the effect of dwell on fatigue crack growth resistance at elevated temperatures in Ti 6246. Understanding the effects at elevated temperature is particularly important due to the application of the alloy, being used for a compressor disc. Evans (2004) [15] explored Ti 6246 high temperature sensitivities with temperatures ranging from 450 to 550°C via fatigue crack growth. The effect of creep and environmental influences were investigated throughout the study. Mechanical tests were carried out in both air and vacuum conditions as well as under cyclic and dwell fatigue loading cycles. Results are displayed in Figure 4.7. Findings showed how both environmental damage and creep affected crack growth rates. For example, results showed how by introducing a two minute dwell period in vacuum, the crack growth rate was increased by a factor of approximately four times compared to 1 Hz crack growth in vacuum. This increase in crack growth rate under dwell loading was found to be a result of creep.

The two minute dwell test in vacuum conditions was compared to a two minute dwell test in air in order to see the effect of the environment. It was found that the dwell test carried out in air had a crack growth rate approximately twice as fast as the test carried out under vacuum. The difference in crack growth rates between the two environments was deduced to be due to oxidation in the air test. It was also found that the introduction of dwell periods had the greatest effect on crack growth rate when the R ratio was higher, thought to be due to higher peak stresses being used. This was linked with more creep damage mechanisms being applied at the crack tip.

Finally, as previously mentioned, increases in crack growth rate when dwell periods were introduced was strongly linked to creep damage. This was reinforced on studying the crack obtained via metallographic sectioning. It was clear to see creep damage had occurred as separation at the interface between α and β ahead of the crack tip and in the matrix was observed as shown in Figure 4.8.

Chapter 5 - Experimental Methodology

5.1 Introduction

This study focuses on the titanium alloy Ti-6Al-2Sn-4Zr-6Mo (Ti 6246) used in compressor discs in the intermediate section of the compressor in gas turbine aero engines. Material was provided and processed by Rolls-Royce plc. with a nominal composition given in Table 5.1.

Ti 6246 is an α-β heat-treatable alloy which presents both the benefits from the high temperature strength capabilities of Ti-6Al-2Sn-4Zr-2Mo-0.08Si (Ti 6242S) with the short term, greatly improved strength capabilities found in a fully hardened α-β alloy. Furthermore, Ti 6246 can be adequately heat-treated in larger section sizes than the more commonly used Ti- 6Al-4V (Ti 64) with properties being influenced by the thermo-mechanical history and processing routes. Typical heat treatment conditions of Ti 6246 are shown in Table 5.2. The Ti 6246 provided by Rolls-Royce plc. was β processed allowing for the best combination of good low cycle fatigue and fatigue crack growth resistance to be achieved, resulting in a fully Widmänstatten microstructure.

5.1.1 β Processing Route

The processing route resulting in a fully Widmänstatten microstructure is shown in Figure 5.1. A homogenization treatment was applied in the β phase field following deformation in either the α-β or β phase field. The cooling rate from the homogenization temperature is crucial as this influences the final microstructure in terms of α lamella, α colony size and any α laths formed at the β grain boundaries. Following this, an ageing treatment or stress relieving treatment is usually applied. It is also possible to remove the homogenization step and perform aging directly following the β phase field deformation. However, this process is much more difficult to control and reproduce [98].

Mechanical properties are sensitive to microstructure with the fully lamellar structure being particularly influential due to the effects of α colony size. The colony size attained depends on the cooling rate from the β heat treatment. Colony size affects slip length and therefore affects yield stress. For example, a faster cooling rate results in smaller colony sizes which equate to smaller slip lengths and hence an increased yield stress.

5.1.2 Variation within the turbine entry temperature

During the course of each individual flight-cycle, components within the gas turbine engine are subject to a variety of temperatures from initial take off to landing (Figure 5.2) [16]. It is therefore crucial to test individual components at temperatures actually experienced throughout each flight-cycle. Temperatures chosen for this project were based on current and future operating temperatures compressor discs located in the intermediate pressure and front end of the high pressure compressor section of the engine are likely to be subject to.

5.2 Specimens

All Ti 6246 specimens were provided by Rolls-Royce plc. The specimens were approximately 88 mm in overall length with a gauge length of approximately 24 mm as displayed in Figure 5.3. Specimens provided either had a cross section of 7 x 7 or 10 x 10 mm^2. A sharp notch of depth approximately 0.2 mm was machined into one of the 4 corners of the specimen in the centre of the gauge length prior to being received to be used in corner crack mechanical tests. The adopted testpiece geometry typically results in a crack profile resembling a quarter circle. Square section test specimens were used for the project as previous crack growth data used for lifing of gas turbine discs were conducted using square section corner crack specimens and hence allows for consistency within the data.

5.3 Mechanical Testing

5.3.1 Mechanical Testing Preparation

Prior to mechanical testing, specimens were all ultrasonically cleaned using an ethanol bath to ensure all dirt was removed from the surface of the specimens. In order to measure changing crack lengths throughout all mechanical tests, the direct current potential drop (DCPD) technique was used [99, 100]. Two insulated platinum probe wires were spot welded to either side of the corner crack notch, approximately 0.1 mm apart. A constant current was passed through the specimen and as the crack length increased the electrical resistance was increased which lead to an increase in the potential difference (PD). The changing PD was continuously monitored on a chart recorder against a function of time. Following the test, the change in PD was converted to crack length based on an appropriate PD-crack length calibration curve for the specific specimen geometry. It was assumed based on previous work that a linear relationship exists between PD and crack length up until the crack reaches an a/W (crack length/specimen cross section width) of 0.5. The crack length at a given point (a_x) can be found using the following equation:

$$a_x = \left(\frac{(a^{2-a_1})}{(pd_2 - pd_1)}(\mathrm{PD}_x - \mathrm{PD}_1)\right) + a_1 \qquad (Equation\ 5.1)$$

Where a_1 and a_2 are the initial and final crack lengths respectively, PD_1 and PD_2 are the initial and final PD values respectively, and PD_x is the PD value at the chosen crack length a_x.

Prior to any mechanical testing, fatigue pre-cracking was carried out using an Instron 8501 servo-hydraulic machine in order to produce a straight and sharp fatigue crack. This ensured that both the calibration expression and crack tip shape were not influenced by the machined notch. A load shedding technique was used with the initial maximum load (Pmax) depending on whether the specimen was of 7 x 7 or 10 x 10 mm^2 geometry. For 7 x 7 mm^2 specimens the initial Pmax was 24 kN which corresponded to a ΔK of 10 MPa√m whereas for the 10 x 10 mm^2 specimens the initial Pmax was 38 kN which corresponded to a ΔK of 8 MPa√m . All pre-cracks were performed using a 10 Hz, sinusoidal waveform in laboratory air at room temperature. Pre-cracks were grown until a/W equalled approximately 0.1 for both 7x7 and 10x10 mm^2 specimens. This gave a pre-crack length of approximately 1.0 mm for the 10x10 mm^2 specimens and 0.7 mm for the 7x7 mm^2 specimens. Regardless of whether the following mechanical tests were performed at a stress ratio of 0.1 or 0.5, the pre-cracks were always performed in the same way with a stress ratio of $R = 0.1$.

5.3.2 Equipment

For all fatigue mechanical tests carried out similar equipment was used. High frequency tests carried out in laboratory air for the constant range load and threshold tests were performed using an Instron 8501 servo-hydraulic machine. The machine was equipped with a 50 kN load cell and had a vertically opening cylindrical book furnace which utilised indirect resistance heating. For elevated temperature tests carried out on this machine, the temperature was monitored using an N-type thermocouple with the tip of the thermocouple being in contact with the surface of the specimen in the centre of the gauge length. For room temperature tests, the furnace was left open. The testing procedure was controlled using the sinusoidal waveform controller within the Instron software package to produce a 10 Hz waveform for Paris regime tests and 15 Hz waveform for threshold tests.

For all mechanical tests carried out under vacuum conditions, a vacuum ESH machine equipped with a 50 kN load cell was used. Four lamps located within the vacuum chamber provided heat for elevated temperature tests. The four lamps worked via concentrated radiation. Temperature was monitored using an N-type thermocouple in a similar way to the tests carried out in laboratory air conditions. The testing procedure was controlled using either a sinusoidal or trapezoidal control panel on the vacuum machine dependant on the cyclic frequency of the particular test. 0.25 Hz tests used a trapezoidal waveform and 10 Hz tests used a sinusoidal waveform.

Finally, for low frequency, 0.25 Hz tests a four column slow ESH machine was used. The machine was equipped with a 50 kN load cell and had a vertically opening cylindrical book furnace fitted to it which was used to heat the specimen to the desired temperature. For elevated temperature tests, temperature was again measured using an N-type thermocouple with the tip of the thermocouple touching the specimen in the middle of the gauge length. For room temperature tests, the furnace was left open. The testing procedure was controlled using the trapezoidal waveform controller within the ESH software package.

All tests required the use of a chart speed recorder and a DVM monitor to measure the change in crack length via the change in PD.

5.3.3 Testing Procedure

Although there were three different types of mechanical tests carried out for this project (threshold, constant amplitude range and dwell tests) part of the testing procedure was similar and therefore will be discussed in this section.

For all 10 x 10 mm^2 specimens, a current of 14 A was used to pass across the specimen to measure the increasing crack length. For the 7 x 7 mm^2 specimens, a current of 7 A was used. In both cases this resulted in a voltage of between 2 and 3 V. For the stress ratio 0.1 tests, the starting ΔK was approximately 10 MPa√m. For the stress ratio 0.5 tests, the starting ΔK was approximately 7 MPa√m.

For all tests being carried out in laboratory air at elevated temperature, prior to the test beginning the specimen was held under a 1 kN load whilst the furnace was heated to the designated temperature. On reaching the correct temperature, the furnace was left for one hour to stabilise. Once this had been completed the mechanical test was started by increasing the load until the mean value was achieved. The potential difference (PD) reading at the mean load was recorded along with the speed of the chart speed recorder, frequency of the test, amps used, temperature and specific type of mechanical test. The test was then switched on.

For tests being carried out in laboratory air at room temperature, once the mean load had been added to the specimen and details mentioned such as initial PD at mean load and test type had been noted down, the test was started.

For tests being carried out under vacuum at both room and elevated temperatures a heat tint was performed after the pre-crack had been completed. This was so that the end of the pre-crack could be easily detected. The heat tint was performed once the specimen was loaded onto the vacuum machine. A 1 kN load was applied to the specimen and the furnace was heated to 450°C and left at this temperature for 30 minutes. The specimen was then left to cool to room temperature before vacuum conditions were applied. Only a partial vacuum could be achieved for all tests with a measured pressure of between 1E-04 and 1E-05 Mbar being reached. Once under a stable vacuum, the lamps were switched on if the test was being performed at elevated temperature and the temperature was left to stabilise for the further hour before beginning the test. If it was a room temperature test, once the vacuum had stabilised, the test was started immediately.

For the vacuum tests, once the test was completed the specimen was returned to air conditions and a further heat tint was performed to allow for the end of the fatigue crack to be visible. The heat tint was performed at a temperature of 410°C for 30 minutes. All tests, once completed, were broken open via fatigue cycling at room temperature in laboratory air conditions. A 10 Hz, sinusoidal waveform was used with an R ratio of 0.1.

5.3.4 Near Threshold Tests

Near threshold tests have been carried out under different conditions with different R ratios, temperatures and frequencies as shown in Table 5.3. A total of 10 near threshold tests were performed for the current study. The fatigue crack growth rates equating to the near threshold stress-intensity factor ΔK were investigated. This refers generally to the value of ΔK obtained as crack growth rate (da/dN) approaches zero. For all threshold tests, a load shedding technique was implemented with majority of tests focusing on a constant R ratio. However, one test had a fluctuating R ratio with a constant value for Kmax. All near threshold tests were conducted in laboratory air.

The equipment used for the near threshold tests has been previously discussed in the equipment section (section 5.3.2) of this chapter along with the beginning testing procedure (section 5.3.3) discussed in the testing procedure section in this chapter. For elevated temperature tests, once the temperature was stable the threshold test was started. For room temperature tests, the test could be started immediately.

Before a load shedding technique was applied to the specimen a constant load range waveform was applied to allow the crack to grow and the ΔK to increase. After the PD had grown by 30 mV, the load shedding procedure was introduced. For the constant R ratio threshold tests where R was either 0.1 or 0.5, the amount of reduction in Pmax was based on the compliance (Y), crack length (a), specimen geometry, ΔK and chosen R ratio. As the PD increased by 10 mV, the cycles were recorded and the mean load and amplitude were altered to meet the required Pmax and Pmin. For the constant Kmax test, Kmin was increased at each stage of the load shedding and so R ratio was also increasing. The reduction in load for the constant Kmax threshold test once the crack had grown 10 mV was related to crack length, specimen geometry and Kmax.

As the PD was increased by 10 mV the number of cycles was recorded and the crack growth rate was calculated in-situ with the test. This was worked out using the following equation:

$$\frac{da}{dN} = \frac{(a_2 - a_1)}{(cycles_2 - cycles_1)} \qquad (Equation\ 5.2)$$

Where a_1 and a_2 are crack lengths and $cycles_1$ and $cycles_2$ are number of cycles corresponding to those crack lengths. Near threshold values were met once da/dN was equal to approximately 1.00E-07 mm/cycle. Once this was achieved, the test was stopped. The final PD and number of cycles was recorded.

Near threshold tests were conducted in air environments only due to issues arising with PD in vacuum conditions. A fluctuating ghost voltage in vacuum conditions meant that the PD being read was not always accurate. As the load shedding technique used for near threshold tests relied on accurate PD readings, it meant that precise testing resulting in reliable data could not be achieved under vacuum conditions.

5.3.5 Constant Load Range Tests

For the current study, a total of 18 mechanical tests were carried out focusing on the Paris regime via constant load range testing. The conditions each of the individual tests were subject to is given in Table 5.4. Different temperatures were used to represent realistic conditions Ti 6246 may experience in service and also to test the elevated temperature capabilities of the alloy. Tests were either carried out in laboratory air or under vacuum to study the effects of environment. The cyclic frequency of the tests was either 0.25 Hz with a trapezoidal waveform or 10 Hz with a sinusoidal waveform. Finally, the R ratio for the tests carried out was either 0.1 or 0.5.

The equipment needed for the constant load range tests was previously stated earlier on in the chapter (section 5.3.2) along with the testing procedure (section 5.3.3). Once the elevated temperature tests were at the assigned temperature and were stable, the test was started. The room temperature tests were started immediately. As the load range was constant for the whole test, the test was left to run until the a/W was equal to approximately 0.5. The test was then stopped (left to cool to room temperature if needed) and fatigued open. The final number of cycles was recorded along with the number of cycles as the crack grew through each 10 mV.

5.3.6 Dwell Tests

In total, 6 dwell tests were carried out for the current study. The details of the conditions of the specific tests are given in Table 5.5. Similarly to the other mechanical tests, the equipment used and the starting testing procedure is given previously in this chapter (sections 5.3.2 and 5.3.3 respectively).

Dwell tests have been carried out as this procedure more accurately mimics a fatigue cycle likely to be placed on the compressor discs during service, in particular, during take-off and climb to full altitude. During all dwell tests, periods of baseline crack growth loading have been used and, in particular, to initiate crack growth after pre-cracking. This is carried out for several reasons. Firstly, it allows for a greater range of ΔK values to be covered in a shorter amount of time as baseline crack growth is used to grow the crack to the desired ΔK value. Exclusively using long dwell crack growth waveform would be extremely time consuming. Secondly, by alternating between baseline and dwell loading, beach lines are formed on the fracture surfaces which are used in measuring the crack length and therefore validating the PD-crack calibration curve. Finally, it allows for direct comparisons between baseline and dwell crack growth rates, as well as any unusual transition crack growth behaviour such as crack tip blunting and re-sharpening to be observed.

All dwell tests carried out followed a similar structure of alternating blocks of 0.25 Hz baseline crack growth and dwell crack growth. Tests were carried out with an R ratio of 0.1. Tests began with a period of 0.25 Hz frequency trapezoidal waveform as shown in Figure 5.4. Once the crack length had increased so that it equated to a given ΔK, a period of dwell crack growth was introduced. Kmax hold dwell tests consisted of a ramp up from minimum to maximum load in 1 second, a hold at Kmax for X amount of seconds, a ramp down from maximum to minimum load in 1 second and finally a hold at Kmin for 1 second as shown in Figure 5.5. For the Kmax dwell tests X was either 120 or 3600 seconds. For the Kmin dwell test, the maximum load was held for 1 second and minimum load was held for X amount of seconds with ramp up to maximum and down to minimum loads also being 1 second as shown in Figure 5.6. For the Kmin dwell test X was equal to 3600 seconds.

Depending on the specific test the number of blocks and length of dwell crack growth varied which was mostly due to time constraints. For 120 second dwell tests, one long segment of dwell fatigue crack growth followed a shorter period of baseline crack growth. Tests were finished with a short period of baseline crack growth. For the 3600 second hold at Kmin, there was a large segment of baseline crack growth before the dwell period was introduced so that higher values of ΔK could be investigated (ΔK ranged from 27 to 34 MPa√m) whilst under the Kmin dwell conditions. The test was finished with a short period of baseline crack growth. For the 3600 second hold at Kmax test in air, the test alternated between blocks of baseline and dwell loading three times, resulting in four blocks of baseline crack growth and three blocks of dwell crack growth. Further details of the combination between baseline and dwell crack growth can be found in the results section in Chapter 8.

All dwell tests were terminated when a predicted crack length, a/W, of 0.5 was reached. The final PD value and number of cycles were recorded. The number of cycles between the crack growth which equated to 10 mV was recorded for the whole test. Specimens were then fatigued open at 10 Hz.

5.3.7 Mechanical Testing Crack Calibration

Once all mechanical tests were finished and specimens were broken open, images were taken on the Keyence VHX-6000 digital microscope. Images were taken of the crack and of the entire fracture surface for each specimen. Images of the crack were used to measure the area of the quarter-circle crack using software on the Keyence microscope. Areas for the pre-crack and final crack were established for all tests as shown in Figure 5.7.

For dwell tests, beach marks were used to measure the area for each block of crack growth which alternated between baseline and dwell fatigue. The areas of the crack were then used to calculate the crack length at each section using the following equation:

$$a_1 = \left(\frac{rea_1}{(0.25\pi)}\right)^{0.5} \qquad (Equation\ 5.3)$$

Where a₁ is the crack length at a measured area of the quarter-circle crack. By using the final crack length and crack length after the pre-crack along with PD values, crack lengths at all PD values in between can be calculated and used to calibrate the results using the following equation:

$$a_x = a_i + \left(\frac{(a_f - a_i)}{(pd_f - pd_i)}(pd_x - pd_i)\right) \qquad (Equation\ 5.4)$$

Where a_x is the crack length of interest and PD_x is the PD value at a_x. a_f and a_i are the final and initial crack length values respectively along with PD_f and PD_i which are the final and initial PD values.

Once the correct crack lengths had been calibrated the compliance values and ΔK values can be adjusted. ΔK refers to the range of nominal stress intensity factor, K. K is calculated using the following equation:

$$K = \sigma\sqrt{\pi a}\, f\left(\frac{a}{W}\right) \qquad (Equation\ 5.5)$$

a is the crack length and W is the width of the specimen. The term $(\frac{a}{W})$ is a factor of compliance which is worked out for corner crack specimens using the following equation:

$$f\left(\frac{a}{W}\right) = 0.6799 + \left(0.119\left(\frac{a}{w}\right)\right) - \left(1.2266\left(\frac{a}{w}\right)^2\right) + \left(7.8729\left(\frac{a}{w}\right)^3\right) - \left(10.396\left(\frac{a}{w}\right)^4\right) + \left(4.714\left(\frac{a}{w}\right)^5\right) \qquad (Equation\ 5.6)$$

The stress intensity factor range, ΔK, can be found using the following equation:

$$\Delta = K_{max} - K_{min} \qquad (Equation\ 5.7)$$

Once the number of cycles had been determined for each recorded crack length and ΔK values were correct, a fatigue crack growth resistance curve can be created which plots crack growth rates (da/dN) as shown by Equation 5.2 against ΔK values. Curves are presented in a log-log plot with log(da/dN) on the ordinate and log(ΔK) on the abscissa.

5.4 Microstructural Characterisation

Prior to any mechanical testing, a comprehensive study of the microstructure of the Ti 6246 alloy was carried via combination of optical, SEM and TEM work. Metallographic slices were obtained by cutting thread rings from the specimen using a Struers Accutom-50 automated cutting machine with a Silicon Carbide disc under constant running coolant. These were then mounted in conductive Bakelite and polished following the procedure shown in Table 5.6. On finishing the final stage, samples were cleaned under running water, immersed in acetone and dried with a hot air current to prevent water marks staining the surface. Samples were then etched using Krolls reagent (2 % HF – 10 % HNO_3 solution). Assessment of microstructure was carried out on an XL-30 scanning electron microscope (SEM) with back scatter images being taken at varying magnifications.

This was to aid further understanding and interpretation of results from various mechanical tests. No significant load had been applied to the specimens used to analyse the microstructure under optical or SEM. The microstructure observed under TEM was a section from a specimen which had been subject to mechanical testing, hence had been under significant load.

5.4.1 Fractography

Following each fatigue test, one half of each specimen was observed under an XL-30 SEM with a 20 kV accelerating voltage and a 6mm spot size. Secondary electron (SE) images were taken of the fracture surface at a working distance of approximately 12 mm. Images were taken at high and low magnifications of locations equating to both high and low ΔK values as well as an overview of the whole crack shape. This was to examine the fracture mechanism throughout each mechanical test as well as any significant features. Striations on the fracture surface were also often observed and may provide validation of measured crack growth rates.

5.4.1.1 TEM

To look at the crack path of some mechanical tests to further investigate effects of oxidation and any subtle differences in crack growth mechanism, transmission electron microscopy (TEM) was used. The mechanical tests chosen to have detailed analysis on were the 0.25 Hz tests carried out at 500°C in vacuum and in air, R ratio 0.1.

Sample Preparation

Prior to TEM work being carried out, samples were prepared using a focused ion beam (FIB). Mechanical test specimens were cut using the Struers Accutom-50 automated cutting machine using a SiC disc so they were roughly 1 cm in height to fit in the FIB machine and cleaned in an ultrasonic bath. The FIB was then used to extract samples for the TEM from an area which equated to a predetermined ΔK value. The FIB lifts samples out to be used in the TEM in the following way:

1) The sample is tilted so that the area of interest is perpendicular to the ion beam used for milling.
2) A protective layer of tungsten (W) between 1 – 3 µm is added to the surface of the area of interest via a combination of the focused ion beam and W-precursor tungsten carboxyl ($W(CO)_6$). This is to ensure the area of interest is protected during the sputtering process.
3) Milling is carried out via a series of Ga-ion beams to create trenches surrounding the area of interest.
4) The sample is tilted to 7° and an undercut is performed on the area of interest. This is then lifted out of the main body of specimen using an omniprobe micromanipulator.
5) The small sample is then welded to a copper grid using FIB W-deposition and is ready for analysis using a transmission electron microscope (TEM)

The value of ΔK was kept similar for both mechanical tests being subject to TEM work in order for direct comparisons of the fracture surfaces to be made.

5.4.2 Interrupted Dwell Tests

To gain a better insight into what is happening during the dwell mechanical tests and to explain any differences in crack growth rates observed, interrupted mechanical tests were carried out. Fatigue pre-cracks were performed on an Instron 8501 servo-hydraulic machine at room temperature with an R ratio of 0.1. Once the crack had reached a size of 2 mm, the specimen was moved on to a Vacuum ESH machine. This machine was chosen for all interrupted mechanical tests regardless of whether the vacuum chamber was needed. Due to the fact the four lamps located within the chamber provide heat via concentrated radiation they could be switched off immediately once the test was complete. Therefore, the temperature within the chamber drops rapidly. This minimises the effects of exposing the specimen to elevated temperatures beyond the specific test conditions. One interrupted test was carried out in air conditions and one was carried out under vacuum conditions.

Once the specimen had been loaded into a Vacuum ESH machine, a 1 kN load was applied whilst the furnace was switched on to 500^{o}C. The temperature was left to stabilise for one hour before the test was started. A 5 Hz, sinusoidal wave form was applied with an R ratio of 0.1. Once the crack had grown to 3 mm in total the dwell period could be introduced. A trapezoidal waveform was used with a one hour dwell added at Kmax. The dwell period was added for a total of just less than five complete cycles. At the end of the fifth hold period, the test was stopped before it could complete the unload-reload cycle. The furnace was switched off to allow for the specimen to cool quickly thus not allowing the crack tip to further oxidise. The load was reduced to 1 kN whilst the furnace cooled to room temperature.

Once cooled, the specimen was removed from the machine and sectioned using a wire-cut electron discharge machine (EDM) with water as a dielectric fluid. The sectioning occurred so that the crack was split into two halves with profiles of the crack path present, rather than exposing the fracture surface. The specimens were then mounted in conductive Bakelite and ground and polished using the procedure outlined above in Table 5.6. A FIB was used to extract samples to be studied under TEM. The differences in the crack tip from the interrupted tests were compared.

5.4.3 Oxidation Studies

To consider oxidation effects, heat treatments were carried out on plain sided Ti 6246 slices. Slices were cut from the thread of the Ti 6246 specimen using the Struers Accutom-50 automated cutting machine with a SiC disc. Slices were then ground and polished using the method previously mentioned in Table 5.6. The slices were then placed in a ceramic boat and put inside a ceramic-lined furnace which was then heated to 500^{o}C for either 1 hour or 2 minutes. After the designated time at 500^{o}C, the slice was removed from the furnace and left to air cool. The slices were then put into a FIB to have “lift outs” taken from them so they could be examined under TEM. EDX was used to measure the thickness of the oxide layer formed on the surface of the slices.

Chapter 6 - Results – Microstructure and Near Threshold Testing

Within this first results chapter, as well as results from near threshold tests, the opportunity to include results on microstructure of Ti 6246 will be utilised. Optical microscopy and scanning electron microscopy (SEM) micrographs of the microstructure of Ti 6246 are shown in Figures 6.1 and 6.2 respectively. Note that on the micrograph from the optical microscope in Figure 6.1 the α phase appears light and the β phase appears dark. Whereas on micrographs from the SEM shown in Figure 6.2 the opposite is true so the α phase appears dark and the β phase appears light. The microstructure of the Ti 6246 used throughout this project is Widmänstatten with coarse needle like primary α laths within a fully transformed β matrix. The Widmänstatten microstructure is made up of coarse primary α laths and continuous fine secondary α laths within the transformed β matrix. Transformed β refers to regions that before cooling were β phase, for example, at the solution treatment temperature, annealing temperature or finishing temperature of the hot working operation. Dependent on the cooling rate from these temperatures the morphology of the β phase changes to become transformed β. A slow cooling rate will see β transform to Widmänstatten α laths, as seen in this project, via nucleation and growth which is seen in Figures 6.1 and 6.2.

From this, the assumption is that the α laths nucleated from the β grain boundaries to lead to parallel colonies being formed which in turn grew towards the centre of the prior β grain [101-103]. In the centre of the grain the α laths develop in a Widmänstatten structure.

Prior β grain size is known to be approximately 500 µm across [104, 105]. Under SEM as shown in Figure 6.2 it is possible to see the coarse α laths as well as finer precipitating secondary α laths within the β matrix. The volume fraction of the transformed β matrix was measured to be approximately 70 % with the volume fraction of primary α phase being found to be approximately 30 %. This was established using a binary image of one of the SEM images taken as shown in Figure 6.3.

As well as optical and SEM images, TEM was carried out on the microstructure of Ti 6246 as shown in Figure 6.4. From this figure, along with Figure 6.2, the thickness of the primary α laths were measured. The average thickness of primary α laths was found to be approximately 1.62 µm. Secondary α within the β matrix is also clearly visible in Figure 6.4.

6.1 Introduction to Near Threshold Testing

Having a clear understanding on the near threshold region of fatigue crack growth in the titanium alloy Ti 6246 is vital and plays a key role in the fatigue life of a component. The threshold value usually indicates a ΔK in which the crack growth is equal to or below 2.00E-08 mm/cycle. For the present study, near threshold ΔK values were achieved due to time constraints, with tests ending on a crack growth rate of 1.00E-07 mm/cycle.

By understanding how different conditions affect ΔK_{th}, such as the effect of frequency or temperature, it is possible to understand when a crack is likely to propagate and when it will arrest. In order to understand the threshold value, mechanical tests were carried out at either room temperature or 500^{o}C, at 0.25 Hz or 15 Hz and at an R ratio of either 0.1 or 0.5. A constant Kmax threshold test has also been carried out which saw the R ratio increase from 0.1 to 0.87 over the course of the test.

6.2 Effects of R Ratio

Figure 6.5 depicts all of the threshold tests which have been carried out during this study at a cyclic frequency of 15 Hz. This includes tests carried out at R ratios of 0.1 and 0.5. Furthermore, the constant Kmax test is also plotted whereby the R ratio was constantly changing in order to keep Kmax constant. By looking at the effect of R ratio, it is clear that there are only some modest differences between the two values of 0.1 and 0.5. But as the R ratio increases in the constant Kmax test from 0.1 to 0.87, the effects increase.

Figure 6.6 shows results from specimens CX 036 and CX 018 which were tested with R ratios of 0.1 and 0.5 respectively at a temperature of 500°C and a frequency of 0.25 Hz. The ΔK_{th} values are given as 3.4 MPa√m for CX 036 and 3.1 MPa√m for CX 018. The crack growth rates before the drop off to threshold occurred are almost identical. For example, at a ΔK of 4 MPa√m, both conditions have a crack growth rate of approximately 3.00E-5 mm/cycle.

For the 15 Hz, 500°C tests, specimens CX 043 and CX 039 were tested at an R ratio of 0.1 and specimen CX 014 was tested at an R ratio of 0.5. Tests have a ΔK_{th} of 4.1, 3.8 and 3.2 MPa√m for CX 043, CX 039 and CX 014 respectively as shown in Figure 6.7 showing that at 15 Hz, R ratio has only a modest effect on ΔK_{th}. However, unlike the 0.25 Hz, 500°C whereby crack growth rates at ΔK values just above threshold values were indistinguishable, the crack growth rates for the 15 Hz tests are slightly different. For example, at a ΔK of 5 MPa√m, the R ratio 0.5 test has a crack growth rate of 2.00-05 mm/cycle whereas the R ratio 0.1 tests has crack growth rates of 1.50E-05 mm/cycle.

When comparing the different R ratios for the room temperature, 15 Hz tests, again there was no observed difference for ΔK_{th} as shown in Figure 6.8. CR 069 was tested at an R ratio of 0.5 with CR 065 and CR 067 being tested at R ratios of 0.1. The ΔK_{th} values for CR 069, CR 065 and CR 067 were 2.8, 2.8 and 3.1 MPa√m respectively. The crack growth rates at low ΔK values as the crack growth rate reduced to ΔK_{th} were also very similar for both R ratio of 0.1 and 0.5 tests. For example, at a low ΔK of 4 MPa√m, the crack growth rates for CR 069 and CR 065 are both approximately 2.00E-6 mm/cycle.

Figure 6.5 displays results from the constant Kmax threshold test. It is clear to see that by increasing the R ratio in order to maintain Kmax, the ΔK_{th} is greatly reduced. Specimen CX 021 was used to carry out this test at 500°C, 15 Hz. For this test, the Kmax was kept consistently at 12.5 MPa√m, to ensure Kmax was not close to K_{1c} for Ti 6246 which is given as 34 MPa√m [43]. The initial R ratio was 0.1 and the final R ratio was 0.87. The ΔK_{th} was significantly reduced to 1.5 MPa√m. Up until a ΔK of 4 MPa√m, the crack growth rate for the constant Kmax test was similar to the other threshold tests carried out at 500°C. However, below a ΔK of 4 MPa√m, the constant R ratio tests started to drop off in crack growth rate as they neared ΔK_{th}. However, for the constant Kmax test, the crack growth rate continued to decline steadily until it reached a ΔK of 2 MPa√m. This was when the crack growth rate started to drop off sharply as it neared ΔK_{th}.

Figure 6.9 shows optical and SEM images taken of CX 021 which was the constant Kmax threshold test. From the SEM images it is clear to see that the crack growth was transgranular. Symmetrical crack growth was achieved forming a uniform crack front.

To summarise the effect of R ratio in terms of threshold value obtained, there is very little difference between carrying out tests at either 0.1 or 0.5 R ratio values. Having a constant Kmax test that ended on a much higher R ratio of 0.87 did affect the ΔK_{th} as ΔK_{th} was greatly reduced in this test.

6.3 Effects of Frequency

The effects of cyclic frequency on ΔK_{th} has been investigated by comparing mechanical tests carried out at 500°C at frequencies of both 0.25 and 15 Hz. Specimen CX 036 was tested at 500°C at 0.25 Hz and as previously mentioned CX 043 and CX 039 were tested at 500°C at 15 Hz. All were carried out at R ratios of 0.1. Looking at Figure 6.10, it is clear to see there are differences between crack growth rates as they near ΔK_{th}. For example, at a ΔK of 5 MPa√m, the 0.25 Hz test crack growth rate is 6.00E-05 mm/cycle whereas the crack growth rate for both the 15 Hz tests is 1.50E-05 mm/cycles. However, despite this difference in crack growth rates at low ΔK values, the ΔK_{th} obtained by both tests is fairly similar. For the 0.25 Hz test, the ΔK_{th} is found to be 3.5 MPa√m whereas the ΔK_{th} for the 15 Hz tests is found to be either 3.8 or 4.1 MPa√m, depending on the specific test specimen. For the 0.25 and the 15 Hz tests, the reduction in crack growth rate as it approached threshold is very similar with all tests seeing a sharp drop off in rate rather than a gradual decline.

Figure 6.11 shows the optical and SEM images taken of specimen CX 043 which was tested at 15 Hz, 500°C. From the images it is clear to see that the crack grew symmetrically in all directions, creating an even quarter circle. The fracture surface appears very flat and smooth, particularly at the near threshold region. The crack growth mechanism is transgranular. Figure 6.12 shows optical and SEM images obtained of specimen CX 036 which was tested at 0.25 Hz at 500°C. From this it seems that the fracture surface, although still transgranular crack growth, appears slightly rougher than the 15 Hz tests.

The effects that cyclic frequency had on the threshold region for tests carried out at an R ratio of 0.1 read across into results for tests carried out at an R ratio of 0.5. Results for 15 and 0.25 Hz tests are shown in Figure 6.13. It is clear that at an R ratio of 0.5, similarly to R ratio 0.1, frequency does not influence ΔK_{th}. However, despite having very similar ΔK_{th} values, at low ΔK values, before the drop off to ΔKth, the crack growth rates were different for the 0.25 and 15 Hz tests. For example, at a ΔK of 4 MPa√m, the 0.25 Hz test had a crack growth rate of 3.00E- 05 mm/cycle whereas the 15 Hz test had a crack growth rate of 1.70E-05 mm/cycle. The ΔK_{th} values were given as 3.1 and 3.2 MPa√m respectively. This is similar to results found for the R ratio 0.1 tests.

In summary at both R ratios of 0.1 and 0.5, changing the frequency affected crack growth rate at low ΔK values but did not influence the ΔK_{th} as these were found to be very similar for both high and low frequency tests. Having a reduced frequency increased the crack growth rates more prominently at low values of ΔK. However, despite this difference in crack growth rate at low ΔK values, the sharp drop off in rate down the ΔK_{th} occurred at similar points giving a very similar ΔK_{th} for both high and low frequencies.

6.4 Effects of Temperature

The effect of temperature on ΔK_{th} was investigated by comparing 15 Hz frequency tests at room temperature (CR 065, CR 067) and 500°C (CX 043, CX 039) for an R ratio of 0.1. Results are shown in Figure 6.14. The ΔK_{th} values were 2.9 and 3.1 MPa√m for the room temperature tests and 3.8 and 4.1 MPa√m for 500°C tests. The fact that the elevated temperature tests had higher ΔK_{th} values as well as having higher crack growth rates than the room temperature was unusual. The crack growth rates for the elevated and room temperature tests are seen to cross over at low ΔK values, which is uncommon.

Despite ΔK_{th} values being similar for all tests, the crack growth rates just above ΔK_{th} were different. For example, at a ΔK of 5 MPa√m, the 500°C tests had a crack growth rate of 1.50E- 05 mm/cycle whereas at the equivalent ΔK of 5 MPa√m, the room temperature tests had an average crack growth rate of 2.50E-06 mm/cycle. The drop off in crack growth rate as the crack approached ΔK_{th} was very different for both tests. The elevated temperature test saw a sharp drop off in crack growth rate down to ΔK_{th} whereas the room temperature test saw a gradual reduction in crack growth rate.

At higher ΔK values of 10 MPa√m, the difference in crack growth rates for the room temperature and 500^{o}C tests were reduced as crack growth rates converged. Despite temperature affecting crack growth rate at near threshold ΔK values, ΔK_{th} did not vary significantly as a result of changing temperature.

Figures 6.15 and 6.11 show optical and SEM images obtained of CR 065 and CX 043 respectively. It is clear from images taken of both room and elevated temperature tests that as threshold is reached, the fracture surfaces are both very flat and smooth with the underlying microstructure visible on both samples. The fracture mode was transgranular. There was no obvious difference between the 2 fracture surfaces despite the difference in test temperature.

This story is consistent for the R ratio 0.5 tests with elevated temperature tests having a slightly higher ΔK_{th} than the room temperature test despite having a much higher crack growth rate in the near threshold region. Similarly to the R ratio 0.1 tests, the rates from the elevated temperature and room temperature tests do cross over as can be seen in Figure 6.16.

In summary, the crack growth rates as the rate descends down to ΔK_{th} value are influenced greatly by the temperature of the mechanical test. For example, elevated temperature tests see a sharp and sudden drop off down to ΔK_{th} whereas the room temperature tests see a much more gradual decline in rate as ΔK_{th} is approached. Despite there being a large difference in

crack growth rates as threshold is approached, the ΔK_{th} achieved at both elevated and room temperatures are fairly similar, with the threshold value for the room temperature tests being only slightly lower than the elevated temperature tests. This is found for both R ratios of 0.1 and 0.5.

6.5 Summary

The way the ΔK_{th} value is affected as a result of changing R ratio, frequency and temperature within this study of Ti 6246 can be summarised in the following way:

1) At both room and elevated temperature, increasing the R ratio from 0.1 to 0.5 has only very modest effects on ΔK_{th}. However, by increasing the R ratio further, to 0.87, the ΔK_{th} can be greatly reduced.
2) Reducing the frequency from 15 Hz to 0.25 Hz at 500°C again caused little change to the ΔK_{th} value. At low ΔK values, the 0.25 Hz frequency test did have a slightly faster crack growth rate than the 15 Hz tests. However, when all tests reached a similar ΔK value, found to be approximately 4 MPa√m, they experienced a sharp drop off in crack growth rate down to ΔK_{th}. This sudden drop off in crack growth rate resulted in ΔK_{th} values being similar for both frequencies. This was true for tests carried out at R ratios of both 0.1 and 0.5.
3) By increasing the temperature from room temperature to 500°C, the ΔK_{th} values obtained for both 0.1 and 0.5 ratio tests were very slightly increased. However, the largest difference as a result of increasing the temperature was observed as crack growth rate approached ΔKth. For example, the room temperature tests saw a gradual decline in crack growth rate down to ΔKth whereas the elevated temperature tests saw a very sudden drop off in crack growth rate. Despite there being a large difference in crack growth rate at low ΔK values, the actual ΔK_{th} values achieved were very similar.

Chapter 7 - Results - Constant Load Range Testing

7.1 Introduction

The understanding of the Paris Regime segment during crack propagation whereby there is a linear relationship between crack growth rate and ΔK is essential for all alloys being used in gas turbine engines. It is imperative to understand how Ti 6246 used for compressor discs behaves under different conditions to allow for optimum use of the alloy within the engine and to accurately predict component life. A variety of temperatures were chosen to investigate which ranged from room temperature to 575°C. The primary focus of the project however was 500°C as this is similar to operating temperatures experienced by Ti 6246 compressor discs. In order to investigate the capabilities of Ti 6246 at higher temperatures, mechanical testing was carried out at 575°C. The effects of temperature, stress ratio, environment and frequency on crack propagation were all investigated. Table 7.1 summarises the results for the Paris regime for all the testing conditions with constants from the Paris relationship ($da/dN=C(\Delta K)^m$) given for each individual mechanical test.

7.2 Effects of R Ratio

The effect of R ratio was explored by comparing crack growth rates for constant load range tests carried out at R ratios of 0.1 and 0.5. Tests were performed in air and vacuum conditions at high and low cyclic frequencies. Figures 7.1a and 7.1b show results for the R ratio 0.1 and

0.5 tests carried in air whereas Figures 7.2a and 7.2b show results for the R ratio 0.1 and 0.5 tests carried out under vacuum conditions.

7.2.1 Tests in Air Conditions

Results for mechanical tests carried out in air at R ratios of 0.1 and 0.5 are shown in Figure 7.1a. For the tests at 500°C, 0.25 Hz, there was no difference in crack growth rate between the R ratios of 0.5 and 0.1. This suggests that for those conditions, R ratio had very little influence on crack growth rate. Optical and SEM observations of the fracture surfaces for the 500°C, 0.25 Hz tests at R ratios of 0.5 (CX 020) and 0.1 (CR 061) are shown in Figures 7.3 and 7.4 respectively. It is clear that for both conditions the fracture mechanism is transgranular. The two fracture surfaces look very similar to each other as they are both flat and featureless. The crack in both specimens has grown uniformly, creating an even quarter circle in both cases.

As the frequency is increased to 10 Hz, there is a slight difference in crack growth rate between the two different R ratio conditions as shown in Figure 7.1a. For example, at a ΔK of 12 MPa√m, the crack growth rate of the R ratio 0.5 test is roughly 8.50E-05 mm/cycle whereas the R ratio 0.1 test has a crack growth rate of 5.50E-05 mm/cycle. When the ΔK is increased to 20 MPa√m, the R ratio 0.5 tests crack growth rate is 3.50E-04 mm/cycle whereas the R ratio

0.1 tests crack growth rate is 2.60E-04 mm/cycle. Figures 7.5 and 7.6 show optical and SEM images of the fracture surfaces for the 10 Hz tests at R ratios of 0.5 (CX 070) and 0.1 (CX 034) respectively. Similarly to the 0.25 Hz tests, the fracture surfaces for both mechanical tests show transgranular fracture. Both the fracture surfaces are very similar to each other and there are no obvious differences between high and low values of ΔK with the fracture surface appearing flat. Again the cracks have grown symmetrically, creating an even quarter circle.

Figure 7.1b compares R ratios 0.1 and 0.5 in air at room temperature. 0.25 and 10 Hz frequencies are shown in this figure. When considering the room temperature tests at 0.25 Hz, similarly to the elevated temperature tests, there is very little difference in crack growth rates between the R ratio 0.5 and 0.1 tests. However, as the frequency was increased to 10 Hz, there is a very modest difference in rate with the R ratio 0.5 test showing a slight increase in crack growth rate. For example, at a ΔK of 13 MPa√m, the R ratio 0.5 tests crack growth rate is 5.00E-05 mm/cycle whereas the R ratio 0.1 tests crack growth rate is 4.00E-05 mm/cycle. When the ΔK was increased to roughly 22 MPa√m, the R ratio 0.5 tests crack growth rate is 2.80E-04 mm/cycle whereas the R ratio 0.1 tests crack growth rate is 1.80E-04 mm/cycle. The crack growth mechanism for all mechanical tests carried out at room temperature remained as transgranular.

7.2.2 Tests in Vacuum Conditions

Figure 7.2a shows all the results for R ratio 0.5 and 0.1 mechanical tests carried out in vacuum at 500^{o}C. When comparing the two tests carried out at 500^{o}C with a 0.25 Hz frequency, at a low ΔK value of 12 MPa√m, the R ratio 0.5 tests crack growth rate is 5.00E-05 mm/cycle whereas the R ratio 0.1 tests crack growth rate is 3.50E-05 mm/cycle. When the ΔK is increased to 20 MPa√m, the R ratio 0.5 tests crack growth rate is 2.70E-04 mm/cycle whereas at the R ratio 0.1 tests crack growth rate is 2.00E-04 mm/cycle. The difference in crack growth rate between the two R ratio conditions was modest but consistent across a range of ΔK values.

When looking at the higher frequency 10 Hz tests at 500^{o}C, there was no obvious difference in crack growth rate between R ratios of 0.1 and 0.5 across a range of ΔK values. The two crack growth rates were very similar as seen in Figure 7.2a.

Figure 7.2b shows results from both R ratios of 0.1 and 0.5 where tests were carried out in vacuum conditions at room temperature and at frequencies of either 0.25 or 10 Hz. The tests carried out at 0.25 Hz at room temperature saw a more notable difference in crack growth rate between the two R ratios. For example the crack growth rate at a ΔK of 13 MPa√m for the R ratio 0.5 is 3.80E-05 mm/cycle whereas the R ratio 0.1 tests crack growth rate is 1.80E-5 mm/cycle. As the ΔK increases, the two crack growth rates converge. For example, at a ΔK of 22 MPa√m, the growth rate for the R ratio 0.5 test is 2.00E-04 mm/cycle whereas the R ratio 0.1 tests crack growth rate is 1.40E-04 mm/cycle.

Finally, at room temperature, 10 Hz crack growth rates for both R ratio 0.5 and 0.1 tests are very similar. For example, at a ΔK of 12 MPa√m, both crack growth rates are approximately 1.70E-05 mm/cycle. As the ΔK is increased to roughly 24 MPa√m both crack growth rates were approximately 1.30E-04 mm/cycle.

7.2.3 Summary

To summarise, altering the R ratio for many conditions such as 0.25 Hz in air at both 500°C and room temperature did not affect crack growth rate in the Paris regime. However, for some conditions, such as 10 Hz in air at both room temperature and 500°C, altering the R ratio did have a subtle effect on crack growth rate in the Paris regime. The R ratio of 0.5 gave a faster crack growth rate than R ratio 0.1. However, any differences observed in fatigue crack growth rate were very modest. In air the largest difference between the R ratios was seen at a frequency at 10 Hz. Under vacuum conditions, the largest difference was seen at low values of ΔK and as ΔK increased, the effects of R ratio on crack growth rate were reduced as crack growth rates converged.

Therefore, with altering the R ratio either not affecting fatigue crack growth rate or only affecting the rate very subtly in specific conditions, it can be assumed that R ratio is not a large factor to consider in the Paris regime of Ti 6246 in terms of fatigue crack growth rate.

7.3 Effects of Environment and Cyclic Frequency

By carrying out mechanical tests in vacuum at a frequency of 0.25 Hz, base levels of fatigue crack propagation can be obtained and compared to tests carried out in air conditions and at higher frequencies. This allows for any direct contribution of the environment on crack propagation to be established. Very similar trends were seen for tests carried out at R ratios of 0.1 and 0.5 and so the primary focus of this section will be on R ratio of 0.1.

7.3.1 R ratio 0.1

Specimens CX 022, CX 037, CR 068 and CR 072 were all used for constant load range tests carried out under vacuum conditions with an R Ratio of 0.1. Specimens CR 063, CX 033, CX 034 and CR 061 were all used for constant load range tests carried out in laboratory air. The temperature for majority of tests was either 500^{o}C or room temperature. However, one test was carried out at 450^{o}C and one test was carried out at 575^{o}C . Either a baseline frequency of 0.25 Hz or a higher frequency of 10 Hz was applied to the specimens. Figures 7.7 and 7.8 show the results obtained from mechanical tests at both 500^{o}C and room temperature respectively. Both figures show tests carried out at an R ratio of 0.1. Across all conditions it is found that mechanical tests carried out in air had a faster crack growth rate than tests carried out under vacuum when other testing parameters were similar. The difference between the environments was greatest at low ΔK values with crack growth rates converging at higher values of ΔK.

For example, at 500°C, the 0.25 Hz test in air has a crack growth rate of 2.00E-04 mm/cycle at a ΔK of 12 MPa√m whereas at the equivalent ΔK the vacuum test has a crack growth rate of 4.00E-05 mm/cycle. As the ΔK is increased to 40 MPa√m, the difference in crack growth rate is greatly reduced. For example, the air test has a crack growth rate of 1.80E-03 mm/cycle whereas the vacuum test has a crack growth rate only slightly lower at 1.30E-03 mm/cycle. The fracture surfaces for both 0.25 Hz tests carried out at 500°C in air (CR 061) and vacuum (CX 037) conditions are shown in Figure 7.4 and 7.9 respectively. Both appear similar and show a transgranular crack growth mechanism. Both are relatively flat and featureless. However, as the ΔK was increased in the air test it is possible to see more secondary cracking and tearing. For the vacuum test there is no obvious secondary cracking at either high or low ΔK locations.

A similar pattern emerged for the 10 Hz tests regarding the effect of environment with tests converging as the ΔK increased for the 500°C tests as shown in Figure 7.7. At a low ΔK of 12 MPa√m, the air test has a crack growth rate of 5.80E-05 mm/cycle whereas the vacuum test has a crack growth rate of 2.00E-05 mm/cycle. As the ΔK increased to 35 MPa√m, the difference in crack growth rate between the 2 conditions is reduced. The air test has a crack growth rate of 9.00E-04 mm/cycle whereas the vacuum test has a crack growth rate of 6.00E- 04 mm/cycle.

At room temperature, as shown in Figure 7.8, environment does affect crack growth rate. As, similar to the 500°C tests, at low ΔK values, air tests have a faster crack growth rate than tests carried out under vacuum conditions. As the ΔK is increased, the crack growth rates converged. For example, for the 0.25 Hz tests in air and vacuum, at a ΔK of 15 MPa√m, the air test has a crack growth rate of 7.50E-05 mm/cycle whereas the vacuum test has a crack growth rate of 2.00E-05 mm/cycle. As the ΔK increased to 40 MPa√m, the air test had a crack growth rate of 8.00E-04 mm/cycle and the vacuum test now had a crack growth rate of 5.00E-

04 mm/cycle. A similar pattern was observed at a frequency of 10 Hz as shown in Figure 7.8. Figures 7.10 and 7.11 show the fracture surfaces for the air (CX 033) and vacuum (CR 068) tests carried out at 0.25 Hz at room temperature. The fracture mechanism is transgranular for both tests. Figure 7.10 of the test carried out in air shows significantly more secondary cracking at high ΔK values than Figure 7.11 which shows the vacuum test. The 10 Hz room temperature tests also tell a similar story with the largest impact of environment occurring at low ΔK values. As the ΔK is increased, the crack growth rates converge.

As well as the effect of environment, the effect of frequency is also considered in the Figures 7.7 and 7.8. At 500^{o}C, frequency plays are role in affecting crack growth rate, particularly in air environments. In air, the 0.25 Hz test has a crack growth rate of 2.50E-04 mm/cycle at a ΔK of 15 MPa√m. The 10 Hz test, at the same ΔK, has a crack growth rate of 1.30E-04 mm/cycle. As the ΔK is increased to 35 MPa√m, the crack growth rates converge with the 0.25 Hz test having a crack growth rate of 1.30E-03 mm/cycle and the 10 Hz test having a crack growth rate of 1.00E-03 mm/cycle. In vacuum conditions, the crack growth rates between the 2 different frequencies are fairly similar with the 0.25 Hz test only being slightly faster throughout the test.

At room temperature, the differences in crack growth rates as a result of frequency are reduced. Tests carried out in air at frequencies of 0.25 and 10 Hz have very similar crack growth rates throughout the test, as do 0.25 and 10 Hz tests carried out under vacuum conditions. These results of crack growth rates, across both 500^{o}C and room temperature, suggests that the environment has more of an impact on crack growth rate than frequency does both at room and elevated temperatures. When comparing different frequencies, all crack growth rates were relatively similar, with less variation found.

7.3.2 R ratio 0.5

Figures 7.12 and 7.13 show results looking at both the effect of environment and cyclic frequency for tests carried out at an R ratio of 0.5 at 500°C and room temperature respectively. From these figures it is clear that they follow a similar pattern to the tests carried out at an R ratio of 0.1. In terms of the effect of environment, when the tests were carried out at 500°C, for tests carried out at 0.25 and 10 Hz frequencies the air tests had a faster crack growth rate than the equivalent tests carried out under vacuum conditions. Similarly to the R ratio 0.1 tests, the largest effect of environment is found at low ΔK values. As the ΔK is increased, crack growth rates are seen to converge. At room temperature the results are also similar to those found in the R ratio 0.1 tests. At low ΔK values, the tests carried out in air have a faster crack growth rate than those carried out under vacuum. As the ΔK is increased, the crack growth rates converge.

The effect frequency has on fatigue crack growth rate is also similar to results found for the R ratio 0.1 tests. For both vacuum and air conditions at 500°C, the 0.25 Hz test has a faster crack growth rate than the 10 Hz test as shown in Figure 7.12. The largest differences in crack growth rate our observed at low ΔK values. As ΔK increases, crack growth rates converge. At room temperature, the air tests with frequencies of 0.25 and 10 Hz have very similar crack growth rates throughout the test. The tests carried out under vacuum conditions have a slight difference in crack growth rate due to frequency however it was only modest. The largest difference in crack growth rate is observed at low ΔK values and as the ΔK increases, the crack growth rates converge. Finally, similarly to the R ratio 0.1 tests, results show that altering the environment has a larger impact on influencing the crack growth rate compared to altering the frequency.

7.3.3 Summary

In summary, the environment mechanical tests are carried out in does influence crack growth rate. Across both R ratios of 0.1 and 0.5, the tests carried out in air conditions rather than vacuum conditions are found to have faster crack growth rates. The influence of environment is larger when tests are carried out at elevated temperature rather than room temperature. For example, at 500°C, 0.25 Hz, the fatigue crack growth rate of the air test was increased by a factor of six compared to the vacuum test at a ΔK of 12 MPa√m. At room temperature, at a ΔK of 12 MPa√m, the crack growth rate for the air test is only increased by a factor of three compared to the vacuum test. Across all conditions however, as the ΔK increases, the effect of environment is reduced as crack growth rates converge.

Furthermore, the frequency the mechanical tests are carried out at is seen to have a modest effect on crack growth rate across both R ratios of 0.1 and 0.5. The largest difference in crack growth rate is observed between the 500°C tests carried out in air at 0.25 and 10 Hz at low ΔK values. As the ΔK increases, the crack growth rates converge. The influence of frequency is not as prominent as the influence of environment. For example, the 500°C at 0.25 Hz test fatigue crack growth rate is only increased by a maximum factor of approximately 2.3 times compared to the crack growth rate of the 10 Hz test. Whereas tests in air gave a maximum increase in crack growth rates by a factor of approximately six times, compared to tests in vacuum.

For R ratio of 0.1 tests, at room temperature, frequency is found to have no significant effect on crack growth rates under both air and vacuum conditions. Tests carried out in air at 10 and 0.25 Hz see very similar crack growth rates as do tests carried out at 10 and 0.25 Hz under vacuum conditions.

7.4 Effects of Temperature

Compressor discs are likely to experience a range of temperatures and so it is essential to understand how this will affect the component. Mechanical tests were carried out at a range of temperatures under different frequencies and environments. Specimen CX 044 was used for a mechanical test at 575^{o}C in air at 0.25 Hz and CX 023 was used at 450^{o}C in air at 0.25 Hz. Specimens CX 034 and CR 061 were subject to 500^{o}C in air at 10 and 0.25 Hz respectively whilst CR 072 and CX 037 were subject to 500^{o}C in vacuum at 10 and 0.25 Hz respectively. Specimens CR 063 and CX 033 were tested at room temperature in air at 10 and 0.25 Hz respectively with CX 022 and CR 068 being tested at room temperature in vacuum at 10 and 0.25 Hz respectively. All of the above described tests were carried out at an R ratio of 0.1.

7.4.1 R ratio 0.1

Results from the air tests at a range of temperatures at 0.25 Hz are displayed in Figure 7.14. This shows how by increasing the temperature the crack growth rate is increased. The largest increase in crack growth rate is seen by increasing the temperature from room temperature to 575^{o}C. Comparing the crack growth rates for the 500 and 575^{o}C test show how the rates are broadly similar. For example, comparing crack growth rates for the 500 and 575^{o}C tests at a ΔK of 12 MPa√m, the 575^{o}C test has a crack growth rate of 2.90E-04 mm/cycles whereas the 500^{o}C test has a crack growth rate of 2.00E-04 mm/cycle. As the ΔK is increased 35 MPa√m, the crack growth rates converge and both tests have a crack growth rate of approximately 1.40E-03 mm/cycle. Optical and SEM images of the 575^{o}C test (CX 044) are shown in Figure

7.15. The optical image shows uniform crack growth resulting in an even quarter circle but the darker colour on the fracture surface compared to tests carried out at 500°C, for example in Figure 7.4, shows how the oxidation thickness has increased with the increase in temperature. The SEM images show how even at this elevated temperature, the crack growth mechanism remains transgranular. Tearing and secondary cracking are obvious on the fracture surface at high values of ΔK.

By comparing the 0.25 Hz room temperature and 500°C tests, it is clear how much temperature does affect crack growth rates. For example, at a ΔK of 12 MPa√m, the crack growth rate for the 500°C test is 2.00E-04 mm/cycle whereas the room temperature test has a crack growth rate of only 5.30E-05 mm/cycle. As the ΔK is increased to 35 MPa√m, the crack growth rates converge. The 500°C test now has a crack growth rate of 1.40E-03 mm/cycle whereas the room temperature test has a crack growth rate of 6.20E-04 mm/cycle.

When tests are carried out under vacuum conditions, temperature still affects crack growth rate as shown in Figure 7.16. For example, comparing the 0.25 Hz test at room temperature and 500°C at a ΔK of 12 MPa√m, the 500°C test has a crack growth rate of 3.00E-05 mm/cycle whereas the room temperature test has a crack growth rate of 1.20E-05 mm/cycle. As the ΔK is increased to 40 MPa√m, the 500°C tests crack growth rate increases to 1.20E-03 mm/cycle whereas the room temperature test crack growth rate increases to 4.50E-04 mm/cycle. The rates for these conditions were not seen to converge as ΔK increases.

7.4.2 R ratio 0.5

The results for the R ratio 0.5 tests carried out in air are shown in Figure 7.17. From this it is clear to see that the effect temperature has on crack growth rate at this R ratio is very similar to the effect temperature has on crack growth rate at an R ratio of 0.1. At low values of ΔK, temperature influences crack growth rates more than at high ΔK values. There is a large difference in crack growth rates between the different temperatures at low ΔK but as ΔK increases, crack growth rates converge. Similarly to R ratio 0.1 tests, the largest difference in crack growth rate as a result of changing temperature is found in air at 0.25 Hz at a ΔK of 8 MPa√m. As the ΔK increases to 20 MPa√m, the crack growth rates converge. Figure 7.18 shows results for R ratio 0.5 tests carried out under vacuum conditions. The results are similar to the R ratio 0.1 tests carried out under vacuum, with temperature still subtly influencing crack growth rate. The differences in crack growth rate as a result of changing the temperature are more consistent across all ΔK values as rates are not seen to converge much as ΔK increases.

7.4.3 Summary

To summarise, temperature is found to affect crack growth rate, particularly in air environments. As the temperature is increased, crack growth rates increased across all R ratios of 0.1 and 0.5 tests, in both air and vacuum conditions. The largest effect of temperature is observed in air conditions at a frequency of 0.25 Hz at low values of ΔK. In air conditions, crack growth rates are seen to converge as ΔK values increase. In vacuum conditions, the differences in crack growth rates as a result of temperature are more consistent across all ΔK values.

Finally, regardless of the temperature the tests were carried out at, the crack growth mechanism remains transgranular. No intergranular crack growth is observed on the fracture surfaces.

7.5 Summary

The way the crack growth rate in the Paris regime is altered as a result of changing R ratio, environment, cyclic frequency and temperature is summarised as:

1) Two different R ratios were tested in the present study; these were R ratios of 0.1 and 0.5. For majority of conditions tested, altering the R ratio did not affect the crack growth rate in the Paris regime. For the conditions where R ratio did affect the crack growth rate, such as 10 Hz in air, the effects were only very modest. Under vacuum conditions effects due to altering the R ratio were greatest at low ΔK values and as ΔK increased, crack growth rates converged.
2) The environment Ti 6246 is exposed to affects crack growth rates. Mechanical tests carried out in laboratory air saw faster crack growth rates than when tests were carried out under vacuum conditions. The largest difference in crack growth rate as a result of the different environments was seen at 500^{o}C. At room temperature, crack growth rates for tests carried out in both air and vacuum conditions were very similar.
3) Cyclic frequency was found to have more of an effect on crack growth rate at elevated temperatures than at room temperature. At 500^{o}C in both air and vacuum conditions, tests carried out at a frequency of 0.25 Hz produced faster crack growth rates than tests carried out at 10 Hz. At room temperature, the effect of frequency was reduced in both air and vacuum conditions as crack growth rates for both 0.25 and 10 Hz frequency tests were very similar.
4) Temperature had a large effect on crack growth rate at both 0.25 and 10 Hz frequencies in air conditions. Temperature did affect crack growth rate under vacuum conditions however it was subtle. Elevated temperatures cause crack growth rate to increase, especially at low values of ΔK compared to tests carried out at room temperature. As the ΔK is increased, crack growth rates were seen to converge irrespective of the temperature the test was carried out at in air conditions. Under

vacuum conditions, the differences in crack growth rates were more consistent irrespective of the ΔK value as rates did not appear to converge.

Chapter 8 - Results - Dwell Fatigue Testing

8.1 Introduction

Subjecting material to a period of dwell loading and understanding how this affects the resistance to crack propagation is crucial. Compressor disks are safety critical components within aeroengines and so understanding exactly how they are likely to perform during the flight cycle is essential. The effect of introducing a dwell period to Ti 6246 has been investigated in various ways. For example, the environmental conditions have been altered, so that tests were either carried out in laboratory air or under vacuum. Also due to the fact that the amount of dwell time experienced during a flight cycle may vary, the length of the dwell period has been altered, either being one hour or two minutes. Furthermore, the position of the dwell period within the loading cycle has been varied to be implemented at either Kmax or Kmin hold.

Finally, as an aim of the study was to optimise the use of Ti 6246 as compressor discs, the material's ability to cope at elevated temperatures has been investigated. This is with the intention of utilising Ti 6246 and potentially replacing the heavier alloys such as nickel-base superalloys. This would offer weight savings and improved efficiency. For this reason a one hour dwell test in air was carried out at an increased temperature of 575°C.

The C and m constants for the Paris relationship for the dwell tests are given in Table 8.1. The C and m values given are for the dwell segments only and not baseline loading.

8.2 Effects of Dwell

8.2.1 Air, Kmax Dwell Hold, 500°C, 1 Hour

Before comparing the effect of the temperature and environment on the dwell fatigue crack growth rate, it was important to understand the effect of dwell in comparison to the baseline crack growth. For example, Figure 8.1 depicts results from specimen CX 031 which was a single test carried out at 500°C in air with a dwell hold lasting for one hour at Kmax. From this it is clear to see that four segments of baseline crack growth of 0.25 Hz were alternated with three segments of one hour dwell crack growth. The baseline crack growth shows a very similar rate of propagation to other fatigue tests carried out at a frequency of 0.25 Hz and temperature of 500°C (shown in Figure 7.14) which gives confidence in the difference found between baseline and dwell loading. It is clear to see that across all of the dwell segments, the crack growth rate is increased in comparison to the baseline crack growth at similar values of ΔK. The largest difference in crack growth rate is found at lower values of ΔK.

When comparing the first dwell segment with baseline crack growth, at a ΔK of approximately 12 MPa√m, the crack growth for the dwell segment is 4.00E-04 mm/cycle whereas the baseline crack growth rate is only 1.30E-04 mm/cycle. As the ΔK increases, the difference between the baseline and dwell crack growth rates is reduced as crack growth rates converge. For example, at a ΔK of approximately 25 MPa√m, the dwell segments crack growth rate is 6.20E-04 mm/cycle whereas the baseline crack growth rate is 3.90E-04 mm/cycle.

Another observation from Figure 8.1 is that following each dwell period, on returning to baseline crack growth, the rate of crack growth is lower than the expected rate. After a number of fatigue loading cycles however the crack growth rate is able to return to the expected rate. Similarly, when the dwell loading is introduced following a period of baseline crack growth, the rate is initially faster and then decreases before increasing again, creating a ‘U’ configuration on the fatigue crack growth resistance curve.

Figure 8.2 and 8.3 show optical and SEM images taken of specimen CX 031 which was subjected to one hour dwell hold at Kmax in air at 500°C. From the optical image it is clear to see that there is uniform crack growth in all directions creating an even quarter circle. The fracture surface also shows different colours which relate to oxide thickness and can be used as a guide to help with crack length calibration. Furthermore, the shape of the specimen still remains an even square. The SEM images taken show an overview of the fracture surface and high magnification images to show more detail. From the overview it is clear to see the whole fracture surface is relatively flat without much obvious difference between the baseline and dwell loading. It is clear that there is a transgranular crack growth mechanism throughout the entire mechanical test. It is also possible to see striations on the fracture surface which coincide with the crack growth rate plotted in Figure 8.1. The image captures striations from the transition region from the third dwell period to the fourth baseline period, occurring at a

ΔK of approximately 28 MPa√m. The striation spacing for the dwell loading as seen in Figure **8.1** are found to be approximately 0.78 µm which are much wider than the spacing for the striations measured in the baseline loading. Here, for baseline loading, the striation spacing was measured to be approximately 0.45 µm. These wider striations in the dwell loading equate to a faster crack growth rate. When comparing this to the crack growth rates obtained experimentally, shown in Figure 8.1, at a ΔK of 28 MPa√m, the dwell crack growth has a rate of approximately 8.00E-04 mm/cycle and when the baseline crack growth is introduced, the crack growth rate decreases to 3.90E-04 mm/cycle. These rates match up well to the striation spacing measured for both the dwell and baseline loading. Furthermore, from the fracture surface, it is not possible to see any facets which may have occurred due to the elevated temperature of the test, suggesting creep damage was not a factor in influencing crack growth.

8.3 Effects of K Minimum or Maximum Dwell Hold

As well as the one hour dwell hold at 500°C at Kmax, a similar mechanical test was carried out on specimen CR 073 with the main difference being that the dwell hold was implemented at Kmin. For this mechanical test, only one segment of dwell was carried out with baseline crack growth occurring both before and after the dwell segment. The results of this are shown in Figure 8.4. By comparing the baseline crack growth to other 0.25 Hz, 500°C tests (Figure 7.14), it is clear to see that the baseline rate is accurate. It is also clear from the results that when the dwell hold is introduced at Kmin, it does cause the crack growth rate to increase. For example, at a ΔK of approximately 27 MPa√m, the dwell crack growth rate is 1.20E-03 mm/cycle whereas the baseline crack growth rate is 5.00E-04 mm/cycle. When the ΔK increases to a value of 34 MPa√m, so that it is nearing the end of the dwell segment, the dwell crack growth rate is now 1.60E-03 mm/cycle whereas the baseline crack growth is 7.50E-04 mm/cycle.

Similarly to the one hour dwell hold at Kmax, the crack growth rate is fastest when the dwell period is initially introduced. The crack growth rate then reduces slightly before increasing again after a number of loading cycle, again creating a 'U' configuration of dwell crack growth rate on the fatigue crack growth resistance curve. This does seem to be more subtle however than the one hour hold at Kmax test. Furthermore, unlike the one hour dwell hold at Kmax, on returning to baseline crack growth, the rate is immediately as expected and does not require loading cycles to recover the rate to the expected rate.

Figure 8.5 shows both the one hour dwell tests carried out at 500°C incorporating both the Kmax and Kmin hold results. From the results it is clear to see that regardless of whether the dwell loading was incorporated to fit within the Kmax or Kmin holding position within the loading cycle, it caused the crack growth rate to increase by similar amounts compared baseline crack growth rates. For example, for the Kmax hold dwell test, at a ΔK of 25 MPa√m, the crack growth rate was 1.6 times faster than baseline. For the Kmin dwell hold test, at a ΔK of 35 MPa√m, the crack growth rate was again 1.6 times faster than baseline crack growth.

Figure 8.6 and 8.7 show the optical and SEM images taken of the one hour dwell hold test at Kmin in air at 500°C. The fracture surface appears very similar to the one hour dwell hold at Kmax. The optical image shows the different colours on the fracture surface showing the different oxide thickness and how the crack has grown uniformly into a clear quarter circle shape. The SEM images show how all crack growth followed a transgranular mechanism throughout both baseline and dwell loading. Fatigue striations are visible on the fracture surface for baseline loading and corresponded to crack growth rates plotted in Figure 8.4. The striations were visible and ΔK of 20 and 25 MPa√m and had spacing's of 0.39 and 0.53 µm respectively. Comparing this to the crack growth rates obtained experimentally, as shown in Figure 8.4, at a ΔK of 20 MPa√m, the crack growth rate was 3.20E-04 mm/cycle. At a ΔK of 25 MPa√m, the crack growth rate was 4.70E-04 mm/cycle. Again this shows how striations on the fracture surface gave a good indication of crack growth rate obtained.

8.3.1 Summary

To summarise the effect of the holding position in laboratory air conditions, it can be said that irrespective of whether the dwell period was introduced at Kmax or Kmin, there was an increase in crack growth rate as a result of the extended dwell period of one hour. The fracture surfaces for both mechanical tests appeared similar with transgranular crack growth mechanism throughout and visible fatigue striations present.

8.4 Effects of the Environment

As well as carrying out one hour dwell tests in air at 500°C, a one hour dwell test was also carried out under vacuum conditions at 500°C using specimen CR 071. This was so the effect of environment on dwell crack growth could be investigated. The results from this vacuum test are displayed in Figure 8.8. Looking at the baseline crack growth it is clear to see this matches data from the Paris regime for mechanical tests carried out in similar conditions as shown in Figure 8.8.

Similarly to the dwell tests carried out in air, when the dwell loading is introduced, the crack growth rate is increased. However, under vacuum conditions, the increase is more significant. For example at a ΔK of 16 MPa√m, the dwell loading crack growth rate is 3.80E-04 mm/cycle whereas the baseline crack growth rate is only 9.90E-05 mm/cycle.

Figure 8.9 shows results from the one hour, 500°C dwell tests carried out in both air and under vacuum conditions. It was clear that when the dwell loading is introduced the crack growth rates for both the air and vacuum conditions are very similar and the crack growth rates overlap, both having a crack growth rate of approximately 4.30E-04 mm/cycle at a ΔK of 17 MPa√m. For both the one hour dwell tests in air and vacuum, compared to baseline in vacuum, the crack growth rate is increased by approximately 4.5 times.

In terms of baseline loading in air and vacuum, the environment does affect crack growth rate, particularly at low values of ΔK. For example, at a ΔK value of 15 MPa√m, the air test baseline crack growth rate is 1.8E-04 mm/cycle whereas the vacuum baseline crack growth rate is only 7.50E-05 mm/cycle. When the ΔK is increased to 35 MPa√m, the air baseline crack growth rate is now 8.7E-04 mm/cycle whereas the vacuum baseline crack growth rate is 6.60E-04 mm/cycle. This shows how baseline crack growth rates between air and vacuum conditions are converging as ΔK is increased.

Figure 8.10 and 8.11 show optical and SEM images of the one hour dwell test performed under vacuum conditions. The optical image shows how the crack has grown uniformly creating an even quarter circle shape. The SEM images show how the crack growth is transgranular with both the baseline and dwell loading producing a flat fracture surface. Striations were harder to see on the fracture surface compared to tests carried out in air but some were visible, showing the transition from baseline to dwell loading. The striation spacing matches with the change in crack growth rates obtained experimentally, as show in Figure 8.8. For example, in the baseline period at a ΔK of 16 MPa√m, the striation spacing was measured to be 0.16 µm. When the dwell loading was introduced, at a ΔK of 17 MPa√m, the striation spacing was measured to be approximately 0.40 µm. At a ΔK of 16 MPa√m, the crack growth rate was 9.80E-05 mm/cycle as shown in Figure 8.8. At a ΔK of 17 MPa√m, the crack growth rate had increased to 3.8E-04 mm/cycle. This shows how the measured striation spacing on the fracture surface do match up to the crack growth rates obtained experimentally.

As well as one hour dwell tests being carried out in air and vacuum environments, two minute dwell tests were also carried out in air and vacuum environments using specimens CX 032 and CX 026 respectively. The results are shown in Figure 8.12. From this it is clear to see that when the test is carried out in air rather than under vacuum, the crack growth rate for both the baseline and dwell segments is increased.

During baseline crack growth, at a ΔK of 12 MPa√m, the air test has a crack growth rate of 1.60E-04 mm/cycle whereas the vacuum tests crack growth rate is 4.00E-05 mm/cycle. When the dwell period is introduced, there is an increase in crack growth rate for both test conditions. However, unlike the one hour dwell test which saw the vacuum test crack growth rate match that of the air test crack growth rate (Figure 8.9), the results are less dramatic. When the dwell period is introduced, at a ΔK of 13 MPa√m for the air test, there is an increase in crack growth rate to 2.50E-04 mm/cycle. When the dwell period is introduced in the vacuum test, at a ΔK of 16 MPa√m, the crack growth rate is increased to 1.40E-05 mm/cycle. Comparing the air and vacuum test directly during the dwell period at a ΔK of 20 MPa√m, the air test is found to have a crack growth rate of 4.00E-04 mm/cycle whereas the vacuum tests crack growth rate is 2.60E-04 mm/cycle. Comparing the dwell crack growth rates in air and vacuum both to the baseline in vacuum crack growth rate, the air test sees in increase of 3.3 times. When the dwell loading is introduced in the vacuum test, the crack growth rate is only increased by 1.5 times compared to the vacuum baseline crack growth rate.

8.4.1 Summary

The environment was found to affect crack growth rate during both baseline and dwell loading cycles. For baseline loading, air tests consistently experienced faster crack growth rates than tests carried out under vacuum. However, when subject to one hour dwell, the crack growth rate of the vacuum test was equal to the crack growth rate of the air test. For the two minute dwell tests, the introduction of the dwell period saw an increase in crack growth rate for both air and vacuum conditions over baseline crack growth rates. However, the air test experienced more of an increase in crack growth rate compared to the vacuum test. This was different from the one hour dwell tests whereby the air and vacuum tests crack growth rates were increased to similar rates once the dwell period was introduced.

Therefore, it can be deduced that the environmental conditions do affect crack growth rates, particularly at baseline loading conditions. Any differences due to environmental influences on crack growth rates are likely removed when a one hour dwell hold period is introduced, as crack growth rates became very similar for air and vacuum conditions. For two minute dwell hold, environmental influences still affect crack growth rate as the air and vacuum tests still had different crack growth rates.

8.5 Effects of Temperature

Figure 8.13 shows the results from the dwell test carried out at 575°C on specimen CX 030. Comparing the baseline crack growth to a previous Paris regime test carried out under similar conditions, it is clear to see both results are consistent and show very similar rates of growth. When the dwell period is introduced following a period of baseline crack growth it is clear that crack growth rate is accelerated significantly. When the dwell period is initially introduced, at a ΔK of 11 MPa√m, the crack growth rate increases from 2.40E-04 mm/cycle for baseline crack growth to 4.00E-04 mm/cycle for dwell crack growth.

The rate continues to accelerate rapidly to the point where at the end of the first dwell period, at a ΔK of 13 MPa√m, the crack growth rate is 1.90E-03 mm/cycle. It also shows how the dwell crack growth does not plateau off in a way observed by tests carried out at 500°C. If the dwell period was sustained it seems the rate would continue to rapidly increase. This sharp increase in crack growth rate under dwell loading was thought to be a result of creep damage.

On returning to baseline crack growth from the first dwell period, initially, the baseline crack growth seems to experience some crack retardation as the rate is much lower than expected. After a number of fatigue cycles, the crack growth rate is able to recover and return to an expected rate. When the second period of dwell loading is introduced, it shows a similar story to the dwell periods at 500°C in that the fastest crack growth occurs when the dwell period is initially introduced but immediately appears to reduce before increasing again, creating a ‘U’ configuration of crack growth rate. For example, when the second dwell period is initially introduced, at a ΔK of 16 MPa√m, the dwell crack growth rate is approximately 4.20E-03 mm/cycle whereas the baseline crack growth rate is only 3.60E-04 mm/cycle. After a number of dwell cycles however the rate of the dwell crack growth drops to be 3.30E-03 mm/cycle. The crack growth rate then increases so that at the end of the dwell period, at a ΔK of 20 MPa√m, the crack growth rate is 7.60E-03 mm/cycle. The crack growth rate does not plateau but instead continues to accelerate.

On returning to baseline loading, initially the crack growth rate seems to be much lower than expected. At a ΔK of 20 MPa√m, the crack growth rate is as low as 1.40E-04 mm/cycle. However, after a number of loading cycles however, the crack growth rate is able to recover.

Figures 8.14 and 8.15 show the optical and SEM images of the one hour dwell test in air at 575^{o}C. When comparing the optical image of the fracture surface to one hour dwell tests carried out at 500^{o}C, shown in Figure 8.2, it is clear that there are some differences. The crack at 575^{o}C has not grown uniformly in all directions. For example, the crack has grown anisotropically on one side, resulting in an elongated side of the crack at the edge of the specimen. Furthermore, there is some obvious discolouring of the fracture surface due to oxidation located at the corner away from where the notch was. This suggests a smaller secondary crack could have started growing during the test. Finally, the colour of the fracture surface is different suggesting the oxide layer formed on the surface may be thicker at this higher temperature. Despite the optical image of the fracture surface looking different, the SEM images taken of the fracture surface all looked similar to tests carried out at 500^{o}C, shown in Figure 8.3. The crack growth mechanism remains transgranular but there does appear to be more secondary cracking present which suggests creep damage is influencing crack growth.

A further one hour dwell test was carried out in air at 575°C with the intention of extending the first period of dwell crack growth to see at what ΔK the crack growth rate would plateau off. In Figure 8.13 when the dwell period is introduced it appears the crack growth rate continues to accelerate. The second attempt of the 575°C test failed unexpectedly and also failed away from the notch. This is shown in Figure 8.16. It is clear from visual inspection that there is significant amount of creep damage present with multiple sites of secondary cracking.

8.5.1 Summary

By increasing the test temperature from 500 to 575°C, the crack growth rate under both baseline and dwell fatigue loading is increased. The dwell crack growth rate is increased significantly and the rate is seen to continue to accelerate rather than plateau off, such as seen with the one hour dwell tests carried out at 500°C. At this temperature an unexpected failure occurred during the dwell cycling with a significant amount of secondary cracking and creep damage present.

8.6 Effects of Dwell Time

Both one hour and two minute dwell times have been investigated and compared. The effects of altering the dwell times have been studied in both air and vacuum conditions at 500°C.

8.6.1 Air Tests

Figure 8.17 depicts the results obtained from the two minute and one hour dwell tests. Both tests were carried out in air at 500°C. Therefore, the baseline crack growth for both tests was carried out in identical conditions. From the results it is clear to see that the rates for both the baseline crack growth from the two minute and one hour dwell conditions are very similar, which is to be expected. Due to the fact that the two minute dwell cycle is less time consuming than the one hour dwell cycle, a longer segment of dwell is included for the two minute dwell test. From the results it is clear to see that when dwell loading is introduced, crack growth rates increase compared to baseline crack growth rate. This was true for both dwell hold times of one hour and two minutes. However, the amount the crack growth rate is increased by does depend on the length of time of the dwell hold. For example, at a ΔK of 12 MPa√m, the baseline crack growth rate is approximately 1.40E-04 mm/cycle. The two minute dwell crack growth rate is 2.60E-04 mm/cycle and the one hour dwell crack growth rate is 4.00E-04 mm/cycle.

As the ΔK increases, the difference in crack growth rate between the different dwell hold times is reduced. For example, at a ΔK of 28 MPa√m, both crack growth rates are approximately 7.50E-04 mm/cycle. The crack growth rate for the baseline loading is also seen to be converging with the dwell loading crack growth rates. At a ΔK of 30 MPa√m the baseline crack growth is 5.60E-04 mm/cycle.

8.6.2 Vacuum Tests

Figure 8.18 shows the results from the vacuum dwell tests carried out at both one hour and two minutes at 500^{o}C. The baseline crack growth rates for the two tests are similar which is to be expected as they are carried out under the same conditions. As with dwell tests carried out in air, when a dwell period is introduced, the crack growth rates are increased. This is true for dwell times of both one hour and two minutes. However, as with the air tests, the length of the dwell period does influence how much the crack growth rate is increased by. For example, at a ΔK of 16 MPa√m, the baseline crack growth rate is 9.00E-05 mm/cycle. The crack growth rate for the two minute dwell test is 1.30E-04 mm/cycle and the crack growth rate for the one hour dwell test is 3.8E-04 mm/cycle. This shows that although the two minute dwell hold does cause an increase in crack growth rate compared to baseline loading, it is the one hour dwell hold that sees the largest increase in crack growth rate. The difference in crack growth rates is fairly consistent across all ΔK values for the baseline and two minute dwell tests. However, the one hour vacuum test only covers ΔK values ranging from 16-19 MPa√m and so it is unclear if crack growth rates would have converged if more values of ΔK were covered.

8.6.3 Summary

It is clear from the results that by adding a dwell period of either two minutes or one hour, the crack growth rate increases compared to baseline crack growth for both air and vacuum conditions. However, the length of the dwell period does affect exactly how much the crack growth rate is increased by. For example, for both air and vacuum conditions, having a 1 hour dwell period increases crack growth rates more than having a 2 minute dwell period.

8.7 Summary

The effect introducing a dwell period has on fatigue crack growth resistance can be summarised in the following ways:

1) Across all testing conditions introducing a dwell period, whether it be two minutes or one hour or in air or vacuum, caused a small but significant increase in crack growth rate compared to baseline crack growth rate.
2) On returning to baseline loading following a period of dwell crack growth the crack growth rate was commonly initially retarded, resulting in a lower than crack growth rate expected based on the Paris regime. After a number of fatigue cycles the crack

growth rate recovered and returned to the expected rate. Similarly, it was common to see that when introducing the dwell period following baseline loading the crack growth rate was highest as the dwell period was initially introduced. Immediately crack growth rate reduced before increasing again with loading cycles.

3) Within the loading cycle the location of the dwell hold was not found to affect the increase of crack growth rate because the dwell crack growth rates for dwell tests which had a dwell period incorporated either at Kmax or at Kmin were found to be very similar.
4) The length of the dwell hold did influence how much the crack growth rate was increased by compared to baseline loading. A one hour dwell hold was found to increase crack growth rate more than a two minute dwell hold in both air and vacuum environments.
5) When a one hour dwell test was carried out at 575°C, there was a sharp acceleration in fatigue crack growth rate when the dwell cycle was applied. On a repeat test there was an unexpected, failure away from the notch. This was during dwell loading cycle and severe secondary cracking and creep damage was visible on the specimen.

Chapter 9 - Discussion

Effects of extrinsic testing parameters such as environment, frequency, temperature, dwell time and stress ratio on crack growth resistance are discussed.

Figures 9.1-9.5 show fatigue crack resistance curves with both Paris regime and threshold regions displayed together. Despite threshold tests and constant load range (increasing ΔK) tests being carried out separately on test specimens, it is clear that they form one continuous fatigue crack growth resistance curve with fatigue crack growth rates comparable at equivalent ΔK values. By combining these two tests onto a single crack growth resistance curve it is much easier to see how extrinsic testing parameters affect fatigue crack growth resistance.

9.1 Influence of R ratio in threshold and Paris regime

Figure 9.2 displays results from both R ratios of 0.1 and 0.5 tests carried out in air at 15 Hz at room temperature and 500°C. R ratio does influence fatigue crack growth rate at near threshold ΔK range and actual ΔK_{th} value. It is possible to see from results that as the R ratio is increased from 0.1 to 0.5, the ΔK_{th} decreased, particularly at 500°C. For example, the average ΔK_{th} value for the 500°C tests for the R ratio of 0.1 is 3.8 MPa√m. However, the average ΔK_{th} value for the 500°C tests for the R ratio of 0.5 is 3.2 MPa√m, showing that there is a modest effect of increasing the R ratio from 0.1 to 0.5. Furthermore, results from the constant Kmax test where the R ratio started at 0.1 and increased to 0.87 by the end of the test (as shown in Figure 6.1) also demonstrates the effects of R ratio. For this test the ΔK_{th} was given as 1.6 MPa√m which shows quite a significant reduction in ΔK_{th} compared to both the R ratio of 0.1 and 0.5 tests.

This significant reduction in ΔK_{th} observed when R ratio is increased to 0.87 is thought to perhaps be a result of a reduction in any crack closure effects on each of the crack faces. If this was the case, any contact between the two crack faces at an R ratio of 0.87 would be reduced which would therefore allow the crack to grow more readily and hence achieve a lower ΔK_{th} value. When looking at the fracture surface for the constant Kmax test as shown in Figure 6.5, the surface does appear very flat which could suggest any crack closure effects were minimised. However, when comparing this fracture surface to that of the 500°C, 15 Hz threshold test carried out an R ratio of 0.1, as shown in Figure 6.7, this too looks very flat and hence both fracture surfaces look very similar. For the constant Kmax test, which had a final R ratio of 0.87, to experience a reduction in crack closure effects, it would suggest that the R ratio 0.1 tests would experience crack closure effects. Therefore a slightly rougher fracture surface might be expected, as a result of roughness induced crack closure, for the R ratio 0.1 test. However, the fracture surface produced at an R ratio of 0.1 also looked very similar.

The initial idea of the constant Kmax test with an end R ratio of 0.87 having a much lower ΔK_{th} as a result from a minimisation in crack closure effects came from literature of similar studies investigating the effects of R ratio on threshold for fatigue crack propagation [106-111]. For example, Boyce and Ritchie (2000) [111] studied the effect of stress ratio and maximum stress intensity on fatigue threshold in Ti 64. The R ratios used for the mechanical tests ranged from 0.1 to 0.95. It was found that, as predicted, higher R ratios resulted in lower ΔK_{th} thresholds and faster crack growth rates at near threshold values of ΔK. The reason for R ratios affecting ΔK_{th} in this way was thought to be the result of crack closure which was recognised as being a roughness-induced mechanism present in titanium alloys [111, 112].

Previous research by Anderson (2005) [17] has found that only at R ratios of approximately 0.7 and above are crack closure effects completely removed and both fracture surfaces do not come into any contact throughout the entire loading cycle, even at minimum load[17]. Schematic illustrations for this are given in Figures 9.6 and 9.7. This finding from Anderson could perhaps be used to help explain why there is only a modest difference in ΔK_{th} between R ratio of 0.1 and 0.5 tests but then a significant difference from the constant Kmax test with a final R ratio 0.87. Findings suggest that in the constant Kmax test all crack closure effects would have been reduced. This also implies that for the R ratio 0.1 and 0.5 tests, crack closure effects may still contribute to crack propagation behaviour. If this was true, it could help explain why there is only a modest reduction in ΔK_{th} from the R ratio 0.1 to the R ratio 0.5 tests.

A further consideration for the constant K max test could come from creep effects. It may be possible that at this higher K max, creep contributes to crack growth more and have a stronger influence over the final ΔK_{th} achieved. This could perhaps explain why the drop in rate is not vertical. A higher load used which is associated with achieving a constant K max, compared to R ratio 0.1 and 0.5 tests, may increase any creep contribution responsible for achieving a reduced $\Delta K_{th.}$ Further research is required in order to fully understand this, such as carrying out threshold tests at a constant R ratio, similar to the final R ratio experienced by the constant K max test. This would show whether the final ΔK_{th} reached by the constant K max test was influenced by having a constant K max, or whether having a constant R ratio would also give a similar result.

At room temperature, the difference in ΔK_{th} between tests carried out at an R ratio of 0.1 and 0.5 is very modest. For example, the R ratio 0.1 tests have an average ΔK_{th} of 3 MPa√m whereas the R ratio 0.5 test has a ΔK_{th} of 2.8 MPa√m. The differences between the ΔK_{th} values obtained at room temperature are very similar to the differences obtained for the tests at 500°C which perhaps show the effect of increasing the R ratio is consistent across a range of temperatures.

Moving away from ΔK_{th} values to near threshold crack growth rate, there is still a subtle effect of R ratio for tests carried out at 15 Hz at 500°C. For example, at a ΔK of 5 MPa√m, the R ratio 0.5 test has a fatigue crack growth rate of 2.00E-05 mm/cycle whereas the R ratio 0.1 test has a crack growth rate of 1.40E-05 mm/cycle. At this same ΔK value, the constant Kmax test has an R ratio of 0.6 and has a fatigue crack growth rate of 3.20E-05 mm/cycle. Hence at near threshold values, the crack growth rate is increased with increasing R ratio. At a ΔK of 7 MPa√m, the constant Kmax test has an R ratio of 0.5 and here the crack growth rate is very similar to the R ratio 0.5 test as shown in Figure 6.1. However, both the R ratio 0.5 and 0.1 tests get to a specific ΔK value, which is approximately 4 MPa√m, and experience a rapid decrease in crack growth rate. However, the constant Kmax test keeps a steadily decreasing crack growth rate until it reaches a much lower ΔK value, found to be approximately 2 MPa√m,

before experiencing the same rapid reduction in crack growth rate. A possible explanation for this was proposed by Kirby (1979)[110] who found that as the effect of R ratio increased with decreasing crack growth rate towards ΔK_{th}, a greater dependence was placed upon Kmax. This could perhaps explain why when R ratios were similar between the constant Kmax test and R ratio 0.1 and 0.5 tests the crack growth rates were similar but then as the constant R ratio tests experienced a reduction in Kmax, there was a sudden drop off in crack growth rate at ΔK values much higher than the constant Kmax test. The constant Kmax test reached a much lower value of ΔK before experiencing a rapid decline in crack growth rate to ΔK_{th}.

Furthermore, at room temperature the near threshold crack growth rate is only subtly affected by R ratio. Of the two tests carried out at room temperature at an R ratio of 0.1, one test experienced a crack growth rate at near threshold values that was identical to the room temperature test carried out at R ratio of 0.5. The second R ratio of 0.1 room temperature test had a slightly lower crack growth rate than the R ratio 0.5 test at near threshold values. For example, at a ΔK of 4 MPa√m , the R ratio 0.1 test had a fatigue crack growth rate of 9.00E-07 mm/cycle whereas the R ratio of 0.5 test had a fatigue crack growth rate of 2.10E-06 mm/cycle.

As ΔK is increased further, away from ΔK_{th}, the relationship between log fatigue crack growth rate and log ΔK becomes linear, which is known as the Paris regime. Figure 9.1 displays results for both the threshold region and Paris regime. Here it is clear to see that effects of R ratio are decreased as ΔK is increased. It is clear from Figure 9.1 that as ΔK increases, the fatigue crack growth rates from all conditions are seen to converge. Figures 7.1a and 7.1b also show results for the effects of R ratio on fatigue crack growth in the Paris regime. At 0.25 Hz, in air, at both room temperature and 500°C, R ratio is seen to have no influence on fatigue crack growth rate as both rates between R ratio 0.1 and 0.5 are identical.

At 10 Hz, at both room temperature and 500°C there are subtle differences in crack growth rate between the R ratio 0.1 and 0.5 tests. For example, at a ΔK of 15 MPa√m, at 500°C, the R ratio 0.5 test had a crack growth rate of 1.80E-04 mm/cycle whereas the R ratio 0.1 test had a crack growth rate of 1.50E-04 mm/cycle. At room temperature, at a ΔK of 15 MPa√m, the R ratio 0.5 test had a crack growth rate of 9.00E-05 mm/cycle whereas the R ratio 0.1 test had a crack growth rate of 6.50E-05 mm/cycle. Therefore, despite differences in crack growth rate at this frequency being observed between the two R ratios, they were only very modest.

Although not displayed on Figure 9.1, the influence of R ratio on fatigue crack growth rate in the Paris regime was also investigated under vacuum conditions. Due to difficulties with ghost potential difference (PD) whilst testing near threshold behaviour under decreasing ΔK conditions with crack growth rate in vacuum, this region of the fatigue crack resistance curve was not studied under vacuum conditions. Tests were carried out under vacuum conditions for the Paris region under increasing ΔK conditions with crack growth as shown in Figures 7.2a and 7.2b. Here there are some very modest differences in fatigue crack growth rates as a result of altering the R ratio. The most significant difference in crack growth rate under vacuum conditions was between the room temperature, 0.25 Hz tests carried out at an R ratio of 0.1 and 0.5. At a ΔK of 15 MPa√m, the R ratio 0.5 test had a fatigue crack growth rate of 7.00E-05 mm/cycle whereas the R ratio 0.1 test had a fatigue crack growth rate of 2.80E-05 mm/cycle. A potential reason as to why modest R ratio effects are found at room temperature under vacuum conditions could perhaps be due to the different mean stresses being applied during the test. The mean stress for the R ratio 0.5 test is higher throughout the test compared to the R ratio 0.1 tests. However, evidence for this effect of having a higher mean stress throughout the test causing an increase crack growth rate is limited throughout the rest of the project. Therefore, reasons for seeing the differences in crack growth rates in Figure 7.2b are not fully understood. To fully understand the difference at room temperature under vacuum conditions, further tests are needed to be performed in order to establish what results maybe be within expected degree of scatter and which results are a genuine result of the changing testing conditions.

For the other conditions such as at 500°C at 10 and 0.25 Hz and 10 Hz at room temperature the crack growth rates were all very similar for both R ratios of 0.1 and 0.5.

Due to the fact that under the majority of testing conditions there was very little difference in fatigue crack growth rate in the Paris regime between R ratios 0.1 and 0.5, and even when there was a slight difference, it was only very modest, it was considered here that in the Paris regime, R ratio does not influence crack growth rates to any significant degree. In the Paris regime, crack growth is stable and as the ΔK is continually increasing throughout, the crack remains constantly open. This suggests that there would be no crack closure effects in this region. This could perhaps be the reason why R ratio was found to influence crack growth rate more in the threshold region where crack closure effects may play a role than in the Paris regime where they are thought to not be involved.

9.1.1 Mechanism of Crack Growth

Throughout both the threshold region and the Paris region for all the mechanical tests carried out at room temperature and 500°C (both R ratios of 0.1 and 0.5) the crack growth mechanism remains transgranular. This results in very flat and smooth fracture surfaces which all look very similar. Unlike intergranular crack growth whereby the crack path follows grain boundaries, transgranular crack propagation occurs across the grains. On fracture surfaces, particularly at high values of ΔK, fatigue striations are visible which are thought to be located on primary α laths, (of average thickness of 1.62 μm). Each striation spacing marks an increment of growth for each fatigue cycle if there is a 1:1 correlation between striations and fatigue cycles. This spacing, along with the direction of the striations can be used to compare to the fatigue crack growth rates obtained experimentally. For example, striations were visible for the dwell period of the one hour, air, dwell test at an approximate ΔK of 28 MPa√m, shown in Figure 8.3. The striation spacing was measured to be 0.78 µm. The crack growth rate at this ΔK was given as 8.00E-04 mm/cycle, as shown in Figure 8.1. On returning to baseline crack growth, following dwell crack growth, striations were also visible on the fracture surface. The striation spacing was measured to be approximately 0.45 µm. The crack growth rate at this ΔK was found to be 3.90-04 mm/cycle, shown in Figure 8.1. Thus, in both examples here, the crack growth rates and striation spacings are very similar suggesting a 1:1 correlation.

At 575°C, for the one hour dwell test, the crack growth mechanism is still transgranular but with significant amounts of creep damage. The “m” value obtained for the dwell section of this test was 6.10 as shown in Table 8.1. This is much higher than “m” values obtained for other dwell tests such as the one hour dwell test in air at 500°C which had an “m” value of 1.89. This sharp increase in “m” value for the 575°C test could be a result of creep damage. A one hour dwell test failed prematurely away from the notch, equivalent to the stress rupture of a plain- sided test-piece. Severe secondary cracking and deformation is observed on the specimen as shown in Figure 8.16. Rolls-Royce plc. provided data on stress rupture in Ti 6246 which stated that at 575°C at a nominal stress of 287 MPa, a stress rupture is likely to occur after 300 hours. The nominal stress on the specimen used for the one hour dwell test at 575°C was approximately 289 MPa and failure occurred after approximately 308 hours. This gives a strong indication the unexpected and premature failure was a result of stress rupture. Due to creep damage appearing to dominate at 575°C, this temperature was deemed beyond the temperature capabilities of the Ti 6246 alloy.

9.2 Influence of Cyclic Frequency in Threshold and Paris Regimes

Figures 9.3 and 9.4 show the fatigue crack growth resistance curves for R ratio 0.1 and R ratio 0.5 respectively. Included in the curves are near threshold and Paris regimes. Focusing on the results obtained for the R ratio 0.1 tests at 500°C at 0.25 and 15 Hz, it is clear to see that the frequency has only a very subtle influence on ΔK_{th} value. For example, the ΔK_{th} for the 0.25 Hz test was given as 3.5 MPa√m whereas the 15 Hz test had a ΔK_{th} of approximately 4 MPa√m. This shows that when frequency was reduced, the ΔK_{th} was reduced slightly.

Figure 9.5 shows results for the increased R ratio of 0.5. Comparing the 0.25 and 15 Hz tests at 500°C shows a similar pattern to that of the R ratio 0.1 tests in terms of the ΔK_{th} values obtained. At an R ratio of 0.5 the differences between 0.25 and 15 Hz in terms of the ΔK_{th} are even more modest. For example, the 15 Hz test gives a ΔK_{th} of approximately 3.2 MPa√m whereas the 0.25 Hz test gives a ΔK_{th} of approximately 3.1 MPa√m.

Therefore, this shows that despite ΔK_{th} decreasing when frequency is reduced, it is only by such a subtle amount that they are still very similar and hence frequency does not significantly alter ΔK_{th} values here. Previous research such as by Schmidt and Paris (1973) [106] has suggested that at any frequency below 200 Hz, the ΔK_{th} value is not affected as a result of changing the frequency. Therefore, as 0.25 and 15 Hz are significantly below 200 Hz, it is somewhat in agreement with previous literature that the ΔK_{th} values were very similar for both the 0.25 and 15 Hz tests.

As ΔK is increased slightly above that of the $\Delta K_{th,}$ into near threshold crack growth, frequency was found to have more of an effect on crack growth rate across both R ratios of 0.1 and 0.5. For example, for the R ratio 0.1 tests, at a ΔK of 5 MPa√m, the 0.25 HZ test had a crack growth rate of 6.60E-05 mm/cycle whereas the 15 Hz test had a crack growth rate of 1.50E-05 mm/cycle. Despite this rather large difference in fatigue crack growth rate at near threshold ΔK values, the actual ΔK_{th} values obtained were very similar.

One possible explanation for this is related to the frequency and the time spent during a single fatigue cycle. For example, 0.25 Hz is much slower than 15 Hz in terms of time per cycle so this would allow for more time per cycle for any environmental effects to take place. It could be an increased effect of oxidation that may possibly help to explain why at near threshold ΔK values the crack growth rate for the 0.25 Hz test is much higher than for the 15 Hz test. A frequency of 15 Hz may be too rapid for there to be much influence of the environment on crack growth rate whereas 0.25 Hz, being slower, may allow more environmental effects.

As the crack continues to propagate towards ΔK_{th}, the driving force at the crack tip is reduced as ΔK is reduced. If the idea of the 0.25 Hz test having a larger impact of environmental influence over the 15 Hz test is correct, it may perhaps reach a certain ΔK value in which the driving force to overcome any environmental influence becomes too low so the crack growth is stunted. Hence there is a sudden drop off in crack growth rate as crack growth resistance is increased. The drop off in crack growth rate for both the 15 and 0.25 Hz test is found to be at a ΔK of approximately 4 MPa√m which is why both conditions see a similar ΔK_{th} value.

On increasing ΔK so that the crack growth enters the Paris regime, the effect of frequency on fatigue crack growth rate can be established, as shown in Figure 9.4. It is clear that as ΔK is increased, the effect of frequency is reduced and crack growth rates converge. For example, at an R ratio of 0.1, at a temperature of 500°C, it was mentioned previously that the 0.25 Hz test had a significantly faster crack growth rate than the 15 Hz test at a ΔK of 5 MPa√m. However, as ΔK increases, the effect of frequency is greatly reduced. At a ΔK of 30 MPa√m the 0.25 Hz test had a fatigue crack growth rate of 8.50E-04 mm/cycle whereas the 10 Hz test had a fatigue crack growth rate of 6.50E-04 mm/cycle. This shows how as ΔK is increased, the crack growth rates become similar. This is also true for the R ratio of 0.5 tests, as shown in Figure 9.5. One possible explanation as to why crack growth rates converge as ΔK increases could be due to more limited environmental influences and perhaps the impact of oxidation (as discussed later in 10.2.1).

As well as exploring effects of frequency at elevated temperature for both the threshold and Paris regimes, effects of frequency were also explored in the Paris regime under vacuum conditions and at room temperature for R ratios of 0.1 and 0.5.

Results are given in Figures 7.13 and 7.16 for R ratio 0.1 tests, and Figures 7.17 and 7.18 for R ratio 0.5 tests. At room temperature in air for both R ratios, frequency did not influence crack growth rates. This could be due to the fact that at room temperature any environmental effects such as oxidation may be minimised.

Under vacuum conditions, any effects to crack growth rate as a result of frequency at an R ratio of 0.1 are very subtle. At room temperature, for the R ratio 0.1, 10 and 0.25 Hz frequencies experience identical crack growth rates across a range of ΔK values. At 500^{o}C, for both the R ratios of 0.1 and 0.5, the 0.25 Hz test has a slightly faster fatigue crack growth rate compared to the 10 Hz test. For example, at a ΔK of 25 MPa√m, for the R ratio 0.1 tests, the 0.25 Hz test has a crack growth rate of 3.60E-04 mm/cycle whereas the 10 Hz test has a crack growth rate of 2.00E-04 mm/cycle. It could be possible that this increase in crack growth rate at the slower frequency is still a result of limited environmental effects which may still be able to influence crack growth rates even when under vacuum conditions.

When looking at results for the R ratio 0.5 in Figure 7.18, there does appear to be a modest difference between 10 Hz and 0.25 Hz tests carried out at room temperature with the 0.25 Hz test experiencing a faster crack growth rate. As mentioned previously, it was thought that perhaps the crack growth rates at room temperature would be similar due to the fact at room temperature in vacuum any influence of the environment would be removed. Therefore, the reason for the difference in crack growth rates experienced here is unclear. Further research is needed to fully understand whether this is a result of scatter or whether the results are genuine, and if so, what is causing this difference.

9.2.1 Environmental Influence on Fatigue Crack Growth Rate

It appears that environmental influences are contributing to crack growth rates and could perhaps help to explain why crack growth rates are significantly different at low ΔK values but are seen to converge as ΔK increases for many testing conditions. For example, for the 500°C tests at 0.25 and 10 Hz in air, there is a large difference in crack growth rate at low ΔK values but as ΔK increases, crack growth rates converge. A possible explanation for this may be due to environmental influences and the effects of oxidation. For example, at low ΔK values, the crack growth rate is low and therefore the amount the crack grows per cycle is small. Any influence of oxidation on crack growth rate at low ΔK values would be large with respect to the total distance the crack grows per cycle. A model for this is proposed in Figure 9.8 which demonstrates crack extension at low and high ΔK values. In the figure it is shown how crack

extension could be affected by cycle time as a result of oxide formation. At low ΔK values, oxide cracking ahead of the crack tip can form a large proportion of overall crack extension. As ΔK is increased, oxide thickness ahead of the crack tip is assumed, in this model, stay the same but the distance the crack grows as a result of mechanical fatigue will increase. This therefore lessons the impact of oxidation on overall crack growth which could lead to crack growth rates converging.

As 0.25 Hz is much slower than 10 Hz, there is potentially more time each cycle for (brittle) oxides to develop ahead of the crack tip which, if they fracture early in the unload-reload cycle, could cause an increase in crack growth rate. This would mean that the additional crack growth due to oxide cracking as well as mechanical fatigue would give faster crack growth at 0.25 Hz compared to at 10 Hz. Although, it is noted that to consider this additional crack enhancement to be solely due to the oxide thickness is simplistic because it is possible that there could be a zone of embrittlement due to oxygen in solution ahead of the growing oxide which could also lead to an increase in crack extension. One further possibility is that with oxide cracking the crack tip becomes extremely sharp and this might influence growth by mechanical fatigue.

As ΔK increases to give increasing crack growth rates, the distance the crack grew each cycle as a result of mechanical fatigue would increase. Any oxides ahead of the crack tip would have less of an impact on the total crack growth extension and hence crack growth rates. This would mean that the two crack growth rates would tend to converge as any increases in crack growth rate as a result of oxide formation would be less significant in comparison to the total distance the crack is growing per cycle. Such arguments seem to be supported by the current results, showing how crack growth rates converge as ΔK is increased.

9.3 Influence of Temperature in Threshold and Paris Regime

In terms of measured ΔK_{th} values, the test temperature seems to have little impact for both R ratios of 0.1 and 0.5 as shown in Figures 9.4 and 9.5 respectively. The effect of temperature on ΔK_{th} value is considered at a frequency of 15 Hz. For an R ratio of 0.1, the room temperature test gave an average ΔK_{th} value of 2.9 MPa√m whereas the 500^{o}C test gave an average ΔK_{th} value of 3.9 MPa√m. For the R ratio 0.5 tests, the room temperature ΔK_{th}value was 2.8 MPa√m whereas the 500^{o}C test gave a ΔK_{th} value of 3.2 MPa√m. However, when looking slightly above ΔK_{th}, at near threshold ΔK values, it is apparent that temperature can affect crack growth rate more dramatically. For example, for the R ratio 0.1 tests, at a ΔK of 4 MPa√m, the 500^{o}C test has a crack growth rate of 8.50E-06 mm/cycle whereas the room temperature test has a crack growth rate of 1.00E-06 or 2.00E-06 mm/cycle, depending on which specific test is considered. As well as there being large differences in crack growth rate at near threshold ΔK values, the way in which crack growth rates are reduced as the ΔK_{th} value is approached are very different in both the R ratios 0.1 and 0.5. For example, the 500^{o}C tests experience a sudden drop off in fatigue crack growth rate at approximately a ΔK of 4 MPa√m. The room temperature tests all have a gradual reduction in crack growth rate with no sharp drop off or rapid increase in crack growth resistance.

A potential explanation for this difference in crack growth reduction down to ΔK_{th} value between room temperature and 500°C could possibly, once again, be related to environmental influence. At room temperature, it is unlikely there would be much environmental influence on crack growth behaviour. However, at 500°C it is likely environmental effects were contributing in some way. If this was correct it would suggest that the mechanism driving crack growth was different between the room temperature and 500°C tests which could explain where the difference in crack growth to ΔK_{th} value comes from. Despite this potential difference in crack growth mechanism, the fracture surfaces for all tests were very similar and crack growth remained transgranular.

A final note on the ΔK_{th} values obtained at room temperature and 500°C is the fact that the room temperature ΔK_{th} values are lower than the 500°C which is unusual. As the crack growth rates near threshold ΔK were lower for the room temperature tests, it would be expected that the ΔK_{th} value would be higher. This also led to the crack growth rates crossing over between the room temperature and 500°C tests. This unusual phenomenon of the 500°C tests having a higher ΔK_{th} value than the room temperature tests is seen at R ratios of both 0.1 and 0.5.

A tentative explanation for this observation could be due to oxygen induced crack closure. It has previously been found that at elevated temperatures, oxide induced crack closure becomes particularly dominant at near threshold crack growth rates [113]. It is possible this could cause crack arrest as at higher temperatures it is possible that the oxides are more difficult to crack and hence a higher ΔK_{th} value could be obtained. However, on the fracture surfaces of the 500°C tests there was no obvious oxide formation. Another possible explanation could be related to a hydrogen embrittlement effect at room temperature. If time had permitted further testing would have been carried out in vacuum and/or inert gas conditions, to consider further any potential role of hydrogen. The exact reason for the cross over in crack growth rates between

500°C and room temperature at near ΔK_{th} is unknown, but further work could be carried out to gain a better understanding on the different mechanisms at work under these different conditions.

As well as the effects of temperature on ΔK_{th} and near threshold ΔK crack growth rates, effects of temperature on crack growth rates in the Paris regime were also studied. Figure 7.14 displays results from tests carried out in air at an R ratio of 0.1 and at a frequency of 0.25 Hz. The temperature ranged from room temperature to 575°C. From the results it is clear to see that at low ΔK values, there was a significant difference in fatigue crack growth rates between room and elevated temperatures. For example, at a low ΔK of 15 MPa√m, the room temperature test had a fatigue crack growth rate of 6.80E-05 mm/cycle whereas the 575°C test had a crack growth rate of 3.40E-04 mm/cycle.

Figure 7.14 also shows that as ΔK is increased, the crack growth rates converge. For example, when the ΔK was increased to 35 MPa√m, the crack growth rates were found to converge so that the room temperature test had a crack growth rate of 6.00E-04 mm/cycle and the 575°C test had a crack growth rate of 1.50E-03 mm/cycle.

It could be suggested that the difference in crack growth rate between room and elevated temperature may again be a result of environmental effects. It is possible that oxides forming ahead of the crack tip at elevated temperature may crack and hence cause an increase in crack growth rates over tests carried out at room temperature where oxidation will not be expected to influence crack growth rates. As previously discussed, as ΔK increased, the crack growth rates converged which may be due to the crack growing further per cycle as a result of mechanical fatigue thus lessening any impact of oxides ahead of the crack tip.

At a frequency of 10 Hz, for both R ratios 0.1 and 0.5, temperature had less of an effect on crack growth rates compared to 0.25 Hz. For R ratio 0.1 tests, when comparing tests at 0.25 Hz at both room temperature and 500°C, the maximum crack growth rate increased by was a factor of 4.

However for the 10 Hz tests at room temperature and 500°C the maximum the crack growth rate was increased by was only a factor of 2.3. This difference in the amount that temperature may affect crack growth rates could perhaps be due to the amount of time of the fatigue cycle and therefore how much time there is for any environment influence. Environmental impact such as oxidation may influence crack growth rate less at 10 Hz than at 0.25 Hz due to there being less time during each individual fatigue cycle.

9.4 Influence of Environment in the Paris Regime

Due to threshold tests in vacuum being difficult to perform, the influence of environment on fatigue crack growth resistance was focused on the Paris regime of the fatigue crack growth resistance curve only. Figures 7.7 and 7.8 show results for tests carried out in the Paris regime at an R ratio of 0.1 in both air and vacuum conditions and 500°C and room temperature. Frequencies of 0.25 and 10 Hz are also shown. From this it is clear to see that when tests were carried out in air they had a faster crack growth compared to when they were carried out under vacuum. This was found for both room temperature and 500°C. As with previous results, the largest differences between crack growth rates were found at low ΔK values. As ΔK was increased, crack growth rates were seen to converge. A possible reason for this is similar to ideas discussed already. Environmental effects such as oxidation in air at low ΔK values could potentially be influencing crack growth rate much more significantly than tests carried out under vacuum conditions. This oxidation ahead of the crack tip in the air condition tests could lead to accelerated crack growth, hence there is a large difference between air and vacuum conditions at low ΔK values. As ΔK increased, the distance the crack was growing per cycle along with the speed at which the crack was growing increased. This increase was likely a result of mechanical fatigue for both the air and vacuum conditions. This would therefore decrease any influence of the environment or oxidation ahead of the crack tip which could lead to the crack growth rates converging.

For the R ratio 0.1 tests, at 500°C, 0.25 Hz, at a ΔK of 18 MPa√m, the air test has a crack growth rate of 2.80E-04 mm/cycle whereas the vacuum test had a crack growth rate of 1.20E-04 mm/cycle. Despite this difference in crack growth rate, the fracture surfaces observed under the SEM still looked very similar, both showing transgranular crack growth. In order to gain more understanding into how the environment influenced crack growth, TEM work was carried out on the fracture surfaces of both of the specimens used for these tests. A ΔK value of roughly 18 MPa√m was used for the TEM investigation for both specimens to allow for direct comparisons to be made.

Figures 9.9 and 9.10 show the TEM images taken of the vacuum and air samples respectively. From this it is clear to see that there are some differences in morphology between the two specimens. Examining the crack profile of the test carried out under vacuum, in Figure 9.9, the crack appears to be very smooth with no obvious secondary cracking. There are some slight fluctuations along the way but on the whole it is very smooth and consistent which is a result of the primary α laths and secondary β. It can be seen that there are smooth dips in the profile from each of the primary α laths. The primary α laths are softer than the transformed β and therefore the two phases experience different amounts of plastic deformation [114, 115].

In comparison, the test carried out in air displayed a much rougher crack profile, shown in Figure 9.10. Secondary cracking was present along the profile. The secondary cracking was seen in a primary α lath and not at the interface between the α laths and β matrix. This difference in crack profile is thought to be due to the α laths being sensitive to oxygen. Oxygen in α-titanium is known to have a high solid solubility [116-118] which could therefore make the α laths brittle as a result of oxygen ingress. This could perhaps be the reason why secondary cracking was observed down a primary α lath and not at the interface between the lath and the β matrix. This could contribute to the increased crack growth rate observed in air conditions compared to vacuum conditions at low ΔK values, as brittle primary α laths may allow for the crack to grow more readily.

9.5 Influence of Dwell in the Paris Regime

The influence of incorporating a dwell period on fatigue crack growth rate during the Paris regime of the fatigue crack growth resistance curve was studied. Results were shown in Chapter 8. As shown by the results, there was a small but significant effect of introducing a period of dwell crack growth on the rate of crack propagation. Across all conditions, whether it be different time periods of the dwell hold, different holding positions, different environments or temperatures, there was always a slight increase in crack growth rate when subject to a dwell loading cycle. However, the significance of the increase in crack growth rate was dependent on the conditions of the dwell hold. For example, the crack growth rate was increased by a factor of 3 when the dwell period was one hour at 500^{o}C at Kmax hold in air compared to baseline in air crack growth. However, when the dwell hold was two minutes in air at 500^{o}C, the crack growth rate was only increased by a factor of 1.5 compared to baseline in air crack growth. Conditions for baseline crack growth were 0.25 Hz in air at 500^{o}C.

The “m” values obtained for the dwell loading segments are given in Table 8.1. It was, however, a challenge to calculate “m” values due to the fact that many dwell segments did not possess linear crack growth rates with increasing ΔK values. For example, many experienced the fastest crack growth rates when the dwell period was initially introduced before decreasing slightly and then increasing again. This meant calculating the “m” value was often difficult. For example, from Figure 8.9, it is clear that the one hour dwell tests at 500^{o}C in air and vacuum have very similar crack growth rates and so it would be expected they may have similar “m” values. However, from Table 8.1, it is clear to see that the air test has an “m” value of 1.89 whereas the vacuum test has an “m” value of 0.97. This is due to the fact that for the air test, different dwell segments were used to calculate the “m” value which each had a different gradient of crack growth.

All crack growth remains transgranular throughout both baseline and dwell loading. In other materials, such as nickel-base superalloys, baseline crack growth is found to be transgranular but when a dwell period is introduced the crack growth mechanism becomes intergranular [119, 120]. This may cause fatigue crack growth rates to be significantly faster when subject to dwell crack growth due to the fact that during the static load of the dwell, oxides may rupture along the grain boundaries.

Here, throughout a dwell test performed on Ti 6246 consisting of both 0.25 Hz baseline loading and periods of dwell crack growth, the fracture mechanism remains transgranular. It is thought that perhaps changes in crack growth rates observed are possibly a result of oxidation and potentially plasticity. It was considered that it may also potentially be creep damage which is contributing to the increase in crack growth rate under dwell at the elevated temperature. However, evidence for this is limited for a number of reasons. Firstly, the fracture surfaces for all dwell tests appear flat and smooth with no evidence of any creep voids. Secondly, as will be discussed further within the chapter, is the fact that the dwell test carried out in which the dwell segment was held at minimum load had a very similar crack growth rate to the dwell test carried out at maximum load. Therefore, more focus is placed on the potential role of oxidation effecting crack growth rate during dwell holds.

During the static load of the dwell hold for Ti 6246, an oxide layer may build up ahead of the crack tip. Oxide growth is thought to happen parabolically, as shown in Figure 9.11 [18]. Initially, the oxide grows quickly, but the thicker the oxide gets, the slower the rate of growth becomes, until eventually, after a certain amount of time, the oxide cannot become substantially thicker without cracking first. It is thought that with the one hour dwell tests in both vacuum and air that they had both reached a point in which no further oxide growth would occur without the oxide cracking first.

It can be postulated that during the static hold of the dwell cycle, the oxides do not crack and therefore no crack extension occurs. It is possible the oxides at the crack tip go into a state of compression during the static hold and therefore cannot crack as a result of high local stresses at the crack tip [121, 122]. This is unlike dwell tests carried out on nickel-base superalloys, as here it is thought that oxide cracking can often happen during the static hold period. For Ti 6246 dwell tests, when the unload-reload cycle is implemented, it may cause stress redistribution at the crack tip which could cause the oxides to go from compression into tension and hence likely to cause oxides to crack (and to crack early in the unload-reload cycle).

This is the possible theory as to why when the dwell period is introduced the crack growth rate is seen to increase. Focusing on the dwell tests in air, the one hour dwell test has a faster crack growth rate than the two minute dwell test. Based on the theory previously mentioned, this could be due to the fact that at one hour, the oxide layer has more time to grow compared to the two minute dwell test. Hence, during the unload-reload cycle, there is more oxide to crack and so there is a greater distance for critical crack growth extension. The two minute dwell test may experience some oxide growth and hence could exhibit a faster crack growth rate compared to baseline crack growth. However, it would plausibly not lead to such a significant acceleration in crack growth rate compared to the one hour dwell test, which would have had more time for the oxide ahead of the crack tip to grow.

This potential theory could also help to explain why the crack growth rates for the Kmax and Kmin one hour dwell holds are similar. If the oxide is still able to grow at one hour Kmin hold and cracking only occurs during the reload-unload cycle, it would not matter at what K value, whether it be minimum or maximum, the one hour hold was occurring. The process of the unload-reload or reload-unload cycle would have the same effect for both tests. Hence the oxide would crack in the same way which would cause the same amount of acceleration in crack growth rate for both tests.

Therefore, it is thought that the increase in crack growth rate under dwell loading across all conditions could potentially be a result of oxide cracking ahead of the crack tip early during the unload-reload cycle. It is thought to be related to the amount of time spent at the dwell static hold as this influences how much the oxide can grow but any crack growth rate increase is thought to be related to oxide cracking early in the unload-reload cycle. It appears in this study that position of the static hold during the dwell cycle does not affect crack growth rate since the one hour dwell test held at Kmin produced a crack growth rate that was very similar to the one hour dwell test held at Kmax, as shown in Figure 8.5. This gives further evidence as to why the role of creep in effecting crack growth rate is limited. If creep played a significant role, the dwell test at maximum load crack growth rate would be expected to be much faster than the crack growth rate of the minimum dwell hold test as creep would not be expected to influence the minimum hold crack growth rate. However this was not found to be the case, as the rates were in fact very similar.

A further potential reason, other than the role of oxidation, for why the maximum and minimum dwell hold crack growth rates may be similar may due to different mechanisms playing a role which leads to similar crack growth rates. It is possible that for the maximum hold dwell test, the crack is held open and hence oxygen could diffuse down the open crack allowing more oxidation, however, tensile creep could also be occurring, increasing the amount of damage. For the minimum hold dwell test, although the crack is closed, it is thought it is still possible for oxygen to diffuse down the crack tip, causing oxidation ahead of the crack tip. However, also contributing to the increase in crack growth rate may be due to compressive stresses at the crack tip being relieved slightly due to creep thus increasing the mean stress. This could perhaps cause a 'kick' in crack growth of the proceeding crack growth cycle, hence increasing crack growth rate. It is unclear exactly what is causing the increase in crack growth rate but it is perhaps a combination of all of the mentioned above. However, the most comprehensive and consistent theory is the role of oxidation and oxides cracking during the unload-reload cycle, hence this remains the primary focus of the project.

9.5.1 Oxidation Studies

Oxidation studies were carried out in order to further investigate the proposed theory of oxide cracking during the unload-reload cycle. The amount of oxide growth on an untested slice of Ti 6246 at 500°C at different time intervals was measured. The time intervals were 2 minutes and 1 hour to represent the time spent at the static hold during the dwell cycle.

FIB was used to take “lift outs” of the sample so that the oxide thickness on the surface could be measured and compared. Line scans were carried out across the “lift out” to take an average of oxide thickness. Results showed that when the Ti 6246 slice was subject to one hour at 500°C, the oxide thickness was measured to be approximately 40 nm as shown in Figure 9.12 and 9.13. When the slice was subject to 2 minutes at 500°C, the oxide thickness was reduced and was found to be roughly 25 nm thick as shown in Figure 9.14.

The measured thickness of the oxide from these oxidation studies may be less than the oxide thickness expected from mechanical tests under load due to the fact they were plain slices without any applied stress. Stress assisted oxidation could potentially lead to thicker oxides being observed on specimens used for mechanical tests. A stress-aided oxidation rate parameter that was stress dependent has been defined by Evans et al (2013) [123]. It was found that an enhancement factor of 3-4 could be applied to oxides formed on stress free surfaces to give similar results to stress assisted oxidation thicknesses. Applying this enhancement factor to the measured oxide thicknesses for the plain sided, unstressed, one hour and two minute dwell tests at 500°C may give an indication of the oxidation thickness expected under load. For example, the one hour dwell mechanical test at 500°C might grow an oxide thickness ahead of the crack tip of up to 0.16 µm. The two minute dwell tests may have an oxide thickness of up to 0.10 µm.

For the one hour dwell test in air, at a low ΔK of 12 MPa√m, the baseline crack growth was 1.40E-04 mm/cycle whereas the dwell crack growth was approximately 3.50E-04 mm/cycle, as shown in Figure 8.1. The difference between these rates was 2.10E-04 mm/cycle. This shows that per cycle, the dwell test is growing 0.21 µm further compared to baseline crack growth. Having an estimate of 0.16 µm for oxidation growth based on a plain sided test is therefore consistent.

For the two minute dwell test, at a ΔK of 12 MPa√m, the baseline crack growth was 1.60E-04 mm/cycle whereas the dwell crack growth rate was 2.40E-04 mm/cycle, as shown in Figure 8.12. The difference between these two crack growth rates is 8.00E-05 mm/cycle. This again shows that per cycle, the dwell test would be growing 0.08 µm further compared to the baseline test. Comparing this to the estimation of oxide thickness under load based on the two minute stress free sample of 0.1 µm, it is again consistent.

Furthermore, when increasing the ΔK for the one hour dwell test to 25 MPa√m, the dwell crack growth is 6.00E-04 mm/cycle. The baseline crack growth rate at a similar ΔK is approximately 3.90-04 mm/cycle. The difference between the two rates is 2.00E-04 mm/cycle. Therefore, per cycle the dwell loading is growing 0.21 µm further compared to the baseline loading. Again this is consistent with the predictions made based on the plain sided one hour test of 0.16 µm.

Any enhancement due to oxidation can be regarded as independent of ΔK, as differences between crack growth rates under one hour dwell and baseline loading were similar when compared at two different ΔK values. Therefore, in this model, differences in crack growth rates as a function of dwell time at any ΔK are related to differences in oxide thickness alone. At high ΔK values, the majority of crack growth rate will naturally derive from mechanical fatigue and is not enhanced greatly by oxide formation.

Based on these results for the one hour and two minute plain sided stress free samples at 500°C, a prediction was made on oxide thickness with the stress enhancement factor added for samples exposed to one second at 500°C. Based on the oxidation thickness for the one hour and two minute tests, a parabolic rate constant, k_p, was established. Using the gradient between oxide thickness at one hour and two minutes, k_p was given as 4.00E-06. This value of k_p could then be used in the following equation to predict oxide thickness at one second [124, 125]:

$$\mathrm{x}^2 = 2k_p t \qquad (Equation\ 10.1)$$

Where x is oxide thickness in µm, t is time in seconds and k_p is the parabolic rate constant. The prediction estimated an oxide thickness of 0.0028 µm when exposed to 500°C for one second. This therefore suggests that at baseline crack growth of 0.25 Hz, oxides would have less influence on crack growth than one hour or two minute dwell times. As crack growth rates increase, the oxide thickness would be tiny in comparison to the crack growth rate and hence at high ΔK values, crack growth rate is not controlled or driven by oxide thickness. For 15 Hz tests, the thickness of oxides are predicted to be vanishingly small.

9.5.2 Dwell under Vacuum Conditions

The proposed theory of oxide cracking during early in the unload-reload cycle could also be applied to the dwell tests carried out under imperfect vacuum conditions employed here, with a pressure of between 1E-04 and 1E-05 Mbar, to explain plausibly why there is an increase in crack growth rate when the dwell period is introduced.

As shown in Figure 8.9, comparing the one hour dwell tests carried out in air and vacuum conditions, the baseline crack growth for the vacuum test is significantly lower than the baseline crack growth rate of the air test. For example, at a ΔK of 12 MPa√m, the vacuum fatigue crack growth rate is 3.50E-05 mm/cycle whereas at the same ΔK, the air fatigue crack growth rate is 1.30E-04 mm/cycle. However, despite this large difference in crack growth rate under baseline loading, when the one hour dwell period is introduced, the crack growth rates become very similar. For example, at a ΔK of 18 MPa√m, both tests experience a crack growth rate of 4.50E-04 mm/cycle. It is perhaps possible that enduring a one hour dwell period provided a long enough static hold time for similar oxide growth to occur in air and vacuum conditions. If this was the case than the amount of crack growth acceleration as the oxides cracked during the unload-reload cycle would be similar, due to the amount of oxide ahead of the crack tip being similar. This would result in very similar crack growth rates for both air and vacuum conditions.

The baseline crack growth rates for both the vacuum and air tests are likely to be different due to the fact 0.25 Hz may not enough time for any influence of the environment or oxide growth under vacuum conditions. However, in the air test, 0.25 Hz may be enough time for environmental influence resulting in oxide growth and hence this could be the reason as to why there is an increase in crack growth rate for baseline loading in air compared to vacuum conditions.

For the two minute dwell tests in vacuum and air, when the dwell period was introduced, the crack growth rates did not become equal, as seen in the one hour dwell tests. It is again possible that the proposed theory of oxide cracking during the unload-reload cycle could help to explain this. As shown in Figure 8.12, the baseline crack growth rates for the air and vacuum conditions are different. For example, at a ΔK of 12 MPa√m the air test has a crack growth rate of 1.70E-04 mm/cycle whereas the vacuum test has a crack growth rate of 5.20E-05 mm/cycle. When the dwell period is introduced, both conditions do experience an increase in crack growth rate, but they do not become equal. For example, at a ΔK of 20 MPa√m, which is approximately in the middle of the dwell segment for both tests, the air test has a crack growth rate of 4.00E-04 mm/cycle whereas the vacuum test has a crack growth rate of 2.80E- 04 mm/cycle. The crack growth rates not becoming equal for the air and vacuum conditions when the dwell period is introduced could possibly be due to the fact that with a two minute dwell time, the two minutes is not a long enough static hold time for oxides to grow and reach a point in which no further growth could occur. However it may be long enough for limited amounts of oxide growth.

The rate that oxides grow in vacuum and air conditions is likely to be different so that in two minutes, there is likely to be more oxide growth in air than under vacuum. This could mean that there is a greater thickness of oxide to crack during the unload-reload cycle in the air test which would result in a faster crack growth rate, which is what was observed from the results in Figure 8.12. However, even under vacuum conditions, it is possible there may some oxide growth, albeit limited, which could explain why the two minutes dwell in vacuum crack growth rate is faster than the baseline vacuum crack growth rate.

Figure 9.15 plots air and vacuum crack growth rate data taken from a single ΔK value for tests at an R ratio of 0.1 at 500^{o}C at different test frequencies or dwell times. The ΔK the crack growth rates are plotted from is 20 MPa√m. Here it is clear to see that at higher frequencies the crack growth rates appear very different for both air and vacuum data. However, as dwell time increases, the crack growth rates do become similar and after one hour dwell, they become equal. It is this sort of shape of curve which is predicted to be occurring during the dwell tests in terms of oxidation effects. For baseline crack growth at 0.25 Hz, the crack growth rates are likely to be different due to the fact the air test may be experiencing more environmental influence such as modest oxidation effects compared to the vacuum test. For a two minute dwell test, the crack growth rates for both air and vacuum tests are both increased compared to baseline crack growth. However, the air test crack growth rate increases much more than the vacuum test crack growth rate. This could be because in air, the oxides may grow quickly and hence become thicker in two minutes than in vacuum. Oxides may start to grow within the two minute holding time but grow slowly and hence do not become as thick. For the one hour dwell tests, it is observed that both the air and vacuum tests have a very similar crack growth rate as shown in Figure 8.9. It appears that after one hour, both air and vacuum conditions are able to reach an oxide thickness that is very similar to one another. Without cracking the oxide, it seems no further oxide growth could occur. Figure 9.15 gives the impression that the one hour dwell test in air reaches a point in which no further oxide growth could occur fairly quickly, after two minutes but significantly before one hour. It seems that for the vacuum test, the oxide growth may be slow but nonetheless does still occur. This could be a result of only a partial vacuum being achieved, rather than a hard vacuum. Before one hour, the oxide may be able to reach a point in which it has grown sufficiently to match that of the thickness for the air test after one hour. Hence, it reaches a point in which no further growth could occur. Due to oxides growing slower under vacuum than in air, it is likely a much larger proportion of the one hour static hold time is being used for oxide growth in vacuum compared to in air.

Figure 9.16 shows crack growth rates for the different frequency tests carried out in air at a ΔK of 28 MPa√m. Compared to Figure 9.15, which shows crack growth rates at a ΔK of 20 MPa√m, there is less of a difference in crack growth rates between the two minute and one hour dwell times tests. However, there is still a large difference between these two tests crack growth rates and the higher frequency tests.

9.5.3 Evidence for the Oxide Cracking Theory

In order to investigate oxide cracking, interrupted tests were carried out to explore exactly what was happening at the crack tip in terms of oxidation for both air and vacuum tests.

9.5.3.1 Interrupted Tests

Interrupted tests were carried out for both the one hour, Kmax hold dwell tests at 500°C in air and under vacuum conditions. FIB "lift outs" were carried out on both samples of the crack tip for investigation under the TEM. The crack tip was representative of the test being subject to a number of one hour dwell cycles and loading was held at the end of the dwell hold, before the unload-reload cycle and hence before the oxide could crack (if the hypothesis that oxide cracking occurs only on the unload-reload cycle is correct).

The baseline loading for these two interrupted tests presented different crack morphologies. Figure 9.17 shows the test carried out in air and from this it is clear to see that there is significant amount of secondary cracking along the entirety of the crack length with some cracks branching off from the secondary cracks. Once the dwell period was introduced there were still large amounts of secondary cracking present. The crack appears to sometimes follow the interface between primary α and β matrix but other times it appears to cut straight through the primary α laths. The crack path cutting through the primary α laths appears to be slightly more dominant compared to following the interface. The crack path cutting through primary α laths is in agreement with the striation growth mechanism, as it is thought that striations form on the primary α laths. As on the fracture surface for the one hour dwell tests striations were visible, as shown in Figure 8.3, it is consistent that cracks may cut through primary α laths.

When looking directly at the crack tip in Figure 9.18 it appears the crack splits into two and so it is unclear which is the main crack and which is a secondary crack. Both crack tips were included in the FIB “lift out”.

Figure 9.19 shows the crack for the test carried out under imperfect vacuum conditions with a pressure of between 1E-04 and 1E-05 Mbar. It is immediately clear to see that this crack profile is different from the test carried out in air as there is no secondary cracking along the crack. The crack path is seen to be cutting directly through the primary α laths and does not obviously following the interface between α and β. This would result in a very flat fracture surface due to the fact the crack is cutting straight through the laths. The crack tip is very clear due to the fact there was no secondary cracking or branching shown in Figure 9.20. It is also worth noting that here it is possible to see dark marks along the crack which are a result of etching effects. The crack here is in the precrack stage of growth which occurs at 15 Hz.

The FIB “lift out” of the crack tip of the interrupted test in air and vacuum were looked at under the TEM, as shown in Figures 9.21 and 9.22. Figure 9.21 displays the measurement taken of the length of oxides ahead of the crack tip for the primary crack in air. The oxidation ahead of the crack tip was found to be approximately 0.14 µm. From the FIB “lift out” of the vacuum interrupted test, after inspection from the TEM, it can be seen that the oxidation ahead of the crack tip was measured to be 0.13 µm as shown in Figure 9.22. The measurements for the oxide ahead of the crack tip were thus found to be very similar for interrupted tests carried out in both air and imperfect vacuum conditions.

Figure 9.23 shows an EDS map and EDS linescan created for the primary crack of the 500°C air test. Here areas of oxygen penetration can be seen with Ti-rich oxides formed. It can be seen that there are titanium rich oxides at the crack tip and a high dislocation density surrounding the crack tip.

For the interrupted vacuum test, Figure 9.24 shows an image captured before the crack tip. Here it is possible to see that α laths close to the crack were bent and deformed. There are also regions close to crack which had been subject to recrystallization. Bending of the α laths and areas of recrystallization are indications of plastic deformation [126, 127]. Figure 9.25 shows an EDS map and linescan created for the primary crack tip of the vacuum test at 500°C showing how much oxygen penetration was present. Interestingly, the EDS maps of the vacuum test appear to show black "voids" along the crack. It is thought that each of these black "voids" may represent the end of each dwell cycle. It is possible to count four of these "voids". The crack extension over each cycle based on the "voids" is measured to be approximately 3.25E-04 mm. In Figure 8.8, for the one hour dwell test under vacuum conditions, the crack growth rate is approximately 3.80E-04 mm/cycle, at a ΔK of 17 MPa√m. This shows that the two crack growth rates per cycle are very similar. The interrupted test was carried out at a slightly lower ΔK of 15 MPa√m which could therefore explain the slightly lower measurement of crack growth per cycle observed for the interrupted test compared to the one hour dwell vacuum test.

At the crack tip, there appears to be a build-up of oxide formation but as the test was stopped before the unload reload cycle, the oxide is thought to not have broken. This could be the reason why there are four black "voids" visible, as each of these represent a whole cycle, including the unload reload cycle.

From these results it is clear to see that theory mentioned previously has gained further evidence to support it. The fact that the oxide ahead of the crack tip is a similar length for both the air and vacuum tests (with a pressure of between 1E-04 and 1E-05 Mbar) supports the idea that even in vacuum conditions, the static load of one hour is long enough for oxides to build up. During the unload reload cycle the oxide cracks and hence the crack growth rate is accelerated. Due to the fact that the length of oxide has been measured to be very similar for both the air and vacuum tests shows how the increase in crack growth rates should be similar.

9.5.4 Plasticity in Dwell Tests

Figure 8.1 displays results from the one hour dwell test at 500°C at Kmax hold in air. From this it is clear to see that through each of the three transitions of baseline to dwell loading, the crack growth rate was highest when the dwell period was initially introduced. The crack growth rate does appear to decelerate as the crack length increases before increasing again. This leads to a 'U' configuration on the fatigue crack growth resistance curve. It is thought that the initial high crack growth rate followed by a decrease in rate could be due to high levels of plastic strain in the immediate vicinity of the crack tip. It is thought these high plastic strain levels, as a result of being under a tensile load for one hour, could cause the material to plastically yield and hence result in crack tip blunting [128, 129]. Crack tip blunting during the dwell period may cause the crack growth rate to decrease initially. However, with increasing ΔK the crack growth rate is able to increase with crack length increase, as expected with the Paris relationship. This suggests perhaps that the local crack tip plasticity reaches a "steady-state" and after which a fracture mechanics approach can be applied routinely.

Further support for transient local plasticity and crack tip blunting occurring during and after dwell loading is found on returning to baseline loading. From Figure 8.1 it is obvious to see that on returning the baseline loading, there are large tails at the start of each of the baseline loading segments. It is possible this crack growth retardation is a consequence of the crack tip becoming blunt during the dwell loading. However, after a number of fatigue loading cycles during baseline loading, it is possible that the crack tip is able to resharpen. Once this happens, the crack growth rates are able to recover and return to the expected baseline rates, based on the Paris regime.

The results from one hour dwell tests with Kmin and Kmax holds are shown in Figure 8.5. From this it is clear that for the Kmin test, on returning to baseline crack growth following dwell crack growth, the crack growth rate matched the expected crack growth rate and did not experience any crack growth retardation. This could suggest that under one hour dwell at Kmin, the load was not high enough for stresses at the crack tip to cause significant crack tip blunting. Further support for this is from the crack growth rates for the dwell loading for the Kmin and Kmax tests. The crack growth rates appear to show that the Kmin test has a crack growth rate that is very subtly raised above the crack growth rate for the Kmax test. This could again potentially show that for the Kmin test, there was less crack tip blunting occurring during dwell loading compared to the Kmax test. This could suggest that the crack tip may be slightly sharper and hence this could lead to a slight increase in crack growth rate. However, an issue with this is that for the Kmin test, when the dwell period is introduced, it does appear that the crack growth rate was highest as the dwell period is initially introduced but then decreased as the crack length increased, before the crack growth rate increased again. This creates a similar profile of crack growth rate to that experienced by the Kmax one hour dwell test. This therefore does perhaps suggest that when the dwell period was introduced following baseline crack growth, even when the dwell period was at Kmin, the strain levels around the crack tip may be high enough to cause some degree of crack tip blunting. It may be a case that there was less blunting in the Kmin one hour dwell test than the Kmax one hour dwell test. Having less blunting perhaps could have meant that on returning to baseline loading following dwell loading, the crack tip did not need to significantly resharpen enough for any crack growth retardation to occur.

Although seeing results from the dwell tests that did experience the highest crack growth rate when the dwell period was initially introduced before falling slightly as the crack grew and then increasing again, creating a ‘U’ configuration was common, it was not observed for every dwell test. The tails of crack retardation on baseline crack growth following dwell loading were again common but not observed on every test. The reason for this still remains unclear but perhaps crack tip blunting under dwell loading is more prominent in certain conditions. If time had permitted, further work would have been carried out into the idea of crack tip blunting during the dwell period and crack tip resharpening during the baseline loading, with the possibility of the two loading cycles producing different steady-state crack tip shapes.

9.6 Crack Growth Rates based on Oxide Cracking Model

Throughout the project so far, a model has been proposed, shown in Figure 9.8, which suggests why crack growth rates are seen to be different at low ΔK values for different conditions but then as ΔK increases, crack growth rates converge. It is proposed that at low ΔK values, the distance the crack is growing each cycle is small and therefore a given contribution of oxide cracking ahead of the crack tip can be a significant proportion of the overall crack extension. During dwell loading and lower frequency tests, there is more time for oxides to form ahead of the crack tip which crack and hence produce faster crack growth rates compared to higher frequency tests. As the ΔK increases, the distance the crack grows each cycle increases as a result of mechanical fatigue, therefore lessoning the impact of oxides ahead of the crack tip. This results in crack growth rates converging.

From experimental work, including mechanical tests to establish crack growth rates, oxidation studies on plain sided, stress free samples and interrupted tests, oxide growth ahead of the crack tip for two minute and one hour dwell times have been established. It was found that there appears to be maximum length of oxide formed ahead of the crack tip of 160 nm, as this was estimated from the one hour stress free sample at 500°C. The actual oxide thickness measured from the stress free sample was 40 nm but a stress enhancement factor of four was applied to estimate likely oxide thickness when stress was applied. This gave an estimated oxide thickness of 160 nm.

It appears that the oxide would not get much thicker even if the dwell time was increased, due to the parabolic nature of oxide growth, suggested in Figure 9.11. This suggests that there is perhaps a natural limit to the amount crack growth rate can increase by when under dwell loading. For two minute dwell tests, the oxide formation ahead of the crack tip was estimated to be approximately 100 nm based on measurements taken from the plain sided, stress free samples used for oxidation studies. The actual oxide thickness measured was 25 nm for the stress free sample after two minutes but a stress enhancement factor of four was applied. This gave an estimated oxide thickness of 100 nm.

The oxide formed ahead of the crack tip was estimated for 0.25 Hz at 500°C in air based on the one hour and two minute oxide thickness results. It was predicted that the oxide formed ahead of the crack tip at one second would be 2.8 nm and thus the oxide ahead of the crack tip at 15 Hz frequency would be vanishingly small. Because of this the crack growth rate at 15 Hz was thought to be a result of pure mechanical fatigue only. Figure 9.15 shows crack growth rates taken from a single ΔK of 20 MPa√m at a range of frequencies, at 500°C in air and vacuum conditions. There are large differences in crack growth rates between 15 and 0.25 Hz and also between vacuum and air data.

If 15 Hz was assumed to have a negligible effect of oxides ahead of the crack tip, it would be assumed, based on a parabolic growth law for oxide growth and the model shown in Figure 9.8, that the 0.25 Hz test would only grow 2.8 nm further per cycle as a result of oxide formation. However, there is a significantly larger difference in crack growth rates between the two conditions. For example, at a ΔK of 20 MPa√m, each cycle, the 0.25 Hz is growing 1.30E-04 mm/cycle further than the 15 Hz test which equates to 130 nm.

Furthermore, the vacuum data on Figure 9.15 for 15 and 0.25 Hz show very low crack growth rates. At 0.25 Hz in air, the contribution of oxides ahead of the crack tip was estimated to be approximately 2.8 nm. Based on the model in Figure 9.8, mechanical fatigue would be the same for both conditions as the ΔK is the same. Any difference in crack growth rate would be a result of oxide formation at the crack tip. Therefore this suggests that at 0.25 Hz, the air test should grow approximately 2.8 nm each cycle further than the vacuum test. From Figure 9.15, the difference in crack growth rates between the 0.25 Hz air and vacuum test can be found as 1.80E-4 mm/cycle. This equates to 180 nm per cycle, which is obviously significantly larger than expected, based on the model in Figure 9.8.

For the model to be accurate and explain differences in crack growth rates, the oxide thickness predicted for 0.25 Hz would either need to be much thicker or an alternative reason could be that the crack growth rates for 15 Hz in air and 15 and 0.25 Hz in vacuum are much lower than anticipated for some reason.

Even if the oxide formation ahead of the crack tip was much thicker for the 0.25 Hz test in air, this approach still cannot explain the range of crack growth rates observed. For example, the maximum thickness the oxide could possibly be, based on the one hour dwell test, is 160 nm. As the difference between the 0.25 and 15 Hz air test was found to be even greater than 160 nm at 180 nm, any oxide cracking cannot explain the increase in crack growth rate observed.

Having a much lower crack growth rate for the 15 Hz air test and 15 and 0.25 Hz vacuum tests could potentially be a result of the oxide ahead of the crack tip being so thin. There is perhaps potential for this very thin oxide ahead of the crack tip not to crack during each cycle, as a result of a thin oxide being much stronger than a thicker oxide [122]. Therefore each fatigue cycle may not be as damaging and hence crack growth rates would reduce. Also it may be possible that when the oxide is thicker, such as with the dwell cycles, on fracture of the oxides, the crack tip becomes much sharper and this could potentially result in a greater crack extension under the fatigue cycle. If the oxide is only very thin, there is a possibility that the crack tip may be blunter and therefore each cycle would be less damaging. Each fatigue cycle, the crack may propagate a smaller distance and therefore would have a reduced crack growth rate.

Therefore, it is likely that at high frequencies, a more complicated mechanism of crack growth may be occurring due to the presence of a very thin oxide. When oxides ahead of the crack tip have been measured, rather than predicted, the model shown in Figure 9.8 works accurately. Measurements for oxides ahead of the crack tip in air and vacuum at one hour and for two minutes in air are consistent with crack growth rates obtained experimentally. However, extrapolation to higher frequencies of loading, where oxide thickness has not been measured is unwarranted.

Chapter 10 - Conclusions and Future Work

10.1 Conclusions

One focus of this project investigated fatigue crack growth resistance under dwell conditions in the titanium alloy Ti 6246. Effects of extrinsic factors on the near threshold region and the Paris regime were also investigated. The extrinsic factors considered included: R ratio; environment; temperature; and frequency. The main conclusions are:

1) For all fatigue crack growth resistance tests carried out, the crack growth mechanism remains transgranular. Striated crack growth was observed, particularly at high values of ΔK on fracture surfaces for one hour dwell tests. The striations are found on primary α laths. As a block loading waveform of baseline and dwell crack growth was used, the transition between baseline and dwell loading is visible. The striations on the fracture surface were visibly larger in the dwell loading than baseline loading. For the one hour dwell test at 500°C, at the transition between the third baseline and third dwell segments, the baseline striations were measured as 0.45 µm and the striations in the dwell were measured as 0.78 µm. Assuming 1:1 relationship between crack extension each cycle and striation spacing, these measurements matched crack growth rates obtained experimentally. The “m” values for all dwell tests carried out at 500°C were between 0.97 and 2.9.
2) Across all conditions tested, the fatigue crack growth rate was increased when subject to dwell fatigue loading compared to baseline loading. For tests carried out at 500°C increases in crack growth rate were small but significant (up to four times) with the largest increase being for the one hour vacuum dwell test compared to baseline

loading. For the 575°C dwell test, the crack growth rate remained transgranular but the increase in crack growth rate under dwell loading was more dramatic (up to fifteen times) compared to baseline loading. The “m” value obtained for this test was 6.10 which was significantly higher than “m” values obtained for all other dwell tests, with the next highest being 2.90 from the two minute dwell test in vacuum at 500°C. The faster crack growth rate was thought to be due to creep damage. A further 575°C one hour dwell test failed prematurely away from the notch. Time to failure was consistent with stress rupture data provided by Rolls-Royce plc.

3) At 500°C the increase in crack growth rate observed when a dwell period is introduced is thought to perhaps be associated with brittle oxides cracking ahead of the crack tip during the unload reload cycle. Throughout the static hold of the dwell cycle, oxides are able to grow, as confirmed by interrupted mechanical tests. The length of the static hold is thought to influence how thick the oxide can grow and therefore how much crack growth acceleration there is when it cracks. A one hour static hold under vacuum is thought to be enough time for oxides to grow the same amount as they would in air, therefore resulting in similar amounts of crack growth acceleration when they crack.

4) Interrupted tests were performed to mimic one hour dwell tests carried out in air and vacuum conditions. Oxide growth ahead of the crack tip was measured for both the air and vacuum tests and both were found to be approximately 140 nm. The fact that oxide growth ahead of the crack tip was measured to be similar for both air and vacuum conditions suggests that perhaps there would be similar amounts of oxide to crack during the unload reload cycle for both air and vacuum conditions when subject to one hour dwell periods.

5) It was suggested that during some of the dwell tests, plasticity at the crack tip caused crack tip blunting to occur. Evidence for this is seen on the transition from baseline to dwell loading, the fastest crack growth rate is seen as the dwell period is initially introduced. As the crack length increases, the crack growth rate decreases before increasing again. The initial decrease it thought possibly to be due to crack tip blunting during the dwell period. Further support for this is on returning to baseline crack growth, following dwell crack growth, there appears to be dramatic crack growth retardation. This could again be a sign of crack tip blunting occurring in the dwell period. After a number of fatigue cycles, the crack growth rate increases and is able to recover to the expected crack growth rate. This is perhaps a result of the crack tip resharpening.
6) Effects of temperature, frequency and stress ratio on ΔK_{th} and near threshold crack growth were investigated. When temperature decreased from 500^{o}C to room temperature, the ΔK_{th} value decreased from 4 to 3 MPa√m, for R ratio 0.1 tests. The 500^{o}C tests experienced a sharp drop off in crack growth rate to ΔK_{th} whereas room temperature tests had a gradual decline in rate to ΔK_{th}. When frequency was decreased from 15 to 0.25 Hz, the ΔK_{th} value decreased slightly from 4 to 3.5 MPa√m. For near threshold crack growth, the rate was different for 15 and 0.25 Hz tests. The 0.25 Hz test was found to have a faster crack growth rate compared to the 15 Hz test by a factor of 3 times. Stress ratio was found to have very limited effects on $\Delta K_{th,}$ by increasing the R ratio from 0.1 to 0.5, to ΔK_{th} was decreased from 4 to 3.2 MPa√m. For the constant Kmax test, the final R ratio was 0.87, a ΔK_{th} was given as 1.5 MPa√m.
7) Possible explanations for the slight differences obtained for ΔK_{th} and near threshold crack growth at different temperatures and frequencies could be related to environmental effects. At 500^{o}C, there is likely to be more influence of the

environment and potentially oxidation than at room temperature, this could perhaps cause faster crack growth rates at elevated temperatures in near threshold regions. As for frequency, 0.25 Hz is a slower cycle time than 15 Hz and therefore there may be more time for environmental influence to contribute to crack growth, meaning the crack growth rate may be higher. At a certain ΔK, the driving force may become too low for the crack to overcome the environmental effects and there may be a sudden drop in crack growth rate down to $\Delta K_{th,}$ leading to similar ΔK_{th} values being given for both 0.25 and 15 Hz tests. Finally, stress ratio may influence ΔK_{th} as a result of possible crack closure effects. As R ratio is increased, it is suggested that crack closure effects are minimised and thus both fracture surfaces come into less contact. Above R ratio 0.7, it has been said that all crack closure effects are minimised and thus the crack could grow much more readily. This could result in a much lower ΔK_{th}being obtained.

8) Effects of temperature, frequency, environment and stress ratio on crack growth rate in the Paris regime were investigated. Changing the R ratio from 0.1 to 0.5 was found to have very limited effects on crack growth rate with rates for both stress ratios being very similar. At low values of ΔK, there was a large difference in crack growth rate with elevated temperature tests having a significantly faster crack growth rate than room temperature tests. 0.25 Hz tests were also found to have a higher crack growth rate than 10 Hz tests at low ΔK values. Finally, tests carried out in air were found to have faster crack growth rates than test carried out in vacuum at low ΔK values. Across all these conditions, as ΔK increased, crack growth rates were found to converge so that the difference in crack growth rates between these tests was reduced.
9) Crack growth rates being different at low ΔK values and converging as ΔK increases is again perhaps a consequence of environmental influences. Environmental influences may include possible oxides forming ahead of the crack tip which could cause

embrittlement or oxygen going into primary α laths which would increase their brittleness. At low ΔK values, the crack growth rate is slow and the distance the crack advances in one cycle is relatively small. Therefore any effects of the environment, such as from tests being carried out in air rather than vacuum, at elevated temperature rather than room temperature, or at a low frequency of 0.25 Hz rather than a high frequency of 10 Hz, would contribute significantly to overall crack growth. Crack growth is thought to be made up by a combination of mechanical fatigue and environmental effects. As crack growth rate increases, the distance the crack advances in one cycle as a result of mechanical fatigue increases, as does the speed in which the crack is advancing. This could therefore mean that any environmental influences on crack growth rate are lessoned. Hence as ΔK increases, crack growth rates are likely to converge, as mechanical fatigue dominates and controls crack growth rate.

10) Fracture surfaces from the 0.25 Hz, air and vacuum test were studied under TEM. The vacuum test had a much smoother crack profile whereas the air test was jagged and rough with secondary cracking present down the primary α laths. It was thought that oxygen in the air may react with the primary α laths making them brittle which could contribute to increased crack growth rates seen in air compared to vacuum at low ΔK values.

10.2 Future Work

1) Interrupted tests could be carried out to incorporate different dwell times as well as being interrupted at different times during the loading cycle. Two minute dwell time could be used as well as one hour dwell time to compare tests carried out in air and

vacuum conditions. If tests were interrupted at the end of a two minute dwell cycle, before the unload reload cycle occurred, the length of the oxide ahead of the crack tip could be measured and compared for both air, inert gas and vacuum conditions. The point of interruption of these tests could also be altered so that instead of being at the end of the dwell cycle, before the unload reload cycle occurred, the interruption could be at the beginning of a dwell cycle, immediately following an unload reload cycle. It is thought that at this point, the oxide would have just cracked and therefore there would be very little to measure ahead of the crack tip.

2) Understanding any potential crack tip blunting mechanism that occurs during the dwell loading and crack tip resharpening occurring during baseline loading would further help to understand how dwell crack growth can affect crack propagation. It is thought crack tip blunting may occur during the dwell period due to the fact on transition from baseline to dwell loading, the dwell crack growth rate is highest initially but as the crack advances, the crack growth rate decreases but increasing again. On returning to baseline crack growth it was common to see crack retardation, which could again be linked to crack tip blunting in the dwell period.

3) For the threshold tests carried out, it was unusual to see results that crossed over for the 500^{o}C and room temperature tests, resulting in the 500^{o}C tests having a higher ΔK_{th} value than the room temperature tests. This was found for both R ratios of 0.1 and 0.5 tests. Threshold tests under vacuum conditions could be carried out to help gain an understanding as to exactly how oxidation effects ΔK_{th} and near threshold crack growth rates. Furthermore, it is possible that perhaps hydrogen is affecting both ΔK_{th}

and near threshold crack growth for the room temperature tests. It would be helpful to investigate this possible hydrogen affect at room temperature under inert and vacuum conditions. Finally, performing tests to further investigate crack closure effects by measuring the K value of closure would help to clarify what is occurring at near threshold values and why the difference in threshold values were obtained.

Chapter 11 - References

1. Ciokajlo, J.J. and H.B. Ritchie, *Jet engine turbine support*. 1990, Google Patents.
2. Spittle, P., *Gas turbine technology.* Physics education, 2003. **38**(6): p. 504.
3. Peters, M., et al., *Titanium alloys for aerospace applications.* Advanced engineering materials, 2003. **5**(6): p. 419-427.
4. CIEC. *Titanium: Uses of Titanium*. 2015 [cited 2016 22 Aug 2016].
5. Donachie, M.J., *Titanium: a technical guide*. 2000: ASM international.
6. Tong, V., et al., *Using transmission Kikuchi diffraction to characterise α variants in an α+ β titanium alloy.* Journal of microscopy, 2017. **267**(3): p. 318-329.
7. Lütjering, G. and J.C. Williams, *Titanium Based Intermetallics.* Titanium, 2007: p. 337-366.
8. Ankem, S. and C. Greene, *Recent developments in microstructure/property relationships of beta titanium alloys.* Materials Science and Engineering: A, 1999. **263**(2): p. 127-131.
9. Choda, T., H. Oyama, and S. Murakami, *Technologies for process design of titanium alloy forging for aircraft parts.* Kobelco Technology Review, 2015. **33**: p. 44-49.
10. McLean, D., *Mechanical properties of metals*. Vol. 129. 1962: Wiley New York.
11. Suresh, S. and R. Ritchie, *Propagation of short fatigue cracks.* International Metals Reviews, 1984. **29**(1): p. 445-475.
12. Paris, P. and F. Erdogan, *A critical analysis of crack propagation laws.* Journal of basic engineering, 1963. **85**(4): p. 528-533.
13. Eylon, D. and J. Hall, *Fatigue behavior of beta processed titanium alloy IMI 685.* Metallurgical Transactions A, 1977. **8**(6): p. 981-990.
14. Spence, S., W. Evans, and M. Cope. *Dwell fatigue on TI 6246 at near ambient temperatures*. in *ICF 9-Sydney, Australia-1997*. 1997.
15. Evans, W.J., *Time dependent effects in fatigue of titanium and nickel alloys.* Fatigue & Fracture of Engineering Materials & Structures, 2004. **27**(7): p. 543-557.
16. Reed, R.C., *The superalloys: fundamentals and applications*. 2008: Cambridge university press.
17. Anderson, T.L., *Fracture mechanics: fundamentals and applications*. 2017: CRC press.
18. Khanna, A.S., *High temperature oxidation*, in *Handbook of Environmental Degradation of Materials*. 2005, Elsevier. p. 105-152.
19. Whittaker, M., *Titanium in the Gas Turbine Engine*. 2011: INTECH Open Access Publisher.
20. Royce, R., *The jet engine*. 2015: John Wiley & Sons.
21. Klaus, H., *Jet Engines: Fundamentals of Theory, Design and Operation*. 1997, Zenith Press.
22. Eckardt, D. and P. Rufli. *Advanced Gas Turbine Technology: ABB/BBC Historical Firsts*. in *ASME Turbo Expo 2001: Power for Land, Sea, and Air*. 2001. American Society of Mechanical Engineers.
23. Meher-Homji, C.B., *The development of the Whittle turbojet.* Journal of engineering for gas turbines and power, 1998. **120**(2): p. 249-256.
24. Brinkworth, B., *On the aerodynamics of the Gloster E28/39–a historical perspective.* The Aeronautical Journal, 2008. **112**(1132): p. 307-326.

25. Armstrong, F., *Jet Propulsion: a simple guide to the aerodynamic and thermodynamic design and performance of jet engines, Cumpsty N., Cambridge University Press, The Edinburgh Building, Cambridge CB2 2RU. 1997. Illustrated.£ 19.95.* The Aeronautical Journal, 1998. **102**(1016): p. 330-330.
26. Shaw, R.J. and T. Benson. *How Does a Jet Engine Work?* 2014 [cited 2016 Aug 22 2016].
27. Hünecke, K., *Jet engines: Fundamentals of theory, design and operation*. 1997: Airlife.
28. Hall, N. *Turbojet Engines*. 2015 [cited 2015 May 5 2015].
29. Mattingly, J.D. and H. Von Ohain, *Elements of propulsion: gas turbines and rockets*. 2006: American Institute of Aeronautics and Astronautics Reston, Va, USA.
30. Spang III, H.A. and H. Brown, *Control of jet engines.* Control Engineering Practice, 1999. **7**(9): p. 1043-1059.
31. Boyce, M.P., *Gas turbine engineering handbook*. 2011: Elsevier.
32. Gerdemann, S.J., *Titanium process technologies.* Advanced materials & processes, 2001. **159**(DOE/ARC-2002-007).
33. Kroll, W., *The production of ductile titanium.* Transactions of the Electrochemical Society, 1940. **78**(1): p. 35-47.
34. Subramanyam, R., *Some recent innovations in the Kroll process of titanium sponge production.* Bulletin of Materials Science, 1993. **16**(6): p. 433-451.
35. Schutz, R.W. and D.E. Thomas, *Corrosion of titanium and titanium alloys.* ASM Handbook., 1987. **13**: p. 669-706.
36. Lutjering, G. and J.C. Williams, *Titanium (engineering materials and processes).* Chapter, 2007. **8**: p. 337-66.
37. Polmear, I., *Light alloys, metallurgy of the light alloys.* Metallurgy and Materials Science, Arnold, Great Britain, 1995: p. 168-95.
38. Rugg, D., M. Dixon, and F.E. Dunne, *Effective structural unit size in titanium alloys.* The Journal of Strain Analysis for Engineering Design, 2007. **42**(4): p. 269-279.
39. Karthikeyan, T., S. Saroja, and M. Vijayalakshmi, *Evaluation of misorientation angle-axis set between variants during transformation of bcc to hcp phase obeying burgers orientation relation.* Scripta materialia, 2006. **55**(9): p. 771-774.
40. Burgers, W., *On the process of transition of the cubic-body-centered modification into the hexagonal-close-packed modification of zirconium.* Physica, 1934. **1**(7): p. 561-586.
41. Callister, W.D. and D.G. Rethwisch, *Fundamentals of materials science and engineering*. Vol. 21. 2013: Wiley New York.
42. Evans, W. and M. Bache, *Dwell-sensitive fatigue under biaxial loads in the near-alpha titanium alloy IMI685.* International Journal of Fatigue, 1994. **16**(7): p. 443-452.
43. Welsch, G., R. Boyer, and E. Collings, *Materials properties handbook: titanium alloys*. 1993: ASM international.
44. Leyens, C. and M. Peters, *Titanium and titanium alloys: fundamentals and applications*. 2003: John Wiley & Sons.
45. Polmear, I., *Light alloys: from traditional alloys to nanocrystals*. 2005: Elsevier.
46. Logan, K., *Effects of Beta Stabilizers on Quench Delay Susceptibility of Ti-6Al-4V.* 2012.
47. Sommitsch, C., et al., *Microstructure control in processing nickel, titanium and other special alloys*, in *Microstructure evolution in metal forming processes*. 2012, Elsevier. p. 337-383.
48. Lütjering, G., *Property optimization through microstructural control in titanium and aluminum alloys.* Materials Science and Engineering: A, 1999. **263**(2): p. 117-126.
49. Chakrabarti, A., et al. *Microstructure and mechanical property optimization through thermomechanical processing in Ti-6-4 and Ti-6-2-4-6 Alloys*. in *Sixth World Conference on Titanium. III*. 1988.

50. MatWeb. *Titanium Ti-6Al-2Sn-4Zr-6Mo (Ti-6-2-4-6) BSTA*. Pure Metals. Ceramics. Alloys. Polymers 1996.
51. Domun, N., et al., *Improving the fracture toughness and the strength of epoxy using nanomaterials–a review of the current status.* Nanoscale, 2015. **7**(23): p. 10294-10329.
52. Shuangyin, Z., et al., *Heat-treated microstructure and mechanical properties of laser solid forming Ti-6Al-4V alloy.* Rare metals, 2009. **28**(6): p. 537-544.
53. Attallah, M., et al., *Comparative determination of the α/β phase fraction in α+ β-titanium alloys using X-ray diffraction and electron microscopy.* Materials Characterization, 2009. **60**(11): p. 1248-1256.
54. Guo, Y., et al., *Microstructure and microhardness of Ti6246 linear friction weld.* Materials Science and Engineering: A, 2013. **562**: p. 17-24.
55. Sandala, R.S., *Deformation Mechanims of Two-Phase Ttitanium Alloys.* 2013.
56. Materials, A. *Titanium Alloys - Alpha, Beta and Alpha-Beta Alloys* 2001 [cited 2016 26 Aug 2016].
57. Rolfe, S.T. and J.M. Barsom, *Fracture and fatigue control in structures: Applications of fracture mechanics*. 1977: ASTM International.
58. Wicks, B., et al., *The Inadequacy of Safe-Life Prediction: Aero-Engine Fan and Compressor Disk Cracking*. 2003, AERONAUTICAL AND MARITIME RESEARCH LAB MELBOURNE (AUSTRALIA).
59. Ewalds, H. and R. Wanhill, *Fracture Mechanics (Edward Arnold and Delftse Uitgevers Maatschapij, London, 1991).* Google Scholar: p. 82-84.
60. Mach, K.J., D.V. Nelson, and M.W. Denny, *Techniques for predicting the lifetimes of wave-swept macroalgae: a primer on fracture mechanics and crack growth.* Journal of Experimental Biology, 2007. **210**(13): p. 2213-2230.
61. Maiti, S.K., *Fracture mechanics: fundamentals and applications*. 2015: Cambridge University Press.
62. Irwin, G.R., *Analysis of stresses and strains near the end of a crack traversing a plate.* J. appl. Mech., 1957.
63. Bower, A.F., *Applied mechanics of solids*. 2009: CRC press.
64. Isida, M., *Effect of width and length on stress intensity factors of internally cracked plates under various boundary conditions.* International Journal of Fracture Mechanics, 1971. **7**(3): p. 301-316.
65. Rege, K. and H. Lemu. *A review of fatigue crack propagation modelling techniques using FEM and XFEM*. in *IOP Conference Series: Materials Science and Engineering*. 2017. IOP Publishing.
66. Lawson, L., E. Chen, and M. Meshii, *Near-threshold fatigue: a review.* International Journal of Fatigue, 1999. **21**: p. S15-S34.
67. Ding, J., R. Hall, and J. Byrne, *Effects of stress ratio and temperature on fatigue crack growth in a Ti–6Al–4V alloy.* International journal of fatigue, 2005. **27**(10-12): p. 1551-1558.
68. Campbell, F.C., *Fatigue and fracture: understanding the basics*. 2012: ASM International.
69. Laird, C., *The influence of metallurgical structure on the mechanisms of fatigue crack propagation*, in *Fatigue crack propagation*. 1967, ASTM International.
70. Deshpande, V., A. Needleman, and E. Van der Giessen, *Discrete dislocation modeling of fatigue crack propagation.* Acta materialia, 2002. **50**(4): p. 831-846.
71. Weertman, J., *Dislocation crack tip shielding and the Paris exponent.* Materials Science and Engineering: A, 2007. **468**: p. 59-63.

72. Eylon, D., et al., *Microstructure and mechanical properties relationships in the Ti-11 alloy at room and elevated temperatures.* Metallurgical Transactions A, 1976. **7**(12): p. 1817-1826.
73. Hall, J., *Fatigue crack initiation in alpha-beta titanium alloys.* International journal of fatigue, 1997. **19**(93): p. 23-37.
74. Larsen, J.M., J.C. Williams, and A.W. Thompson, *Crack-closure effects on the growth of small surface cracks in titanium-aluminum alloys*, in *Mechanics of fatigue crack closure*. 1988, ASTM International.
75. Kim, H.-M., *The Effect of Slip Character on Low-Cycle Fatigue Behavior of Ti--Al Alloys.* Dissertation Abstracts International, 1981. **42**(3): p. 234.
76. Demulsant, X. and J. Mendez, *Microstructural effects on small fatigue crack initiation and growth in Ti6A14V alloys.* Fatigue & Fracture of Engineering Materials & Structures, 1995. **18**(12): p. 1483-1497.
77. Wagner, L. and G. Lutjering, *Microstructural Influence on Propagation Behavior of Short Cracks in an(alpha+ beta) Titanium Alloy.* Z. Metallkd., 1987. **78**(5): p. 369-375.
78. Liang, R., et al., *Effect of microstructure on fracture toughness and fatigue crack growth behavior of Ti17 alloy.* Metals, 2016. **6**(8): p. 186.
79. Nalla, R., et al., *Influence of microstructure on high-cycle fatigue of Ti-6Al-4V: bimodal vs. lamellar structures.* Metallurgical and Materials Transactions A, 2002. **33**(3): p. 899-918.
80. Dubey, S., A. Soboyejo, and W. Soboyejo, *An investigation of the effects of stress ratio and crack closure on the micromechanisms of fatigue crack growth in Ti-6Al-4V.* Acta Materialia, 1997. **45**(7): p. 2777-2787.
81. Ritchie, R., et al., *Thresholds for high-cycle fatigue in a turbine engine Ti–6Al–4V alloy.* International Journal of Fatigue, 1999. **21**(7): p. 653-662.
82. Bache, M., *A review of dwell sensitive fatigue in titanium alloys: the role of microstructure, texture and operating conditions.* International journal of fatigue, 2003. **25**(9): p. 1079-1087.
83. Harrision, G., et al., *Designing for dwell-sensitive fatigue in near-alpha titanium alloys.* The Institute of Metals, 1986: p. 198-204.
84. McBagonluri, F., et al., *An investigation of the effects of microstructure on dwell fatigue crack growth in Ti-6242.* Materials Science and Engineering: A, 2005. **405**(1-2): p. 111-134.
85. Evans, W. and C. Gostelow, *The effect of hold time on the fatigue properties of a β-processed titanium alloy.* Metallurgical and Materials Transactions A, 1979. **10**(12): p. 1837-1846.
86. Song, Z. and D. Hoeppner, *Size effect on the fatigue behaviour of IMI 829 titanium alloy under dwell conditions.* International journal of fatigue, 1989. **11**(2): p. 85-90.
87. Bache, M. and W. Evans, *Tension and torsion fatigue testing of a near-alpha titanium alloy.* International journal of fatigue, 1992. **14**(5): p. 331-337.
88. Stroh, A., *The formation of cracks as a result of plastic flow.* Proc. R. Soc. Lond. A, 1954. **223**(1154): p. 404-414.
89. Kohn, D. and P. Ducheyne, *Tensile and fatigue strength of hydrogen-treated Ti-6Al-4V alloy.* Journal of Materials Science, 1991. **26**(2): p. 328-334.
90. Hack, J. and G. Leverant, *The influence of microstructure on the susceptibility of titanium alloys to internal hydrogen embrittlement.* Metallurgical and Materials Transactions A, 1982. **13**(10): p. 1729-1738.
91. Neeraj, T., et al., *Phenomenological and microstructural analysis of room temperature creep in titanium alloys.* Acta materialia, 2000. **48**(6): p. 1225-1238.

92. Suri, S., et al., *Mechanisms of primary creep in α/β titanium alloys at lower temperatures.* Materials Science and Engineering: A, 1997. **234**: p. 996-999.
93. Pugh, P., *The Magic of a Name: The Rolls-Royce Story, Part 2: The Power Behind the Jets*. 2015: Icon Books Ltd.
94. Ruffles, P., *The RB 211: the first 25 years.* 1992.
95. Qiu, J., et al., *A comparative study on dwell fatigue of Ti-6Al-2Sn-4Zr-xMo (x= 2 to 6) alloys on a microstructure-normalized basis.* Metallurgical and Materials Transactions A, 2014. **45**(13): p. 6075-6087.
96. Whittaker, R.J., *An Investigation into Cold Dwell Fatigue Behaviour in Ti6246 and Other Aerospace Alloys.*, in *Mettalurgy and Materials*. 2011, University of Birmingham: Birmingham: University of Birmingham.
97. Zheng, Z., D.S. Balint, and F.P. Dunne, *Mechanistic basis of temperature-dependent dwell fatigue in titanium alloys.* Journal of the Mechanics and Physics of Solids, 2017. **107**: p. 185-203.
98. Albrecht, J. and G. Lütjering, *Microstructure and mechanical properties of titanium alloys.* Titanium'99: Science and Technology, 2000: p. 363-374.
99. Merah, N., *Detecting and measuring flaws using electric potential techniques.* Journal of Quality in Maintenance Engineering, 2003. **9**(2): p. 160-175.
100. Pardhi, Y., et al., *Fatigue Crack Propagation Behavior of an Inertia Friction Welded α/β Titanium Alloy.* 2010.
101. Lütjering, G., *Influence of processing on microstructure and mechanical properties of (α+ β) titanium alloys.* Materials Science and Engineering: A, 1998. **243**(1-2): p. 32-45.
102. Ahmed, T. and H. Rack, *Phase transformations during cooling in α+ β titanium alloys.* Materials Science and Engineering: A, 1998. **243**(1-2): p. 206-211.
103. Ackerman, A.K., et al., *The Kinetics of Primary Alpha Plate Growth in Titanium Alloys.* arXiv preprint arXiv:1805.09885, 2018.
104. Pederson, R., *Microstructure and Phase transformation of Ti-6Al-4V*. 2002, Luleå tekniska universitet.
105. Bermingham, M., et al. *Microstructure of cast titanium alloys*. in *Mater. Forum*. 2007. Citeseer.
106. Schmidt, R. and P. Paris, *Threshold for fatigue crack propagation and the effects of load ratio and frequency*, in *Progress in flaw growth and fracture toughness testing*. 1973, ASTM International.
107. Schmidt, R.A., *A threshold in metal fatigue.* 1970.
108. Elber, W., *The significance of fatigue crack closure, Damage Toler.* Aircr. Struct, 1971. **486**.
109. Wolf, E., *Fatigue crack closure under cyclic tension.* Engineering Fracture Mechanics, 1970. **2**(1): p. 37-45.
110. Kirby, B. and C. Beevers, *Slow fatigue crack growth and threshold behaviour in air and vacuum of commercial aluminium alloys.* Fatigue & Fracture of Engineering Materials & Structures, 1979. **1**(2): p. 203-215.
111. Boyce, B. and R. Ritchie, *Effect of load ratio and maximum stress intensity on the fatigue threshold in Ti–6Al–4V.* Engineering Fracture Mechanics, 2001. **68**(2): p. 129-147.
112. Halliday, M. and C. Beevers, *Some aspects of fatigue crack closure in two contrasting titanium alloys.* Journal of Testing and Evaluation, 1981. **9**(4): p. 195-201.
113. Suresh, S., G. Zamiski, and D.R. Ritchie, *Oxide-induced crack closure: an explanation for near-threshold corrosion fatigue crack growth behavior.* Metallurgical and Materials Transactions A, 1981. **12**(8): p. 1435-1443.

114. Niu, H., et al., *Microstructure evolution and mechanical properties of a novel beta γ-TiAl alloy.* Intermetallics, 2012. **31**: p. 225-231.
115. Sauer, C. and G. Lütjering, *Influence of α layers at β grain boundaries on mechanical properties of Ti-alloys.* Materials Science and Engineering: A, 2001. **319**: p. 393-397.
116. Murray, J. and H. Wriedt, *The O− Ti (oxygen-titanium) system.* Journal of Phase Equilibria, 1987. **8**(2): p. 148-165.
117. Okamoto, H., *O-Ti (oxygen-titanium).* Journal of Phase Equilibria and Diffusion, 2011. **32**(5): p. 473.
118. Wu, H., *Oxygen diffusion through titanium and other HCP metals*. 2013, University of Illinois at Urbana-Champaign.
119. Caton, M. and S. Jha, *Small fatigue crack growth and failure mode transitions in a Ni-base superalloy at elevated temperature.* International Journal of Fatigue, 2010. **32**(9): p. 1461-1472.
120. Dahal, J., *Grain boundary deformation and damage mechanisms in intergranular crack growth of a nickel based superalloy.* 2011.
121. Bedworth, R. and N. Pilling, *The oxidation of metals at high temperatures.* J Inst Met, 1923. **29**(3): p. 529-582.
122. Evans, H., *The role of oxide grain boundaries in the development of growth stresses during oxidation.* Corrosion science, 1983. **23**(5): p. 495-506.
123. Evans, H., H. Li, and P. Bowen, *A mechanism for stress-aided grain boundary oxidation ahead of cracks.* Scripta Materialia, 2013. **69**(2): p. 179-182.
124. Evans, H., *Stress effects in high temperature oxidation of metals.* International materials reviews, 1995. **40**(1): p. 1-40.
125. Wagner, C., *Theoretical analysis of the diffusion processes determining the oxidation rate of alloys.* Journal of the Electrochemical Society, 1952. **99**(10): p. 369-380.
126. Gaddam, R., *Effect of boron and hydrogen on microstructure and mechanical properties of cast Ti-6Al-4V*. 2011, Luleå tekniska universitet.
127. Pederson, R., R. Gaddam, and M.-L. Antti, *Microstructure and mechanical behavior of cast Ti-6Al-4V with addition of boron.* Open Engineering, 2012. **2**(3): p. 347-357.
128. Rice, J., *Mechanics of crack tip deformation and extension by fatigue*, in *Fatigue crack propagation*. 1967, ASTM International.
129. Hutchinson, J., *Plastic stress and strain fields at a crack tip.* Journal of the Mechanics and Physics of Solids, 1968. **16**(5): p. 337-342.

Effects of Dwell Fatigue, Temperature, Frequency and Environment in a Titanium Alloy

Georgia Mills

A thesis submitted to The University of Birmingham
for the degree of

Doctor of Philosophy

Volume II

School of Metallurgy and Materials

College of Engineering and Physical Sciences

The University of Birmingham

September 2019

Chapter 2 – Gas Turbine Engines

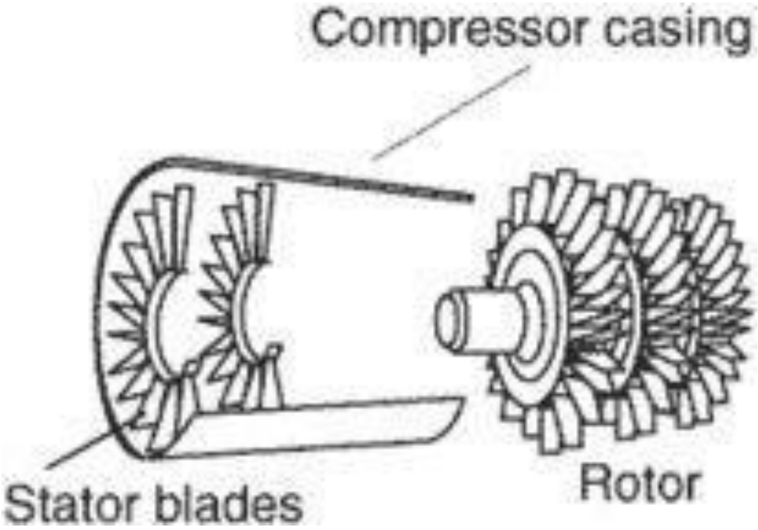

Figure 2.1: A schematic of the compressor section of an aero engine. Stators are often attached to the outer casing of the compressor whereas rotors are able to rotate [1].

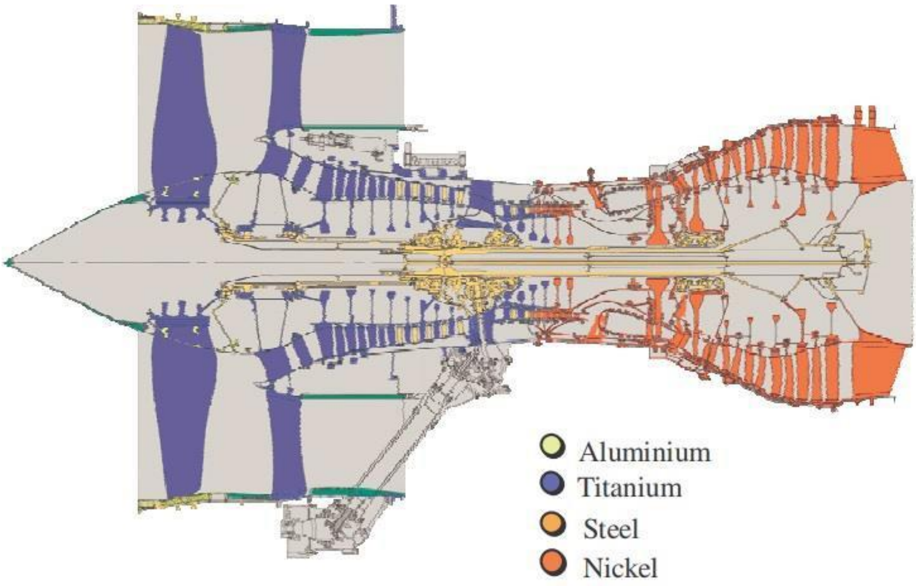

Figure 2.2: A whole aero engine showing where specific materials are used within it. Titanium is shown to be used at the front of the engine in the fan and compressor section [2].

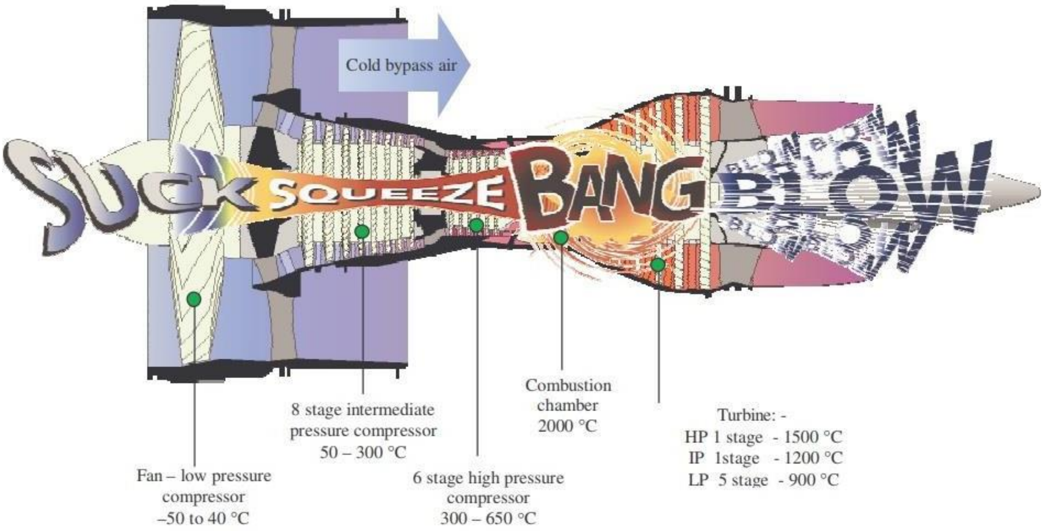

Figure 2.3: The principles of a gas turbine operation based on Newton's third law: suck, squeeze, bang, blow [2].

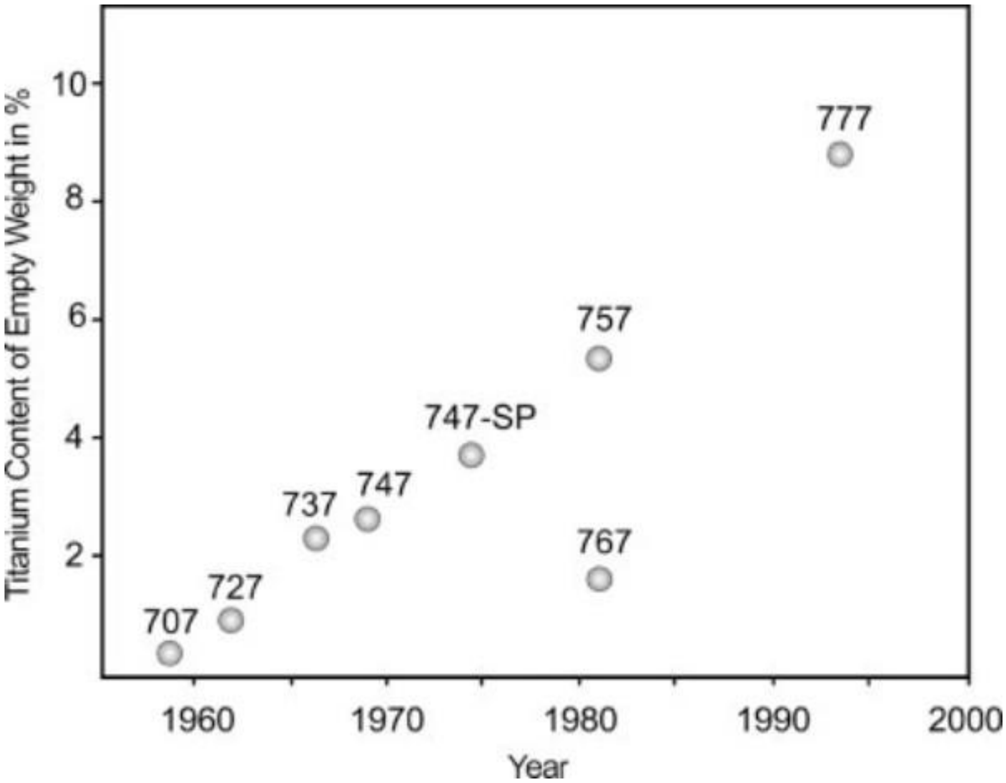

Figure 2.4: The increase in the application of titanium alloys in commercial Boeing aircraft from the 1960's up until the year 2000 [3].

Chapter 3 – Titanium Alloys

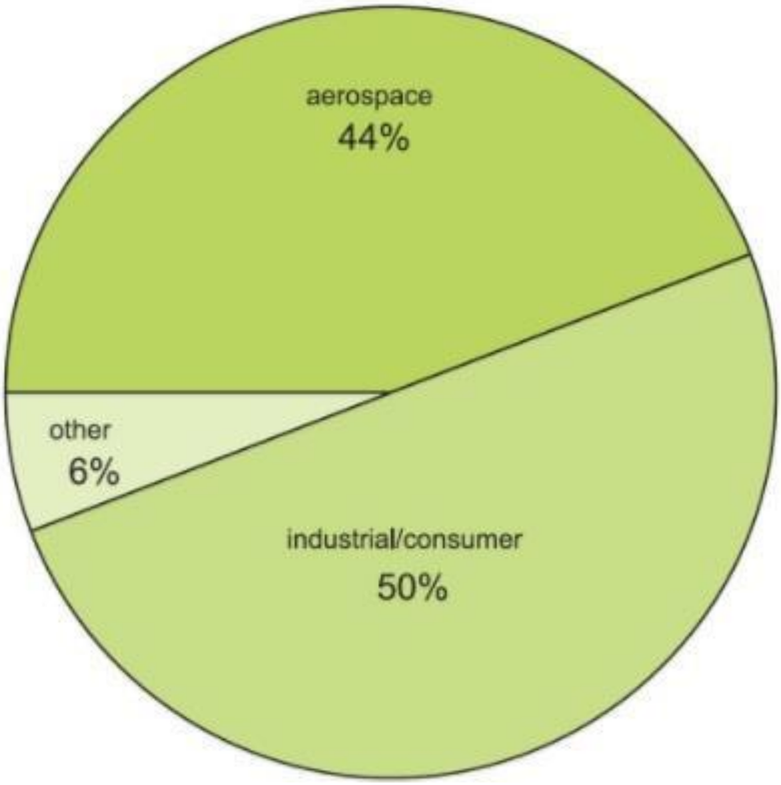

Figure 3.1: Everyday use of titanium alloys. Majority of applications are high value due to the expensive extraction process of titanium [4].

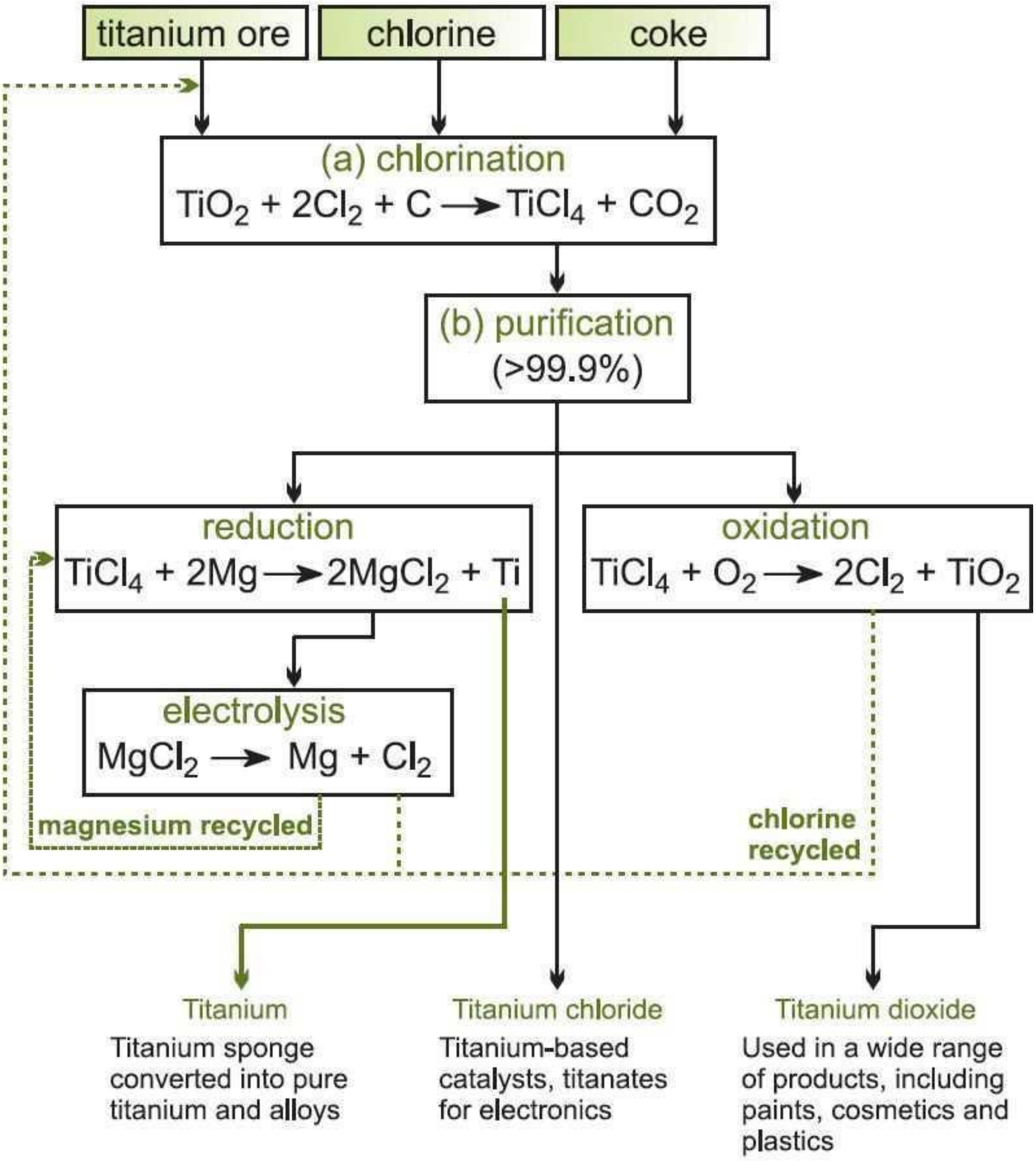

Figure 3.2: The Process of converting titanium ore into useful titanium product [4].

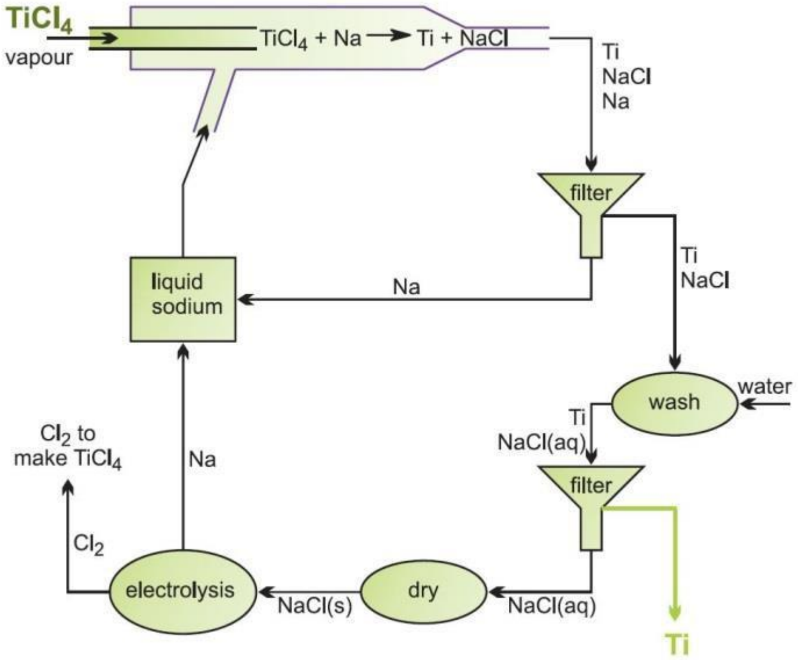

Figure 3.3: The continuous cycle process used for the reduction of titanium chloride [4].

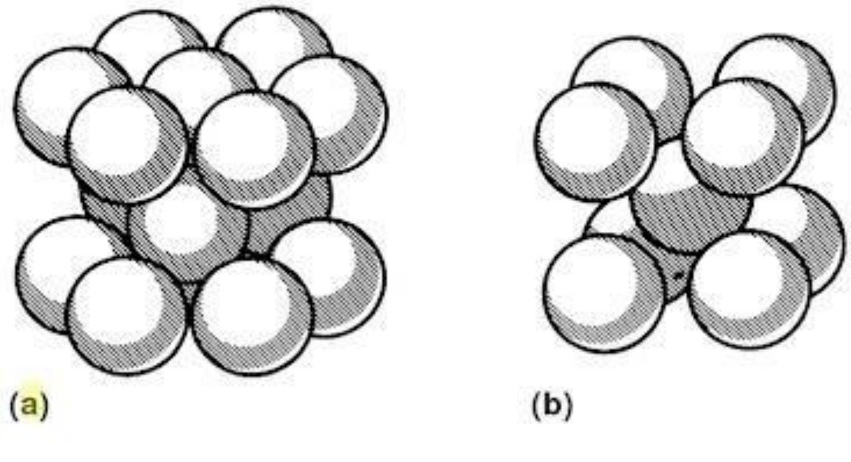

Figure 3.4: The appearance of the crystal structures of titanium at the atomic level. The crystal allotropically transforms from a) alpha phase hexagonal closed packs to b) beta phase cubic, body centred [5].

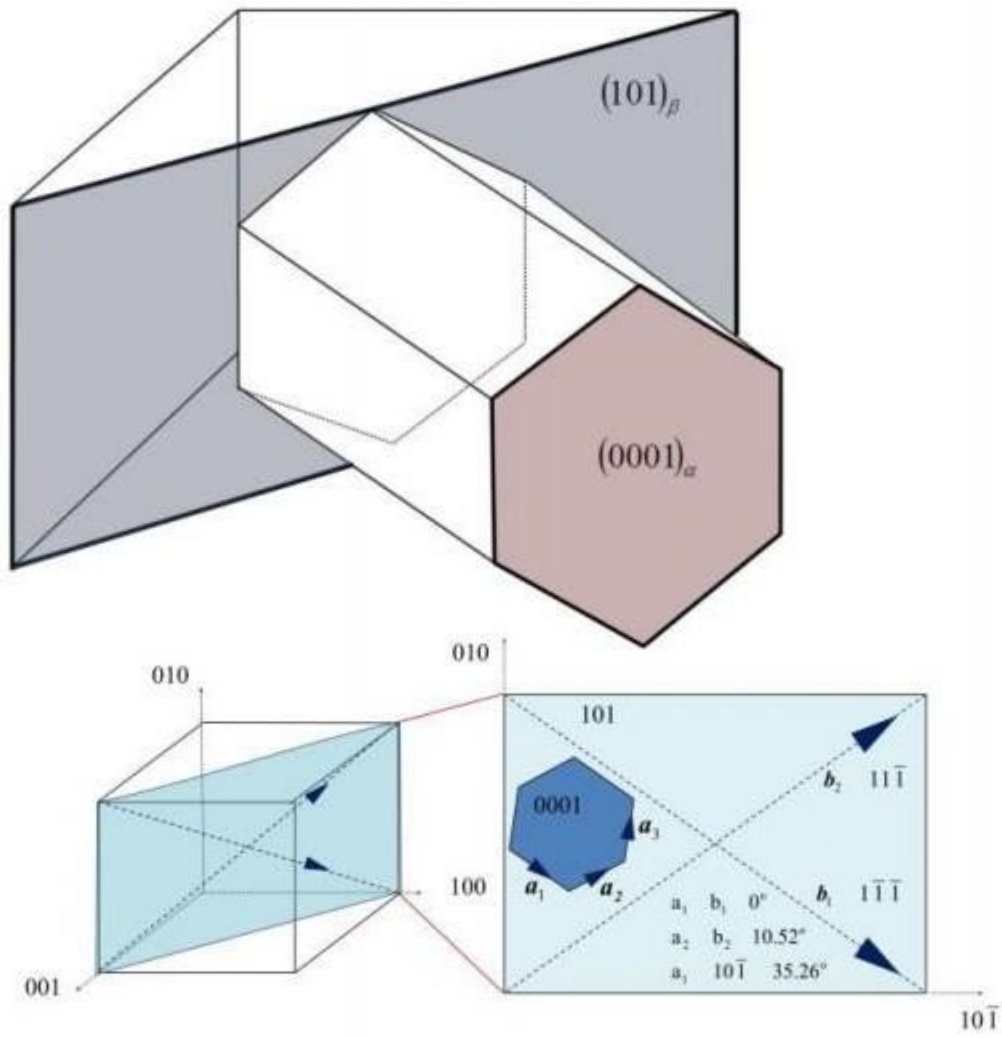

Figure 3.5: The Burgers orientation relationship between alpha (HCP) and beta (BCC) phases in titanium alloys [6].

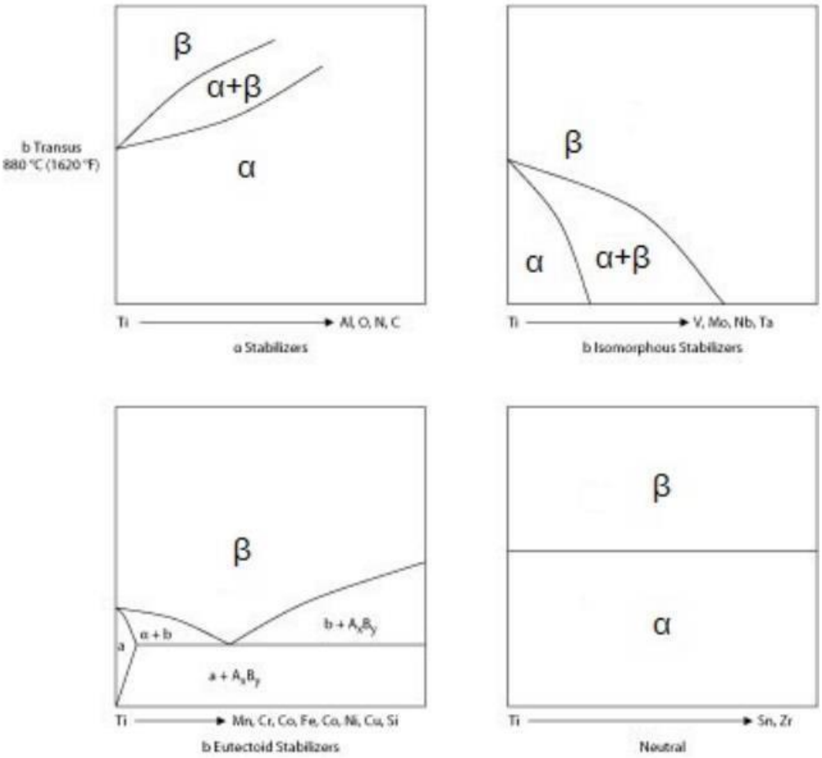

Figure 3.6: Basic phase diagrams for titanium alloys showing how different additional alloying elements alter the beta transus temperature [7].

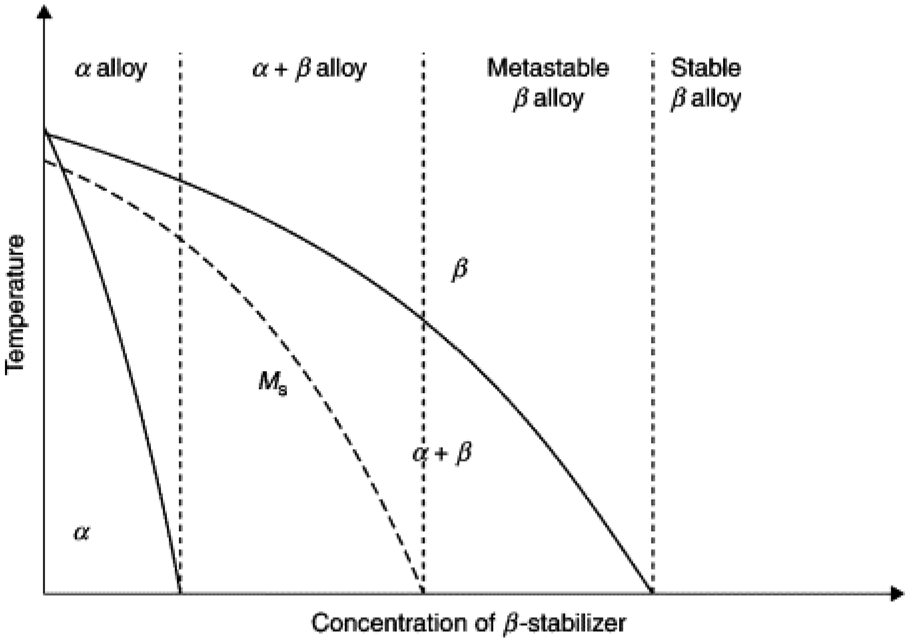

Figure 3.7: Schematic phase diagram of titanium alloys showing the effect of cooling rate and beta stabiliser concentration on titanium alloys formed [8].

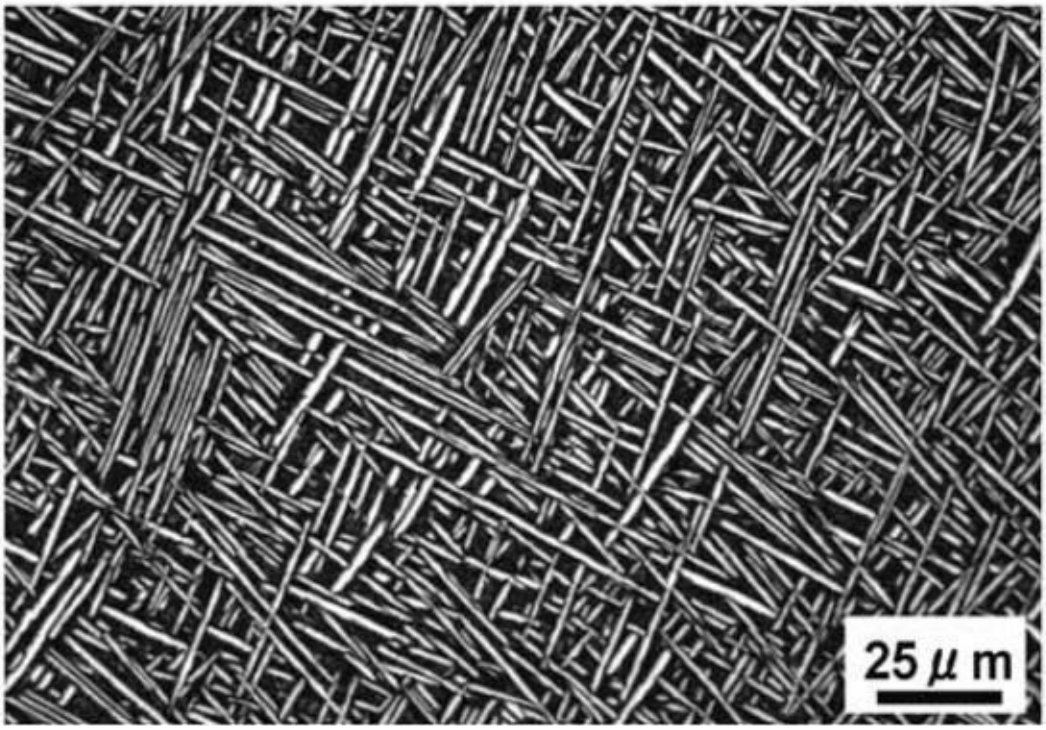

Figure 3.8: Typical beta processed Ti 6246 showing a Widmänstaten microstructure [9].

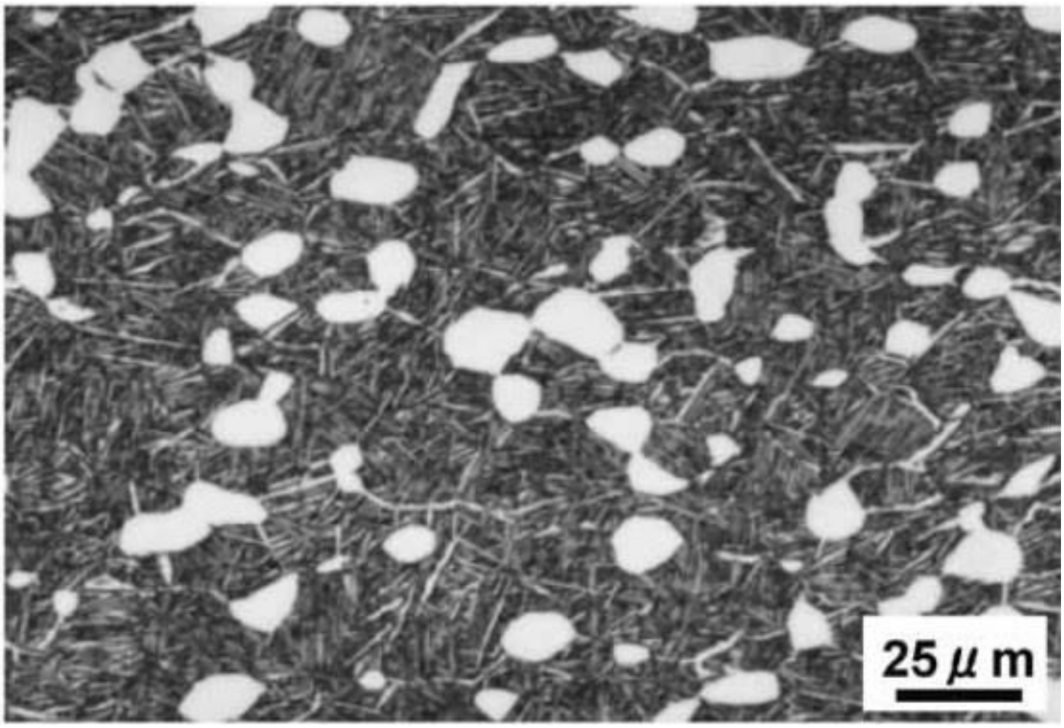

Figure 3.9: Alpha-beta processed Ti 6246 showing a bi-model microstructure [9].

Chapter 4 –Fatigue and Fracture

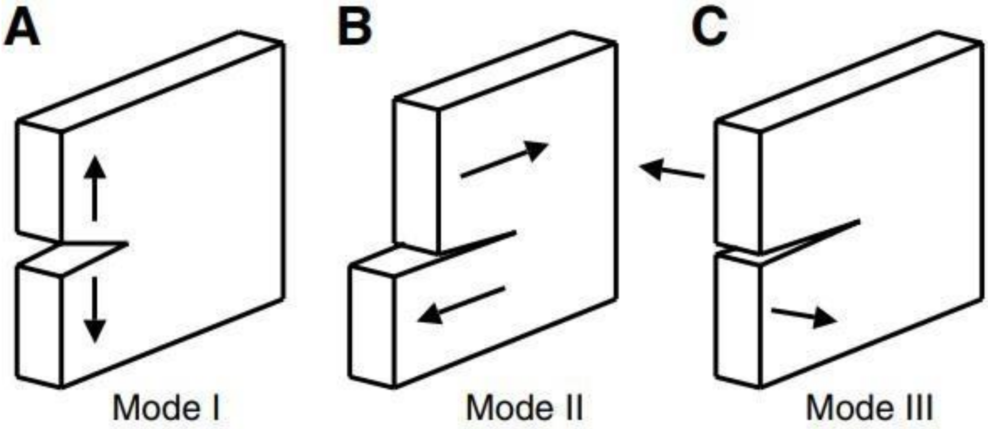

Figure 4.1: The three basic modes of loading: A) mode one (tensile opening mode): B) mode two (in plane shear or sliding mode): C) mode three (tearing or anti-plane shear mode) [10].

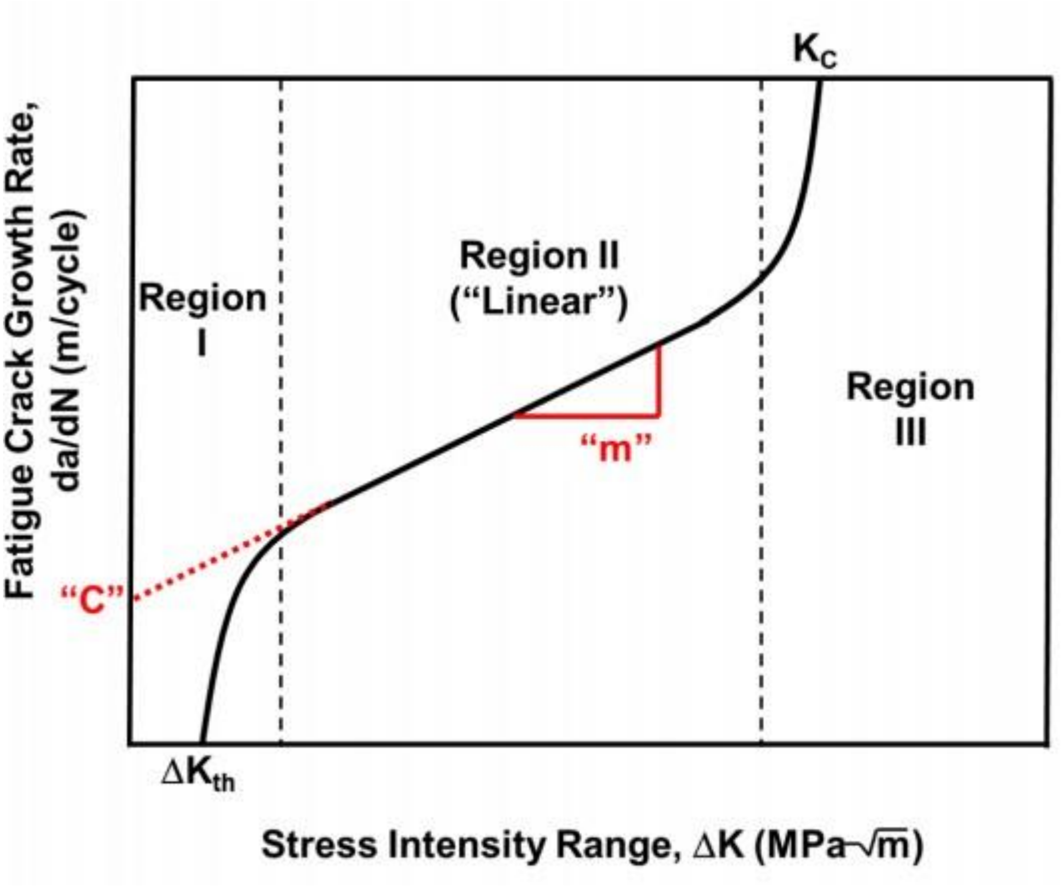

Figure 4.2: Schematic of a fatigue crack growth resistance curve [11].

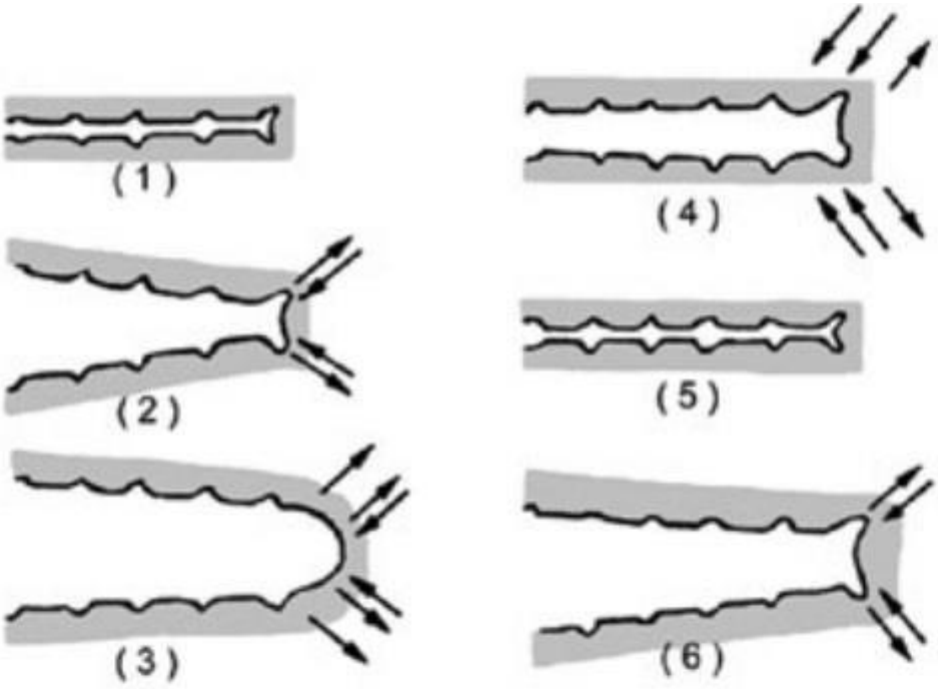

Figure 4.3: Schematic showing the formation of striations during the Paris regime crack growth. Model of plastic blunting and re-sharpening: 1) zero load, 2) small tensile load, 3) peak tensile load, 4) reduction of load, 5) no load, 6) small tensile load in subsequent cycle [12].

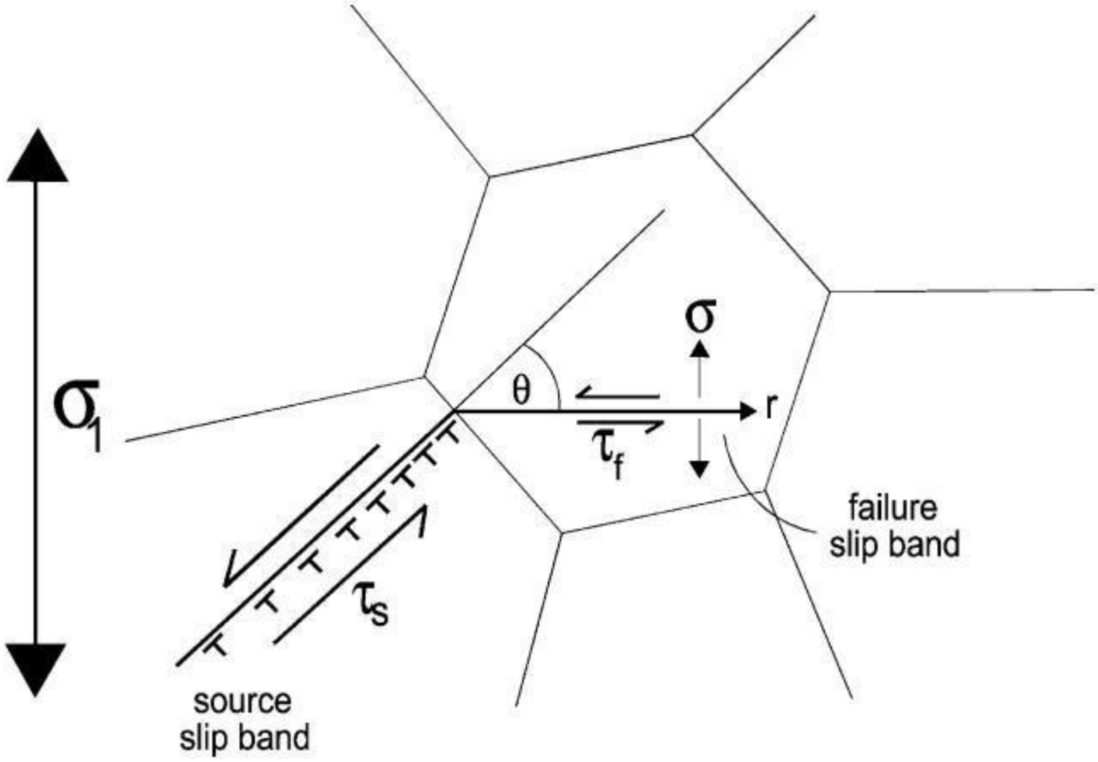

Figure 4.4: Schematic showing the Stroh model for planar slip [13].

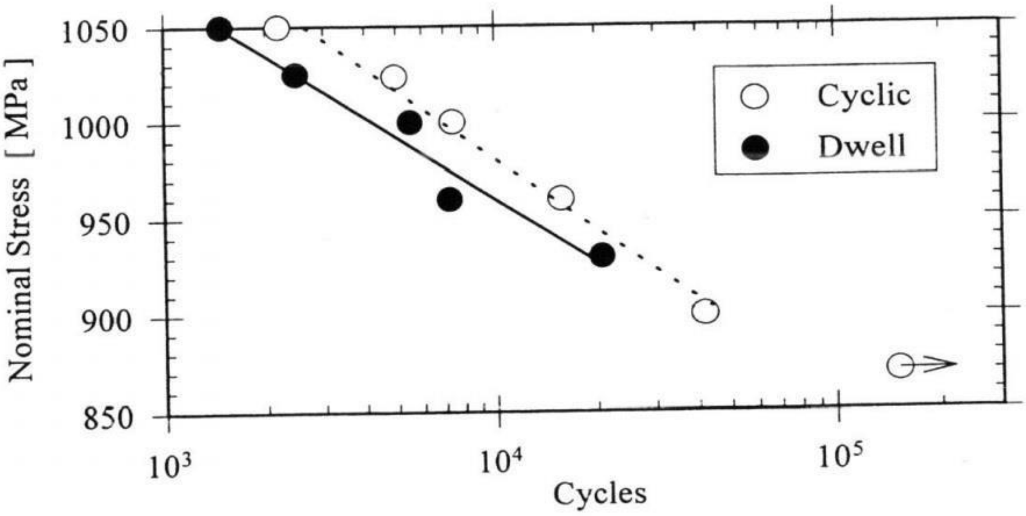

Figure 4.5: Comparison of cyclic and dwell response at 80C from a study by Spence et al (1997). Dwell was found to have more of an effect on total life at higher stress levels. As the stress level was reduced, the results between cyclic and dwell loading converged [14].

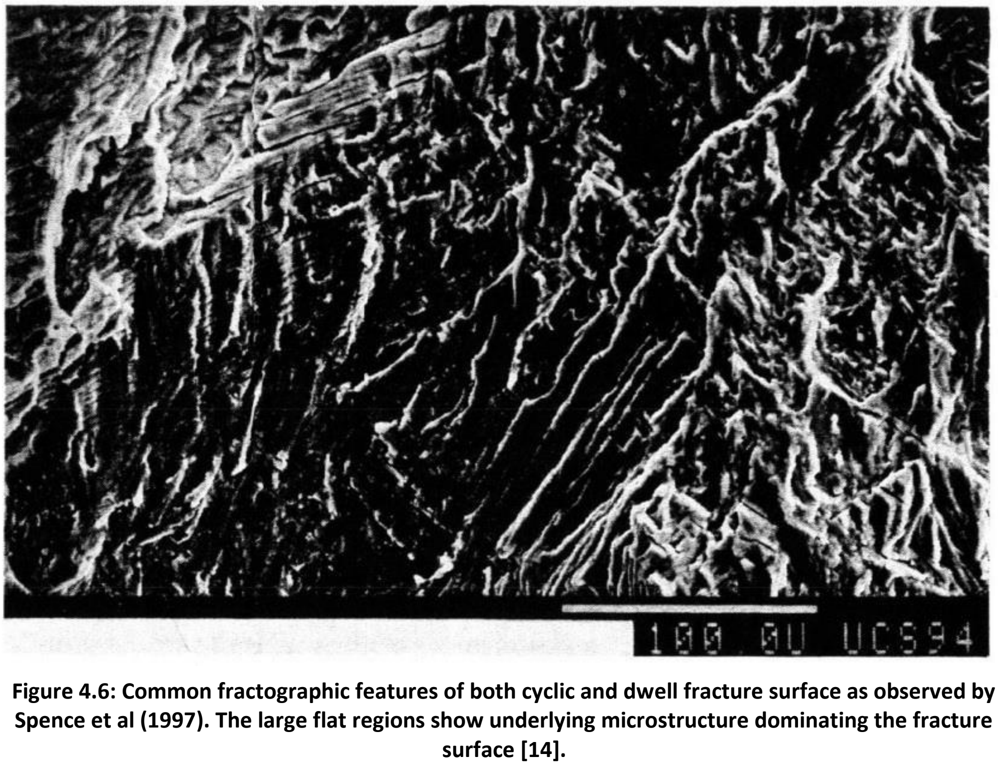

Figure 4.6: Common fractographic features of both cyclic and dwell fracture surface as observed by Spence et al (1997). The large flat regions show underlying microstructure dominating the fracture surface [14].

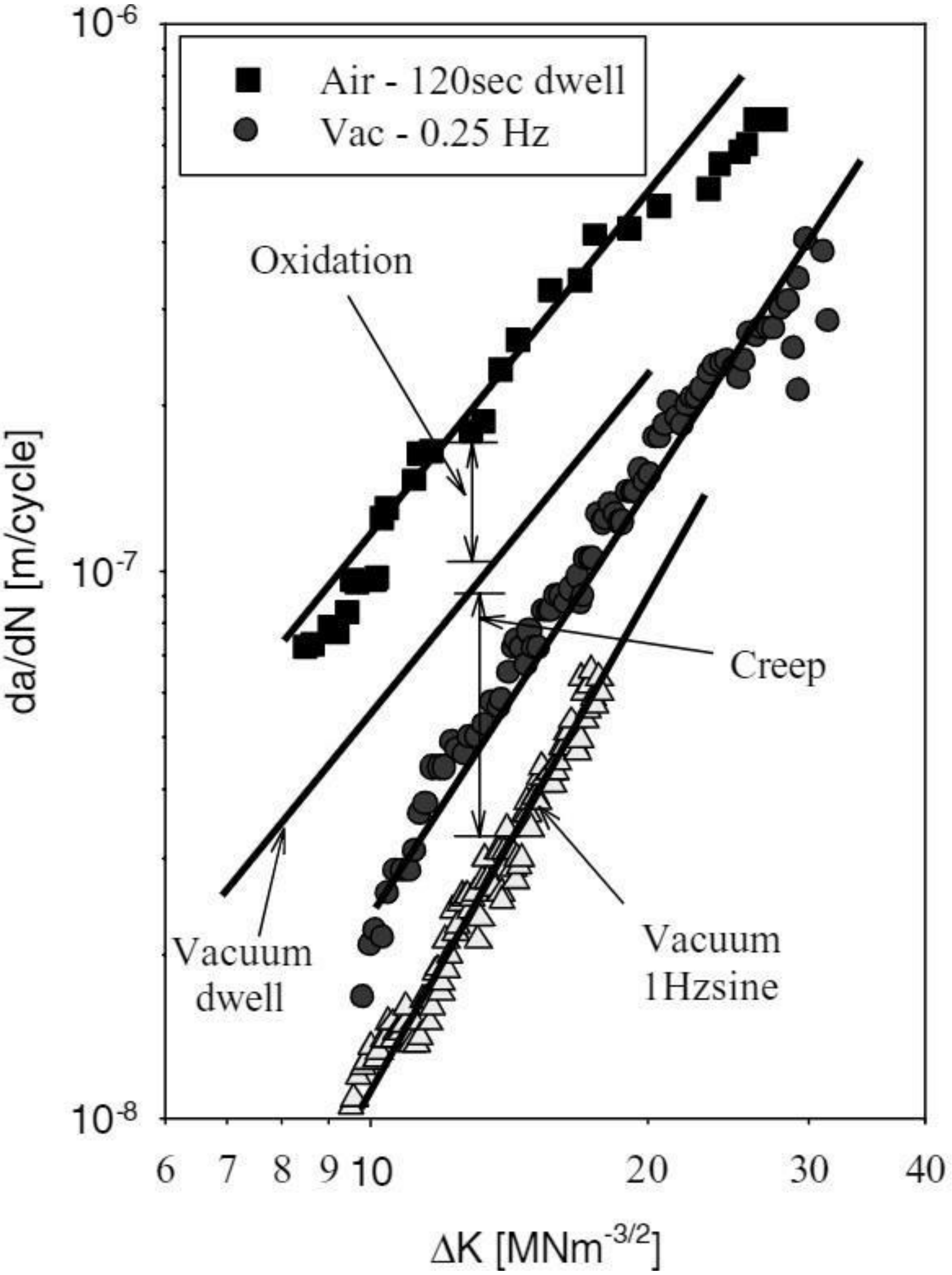

Figure 4.7: Results from Evans et al (2004) investigating the effects of fatigue, creep and environmental conditions on crack growth rate in Ti 6246. [15].

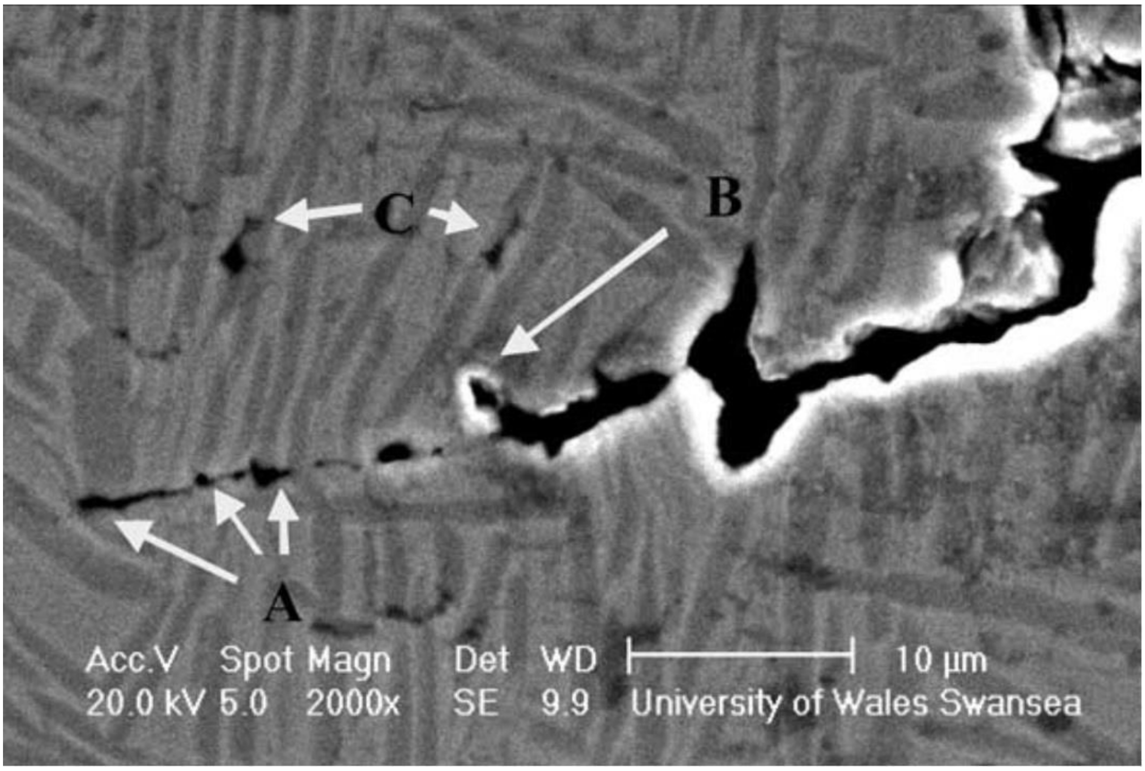

Figure 4.8: Sectioned crack path from Evans et al (2004). Creep damage incurred ahead of the propagating fatigue crack as labelled A, B and C in a Ti 6246 alloy. R = 0.7 at 550°C [15].

Chapter 5 – Experimental Methodology

Table 5.1: Nominal composition of Ti 6246.

	Al	**Sn**	**Zr**	**Mo**	**O**	**N**	**C**	**H**	**Fe**
wt-%	5.5-6.5	1.75-2.25	3.5-4.5	5.5-6.5	0.15	0.04	0.04	0.125	0.15

Table 5.2: Typical heat treatment conditions for Ti 6246.

Heat treatment	**Temperature, °C**	**Time, H**	**Cooling Method**
Stress relief	595-705	0.25-4	Air or slow cool
Solution treating	815-925	1	Water or oil quench
Aging	580-605	4-8	AC
Over-aging	>650	….	….

Table 5.3: Testing parameters for all near threshold tests.

Test Specimen	Temperature °C	Frequency Hz	R Ratio
CX 039	500	15	0.1
CX 041	500	15	0.1
CX 043	500	15	0.1
CX 036	500	0.25	0.1
CR 065	RT	15	0.1
CR 067	RT	15	0.1
CX 021	500	15	Constant Kmax (R Ratio 0.1-0.87)
CX 014	500	15	0.5
CX 018	500	0.25	0.5
CR 069	RT	15	0.5

Table 5.4: Testing parameters for all the constant load range tests.

Test Specimen	Temperature °C	Frequency Hz	Environment	R Ratio
CR 063	RT	10	Air	0.1
CX 033	RT	0.25	Air	0.1
CX 034	500	10	Air	0.1
CR 061	500	0.25	Air	0.1
CX 022	RT	10	Vacuum	0.1
CR 068	RT	0.25	Vacuum	0.1
CR 072	500	10	Vacuum	0.1
CX 037	500	0.25	Vacuum	0.1
CX 023	450	0.25	Air	0.1
CX 044	575	0.25	Air	0.1
CX 024	RT	10	Air	0.5
CR 062	RT	0.25	Air	0.5
CX 025, CX 070	500	10	Air	0.5
CX 020	500	0.25	Air	0.5
CX 015	RT	10	Vacuum	0.5
CX 017	RT	0.25	Vacuum	0.5
CX 019	500	10	Vacuum	0.5
CX 016	500	0.25	Vacuum	0.5

Table 5.5: Testing parameters for all dwell tests.

Test Specimen	Dwell Time S	Dwell Position	Environment	Temperature °C
CX 031	3600	Maximum	Air	500
CX 030	3600	Maximum	Air	575
CR 071	3600	Maximum	Vacuum	500
CX 032	120	Maximum	Air	500
CX 026	120	Maximum	Vacuum	500
CR 073	3600	Minimum	Air	500

Table 5.6: Polishing procedure for Ti 6246.

Step	Disk	Lubricant	Time (mins)
1	Piano 220	Water	15
2	Largo	Diamond suspension - 9 µm	15
3	Dac	Diamond suspension - 3 µm	15
4	Chem	Activated Colloidal Silica	40

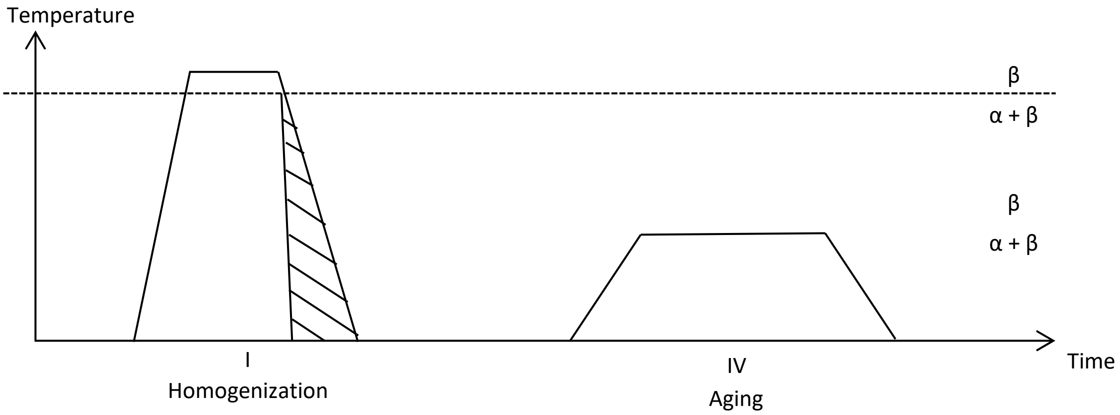

Figure 5.1: Schematic of the processing route for fully lamellar microstructure of alpha-beta Ti-alloys.

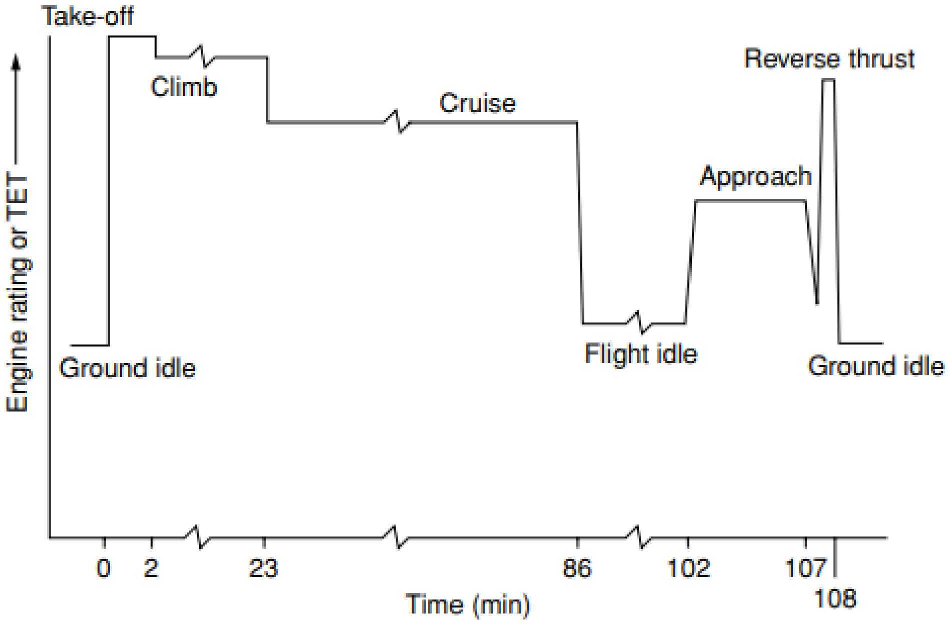

Figure 5.2: Variation in turbine entry temperature (TET) throughout a typical civil flight cycle [16].

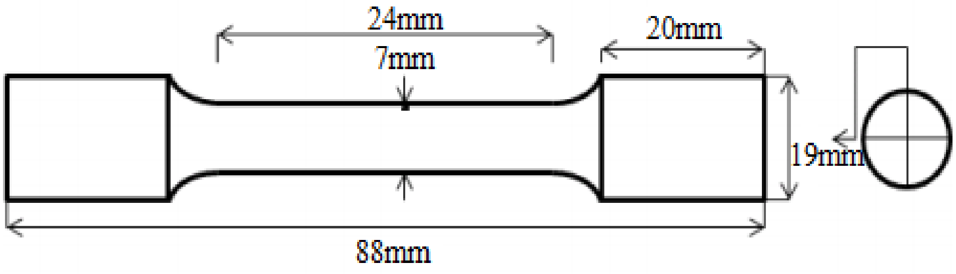

Figure 5.3: Typical geometry for Ti 6246 7x7 corner crack specimens.

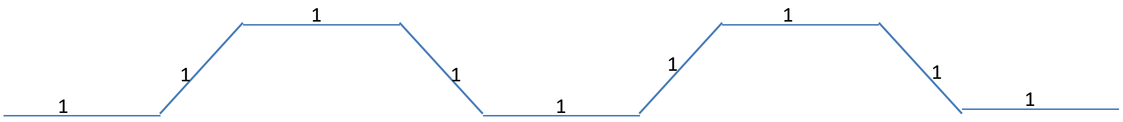

Figure 5.4: 1-1-1-1 baseline trapezoidal waveform.

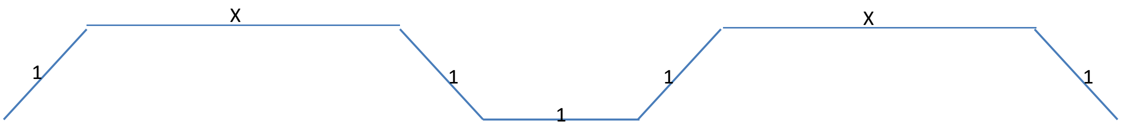

Figure 5.5: 1-x-1-1 maximum dwell hold trapezoidal waveform.

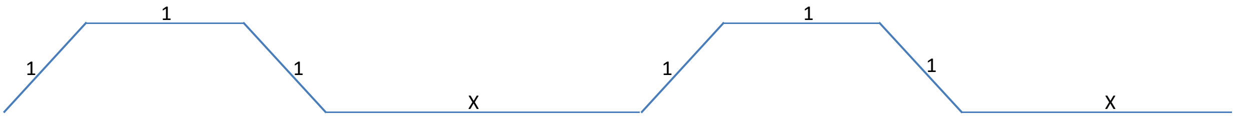

Figure 5.6: 1-1-1-x minimum dwell hold trapezoidal waveform.

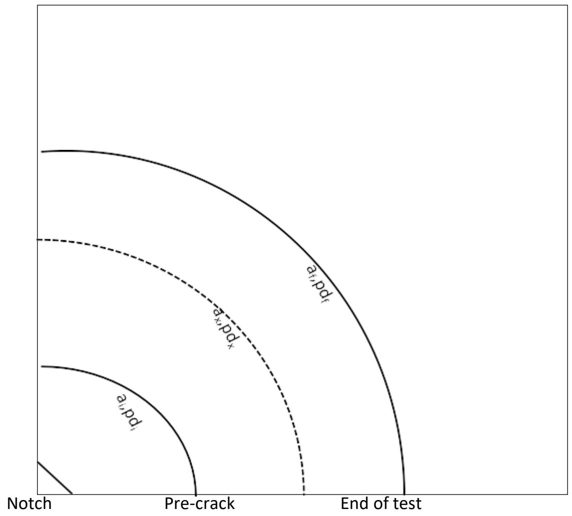

Figure 5.7: Schematic of a fracture surface showing crack areas for pre-crack and final crack with the corresponding PD values.

Chapter 6 – Results – Microstructure and Near Threshold Testing

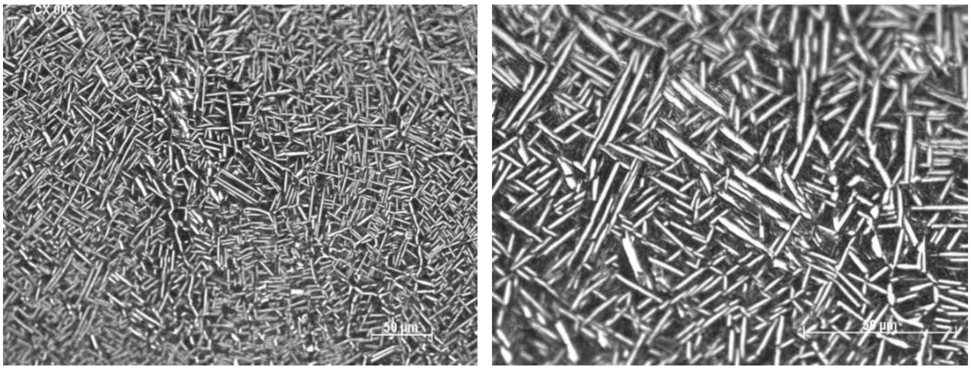

Figure 6.1: Optical microscopy micrographs of Ti6246 Widmänstatten microstructure.

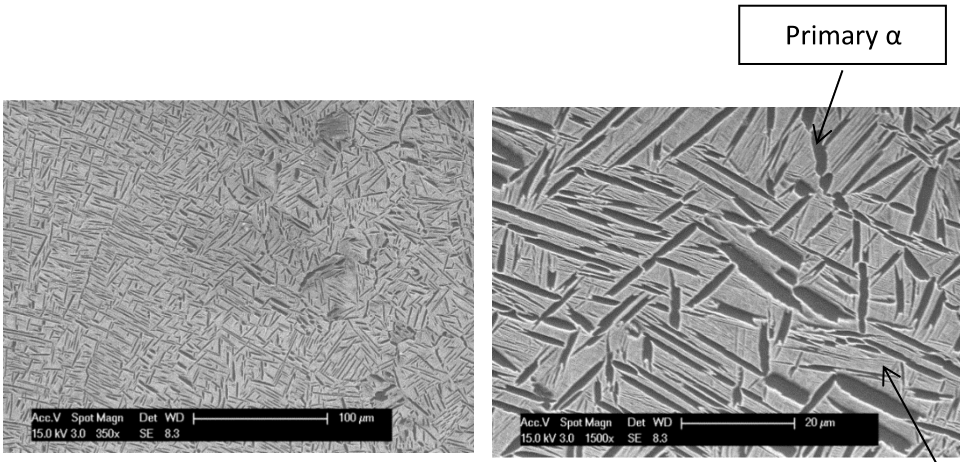

Figure 6.2: SEM micrographs of Ti 6246 Widmänstatten microstructure.

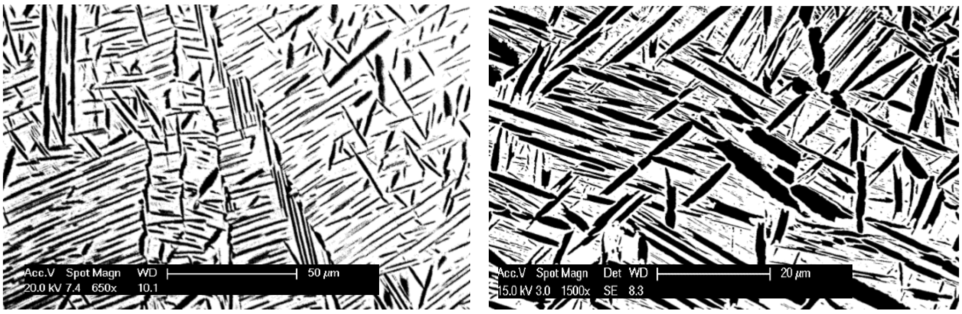

Figure 6.3: Binary Images of Ti6246 used to calculate volume fraction.

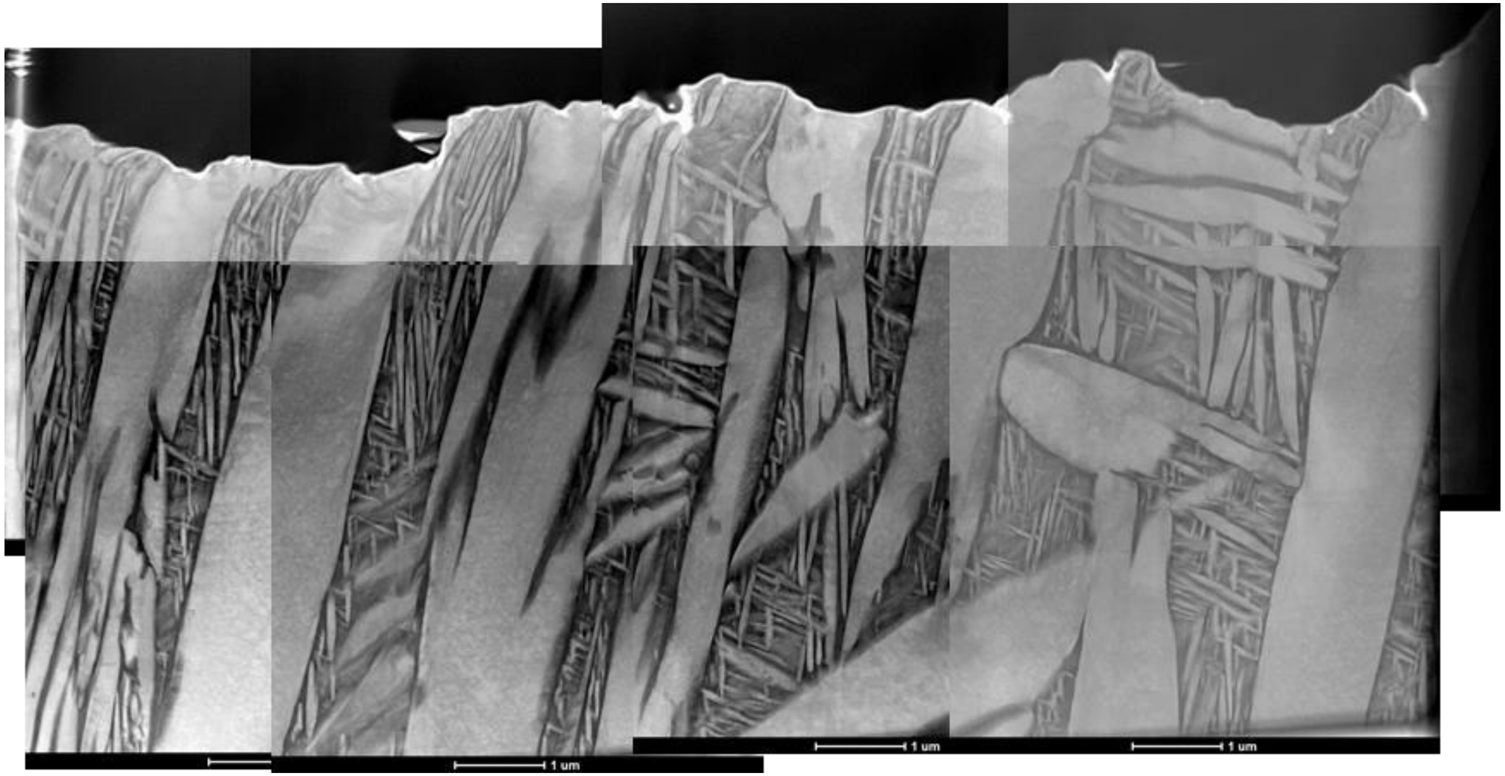

Figure 6.4: TEM image of Ti 6246 Widmänstatten microstructure.

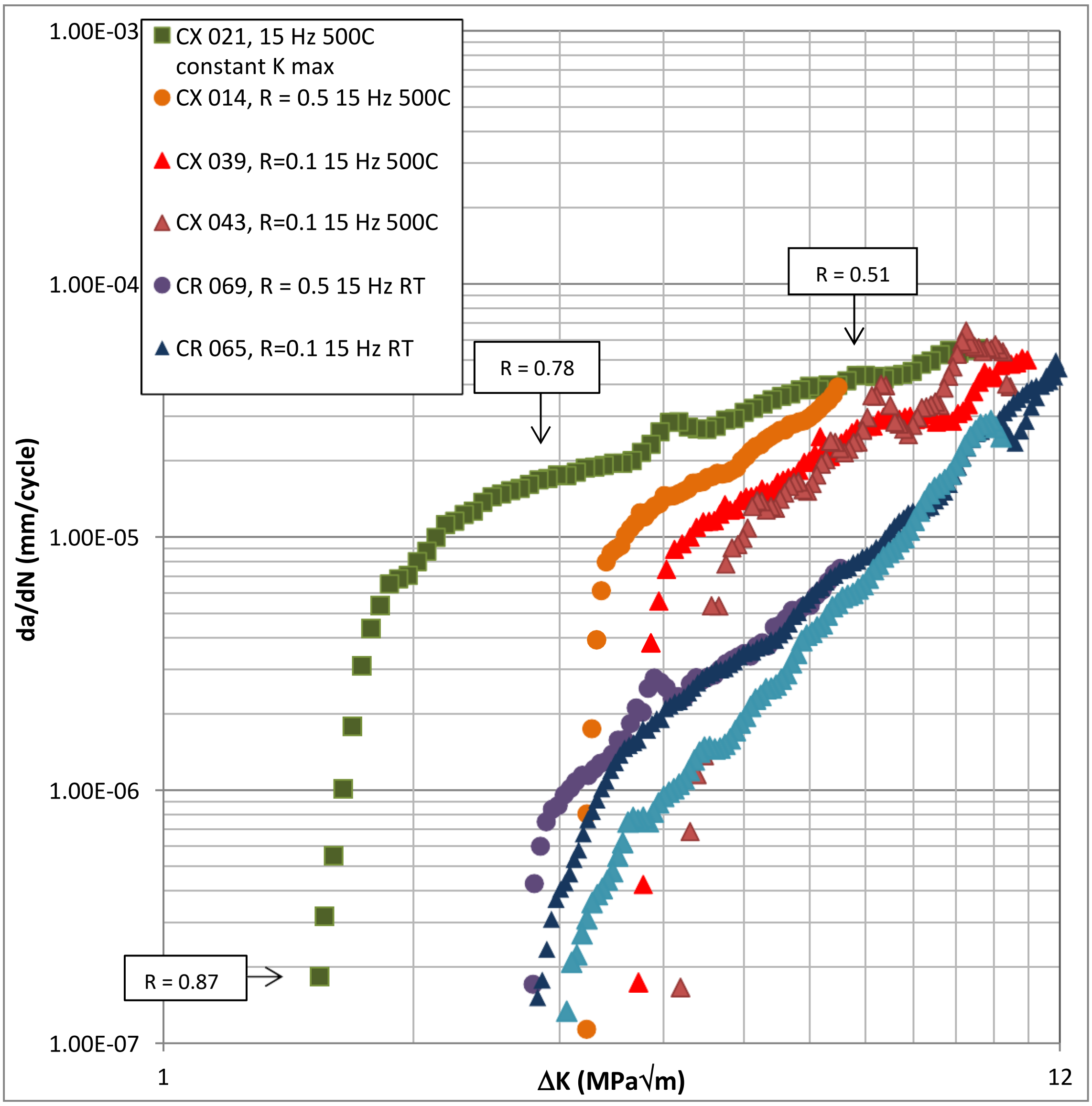

Figure 6.5: Results from all the near threshold mechanical tests carried out at 15 Hz in air, showing R ratios of 0.1 and 0.5 tests and the constant K max test.

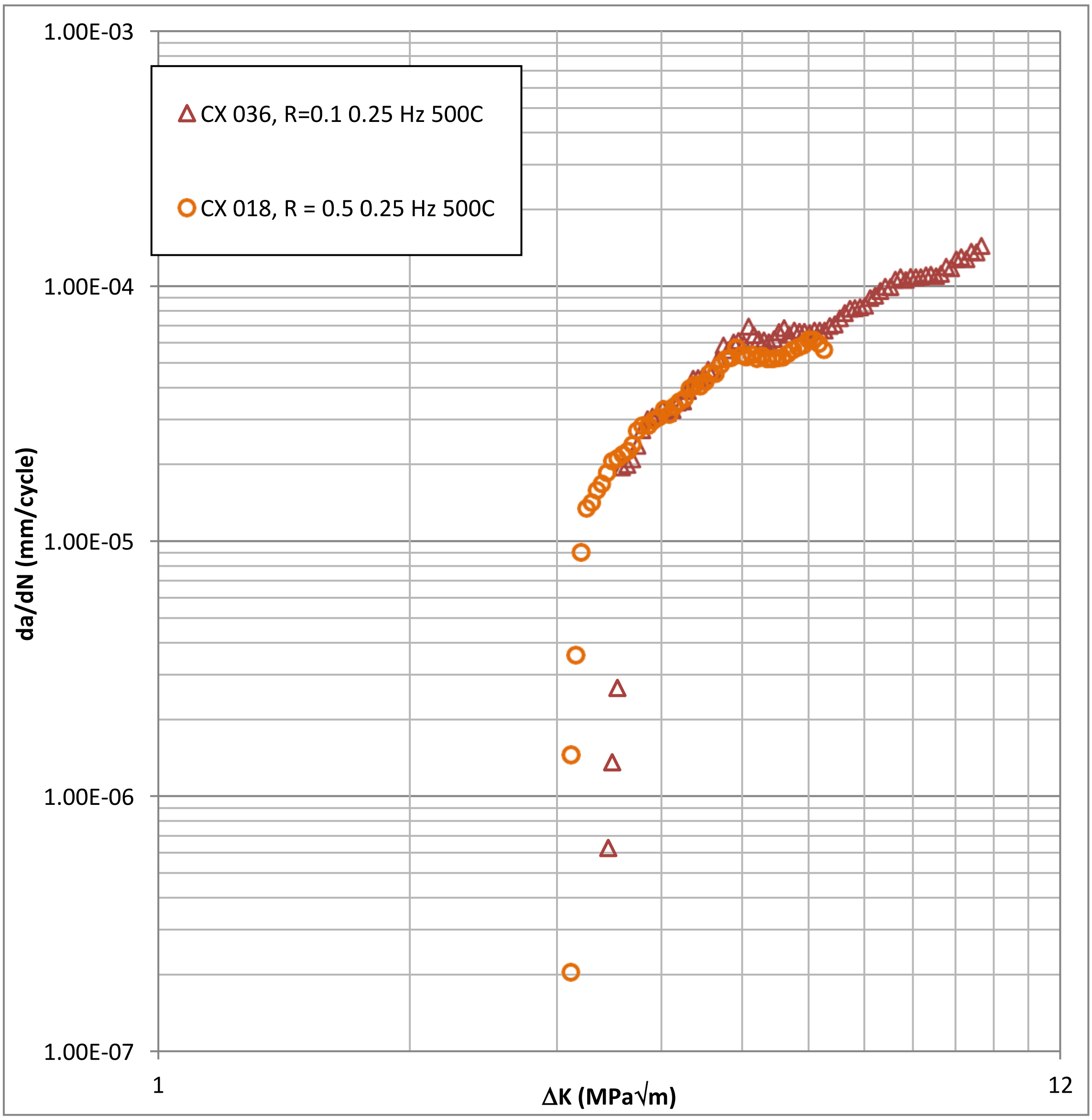

Figure 6.6: Results from the R ratio 0.1 and 0.5 near threshold tests, tested at 0.25 Hz at 500°C in air.

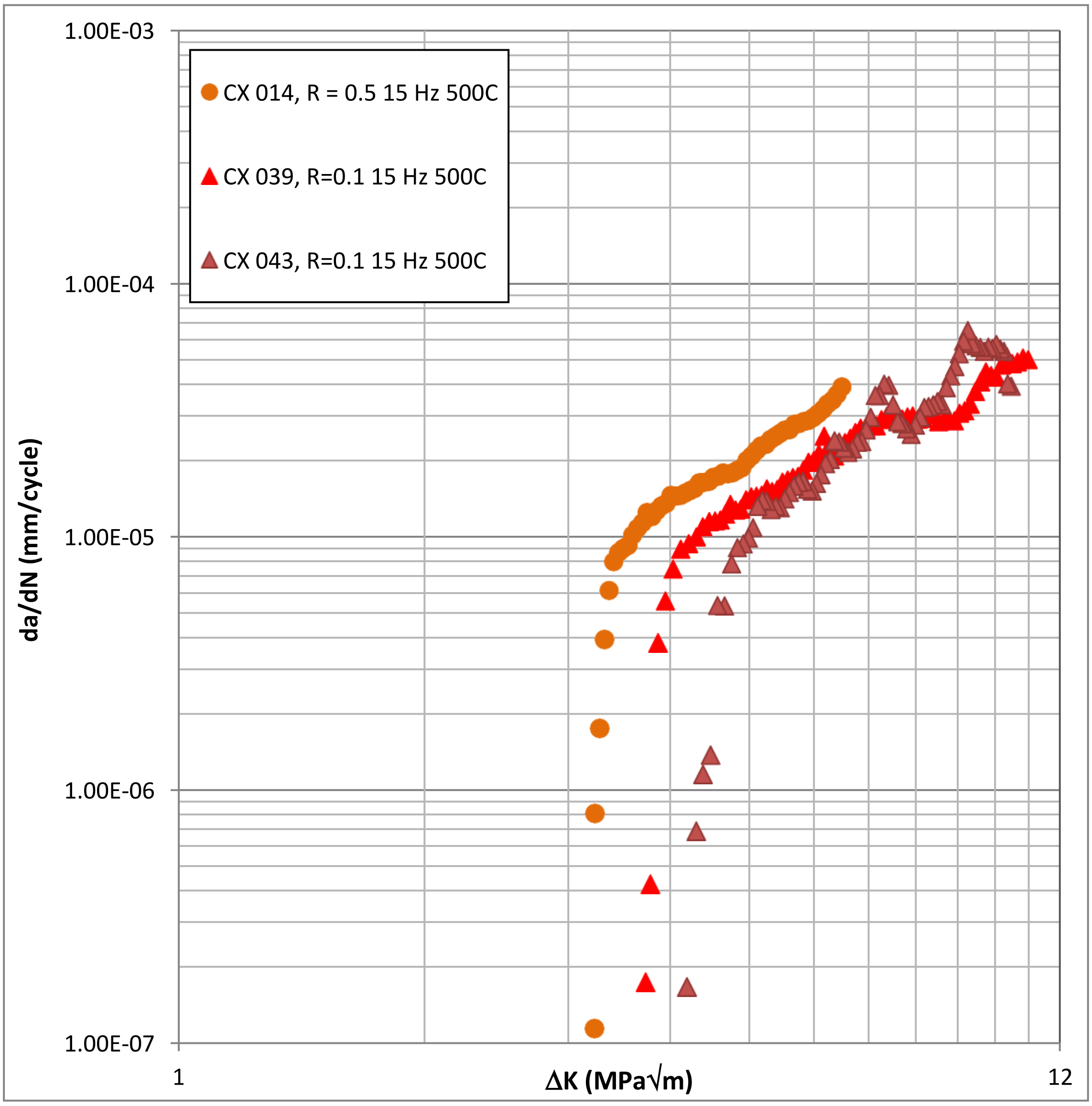

Figure 6.7: Results from the R ratio 0.1 and 0.5 near threshold tests, tested at 15 Hz at 500°C in air.

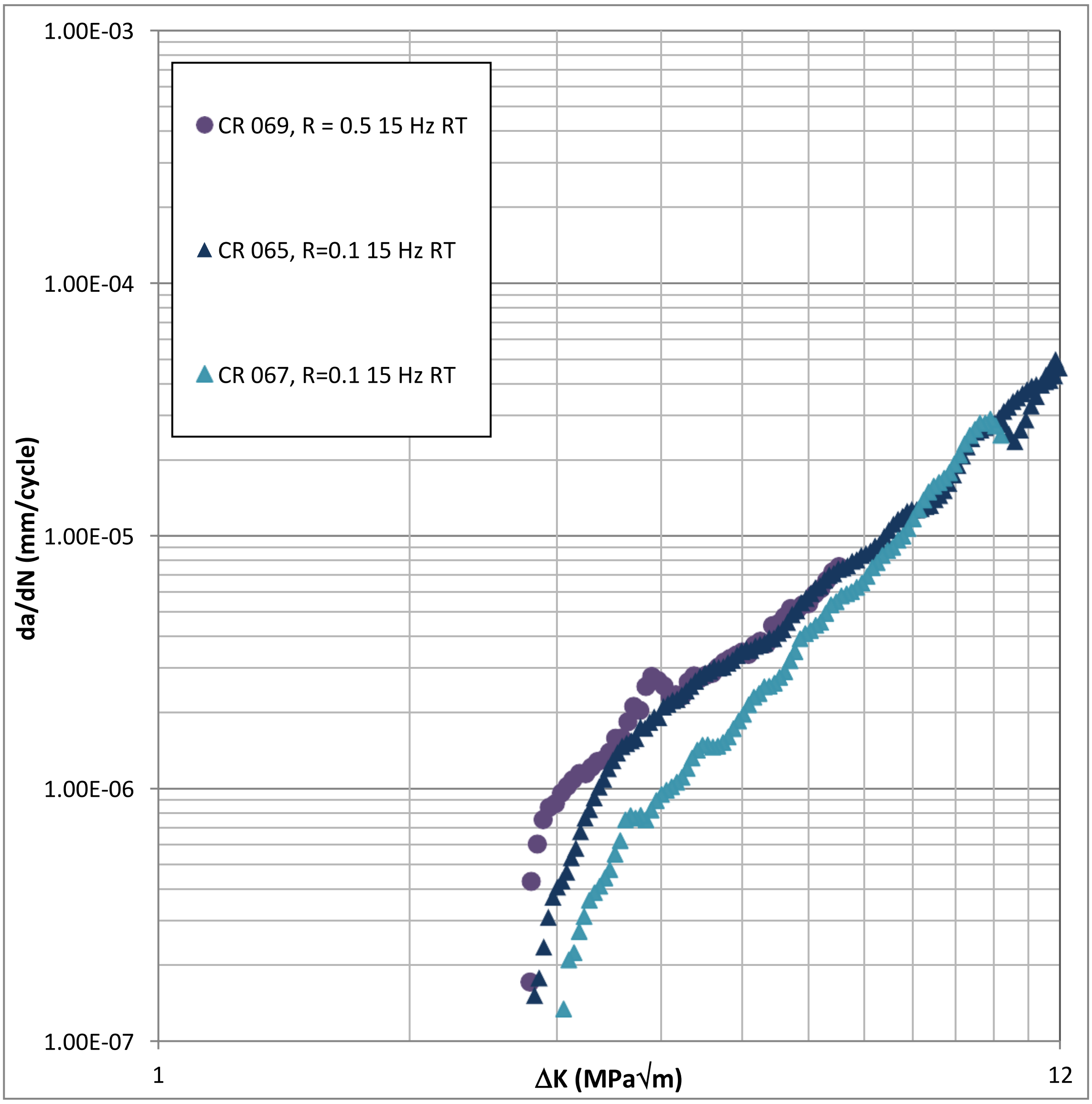

Figure 6.8: Results comparing near threshold tests for R ratio 0.1 and 0.5, 15 Hz, carried out at room temperature.

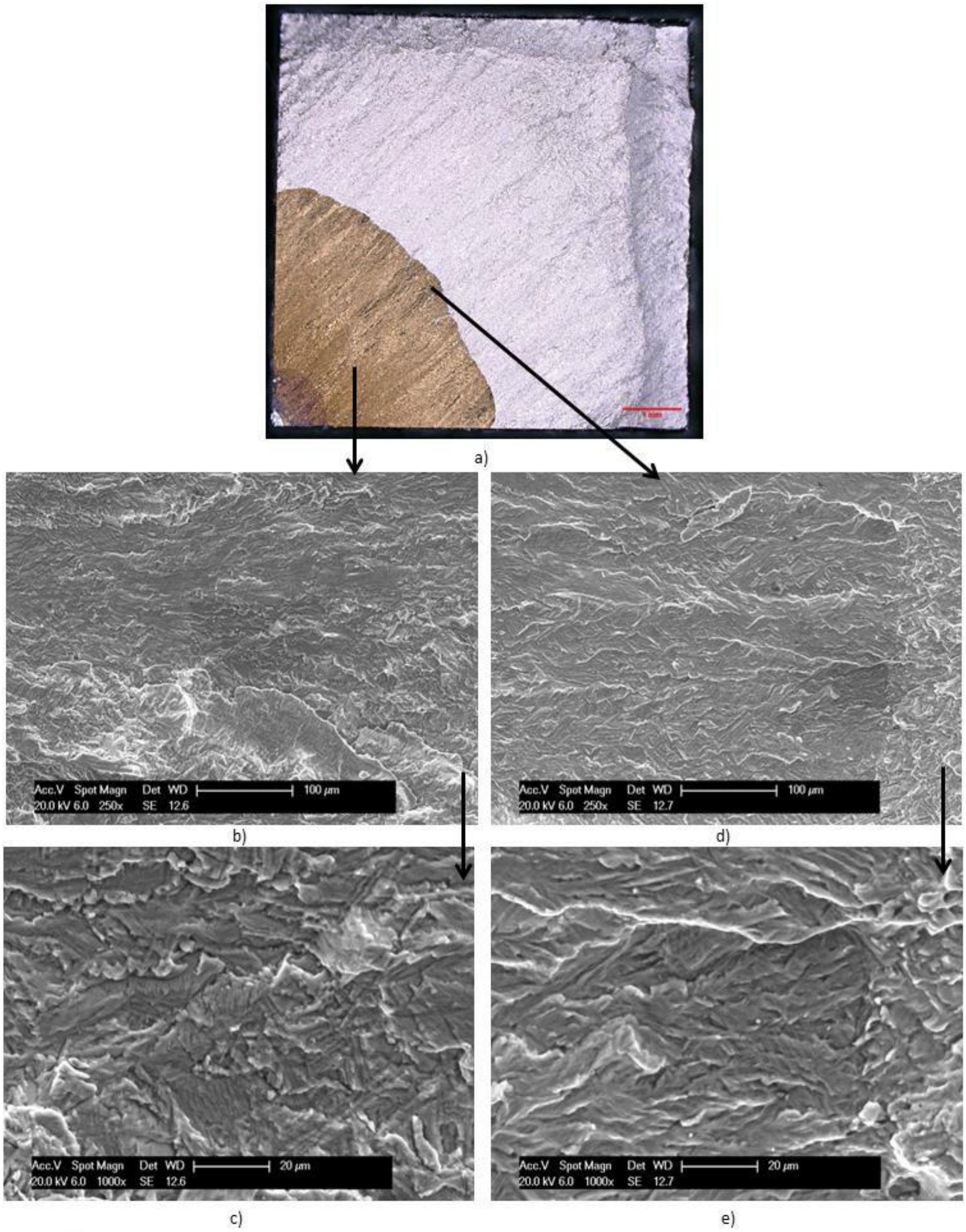

Figure 6.9: Optical and SEM Images captured of specimen CX 021 tested at 500°C, 15 Hz, constant K max, air. Crack growth direction is diagonal from left bottom corner to right top corner. a) Shows optical image of the crack showing uniform crack growth resulting in an even quarter circle. b + c) Show SEM images taken at a high ΔK value. d + e) Show SEM images taken at threshold ΔK value.

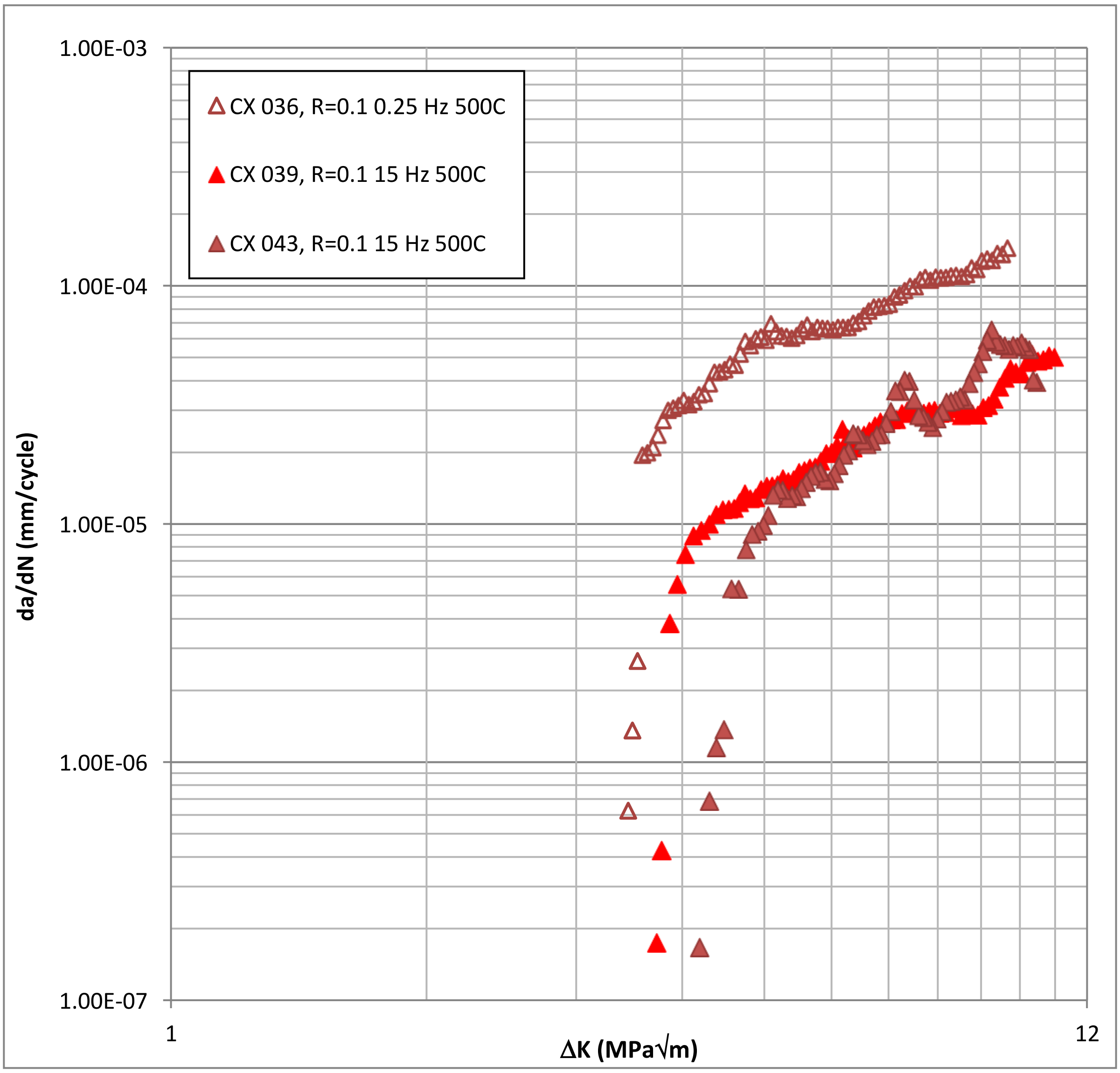

Figure 6.10: Results for the R ratio 0.1, 500^{o}C near threshold tests. Comparing 15 and 0.25 Hz frequencies.

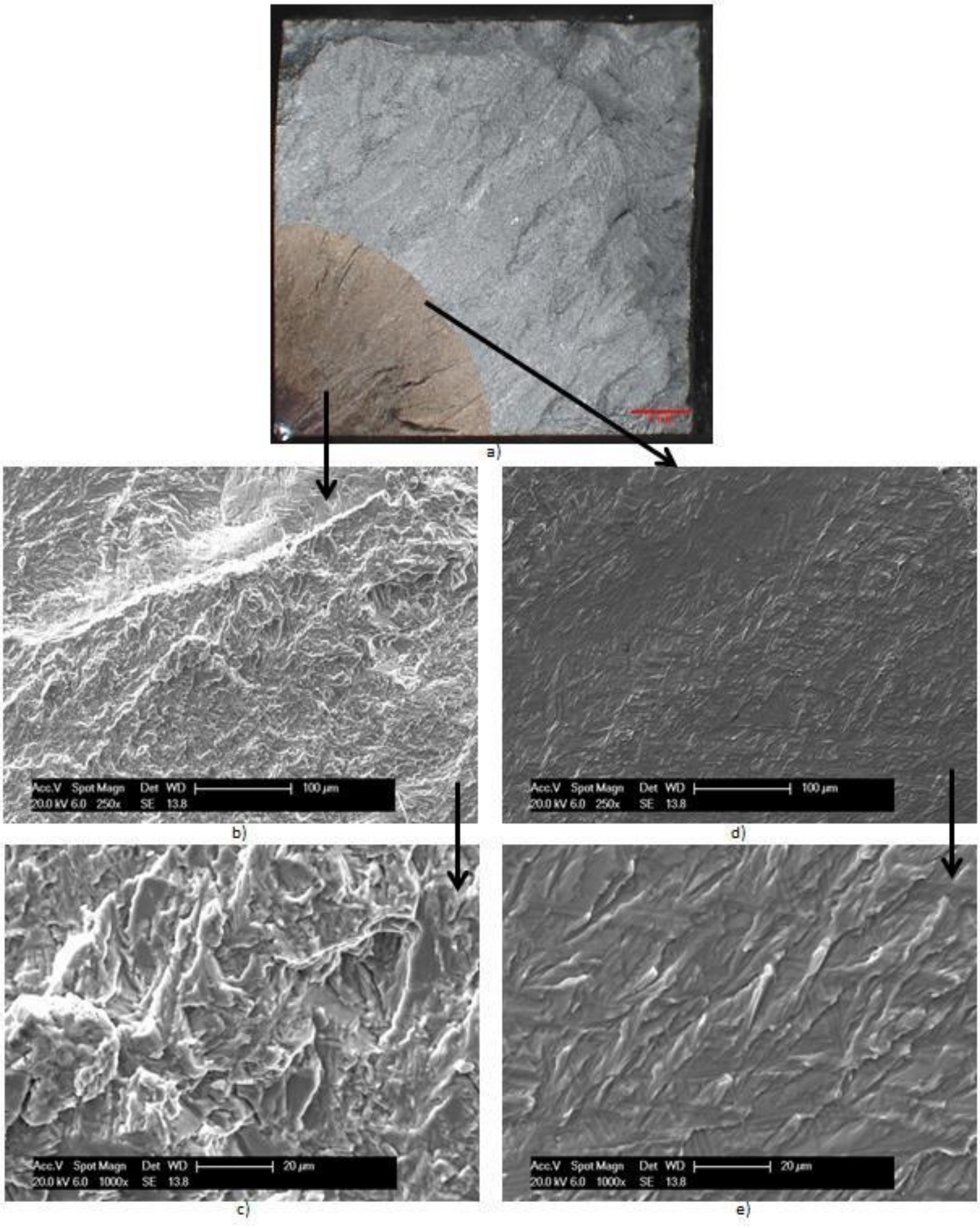

Figure 6.11: Images captured of specimen CX 043 tested at 500^{o}C , 15 Hz, R ratio 0.1, air. The crack growth direction is diagonal from bottom left to top right. a) Shows optical image of the crack showing isometric crack growth creating a quarter circle. b + c) Show SEM images taken at a high ΔK value. d + e) Show SEM images taken at threshold ΔK value. The crack growth mechanism is transgranular.

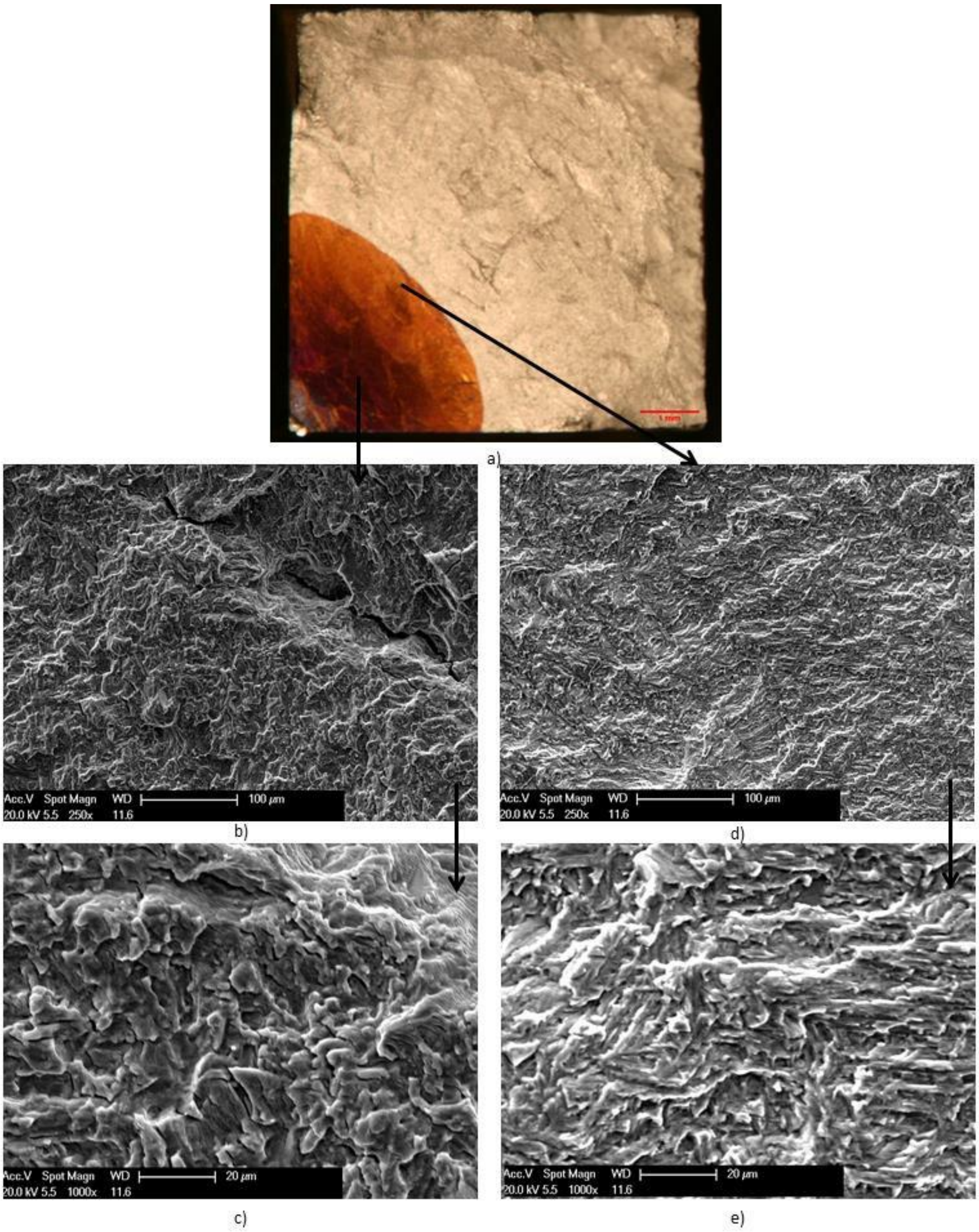

a)

b)

d)

c)

e)

Figure 6.12: Optical and SEM images captured of specimen CX 036 tested at 500°C, 0.25 Hz, R ratio 0.1 in air. The crack growth direction is diagonal from bottom left to top right. a) Shows optical image of the crack showing isometric crack growth creating an even quarter circle. b + c) Show SEM images taken at a high ΔK value. d + e) Show SEM images taken at threshold ΔK value. The crack growth mechanism is transgranular however the fracture surface does appear slightly rough.

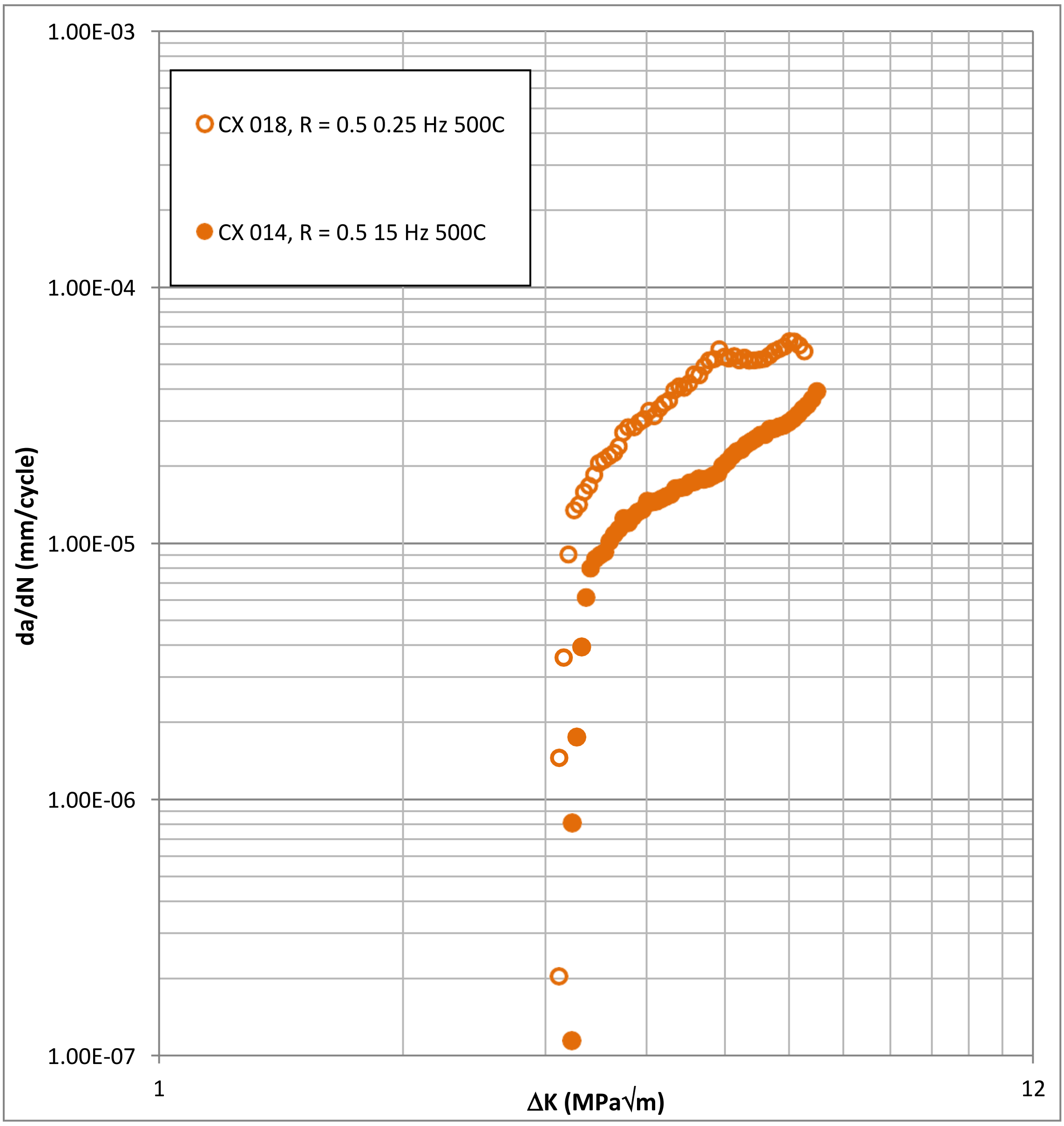

Figure 6.13: Results for the R ratio 0.5, 500°C threshold tests. Comparing 15 and 0.25 Hz frequencies.

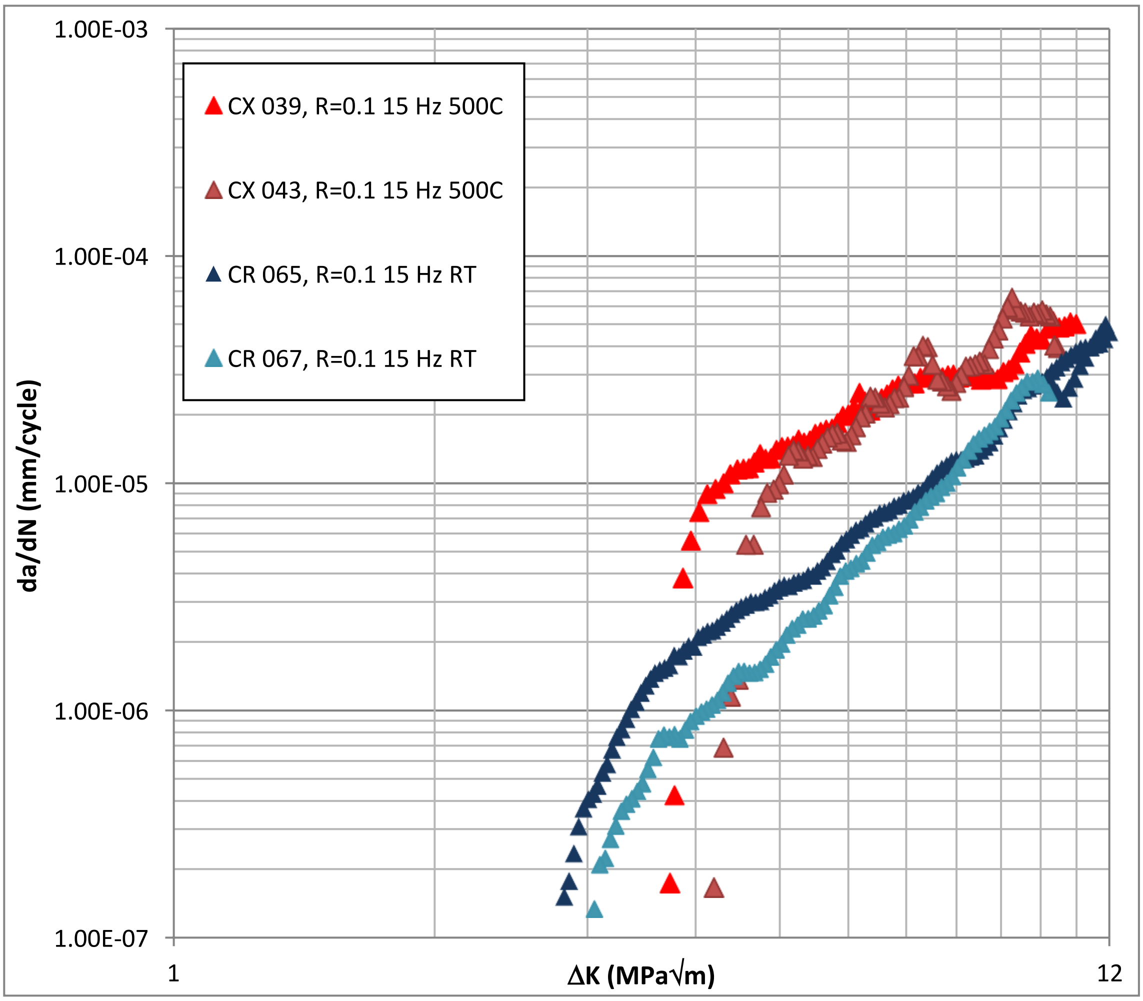

Figure 6.14: Results from the near threshold mechanical tests carried out at 15 Hz in air, R ratio 0.1 at 500°C and room temperature.

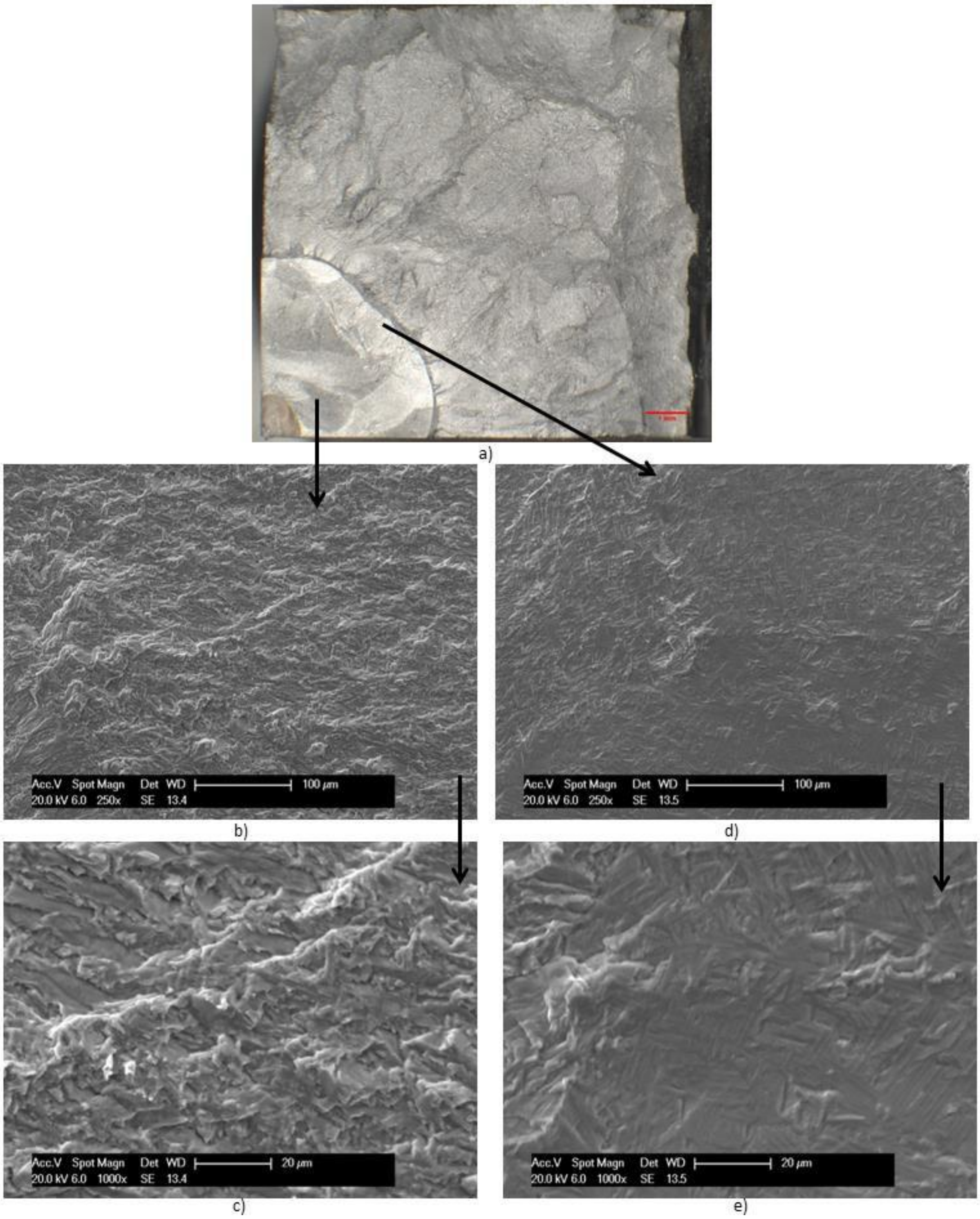

Figure 6.15: Images captured of specimen CR 065 tested at room temperature, 15 Hz, R ratio 0.1 in air. The crack growth direction is diagonal from the bottom left to the top right. a) Shows optical image of the crack showing isometric crack growth creating an even quarter circle. b + c) Show SEM images taken at a high ΔK value. d + e) Show SEM images taken at threshold ΔK value. The fracture surface is very flat showing a transgranular mechanism.

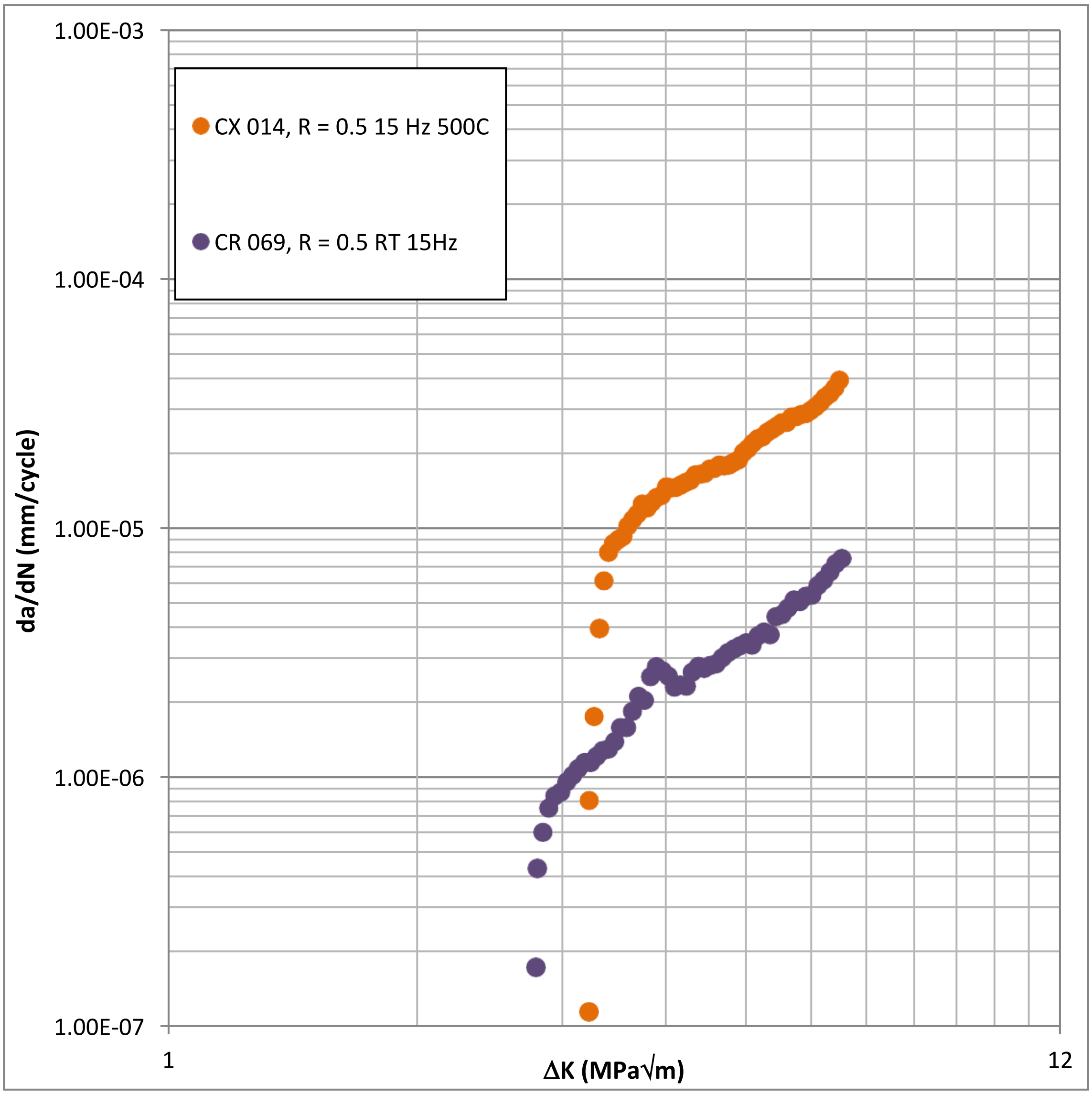

Figure 6.16: Results for the R ratio 0.5, 15 Hz near threshold tests in air. Comparing room temperature and 500^{o}C.

Chapter 7 – Results – Constant Load Range Testing

Table 7.1: Paris constants, C (mm/cycle) and m obtained experimentally.

Specimen	Conditions	C (mm/cycle)	m
CX 022	RT, R=0.1, 10 Hz, Vacuum	2.84E-09	3.39
CR 068	RT, R=0.1, 0.25 Hz, Vacuum	2.84E-09	3.33
CR 072	500C, R=0.1, 10 Hz, Vacuum	2.90E-08	2.75
CX 037	500C, R=0.1, 0.25 Hz, Vacuum	4.41E-08	2.78
CR 063	RT, R=0.1, 10 Hz, Air	8.86E-08	2.43
CX 033	RT, R=0.1, 0.25 Hz, Air	1.04E-07	2.43
CX 034	500C, R=0.1, 10 Hz, Air	1.49E-07	2.48
CR 061	500C, R=0.1, 0.25 Hz, Air	2.25E-06	1.73
CX 023	450C, R=0.1, 0.25 Hz, Air	1.24E-07	2.49
CX 044	575C, R=0.1, 0.25 Hz, Air	8.27E-06	1.38
CX 015	RT, R=0.5, 10 Hz, Vacuum	4.27E-09	3.35
CX 017	RT, R=0.5, 0.25 Hz, Vacuum	3.15E-08	2.80
CX 019	500C, R=0.5, 10 Hz, Vacuum	3.53E-09	3.63
CX 016	500C, R=0.5, 0.25 Hz, Vacuum	4.68E-08	2.87
CX 024	RT, R=0.5, 10 Hz, Air	7.29E-08	2.66
CR 062	RT, R=0.5, 0.25 Hz, Air	1.39E-07	2.35
CX 025	500C, R=0.5, 10 Hz, Air	4.14E-07	2.23
CX 020	500C, R=0.5, 0.25 Hz, Air	5.88E-06	1.37

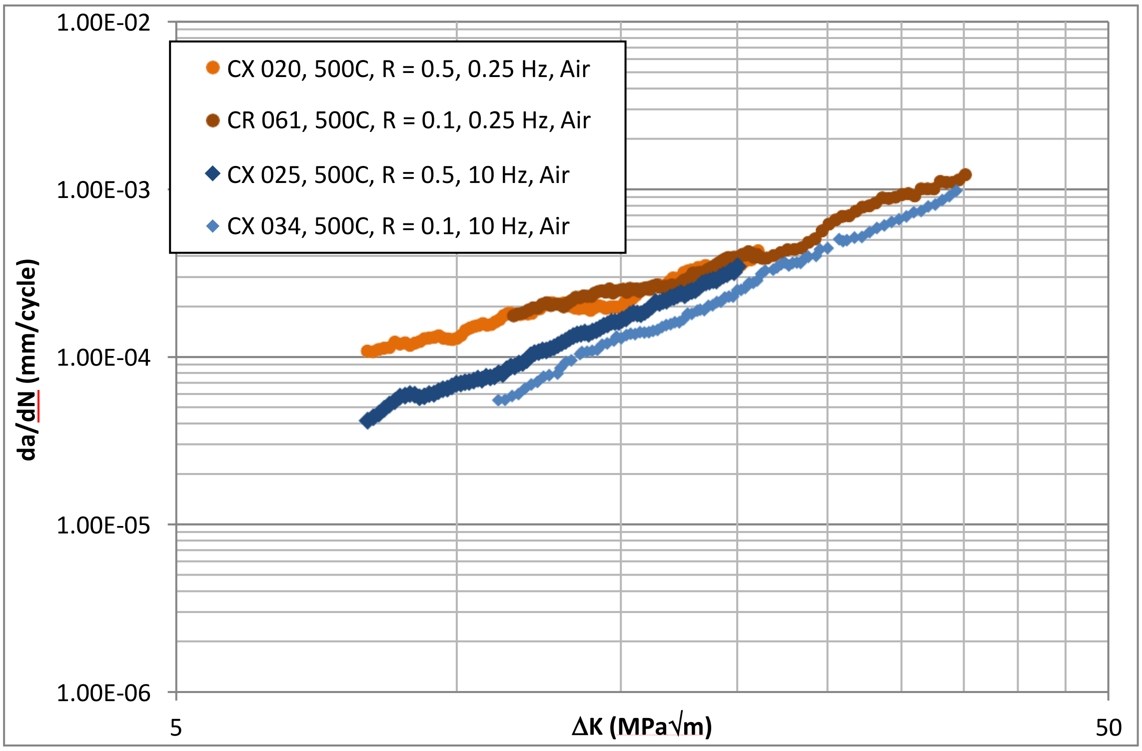

Figure 7.1a: Results for the R ratio 0.1 and 0.5 constant load range mechanical tests carried out in air focusing on the Paris regime at 500°C.

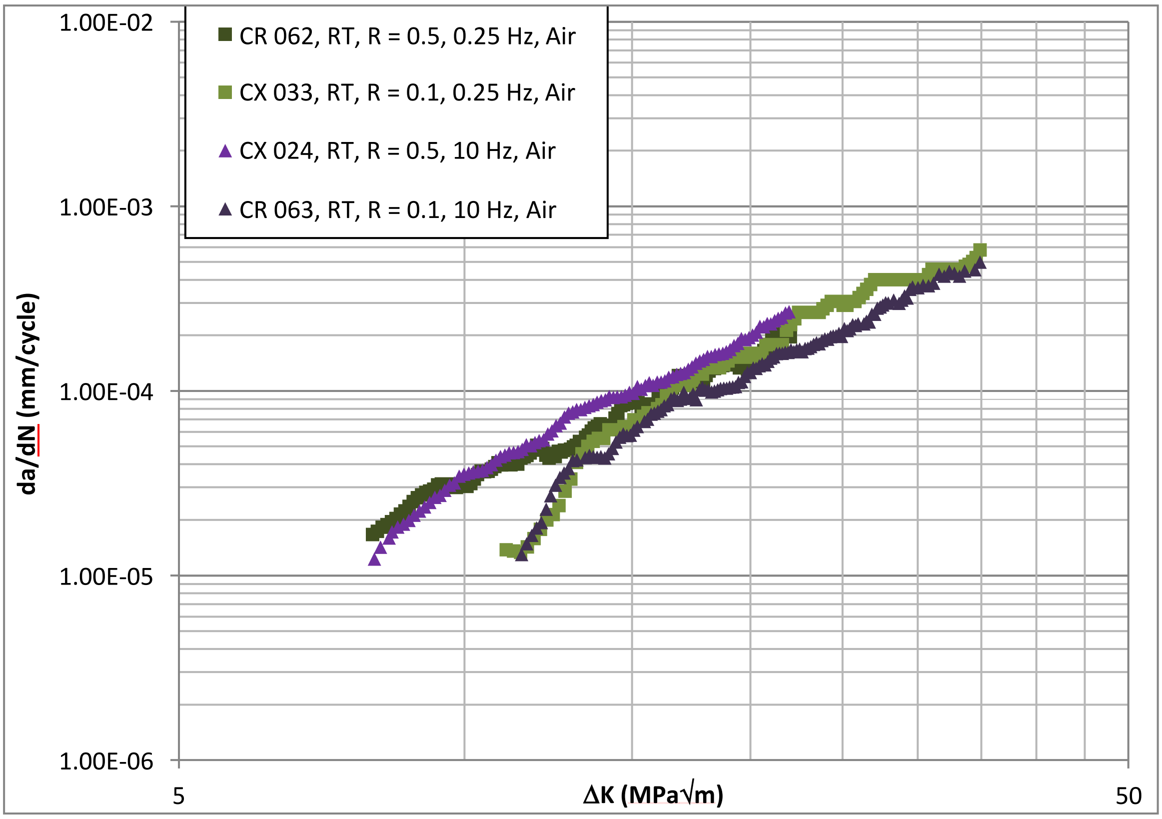

Figure 7.1b: Results for the R ratio 0.1 and 0.5 constant load range mechanical tests carried out in air focusing on the Paris regime at room temperature.

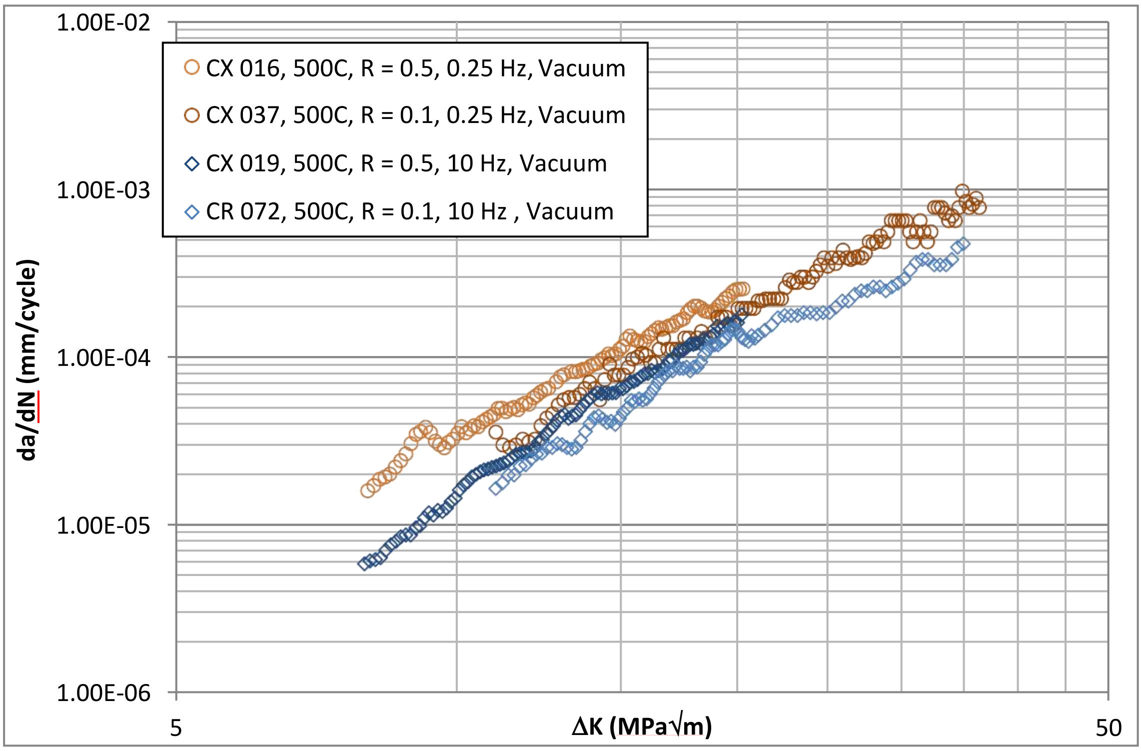

Figure 7.2a: Results for the R ratio 0.1 and 0.5 constant load range mechanical tests carried out under vacuum conditions focusing on the Paris regime at 500°C.

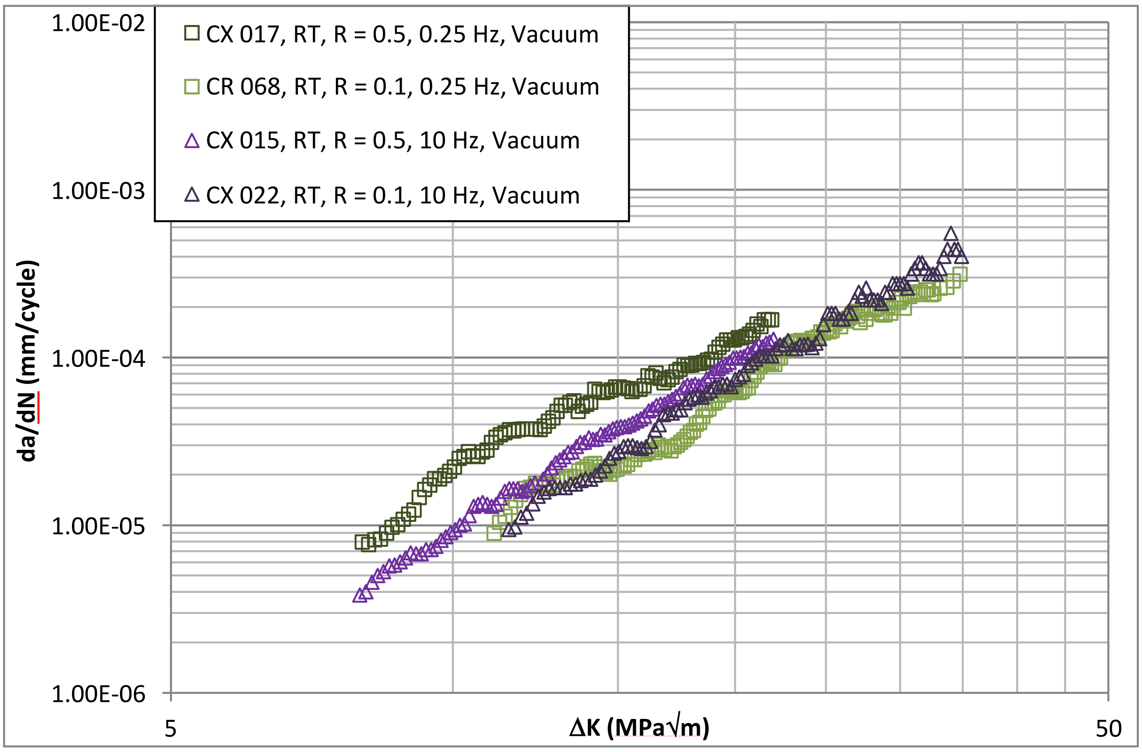

Figure 7.2b: Results for the R ratio 0.1 and 0.5 constant load range mechanical tests carried out under vacuum conditions focusing on the Paris regime at room temperature.

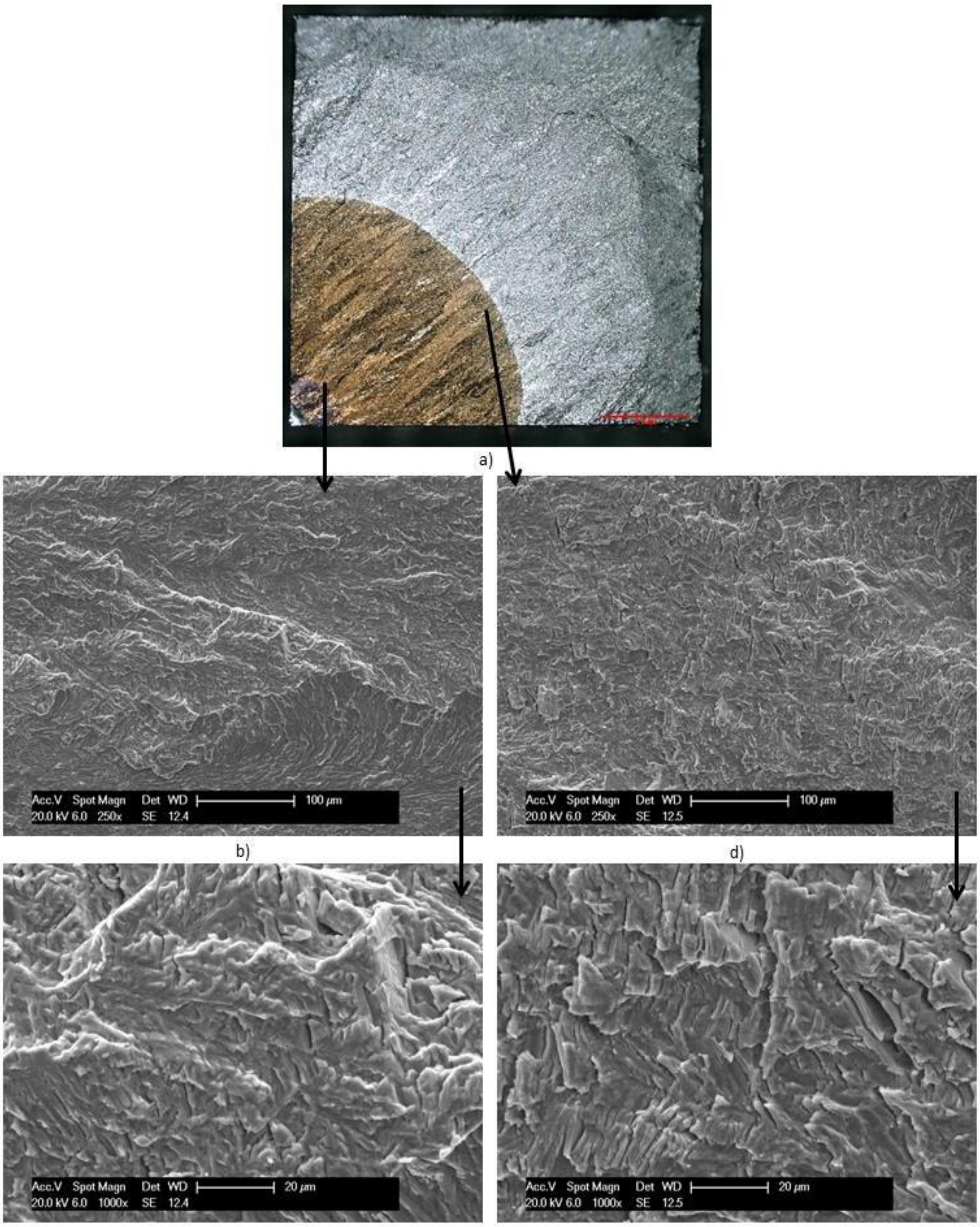

a)

b)

d)

c)

e)

Figure 7.3: Images captured of specimen CX 020 tested at 500C, 0.25 Hz, R = 0.5, air. The crack growth direction is from bottom left to top right. a) Shows optical image of the crack showing isometric crack growth creating an even quarter circle. b + c) Show SEM images taken at a low ΔK value. d + e) Show SEM images taken at high ΔK values. Transgranular crack growth is visible across the whole fracture

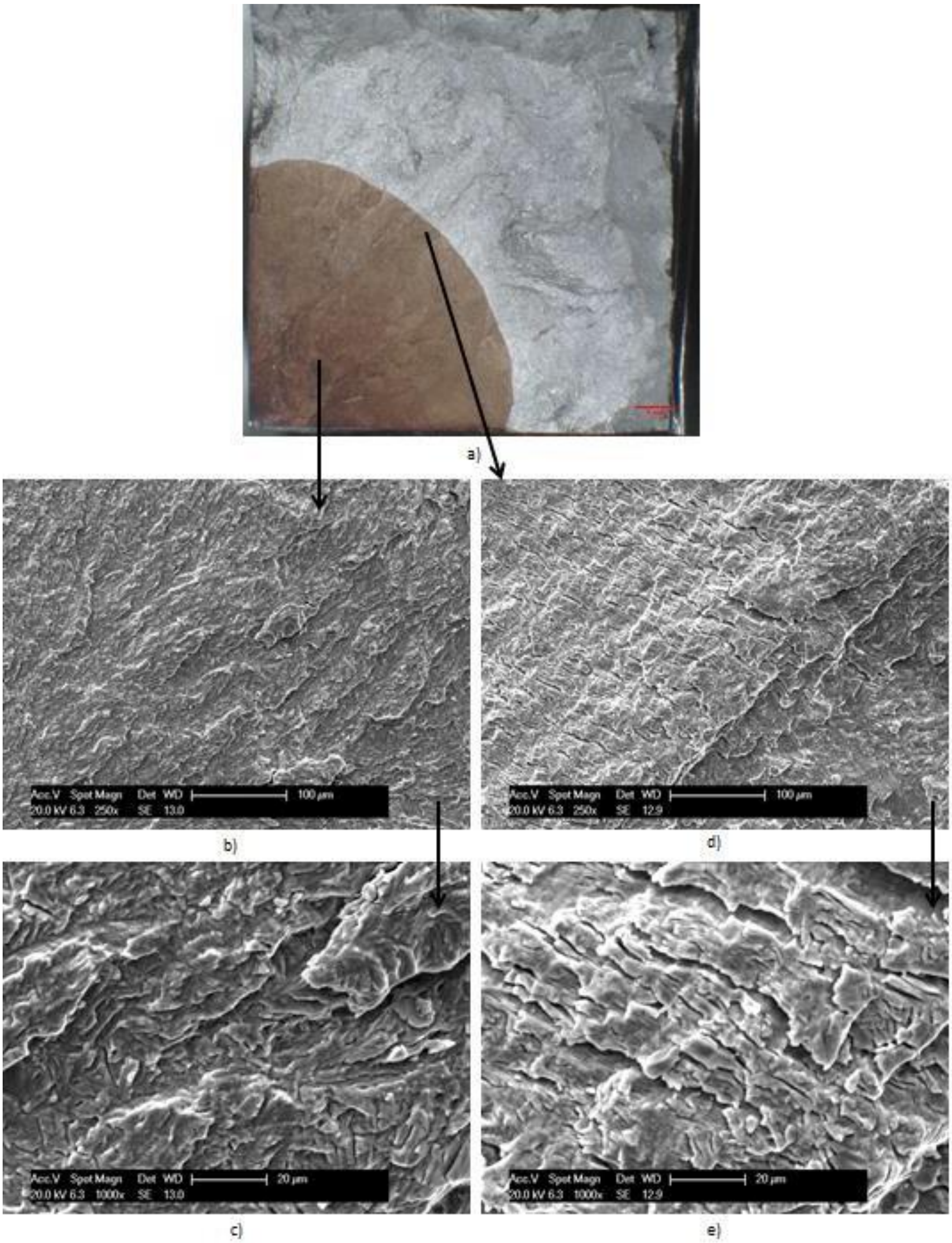

Figure 7.4: Images captured of specimen CR 061 tested at 500C, 0.25 Hz, R = 0.1, air. The crack growth direction is diagonal from bottom left to top right. a) Shows optical image of the crack showing isometric crack growth creating an even quarter circle. b + c) Show SEM images taken at a low ΔK value. d + e) Show SEM images taken at high ΔK values. Transgranular crack growth is visible across the whole fracture surface. At high ΔK values there is significantly more secondary cracking and tearing.

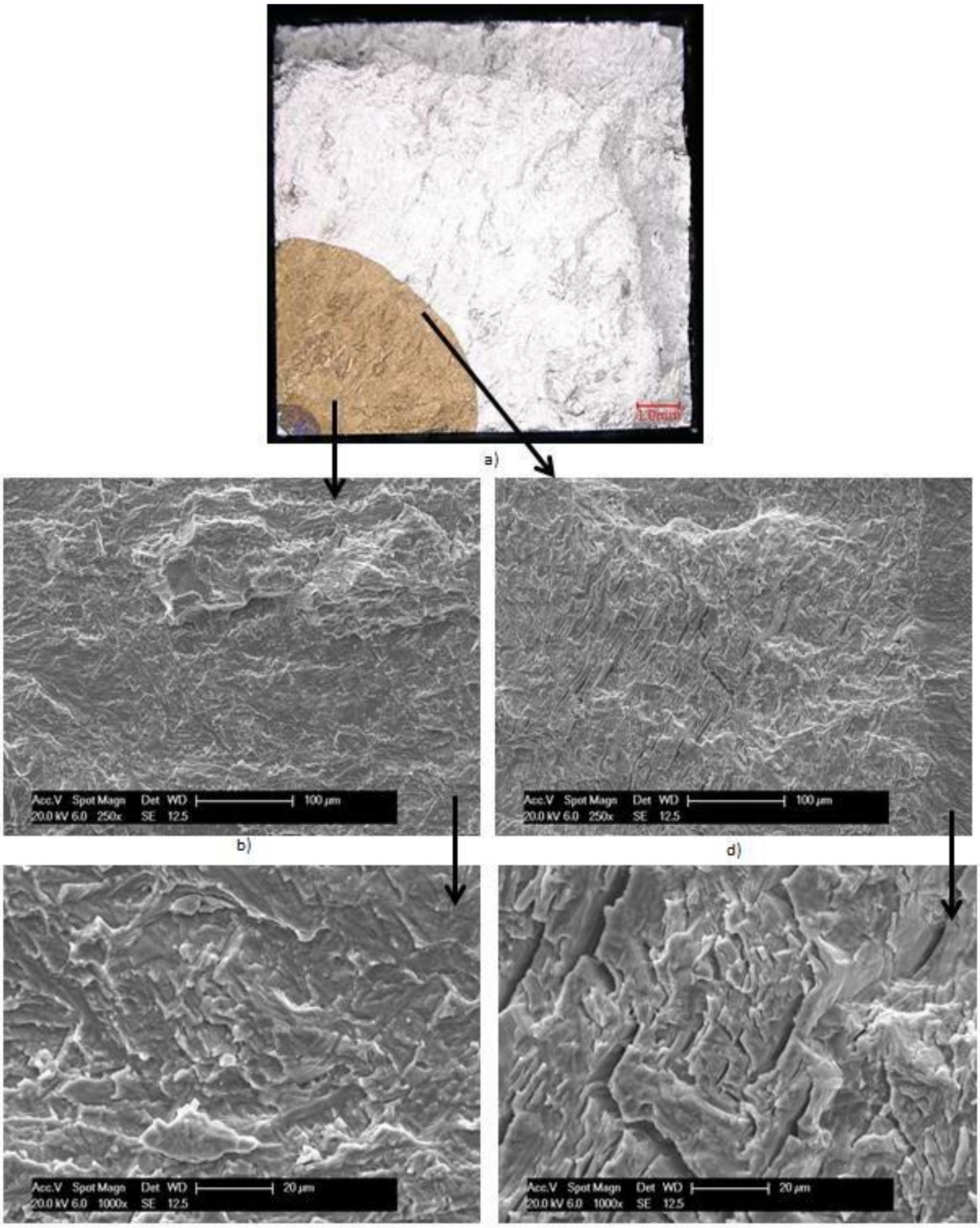

a)

b)

d)

c)

e)

Figure 7.5: Images captured of specimen CX 070 tested at 500C, 10Hz, R = 0.5, air. The crack growth direction is diagonal from bottom left to top right. a) Shows optical image of the crack showing isometric crack growth creating an even quarter circle. b + c) Show SEM images taken at a low ΔK value. d + e) Show SEM images taken at high ΔK values. Transgranular crack growth is visible across the whole fracture surface.

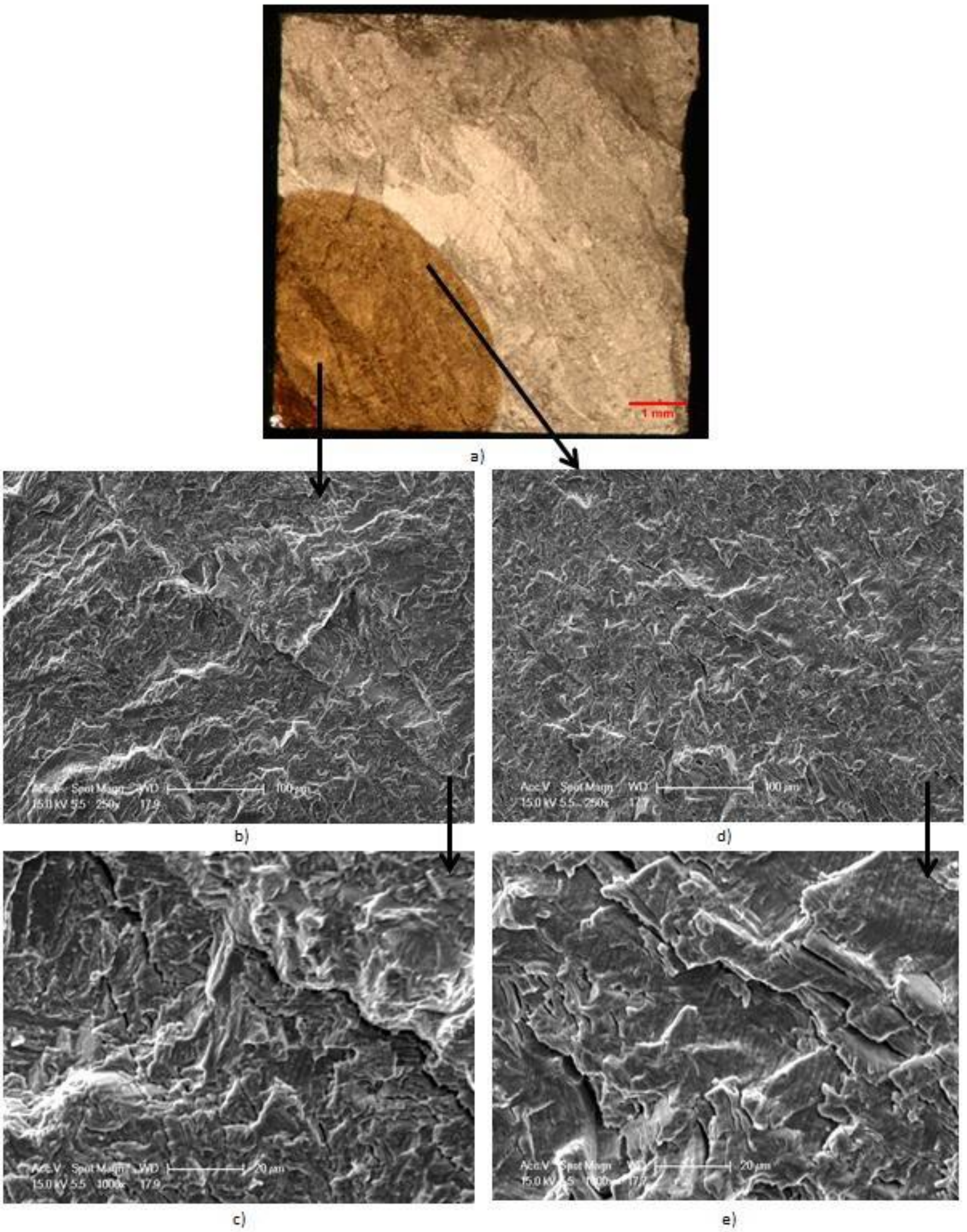

Figure 7.6: Images captured of specimen CX 034 tested at 500C, 10Hz, R = 0.1, air. The crack growth direction is diagonal from bottom left to op right. a) Shows optical image of the crack showing isometric crack growth creating an even quarter circle. b + c) Show SEM images taken at a low ΔK value. d + e) Show SEM images taken at high ΔK values.

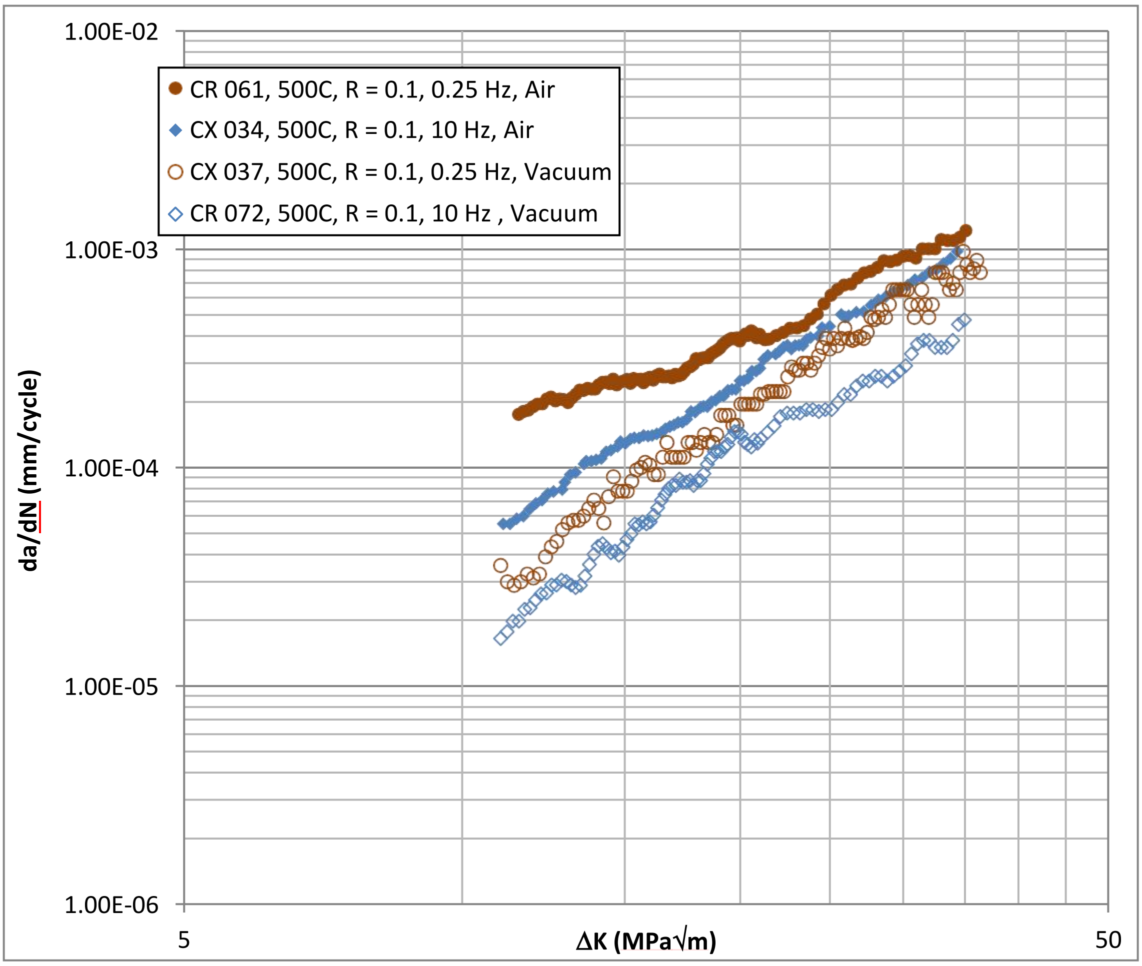

Figure 7.7: Results for the R ratio 0.1 constant load range mechanical tests at 500°C in both air and vacuum conditions. Results show both 0.25 and 10 Hz frequenices.

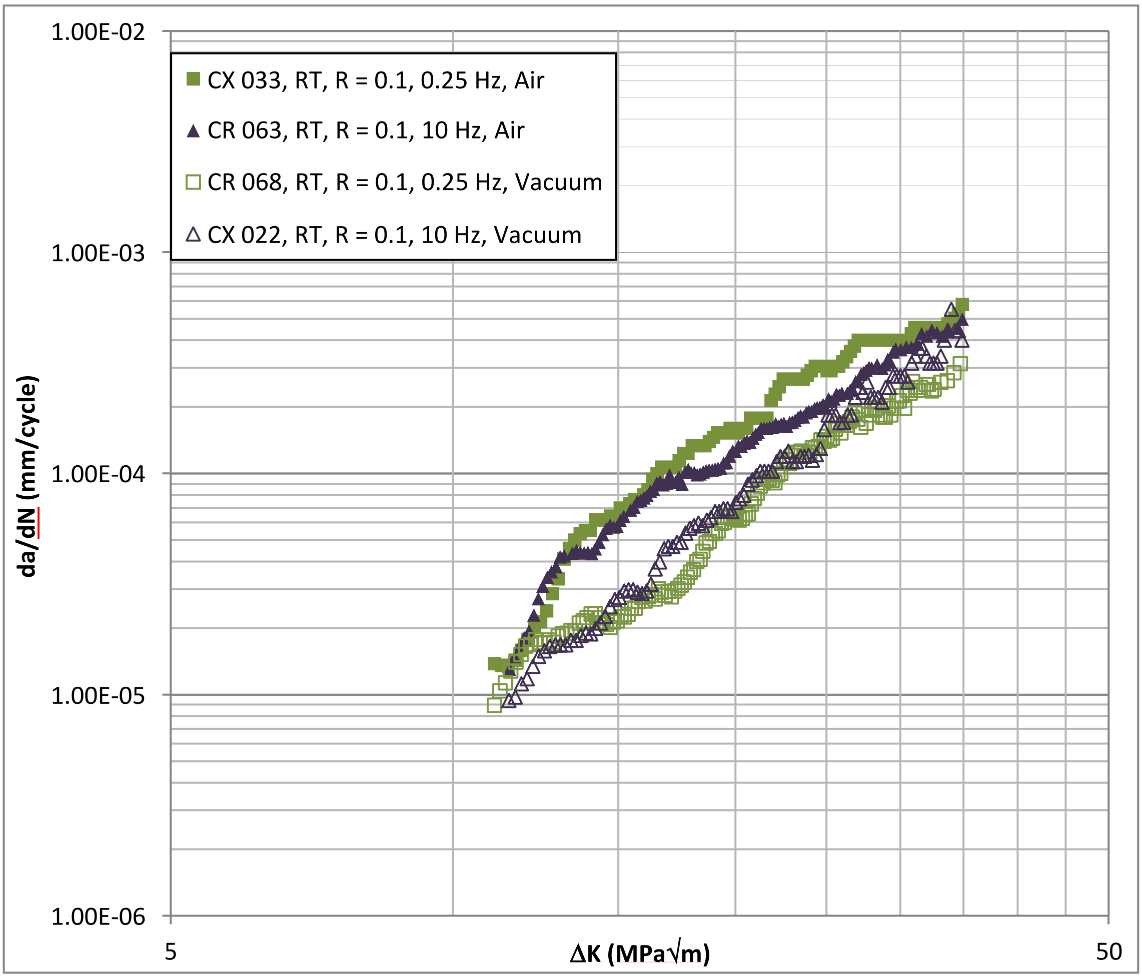

Figure 7.8: Results for the R ratio 0.1 constant load range mechanical tests at room temperature in both air and vacuum conditions. Results show both 0.25 and 10 Hz frequencies.

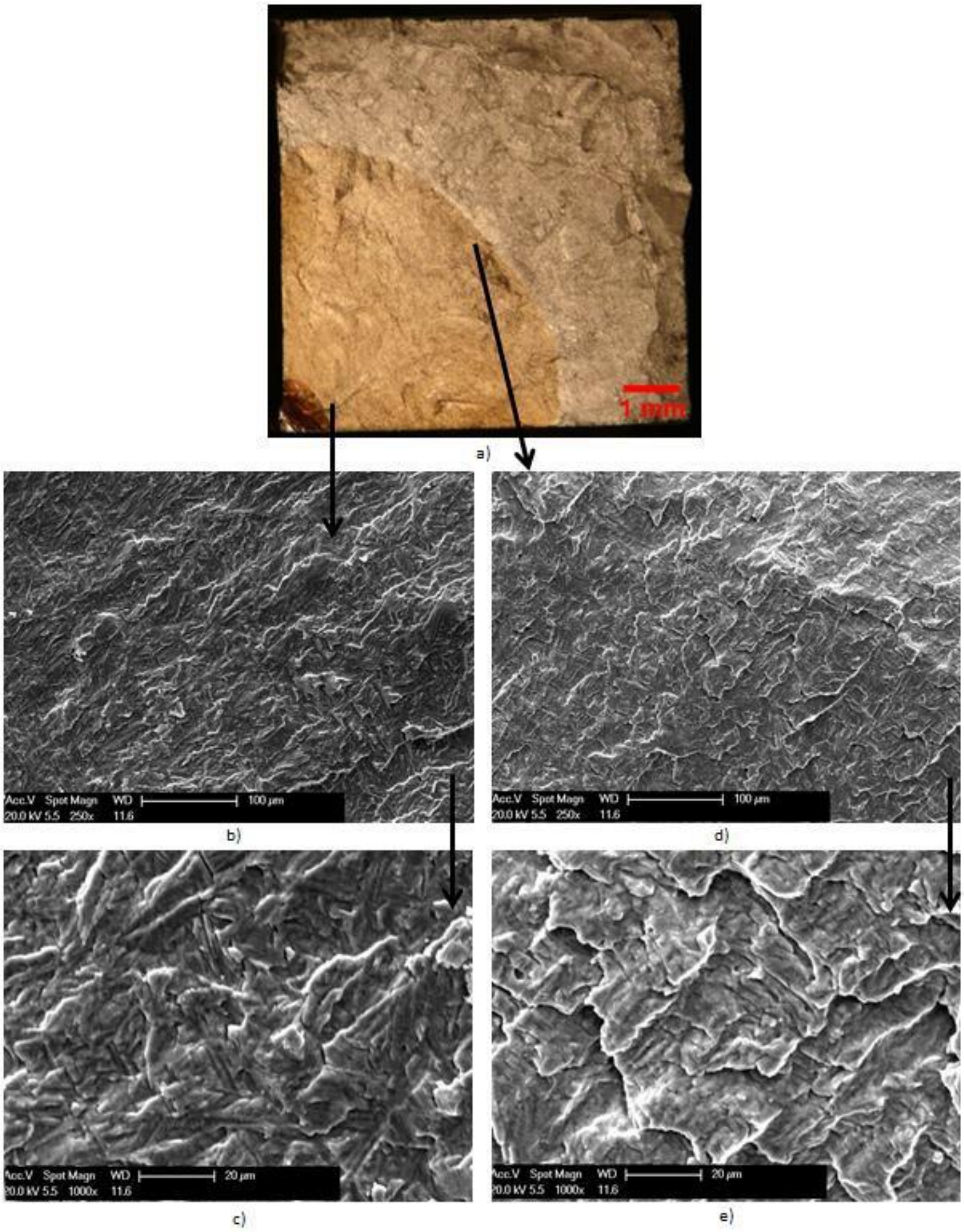

Figure 7.9: Images captured of specimen CX 037 tested at 500°C, 0.25 Hz, R = 0.1, vacuum. The crack growth direction is diagonal from bottom left to top right. a) Shows optical image of the crack showing isometric crack growth creating an even quarter circle. b + c) Show SEM images taken at a low ΔK value. d + e) Show SEM images taken at high ΔK values. All crack growth shows a transgranular mechanism.

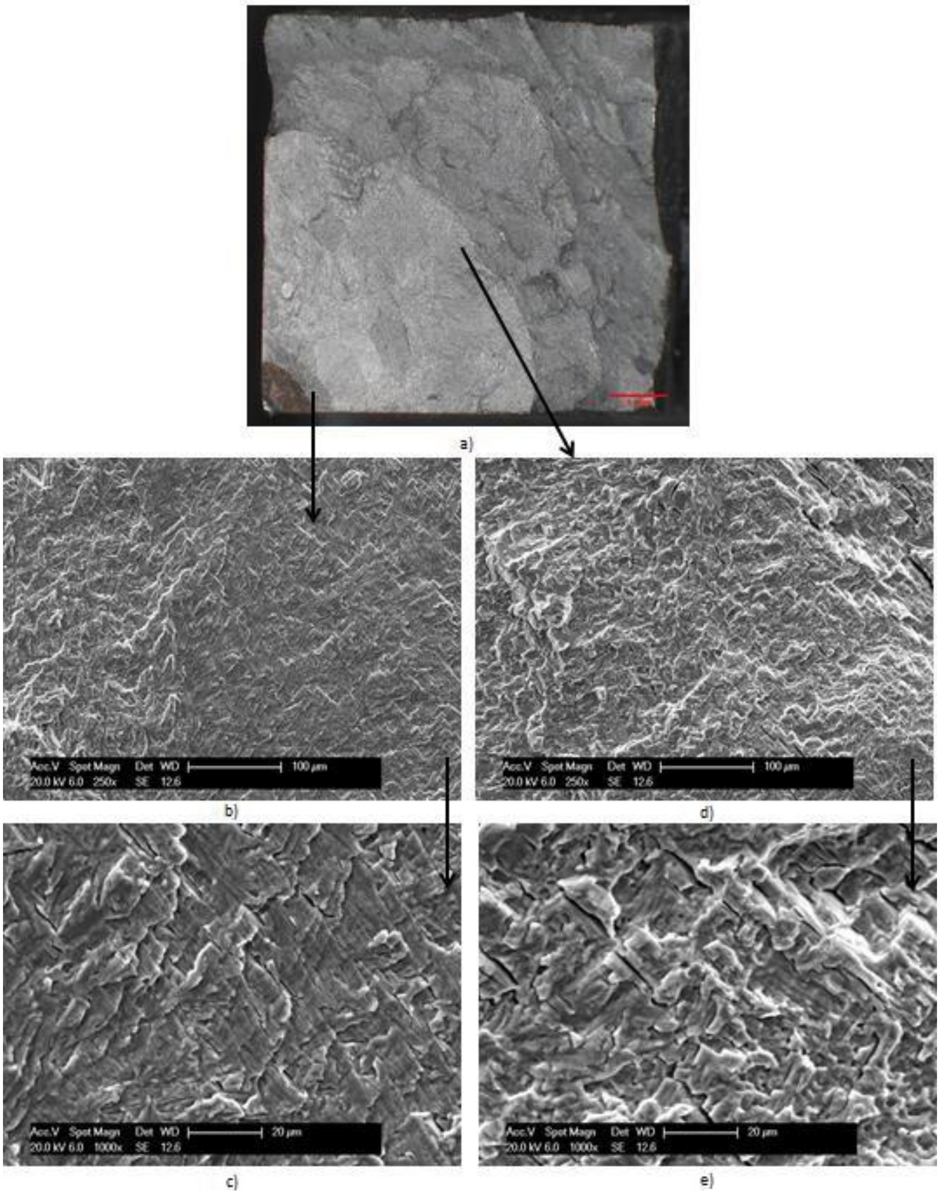

Figure 7.10: Images captured of specimen CX 033 tested at room temperature, 0.25 Hz, R = 0.1, air. The crack growth direction is diagonal from bottom left to top right. a) Shows optical image of the crack showing isometric crack growth creating an even quarter circle. b + c) Show SEM images taken at a low ΔK value. d + e) Show SEM images taken at high ΔK values.

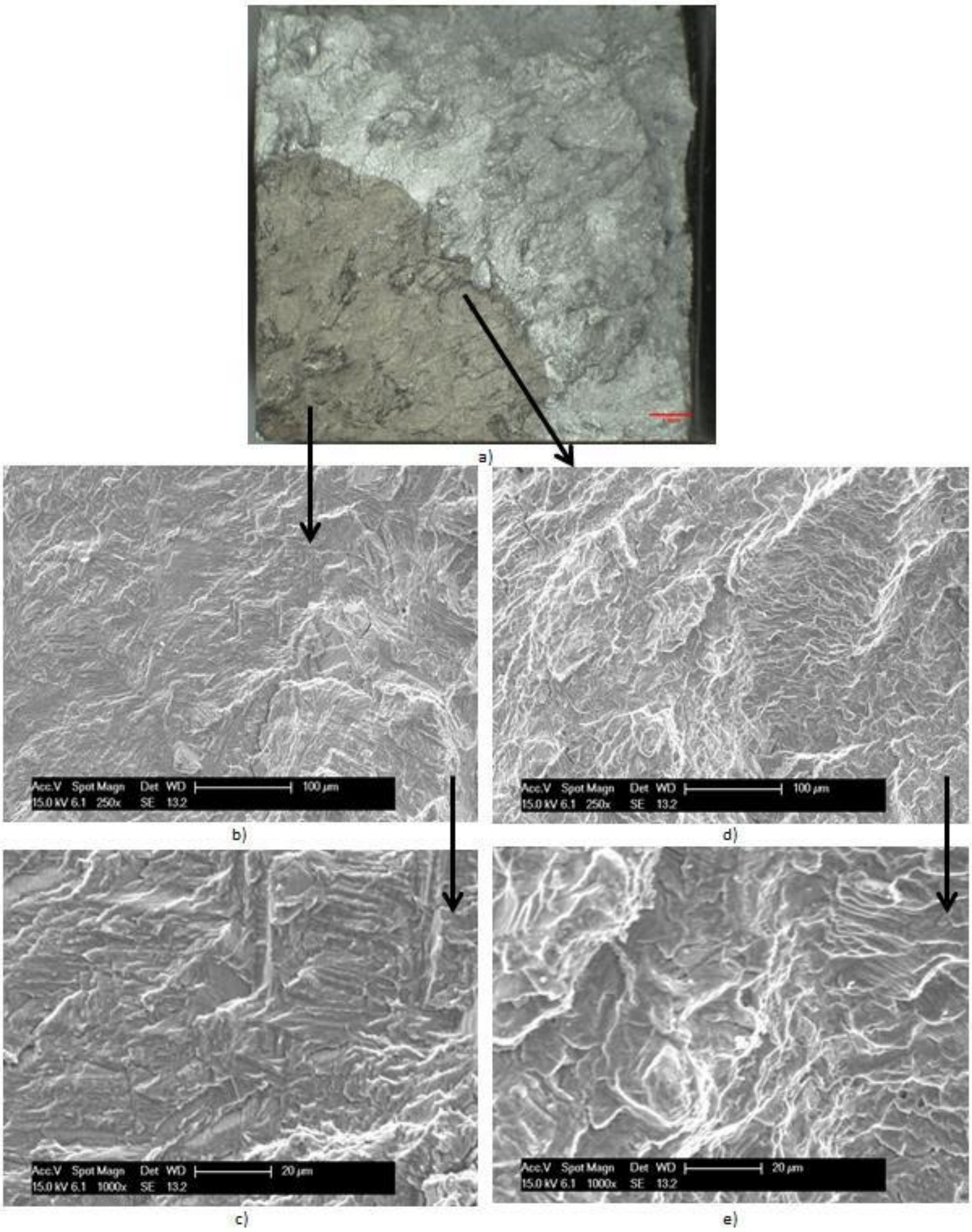

Figure 7.11: Images captured of specimen CR 068 tested at room temperature, 0.25 Hz, R = 0.1, vacuum. The crack growth direction is diagonal from bottom left to top right. a) Shows optical image of the crack showing isometric crack growth creating an even quarter circle. b + c) Show SEM images taken at a low ΔK value. d + e) Show SEM images taken at high ΔK values. Shows less secondary cracking at high ΔK values than tests carried out in air at otherwise similar conditions.

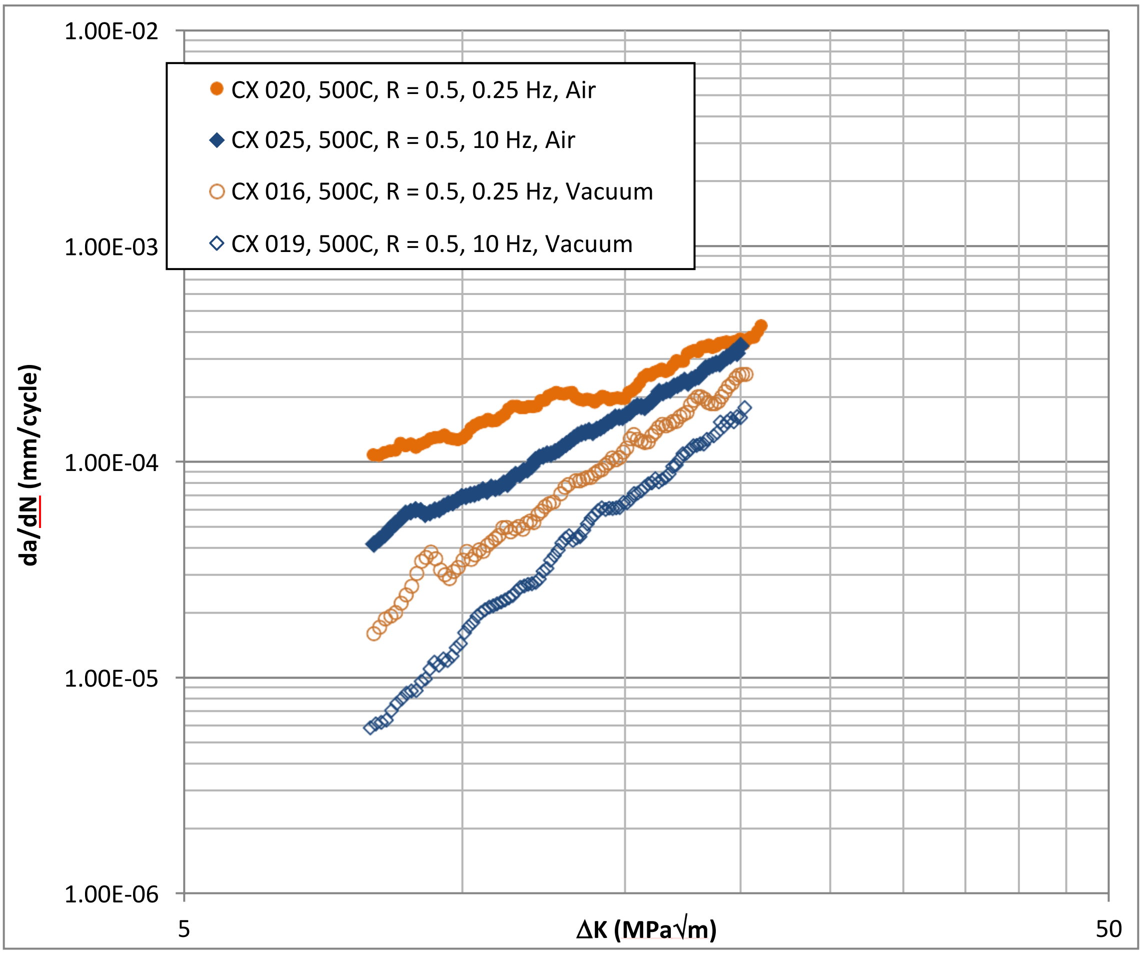

Figure 7.12: Results for the R ratio 0.5 constant load range mechanical tests at 500°C in both air and vacuum conditions. Results are from 0.25 and 10 Hz frequencies.

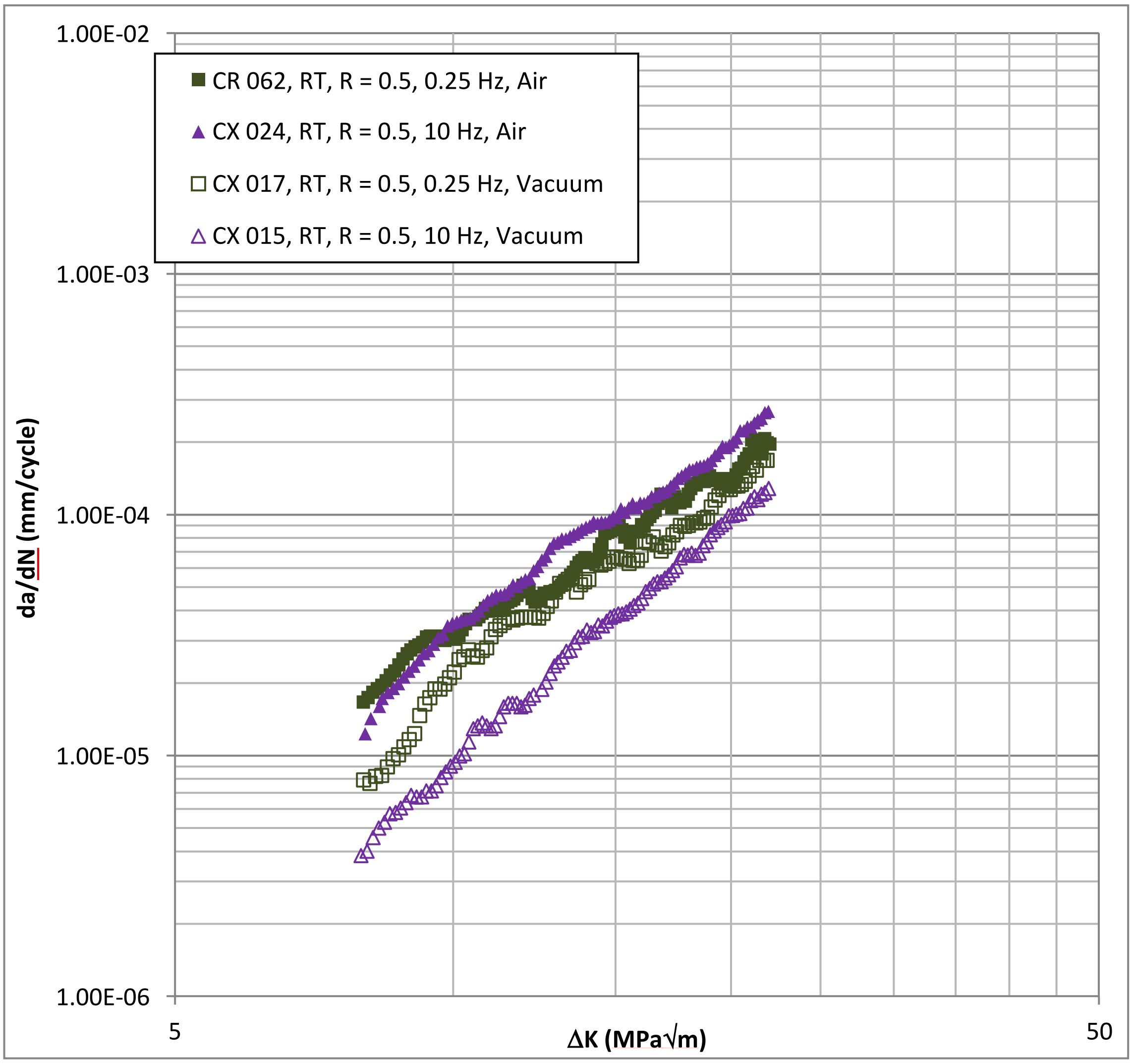

Figure 7.13: Results for the R ratio 0.5 constant load range mechanical tests at room temperature in both air and vacuum conditions. Results are from both 0.25 and 10 Hz frequencies.

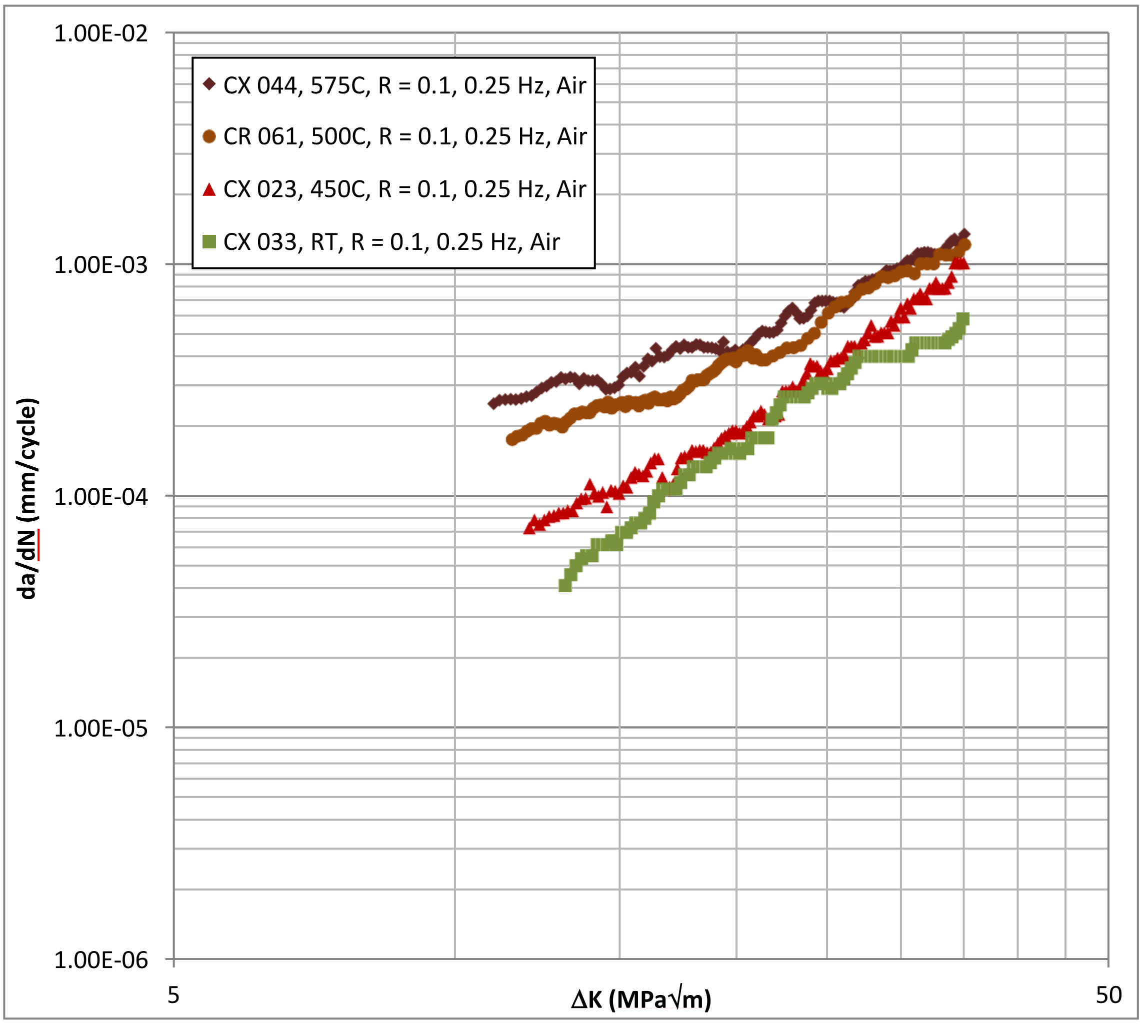

Figure 7.14: Results for the R ratio 0.1 constant load range mechanical tests with a frequency of 0.25 Hz at a range of temperatures in air conditions. Temperatures ranged from room temperature to 575^{o}C.

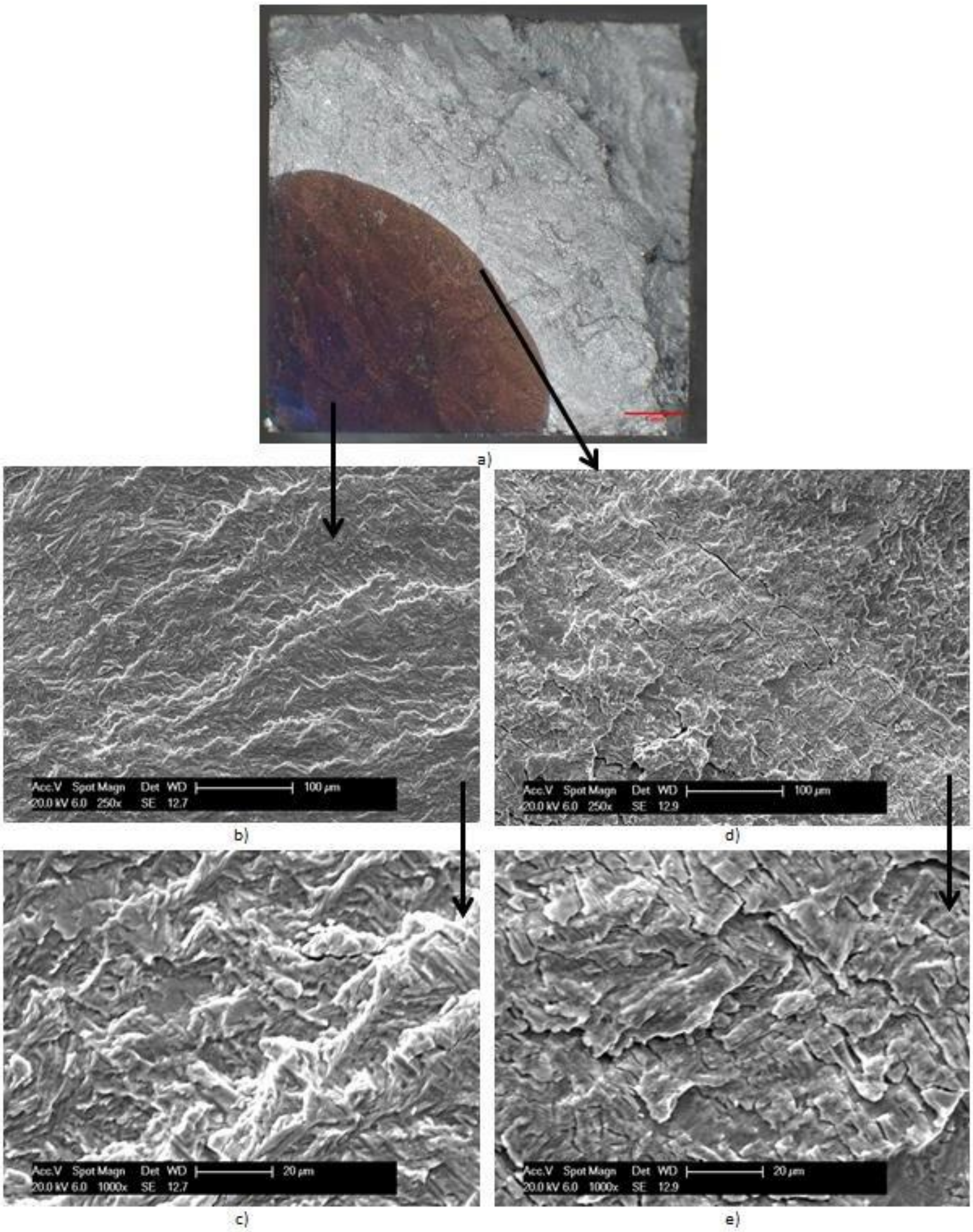

Figure 7.15: Images captured of specimen CX 044 tested at 575^{o}C, 0.25 Hz, R = 0.1, air a) Shows optical image of the crack showing isometric crack growth creating an even quarter circle. The darker colour is a result of greater levels of oxidation from being tested at a higher temperature b + c) Show SEM images taken at a low ΔK value. d + e) Show SEM images taken at high ΔK values with secondary cracking visible on the fracture surface.

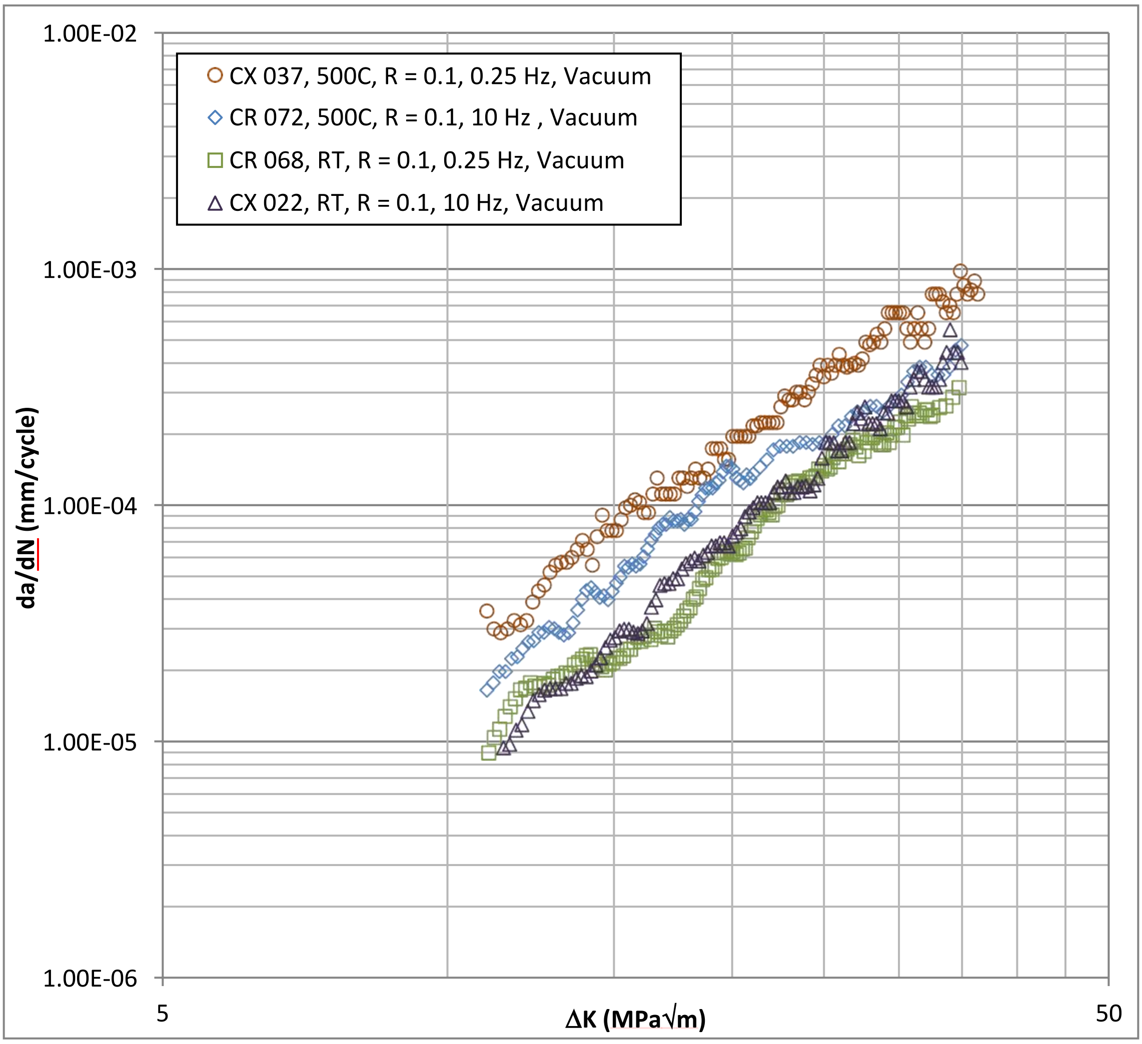

Figure 7.16: Results for the R ratio 0.1 mechanical tests with a frequency of both 0.25 and 10 Hz at room temperature and 500°C under vacuum conditions.

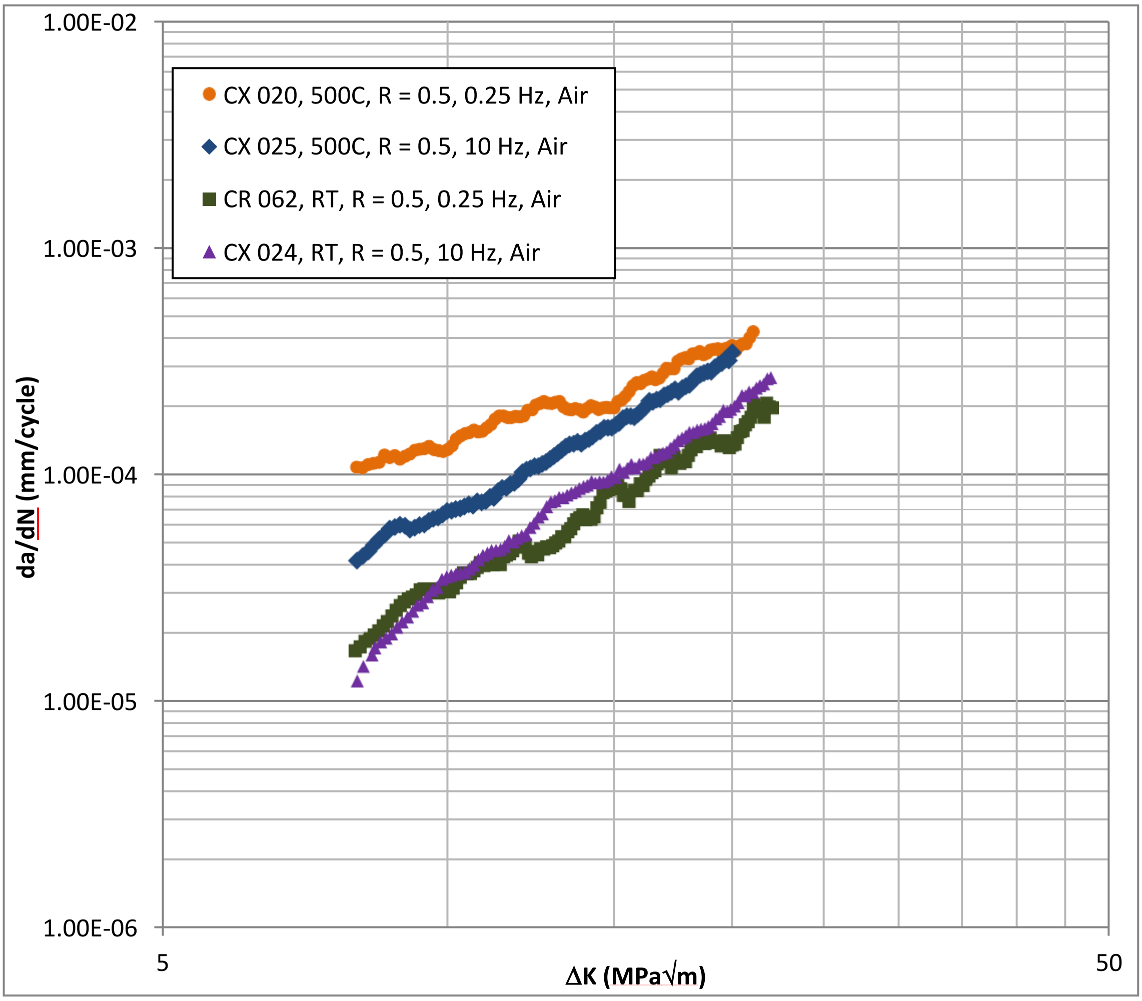

Figure 7.17: Results for the R ratio 0.5 constant load range mechanical tests with a frequency of 0.25 and 10 Hz at both room temperature and 500°C in air conditions.

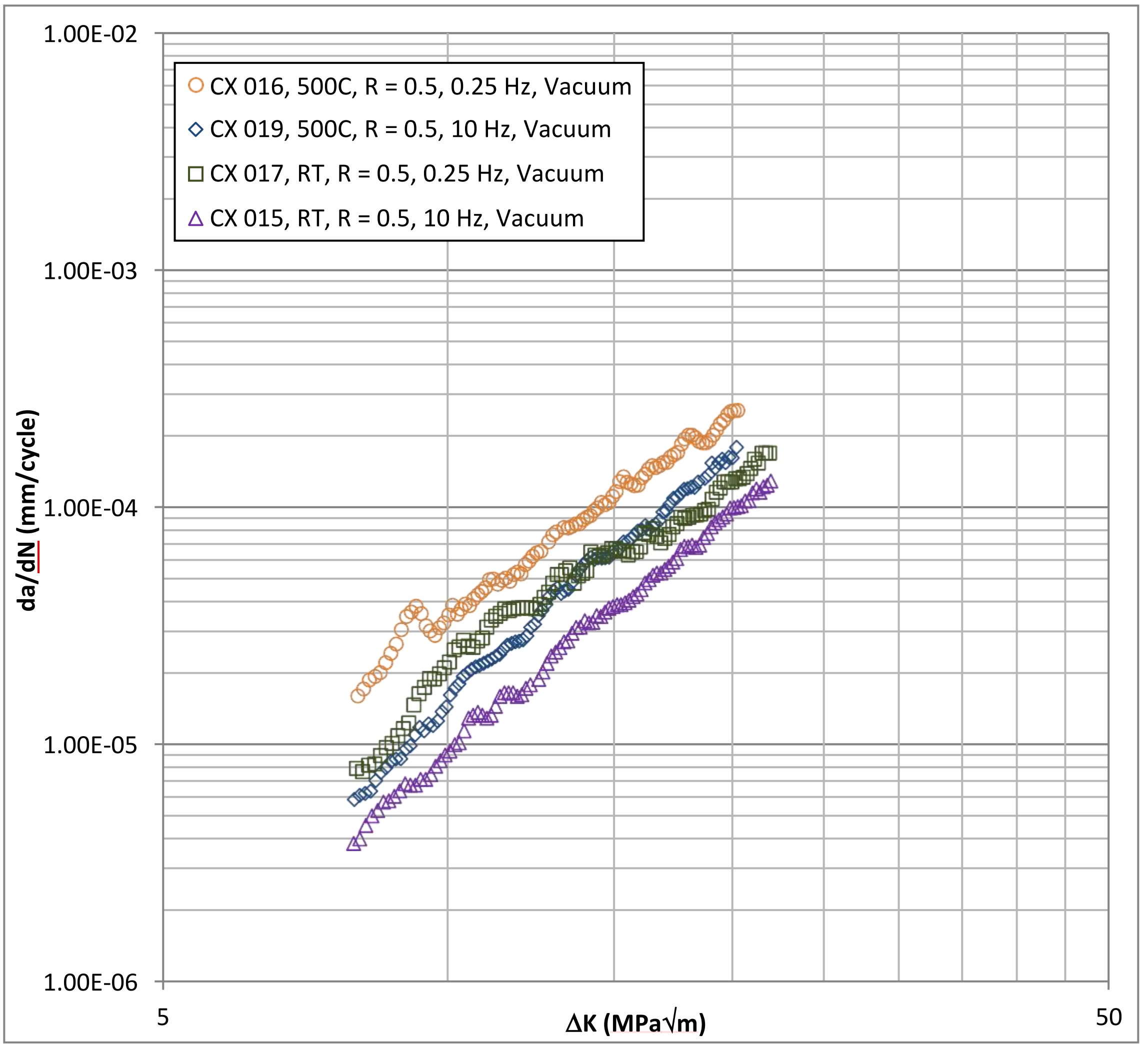

Figure 7.18: Results for the R ratio 0.5 constant load range mechanical tests with a frequency of 0.25 and 10 Hz at room temperature and 500^{o}C under vacuum conditions.

Chapter 8 – Results – Dwell Fatigue Testing

Table 8.1 Paris constants, C (mm/cycle) and m, obtained experimentally for the dwell loading segments for R ratio 0.1.

Specimen	Conditions	C (mm/cycle)	m
CR 071	500C, 1 Hr Dwell, Vacuum, Max	2.71E-05	0.97
CX 031	500C, 1 Hr Dwell, Air, Max	1.40E-06	1.89
CR 073	500C, 1 Hr Dwell, Air, Min	1.42E-07	2.63
CX 030	575C, 1 Hr Dwell, Air, Max	1.0E-10	6.10
CX 026	500C, 2 Min Dwell, Vacuum, Max	3.93E-08	2.90
CX 032	500C, 2 Min Dwell, Air, Max	5.76E-07	2.18

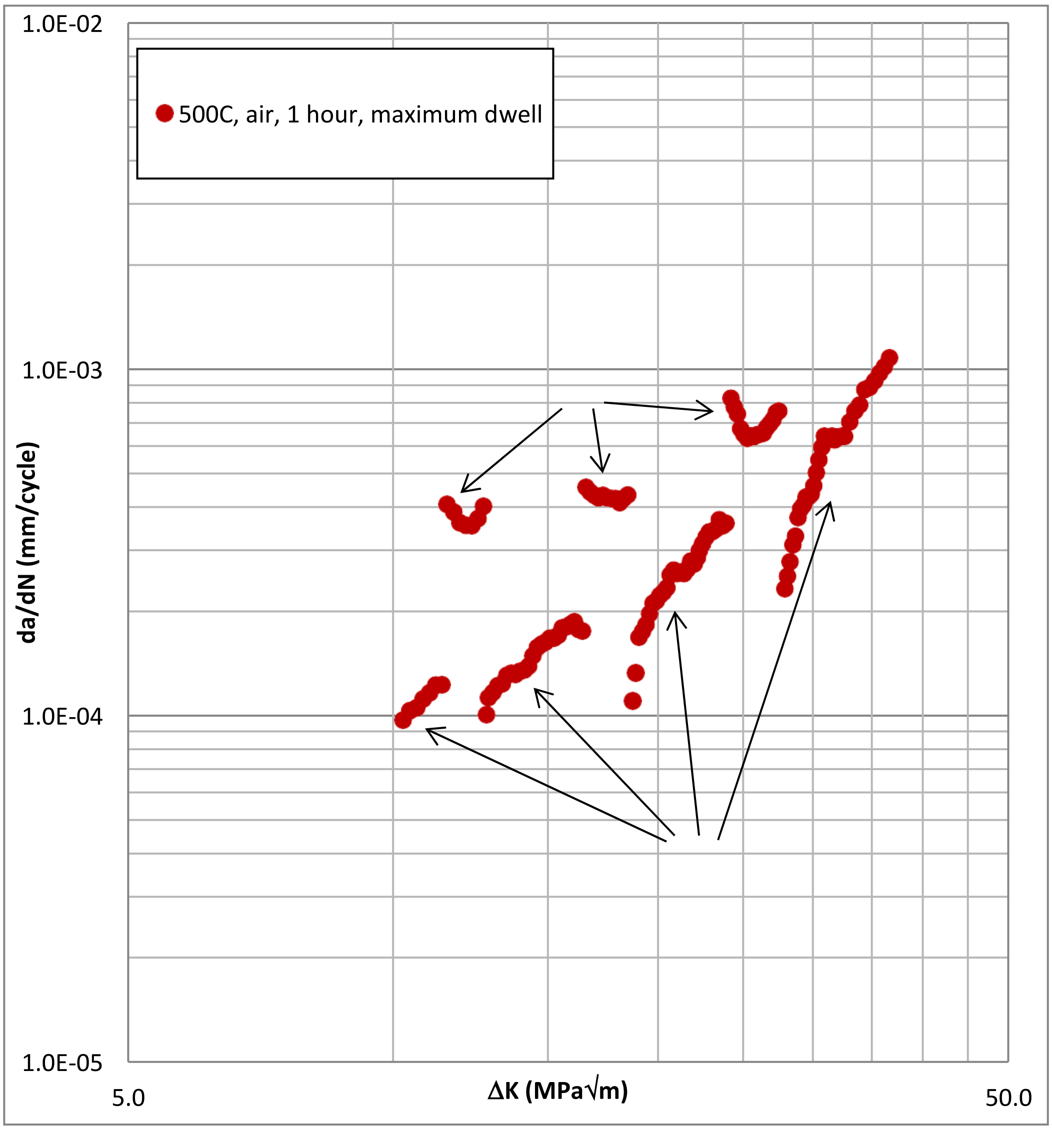

Figure 8.1: Results from CX 031, the one hour maximum hold dwell test in air at 500^{o}C. Showing four periods of baseline crack growth and three periods of dwell crack growth.

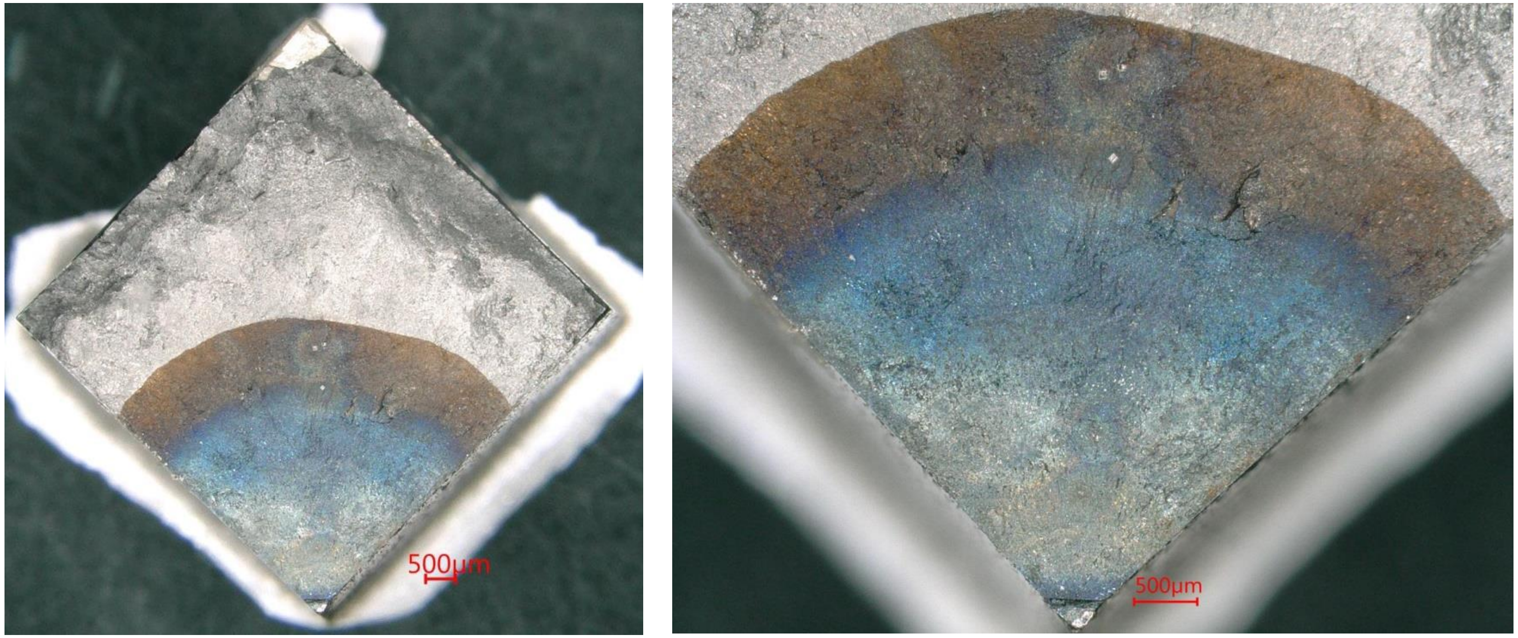

Figure 8.2: Optical Image of CX 031, the one hour dwell at 500^{o}C in air at maximum hold. Showing uniform crack growth in all directions producing a clear quarter circle.

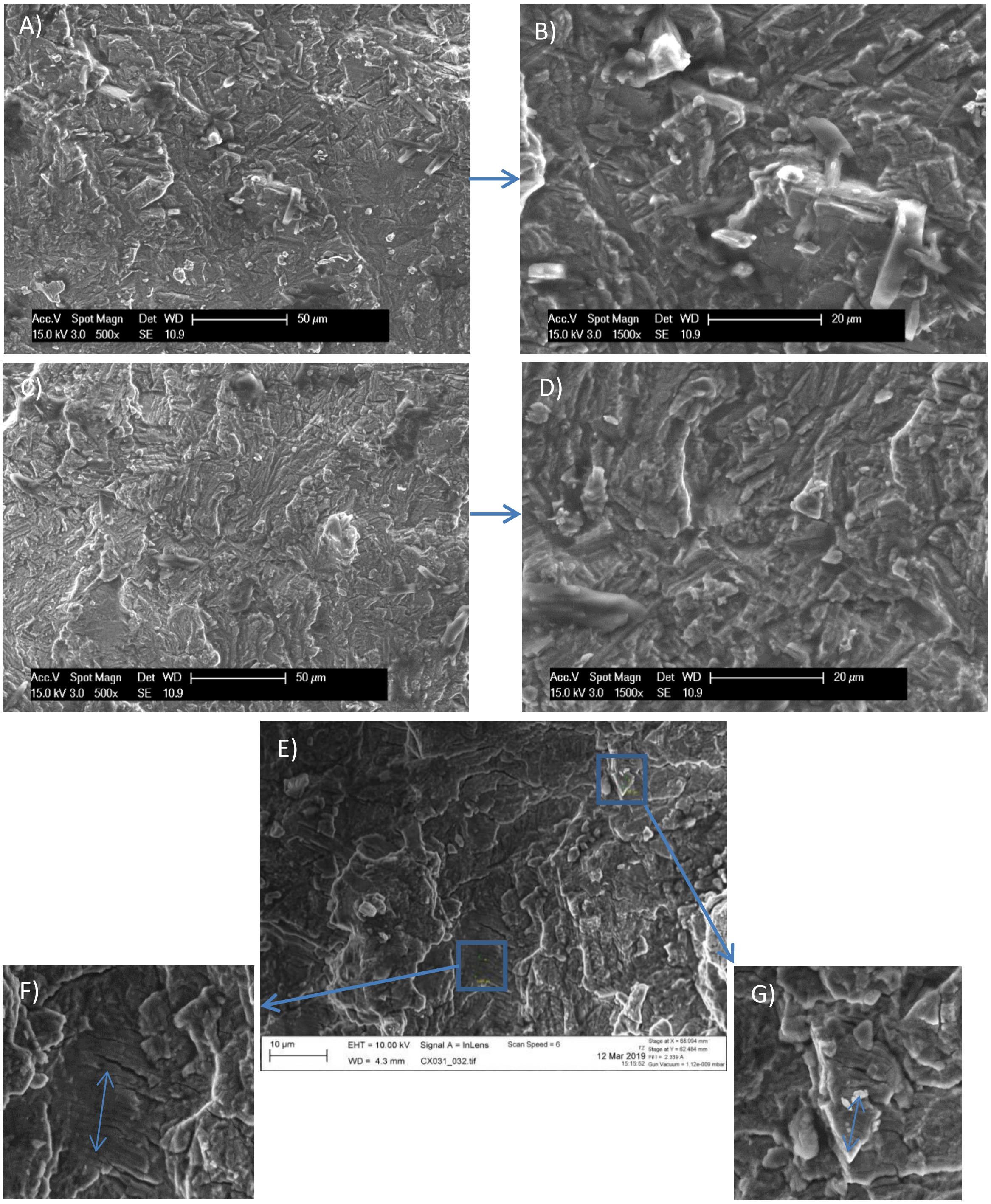

Figure 8.3: SEM images of the one hour dwell at 500°C in air at maximum hold. Crack growth direction is straight from bottom to top. A) Shows the first baseline period with transgranular crack growth. B) Shows a magnified image of A) with transgranular crack growth. C) Shows the first dwell period. Transgranular crack growth is dominating. D) Shows a magnified image of C). E) Shows the transition between the 3rd dwell period and the 4th baseline period of crack growth. There is no obvious transition visible but striations on the fracture surface show the spacing becomes smaller when the baseline period is introduced. F) Shows the striation spacing for the dwell period with each striation found to be approximately 0.78 um. G) Shows the striation spacing for the baseline crack growth period with each striation found to be approximately 0.45 um.

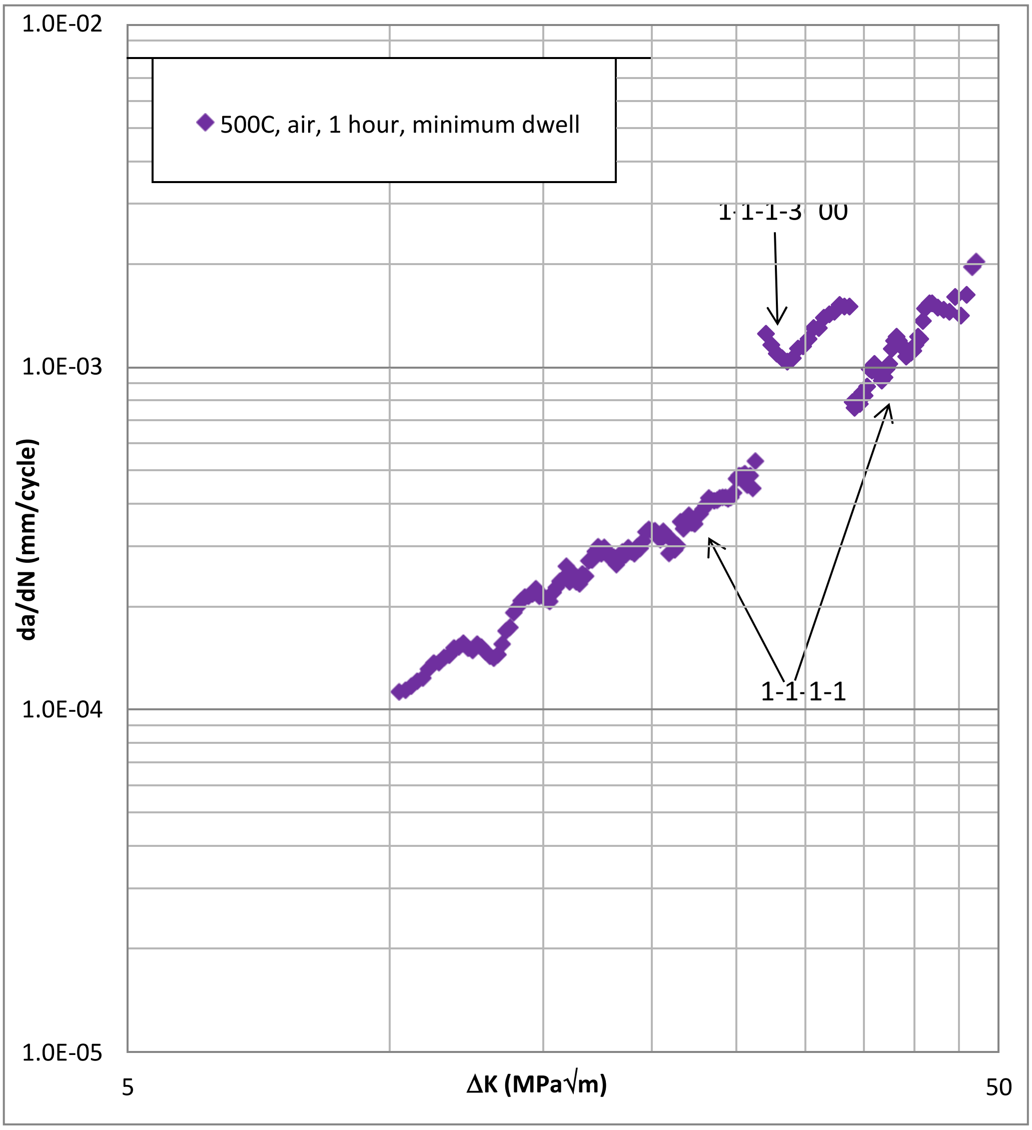

Figure 8.4: Results from CR 073, the one hour minimum hold dwell test in air at 500°C. Showing two periods of baseline crack growth and one period of dwell crack growth.

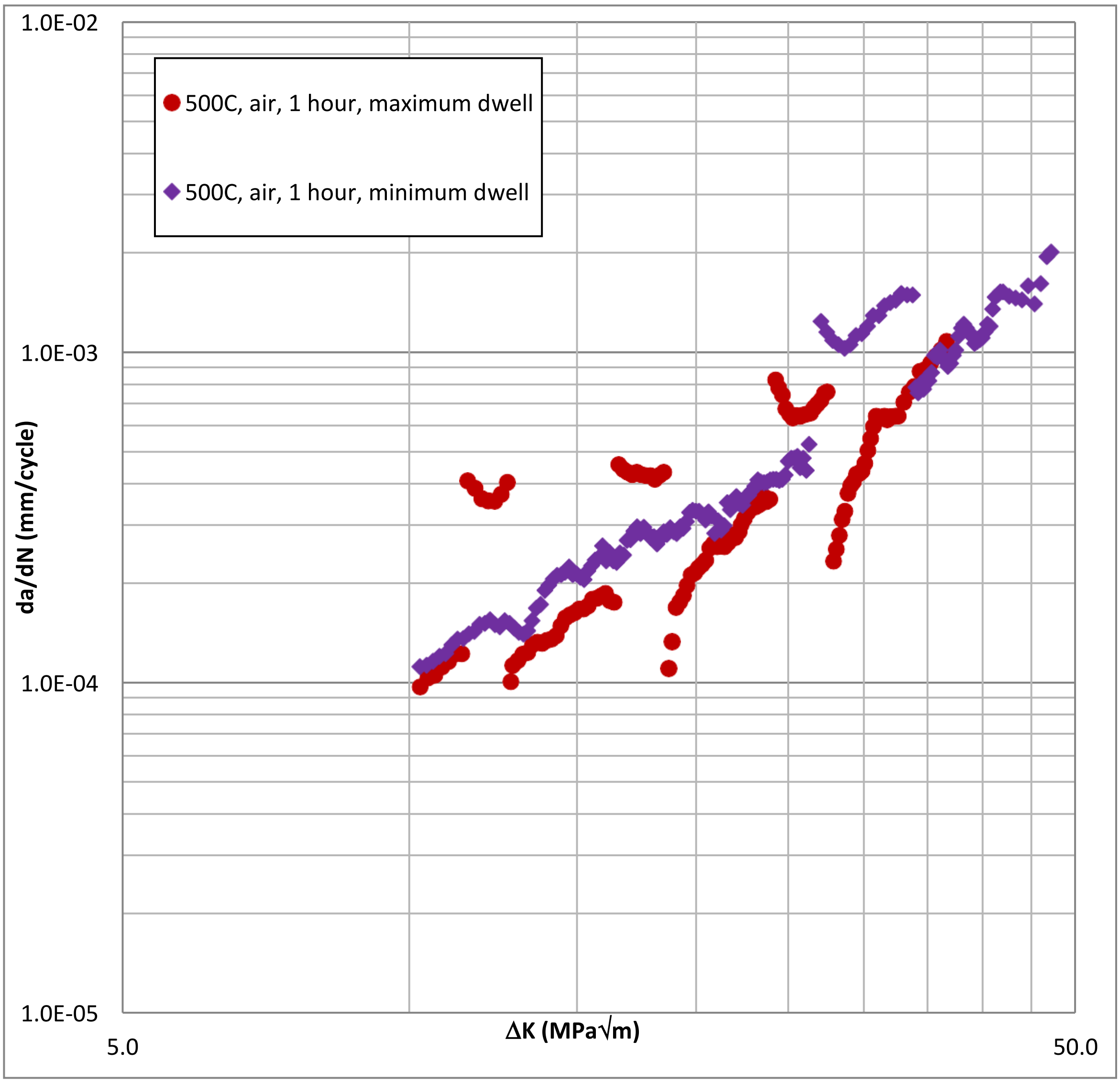

Figure 8.5: Results comparing the one hour maximum and minimum hold dwell tests in air at 500°C. Baseline crack growth rates are very similar.

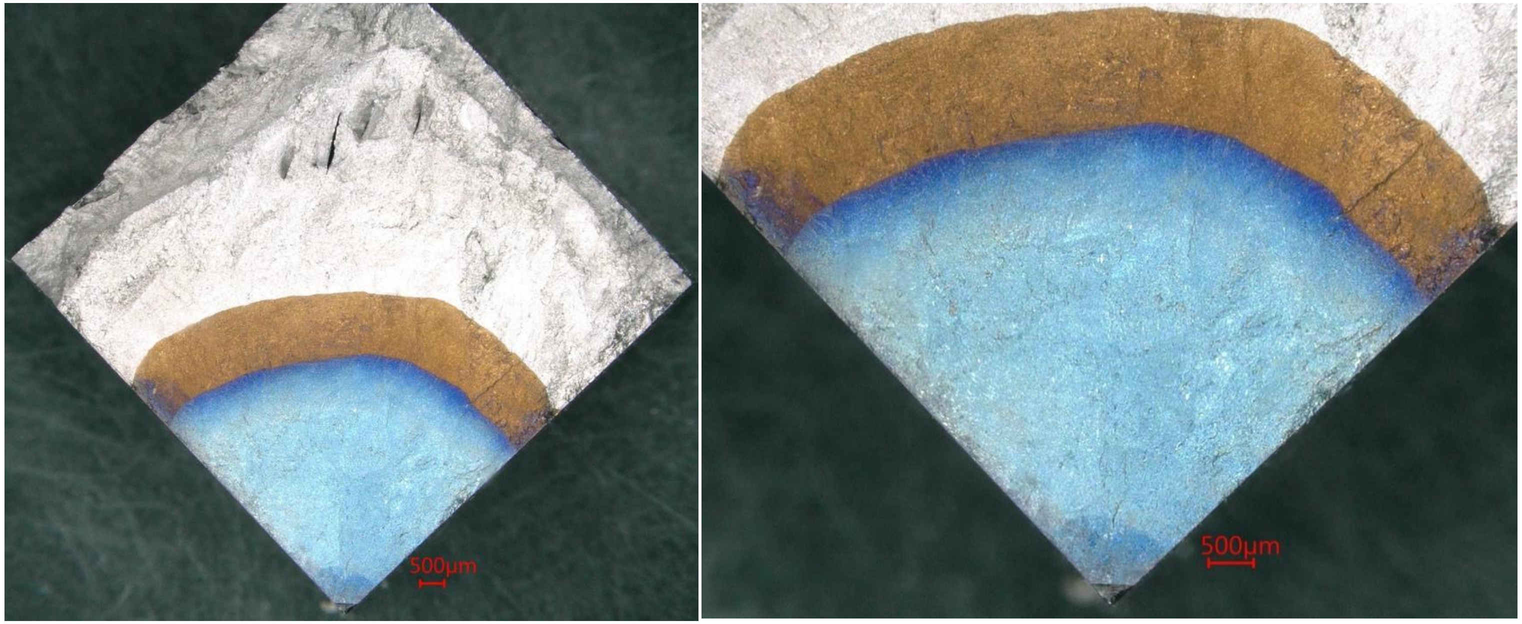

Figure 8.6: Optical Image of CR 073, the one hour dwell at 500^{o}C in air at minimum hold. Showing uniform crack growth in all directions producing a clear quarter circle.

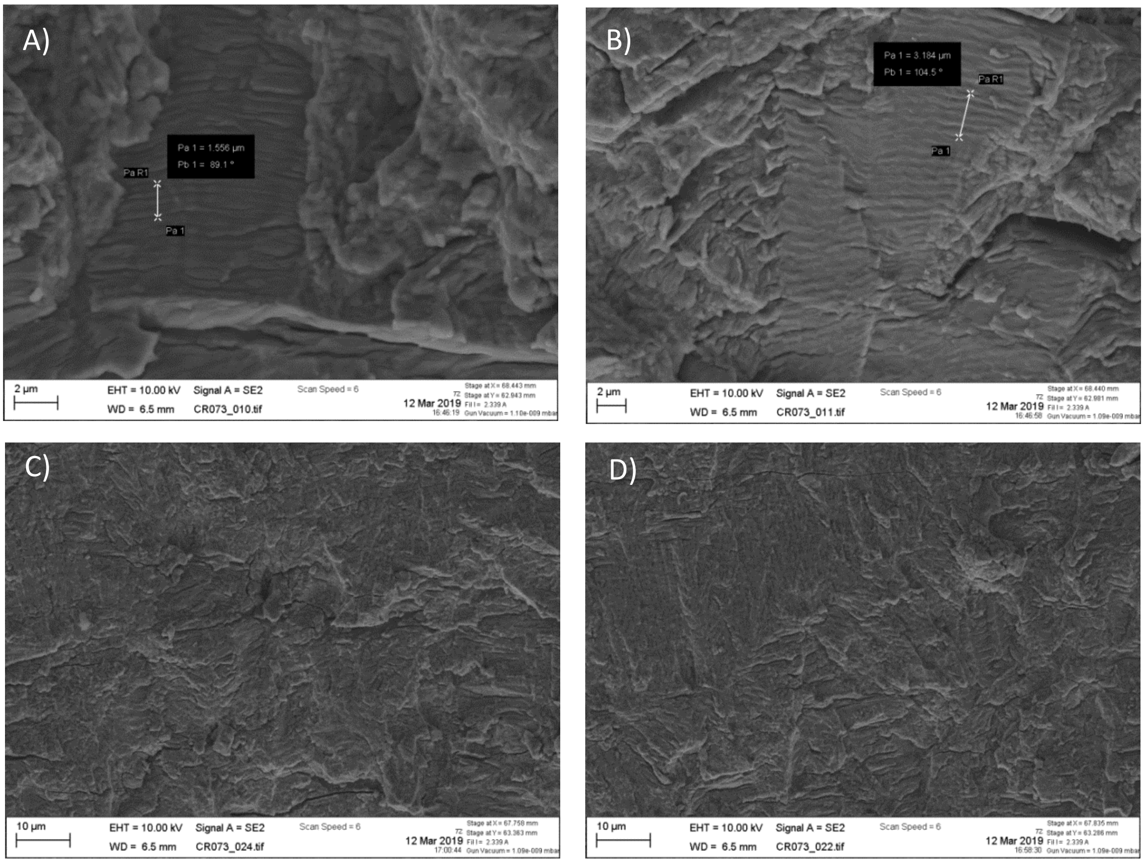

Figure 8.7: SEM images of CR 073, the one hour dwell at 500^{o}C in air at minimum hold. The crack growth direction is straight from bottom to top. A) Shows the first baseline period with striations present, taken at a ΔK of approximately 20 MPa√m. The spacing is measured to be 0.39 µm. B) Shows the first baseline period with striations present, taken at a ΔK of approximately 25 MPa√m with striation spacing measured to be 0.53 µm. Both C) and D) both show dwell crack growth at a ΔK of roughly 28 MPa√m, still transgranular crack growth dominates.

]

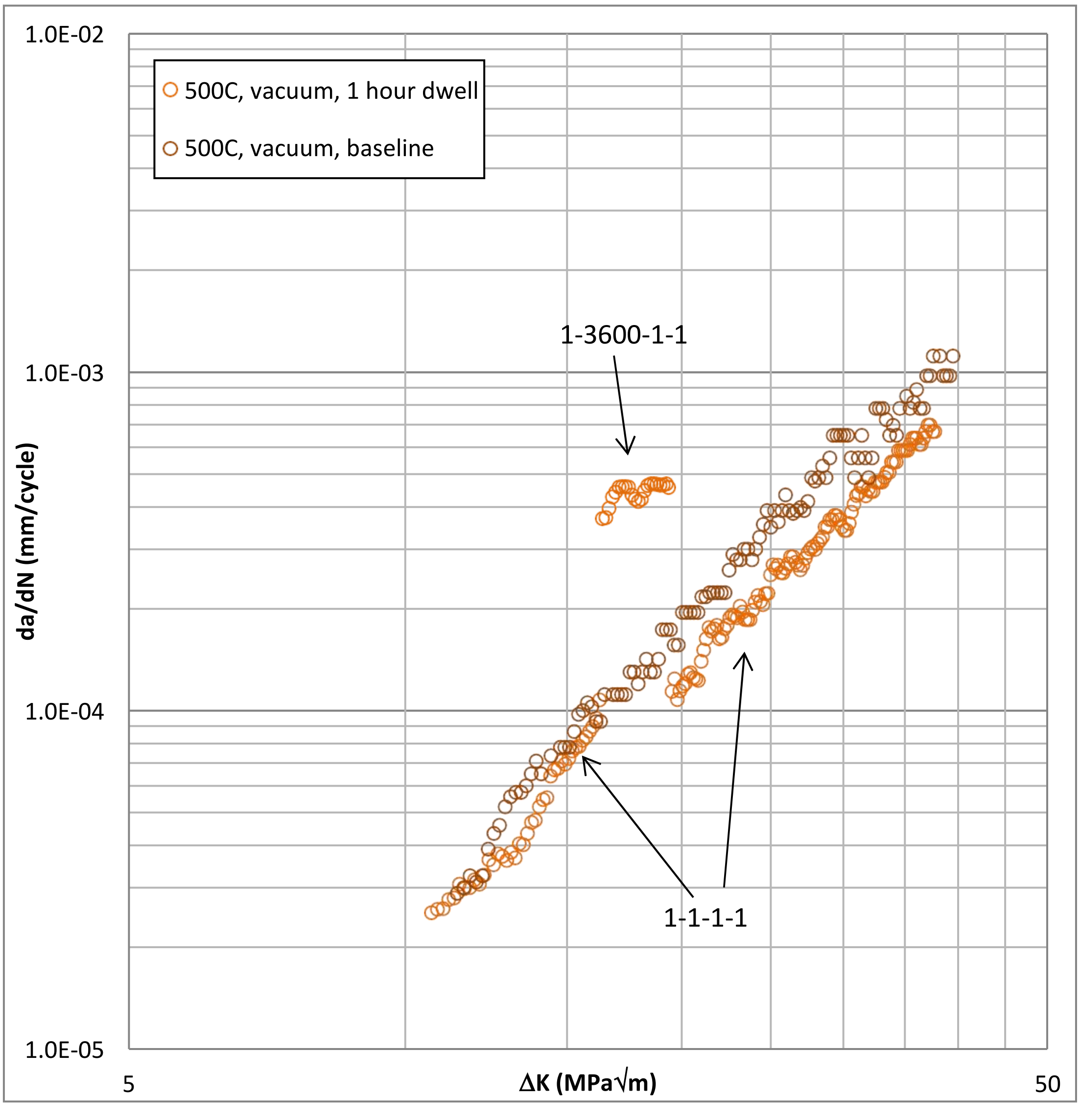

Figure 8.8: Results from CR 071, the one hour maximum hold dwell test in vacuum at 500°C. Showing two periods of baseline crack growth and one period of dwell crack growth. Crack growth from the Paris regime of a test carried out at 500°C under vacuum conditions at a frequency of 0.25 Hz is also displayed showing very similar results to the baseline crack growth data obtained from the dwell test.

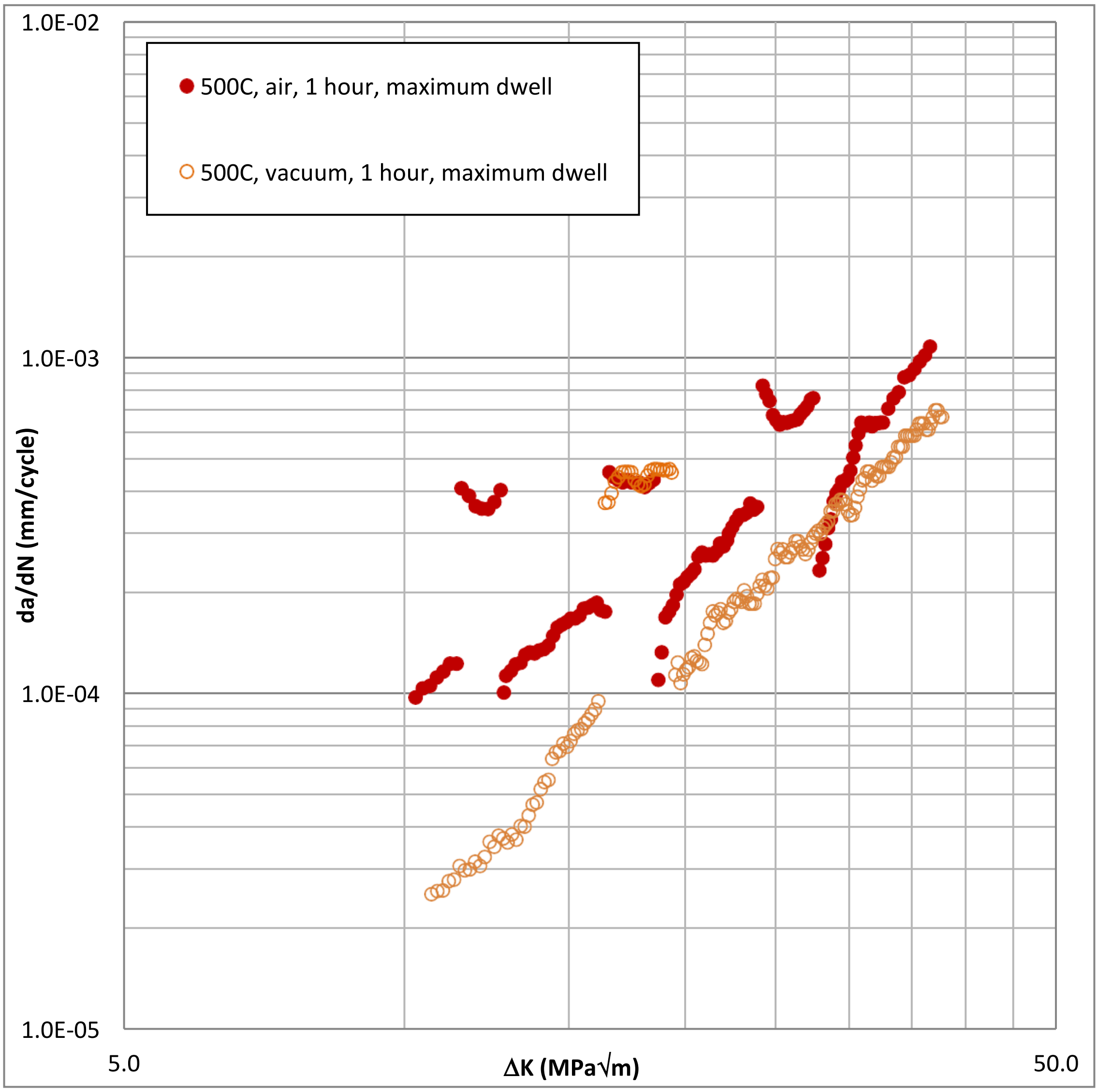

Figure 8.9: Results comparing the one hour maximum hold dwell tests in air and vacuum at 500°C.

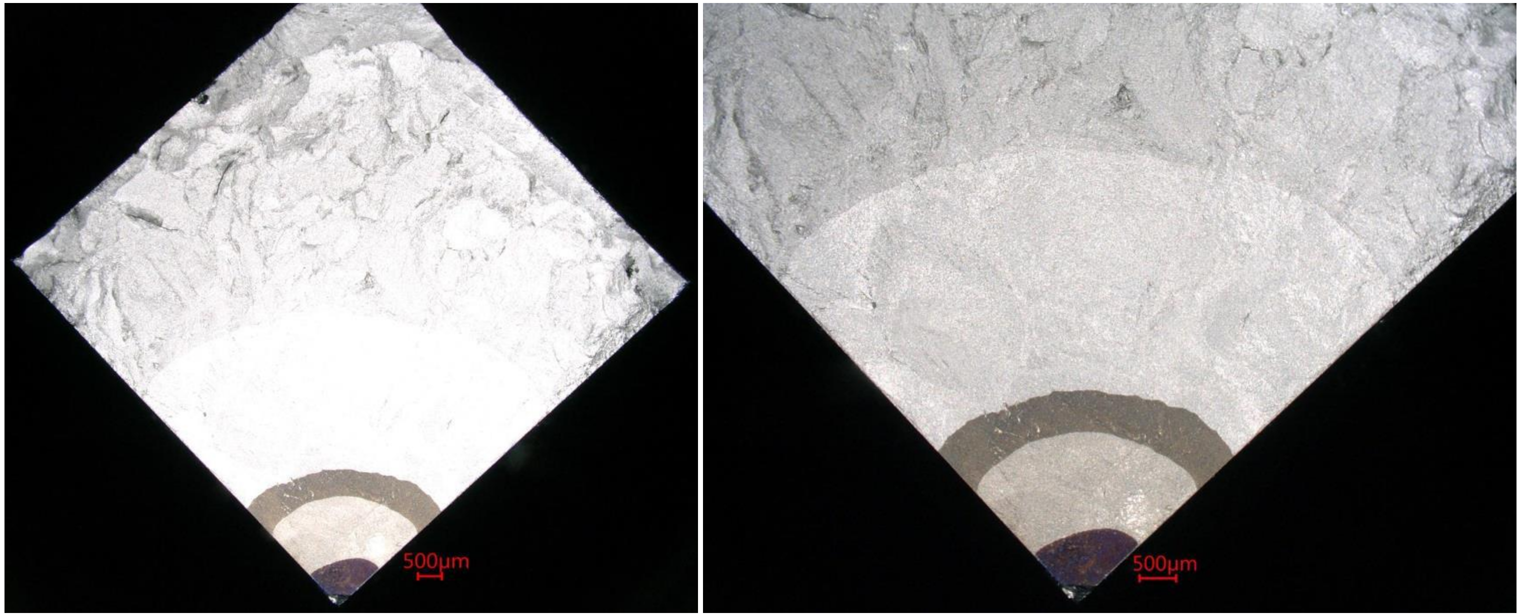

Figure 8.10: Optical Image of CR 071, the one hour dwell at 500°C in vacuum at maximum hold. Showing uniform crack growth in all directions producing a clear quarter circle.

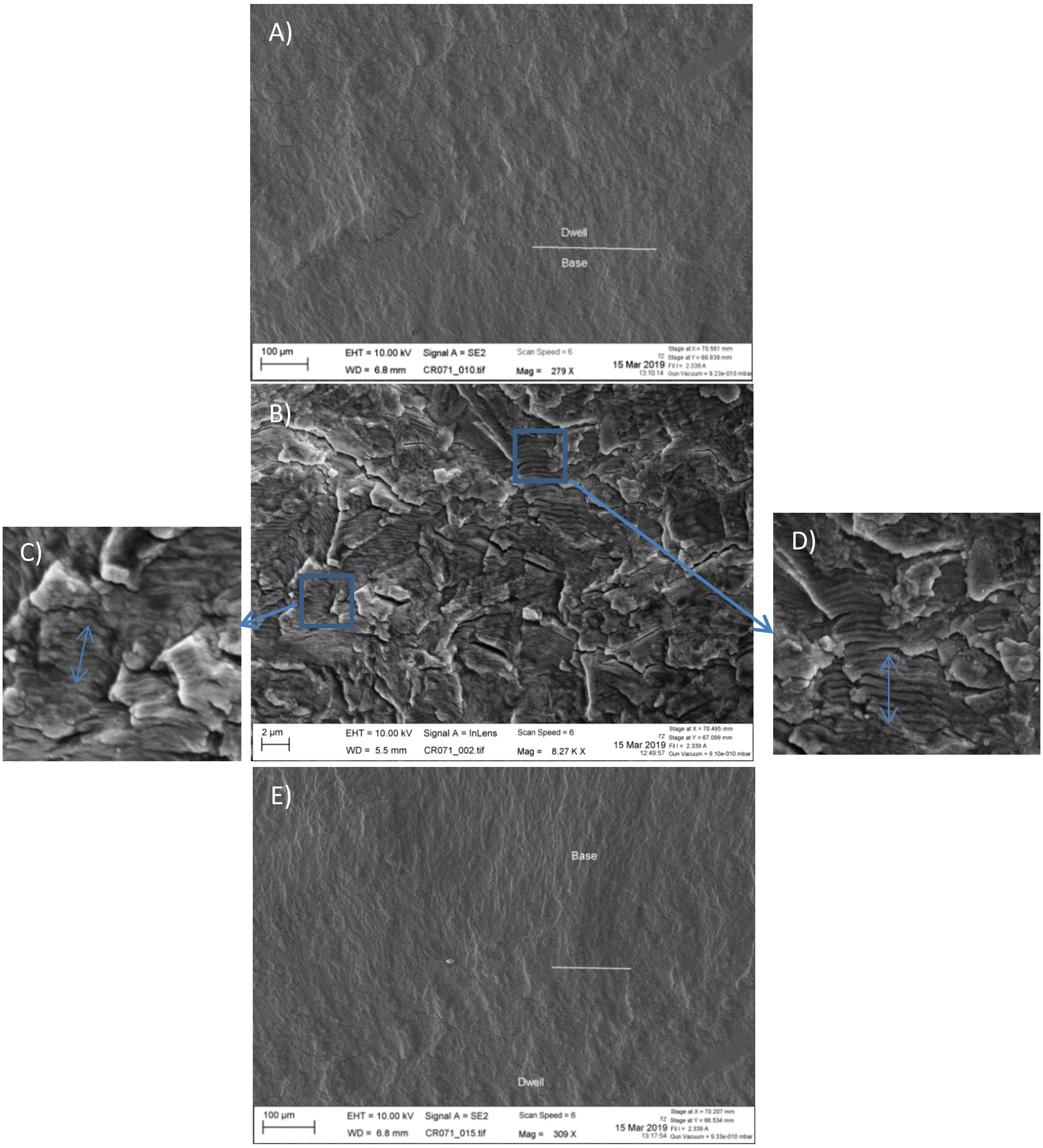

Figure 8.11: SEM images of the one hour dwell at 500^{o}C in vacuum at maximum hold. The crack growth direction is straight from bottom to top. A) Shows the transition from the first baseline crack growth period to the first dwell crack growth period. All crack growth remains transgranular. B) Shows a magnified image of the transition period from baseline to dwell loading with striations on the fracture surface highlighted. C) Shows striation spacing from the baseline crack growth period at a ΔK of 16 MPa√m. Straiation spacing was measured to be approximately 0.16 µm. D) Shows the striation spacing from the dwell crack growth period at a ΔK of 17 MPa√m. Striation spacing was measured to be approximately 0.40 µm. E) Shows the transition from dwell loading to the final baseline loading. The crack growth mechanism remains transgranular.

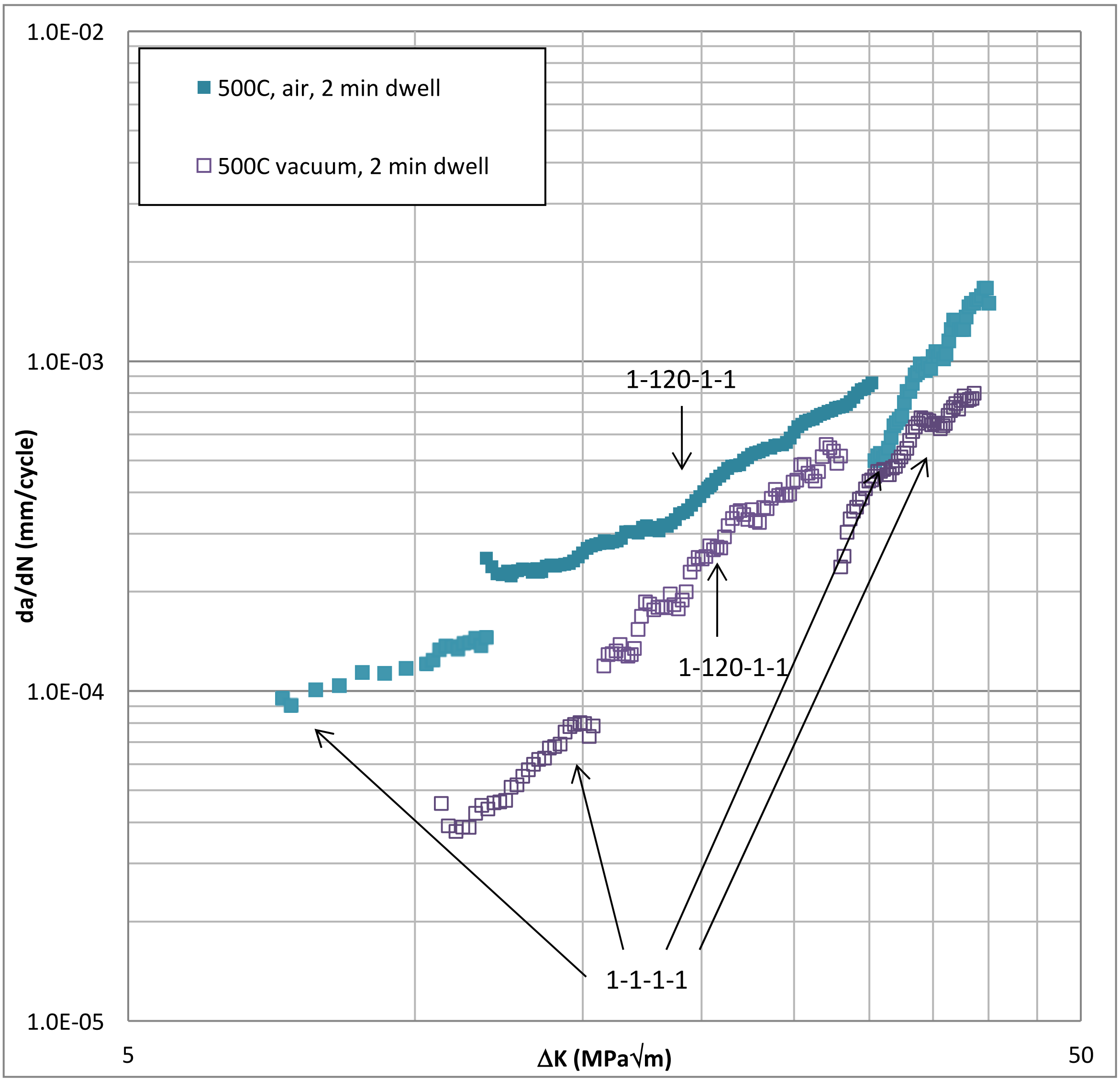

Figure 8.12: Results comparing the two minute maximum hold dwell tests in air and vacuum at 500°C.

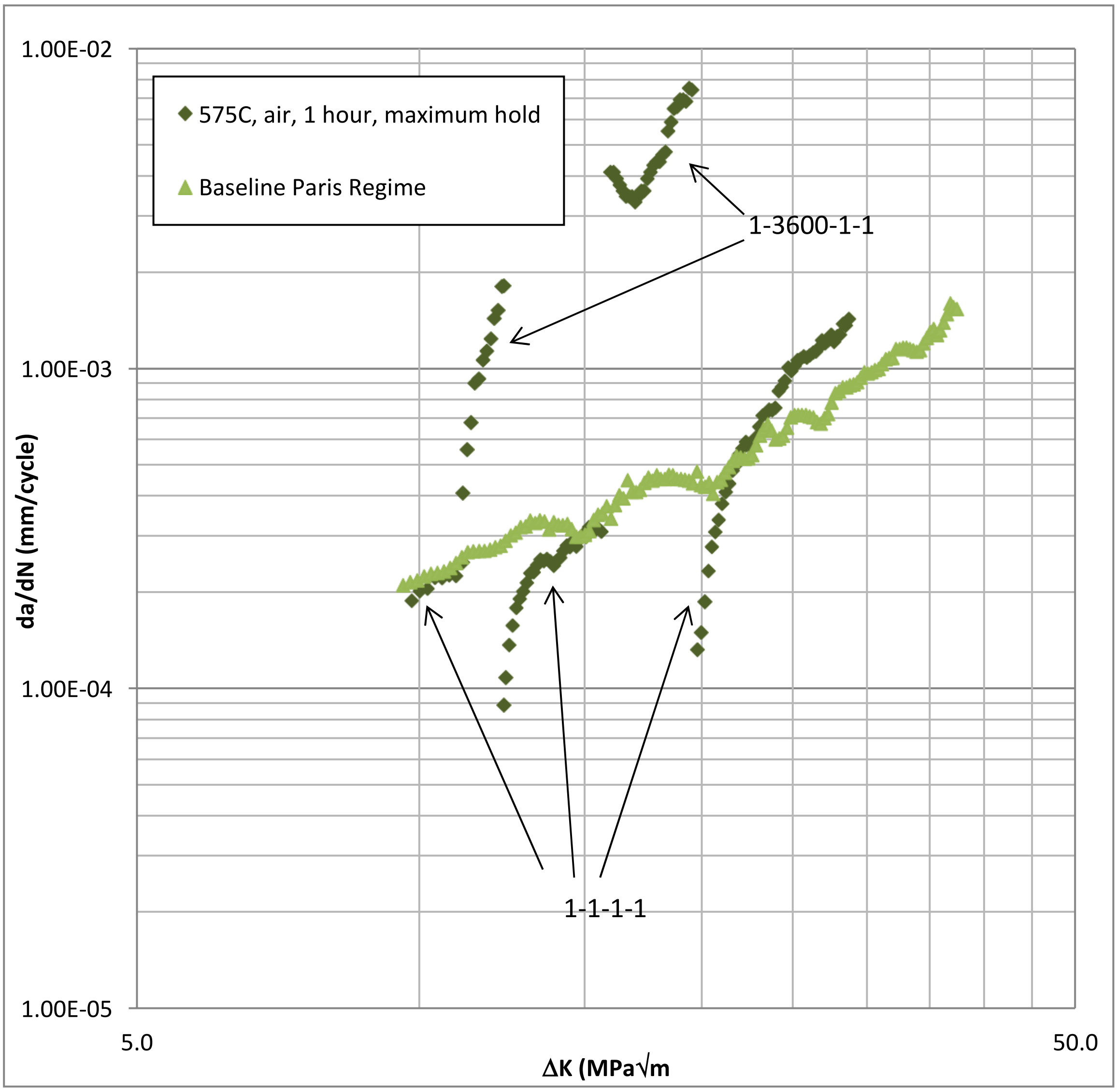

Figure 8.13: Results from CX 030, the one hour maximum hold dwell test in air at 575°C. Showing three periods of baseline crack growth and two periods of dwell crack growth. Data from a 575°C baseline Paris regime test is also included to show the similar rates obtained.

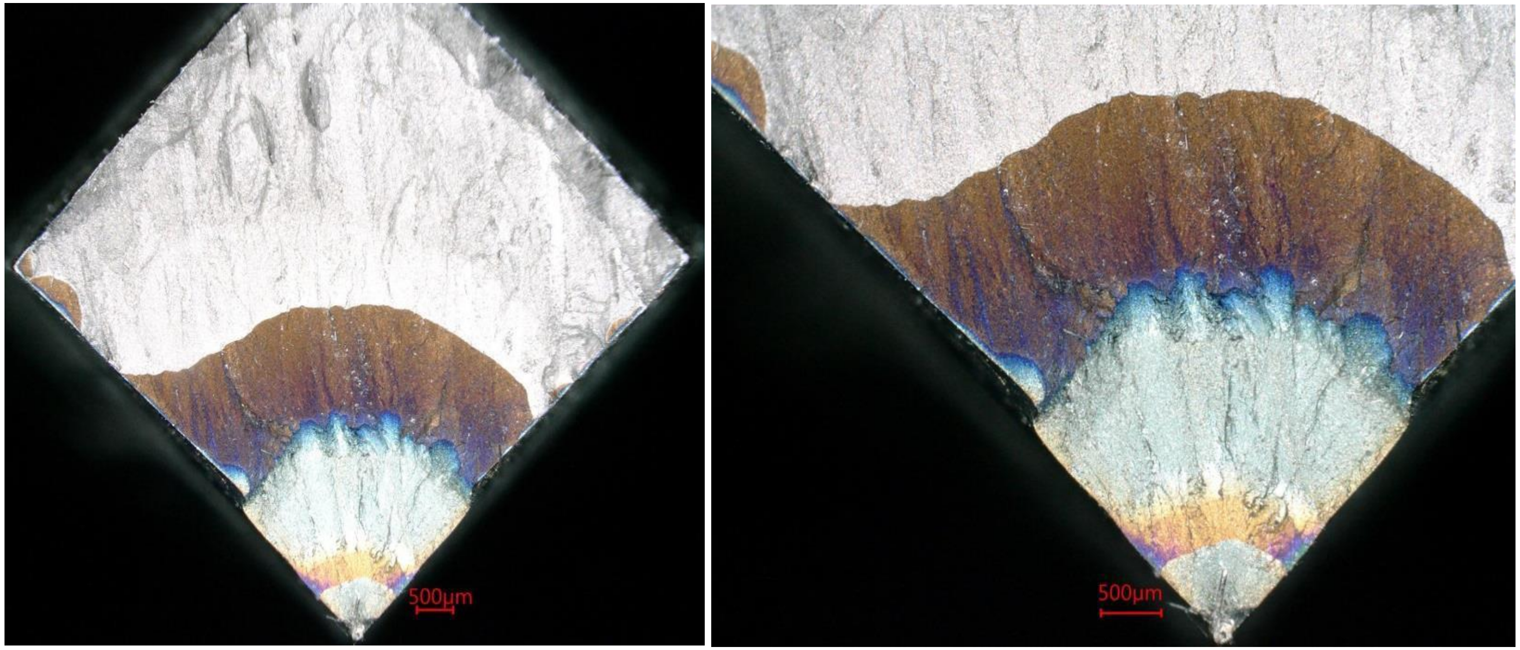

Figure 8.14: Optical Image of CX 030, the one hour dwell at 575^{o}C in air at maximum hold. Some anisotropic crack growth is seen on the fracture surface as well as secondary sights of oxidation on the surface, away from the primary crack.

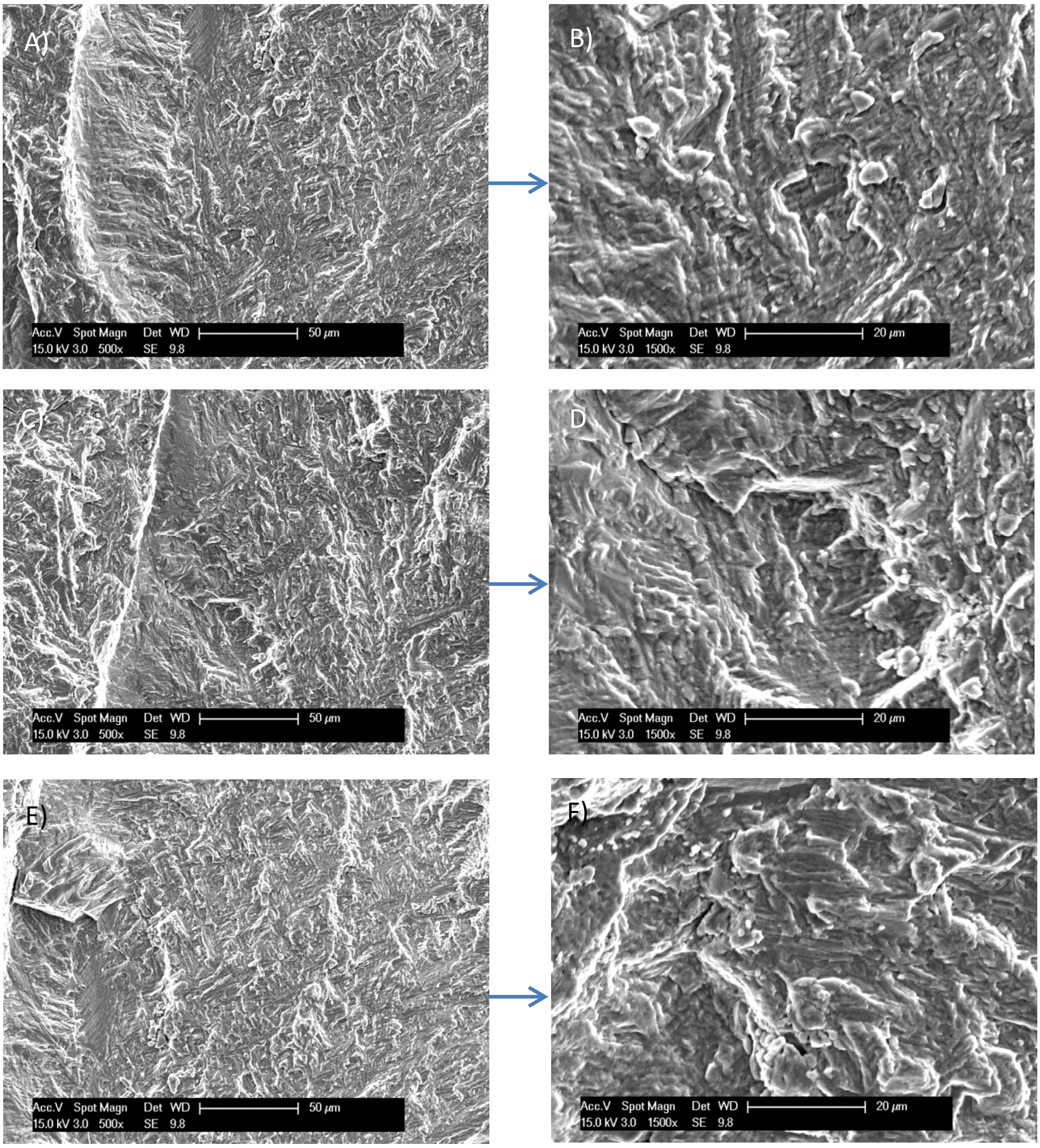

Figure 8.15: SEM images of CX 030, the one hour dwell at 575^{o}C in air at maximum hold. The crack growth direction is straight from bottom to top. Image A + B) Show the first baseline crack growth period with transgranular crack growth. C+D) Show the first dwell period, despite the much accelerated rate the mechanism remains transgranular. E+F) Show the final dwell period, again with a transgranular crack growth mechanism.

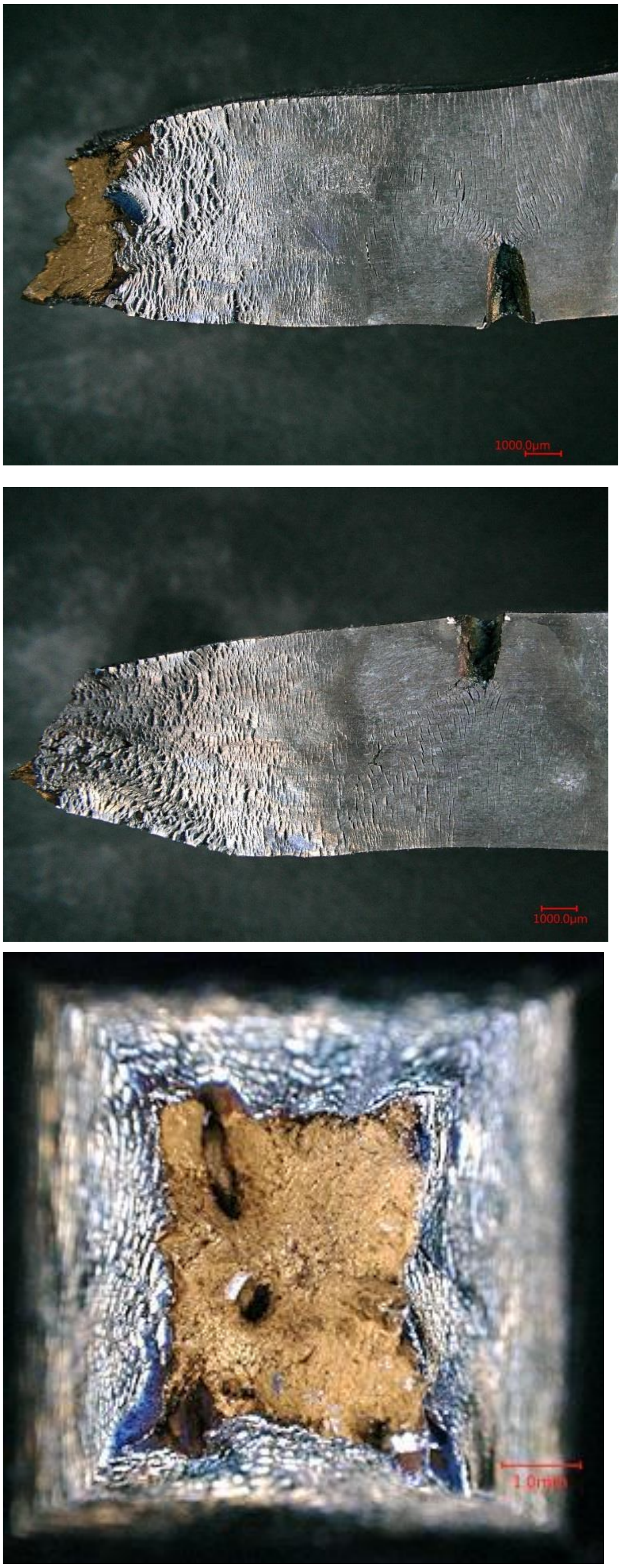

Figure 8.16: Optical image of the 575^{o}C one hour dwell test that failed prematurely away from the notch. Lots of secondary cracking is visible on the specimen surface

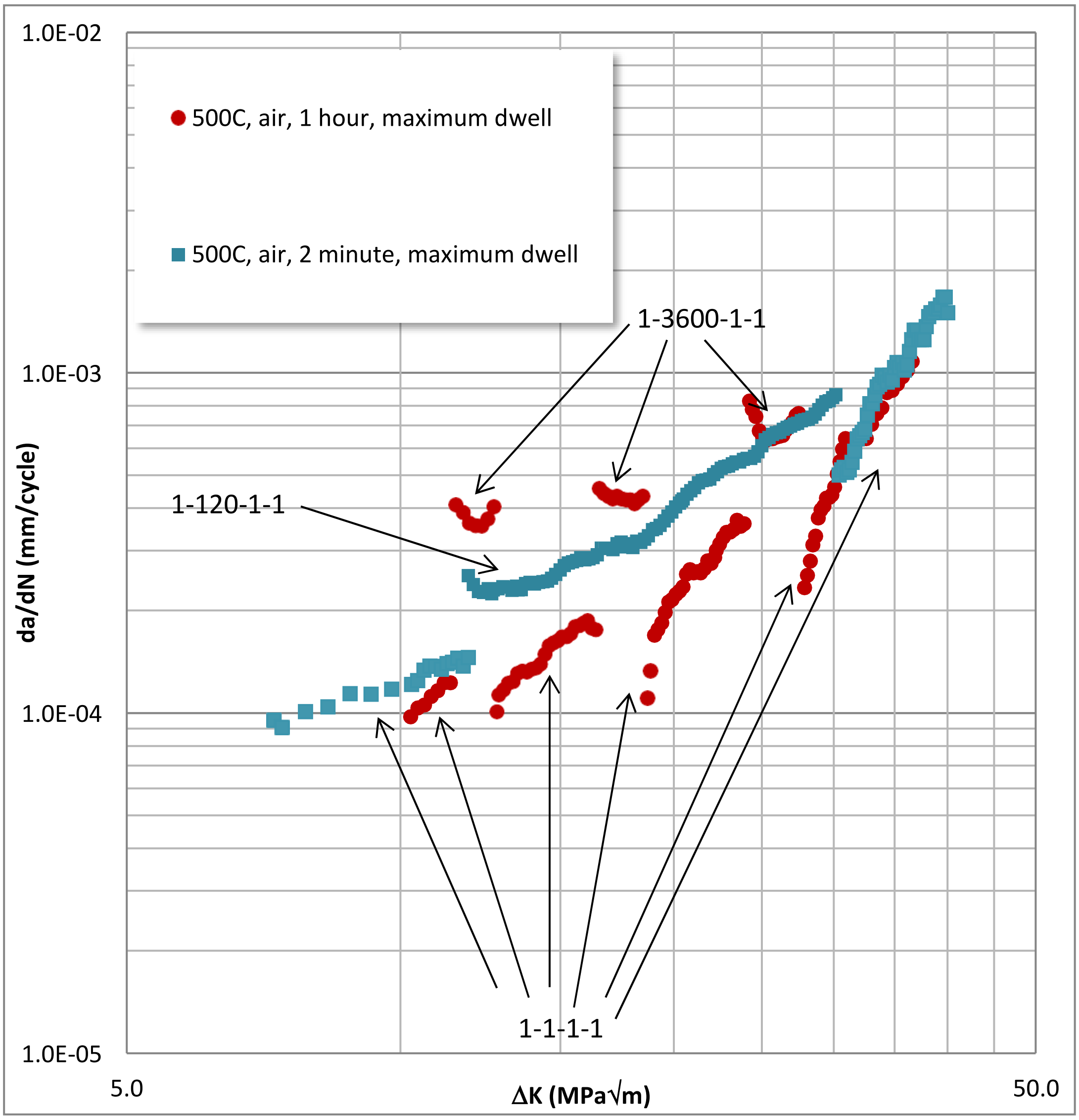

Figure 8.17: Results comparing the two minute dwell test and one hour dwell test at 500°C in air.

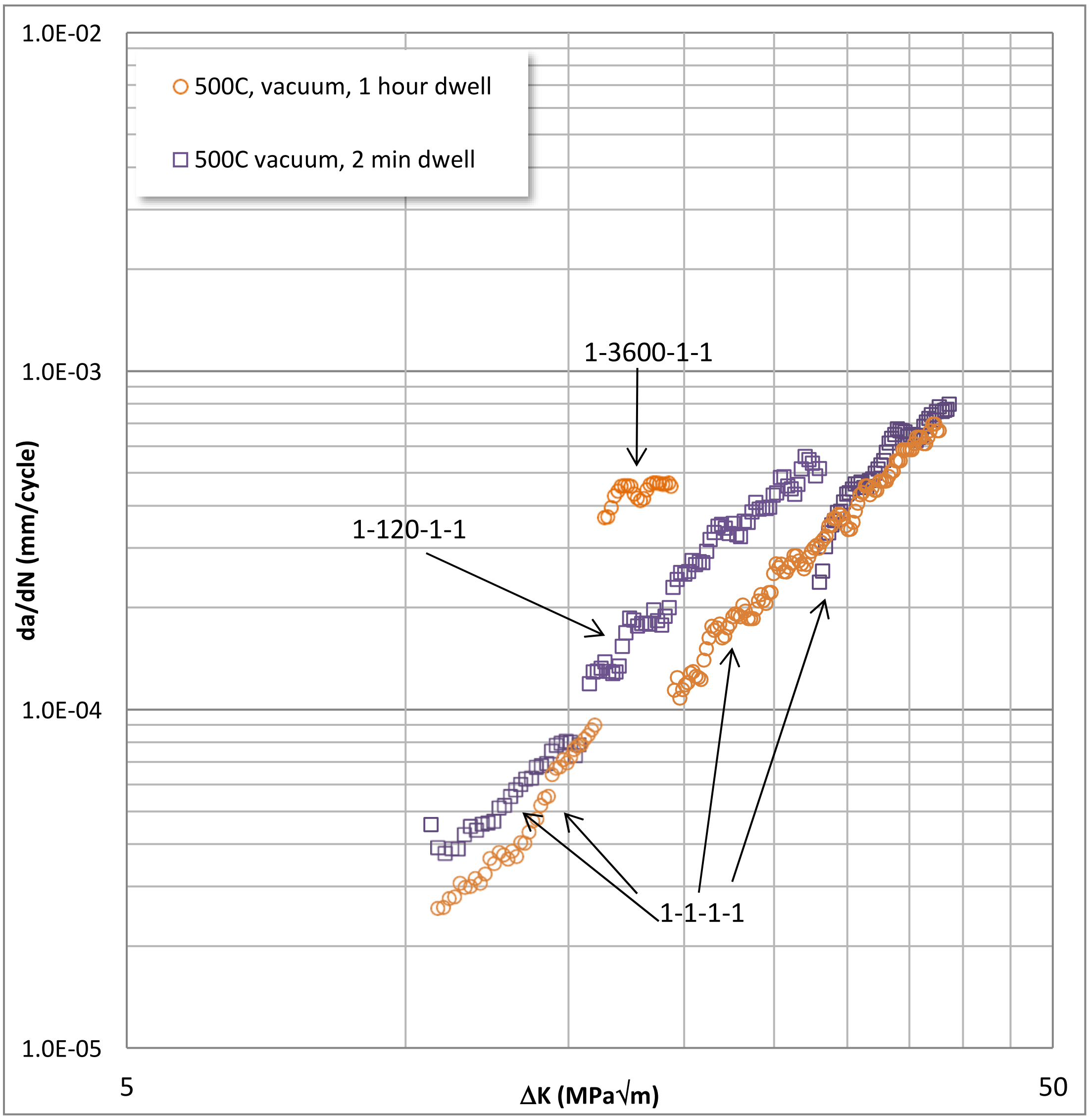

Figure 8.18: Results comparing the two minute dwell test and one hour dwell test at 500°C under vacuum conditions.

Chapter 9 – Discussion

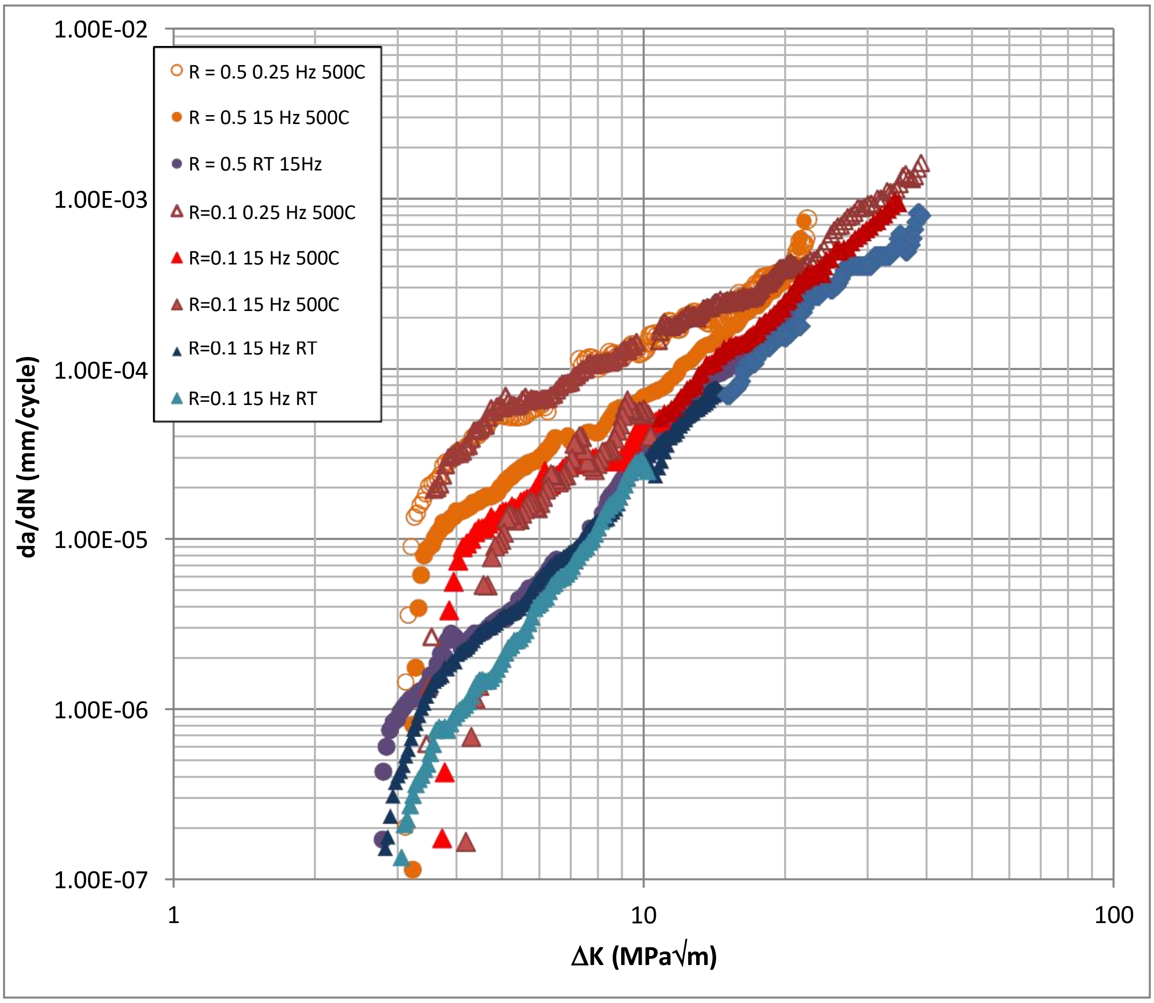

Figure 9.1: Experimentally obtained results for threshold and Paris regimes.

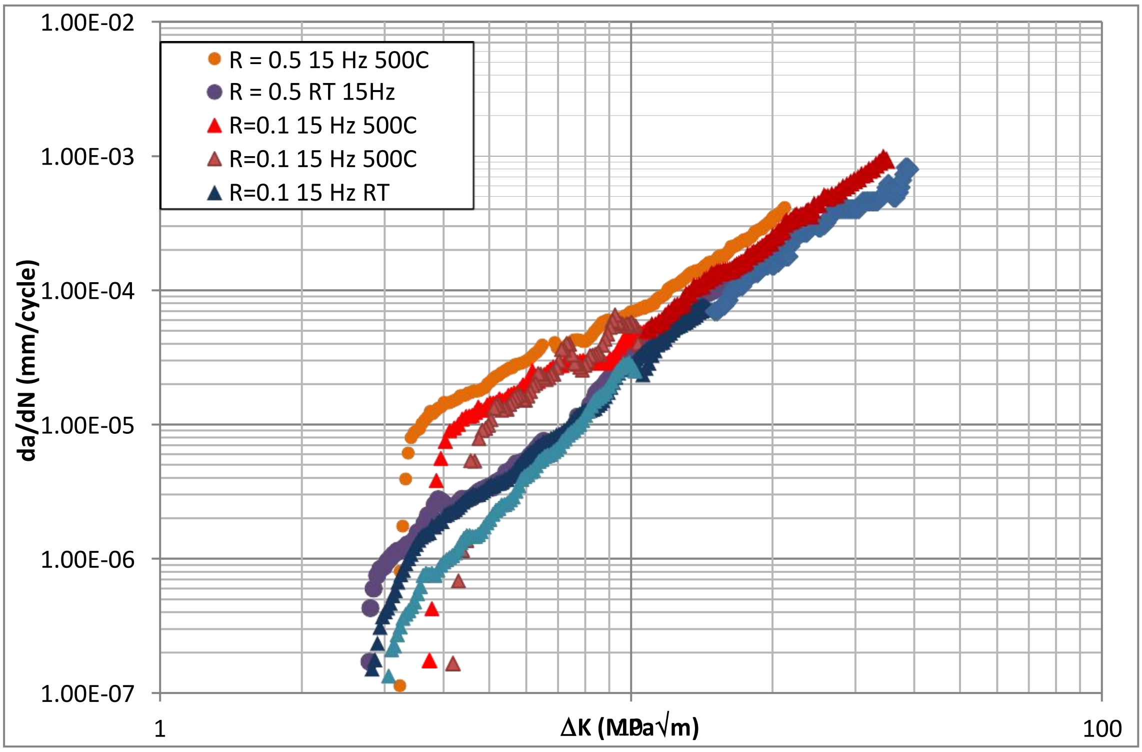

Figure 9.2: Results for threshold and Paris regimes for tests carried out at 15 Hz at R ratios of 0.1 and 0.5.

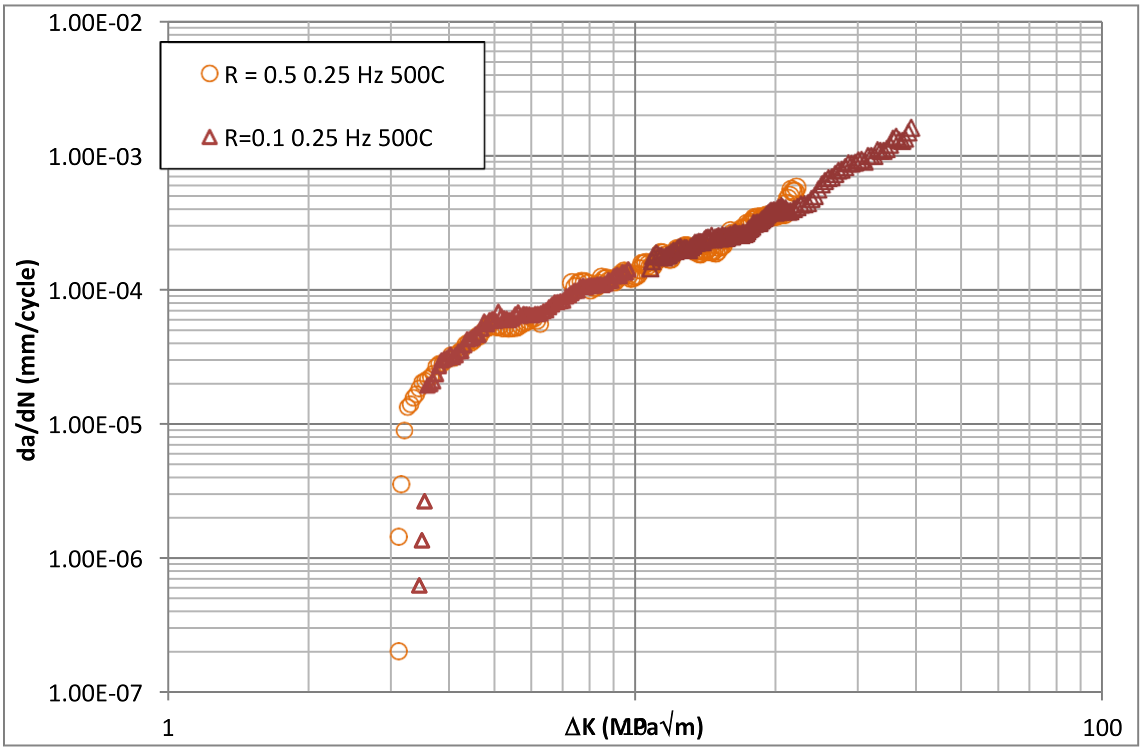

Figure 9.3: Results for threshold and Paris regimes for tests carried out at 0.25 Hz at R ratios of 0.1 and 0.5.

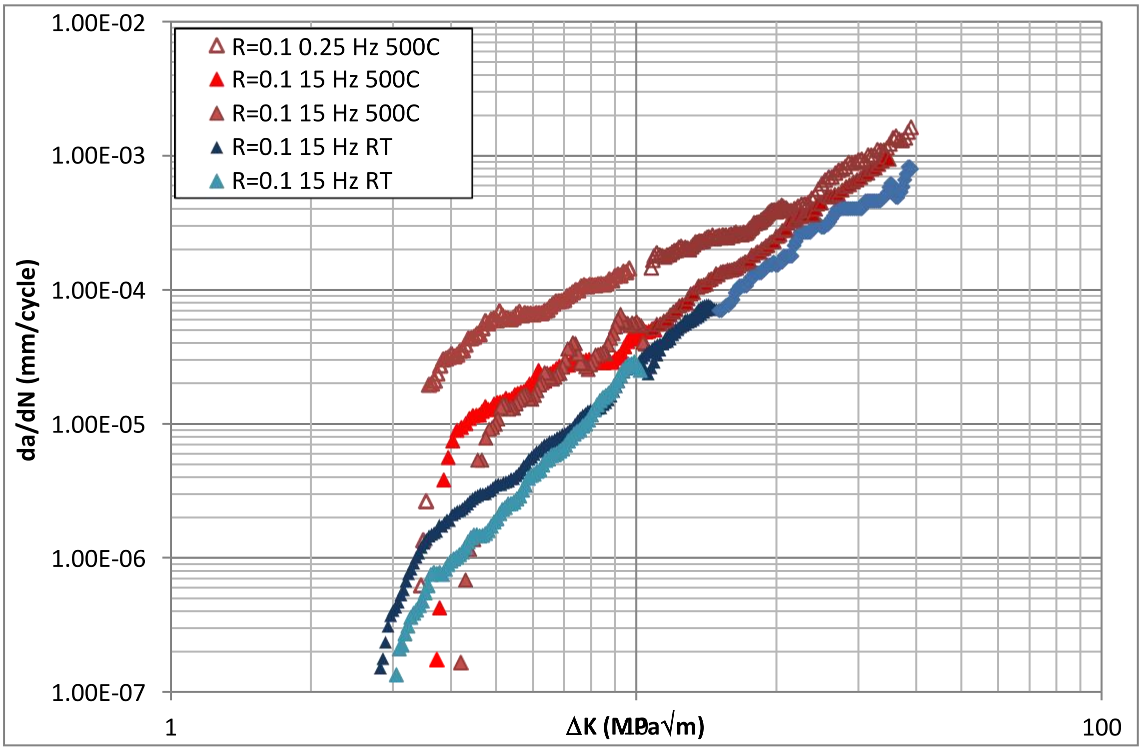

Figure 9.4: Results for threshold and Paris regimes for tests carried out at 15 and 0.25 Hz at an R ratio of 0.1.

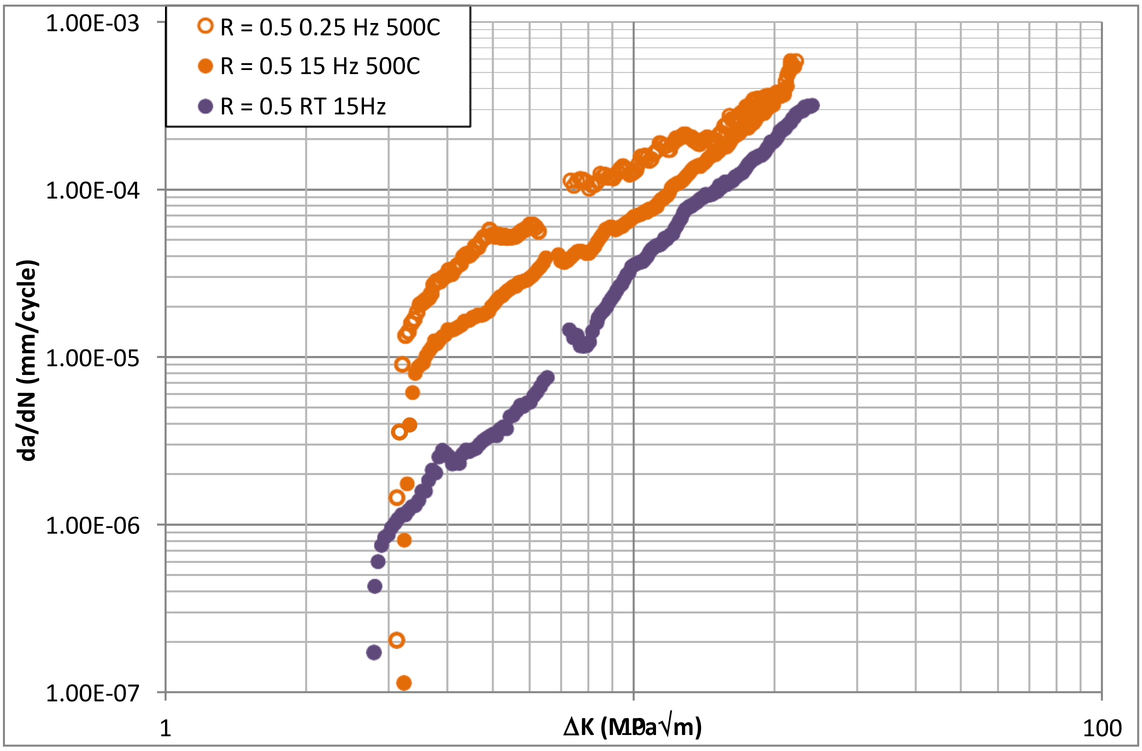

Figure 9.5: Results for threshold and Paris regimes for tests carried out at 15 and 0.25 Hz at an R ratio of 0.1.

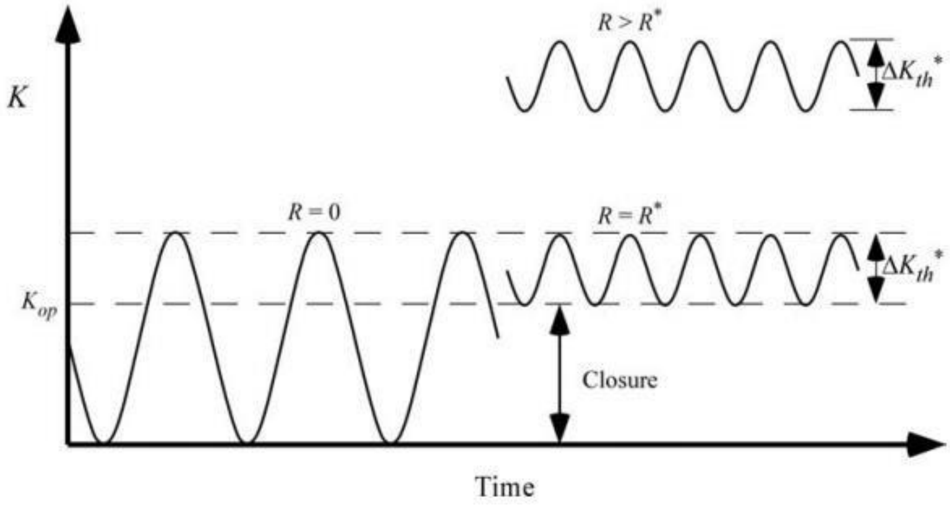

Figure 9.6: Schematic illustration showing the relationship between crack closure behaviour and R ratio [17].

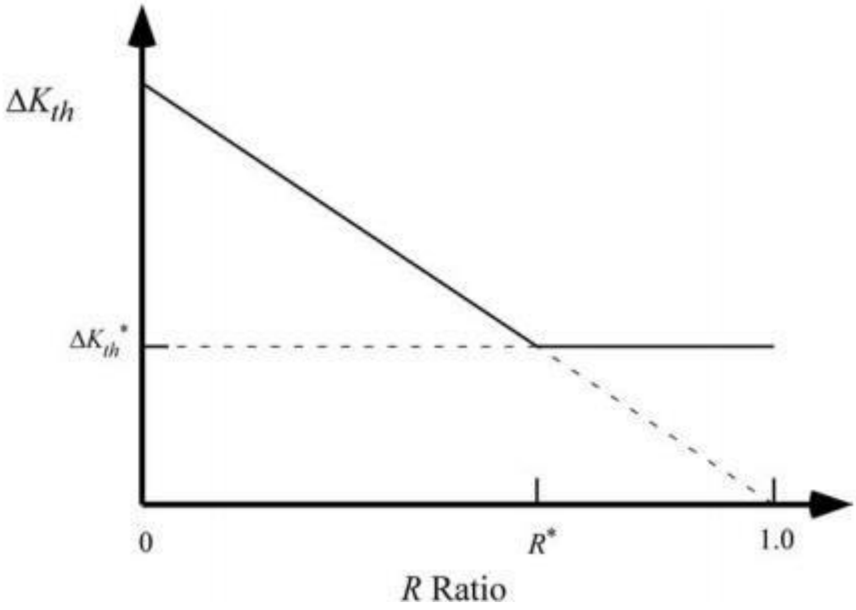

Figure 9.7: Schematic illustration of the effect of R ratio on ΔKth. Showing R ratio only effecting ΔKth above a certain value [17].

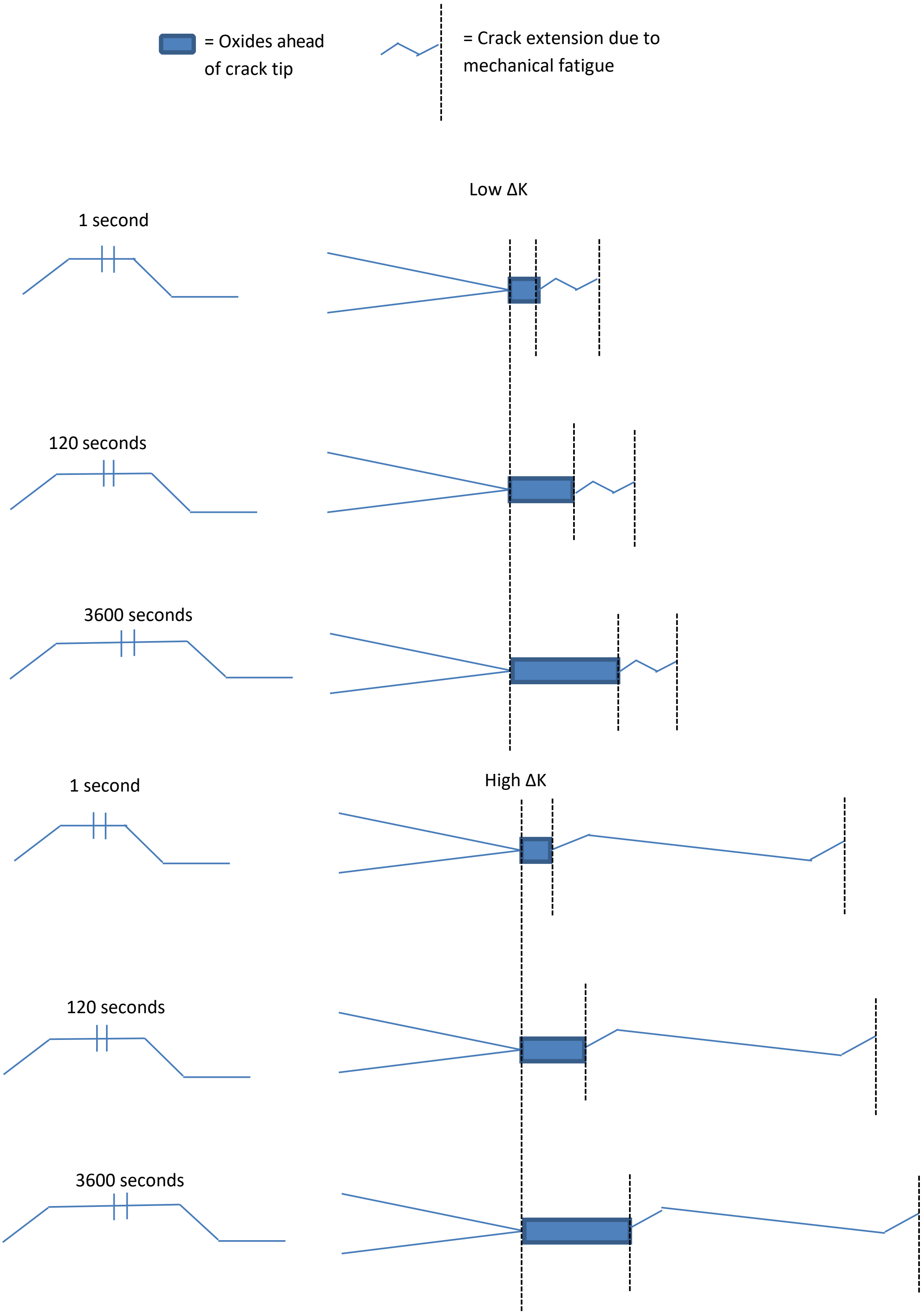

Figure 9.8: Model proposed for crack growth at two ΔK values. At low ΔK, oxides make up a large proportion of overall crack extension. At high ΔK, oxides cracking ahead of the crack tip have less of an impact on overall crack growth as effects of mechanical fatigue are increased.

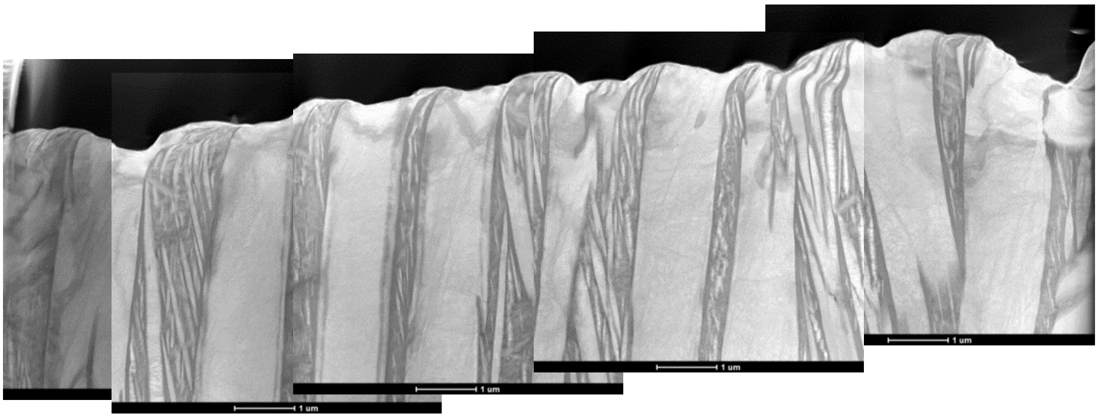

Figure 9.9: TEM image of the 500^{o}C, 0.25 Hz test under vacuum. A smooth crack profile with no secondary cracking is observed. Slight dips are visible at the top of each primary α lath.

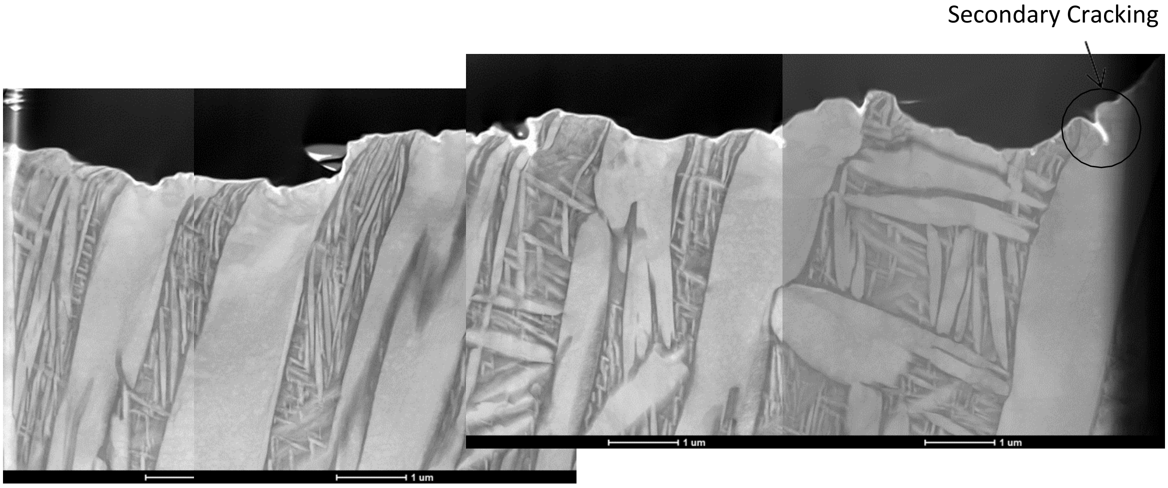

Figure 9.10: TEM image of the 500C, 0.25 Hz test in air. A rough crack profile with secondary cracking of primary α laths is observed.

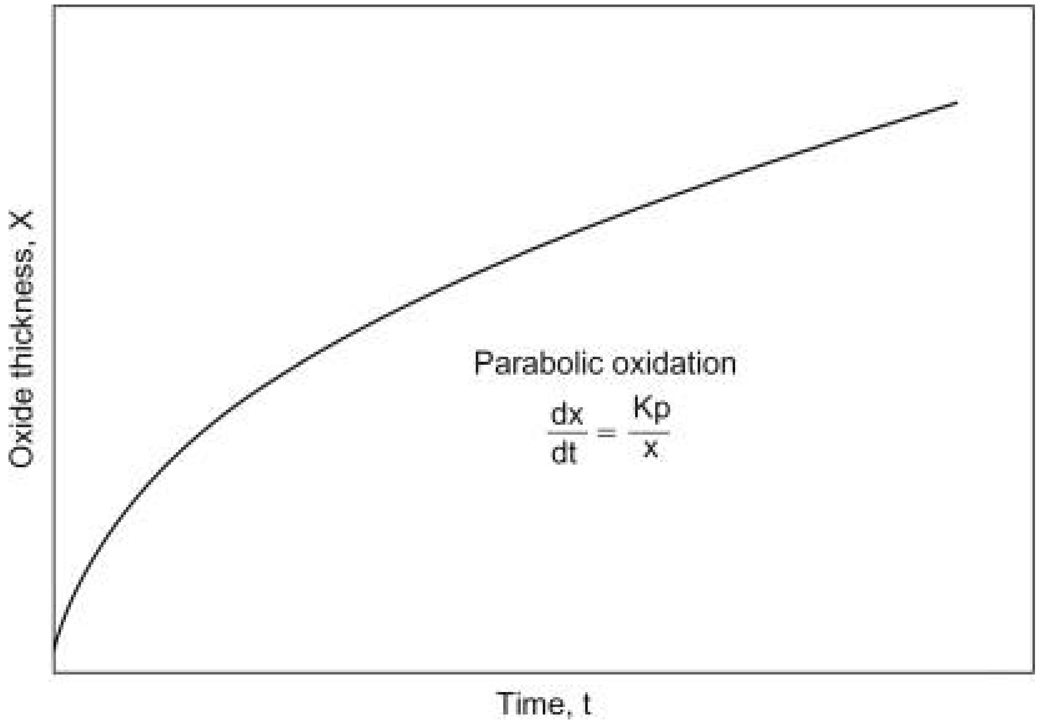

Figure 9.11: The kinetics of parabolic oxidation [18].

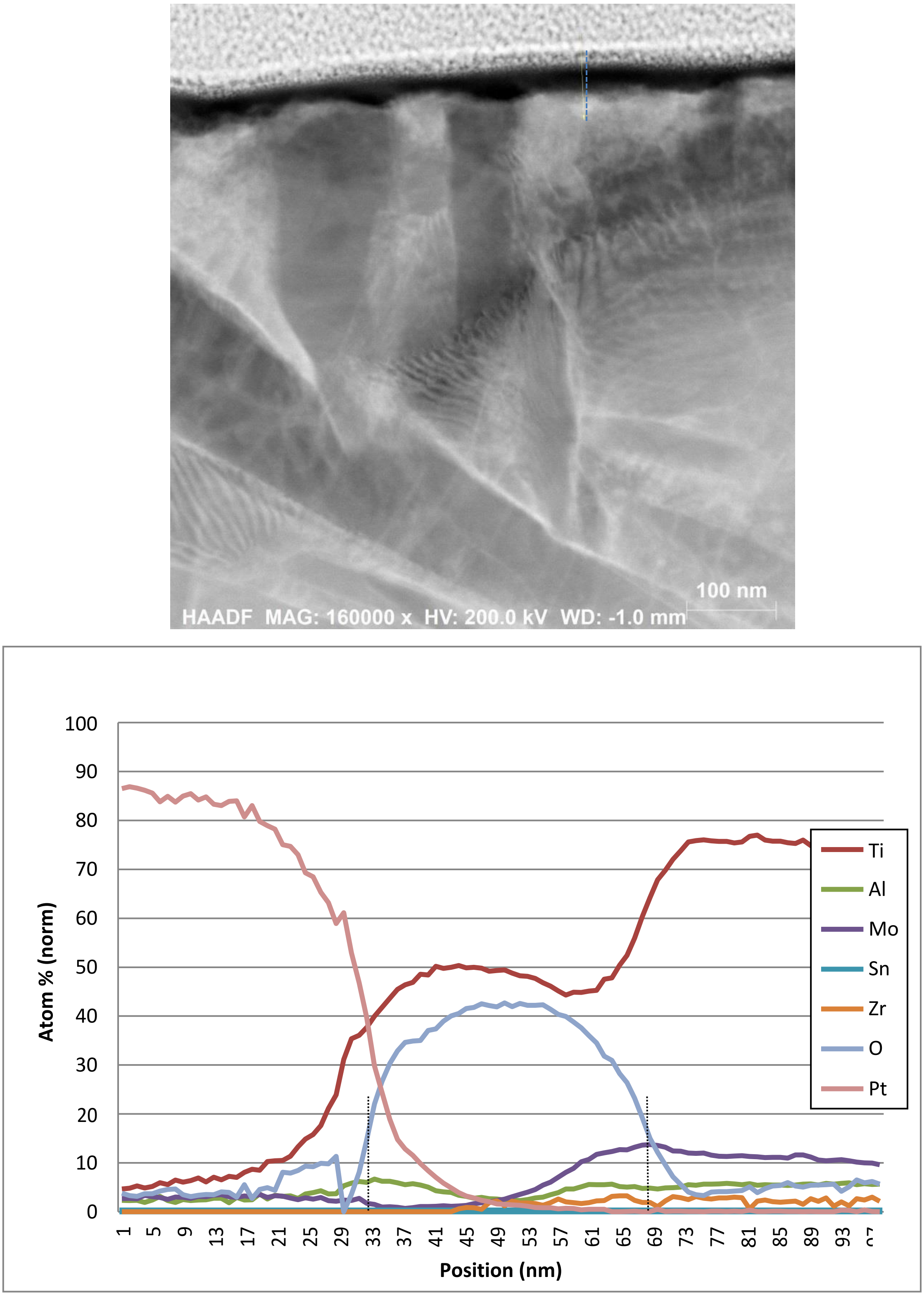

Figure 9.12: EDS line scan showing oxide thickness for the 1 hour, 500°C sample in air. An oxide thickness of approximately 37 nm is measured (and shown on the linescan).

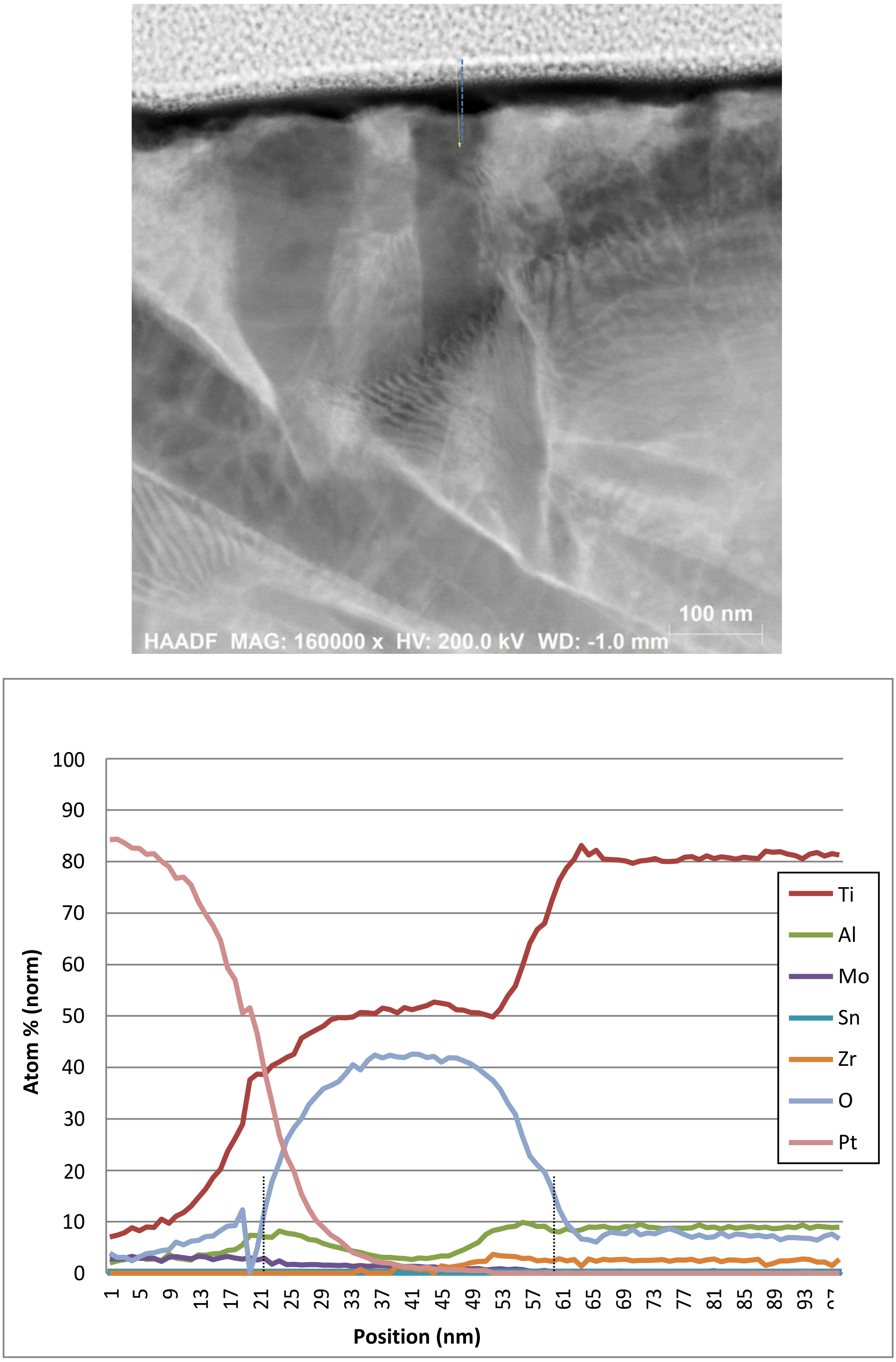

Figure 9.13: EDS line scan showing oxide thickness for the 1 hour, 500°C sample in air. An oxide thickness of approximately 40 nm is measured (and shown in the line scan).

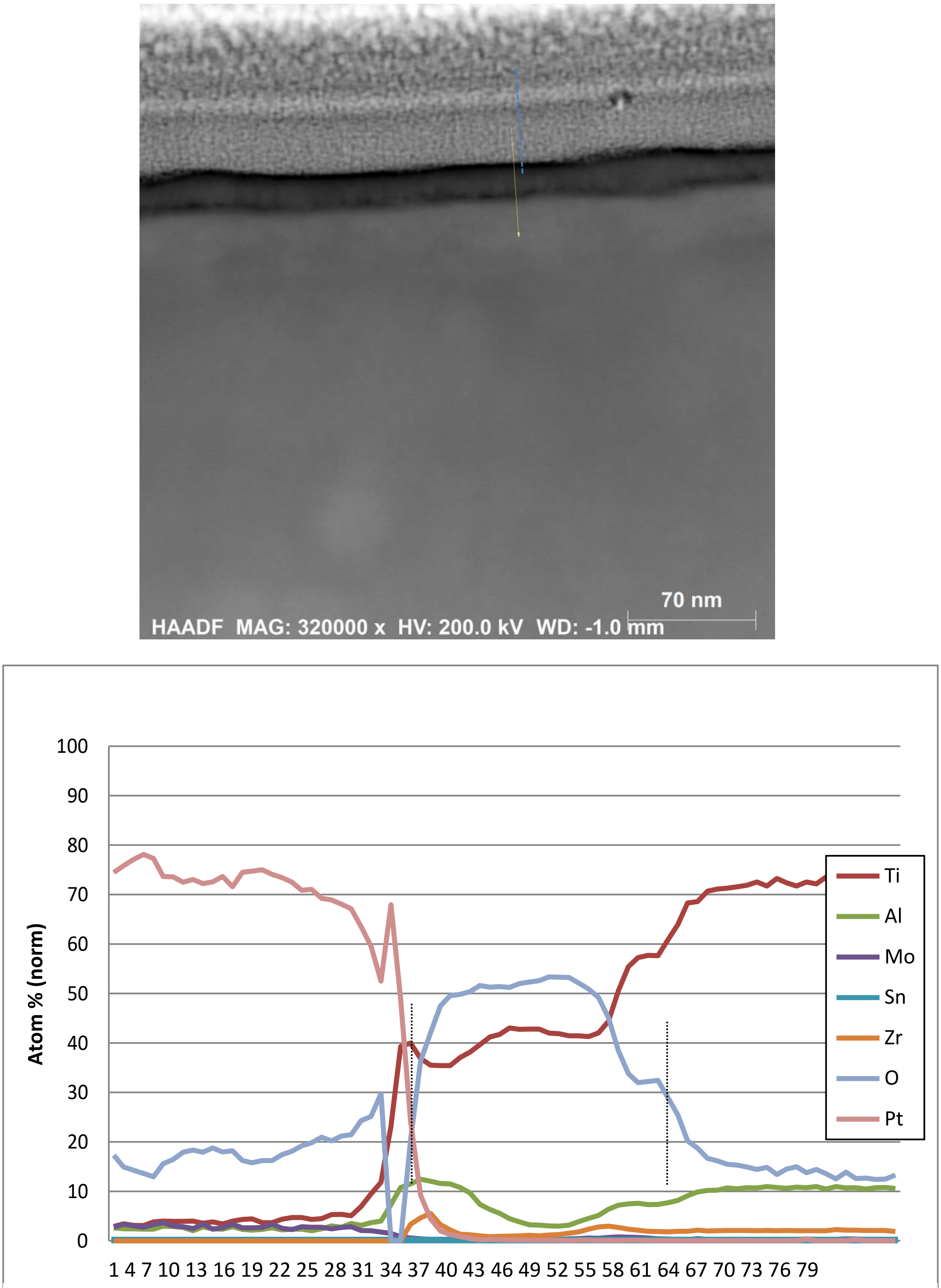

Figure 9.14: EDS line scan showing oxide thickness for the 2 minute, 500°C sample in air. An oxide thickness of approximately 25 nm is measured (and shown in the linescan).

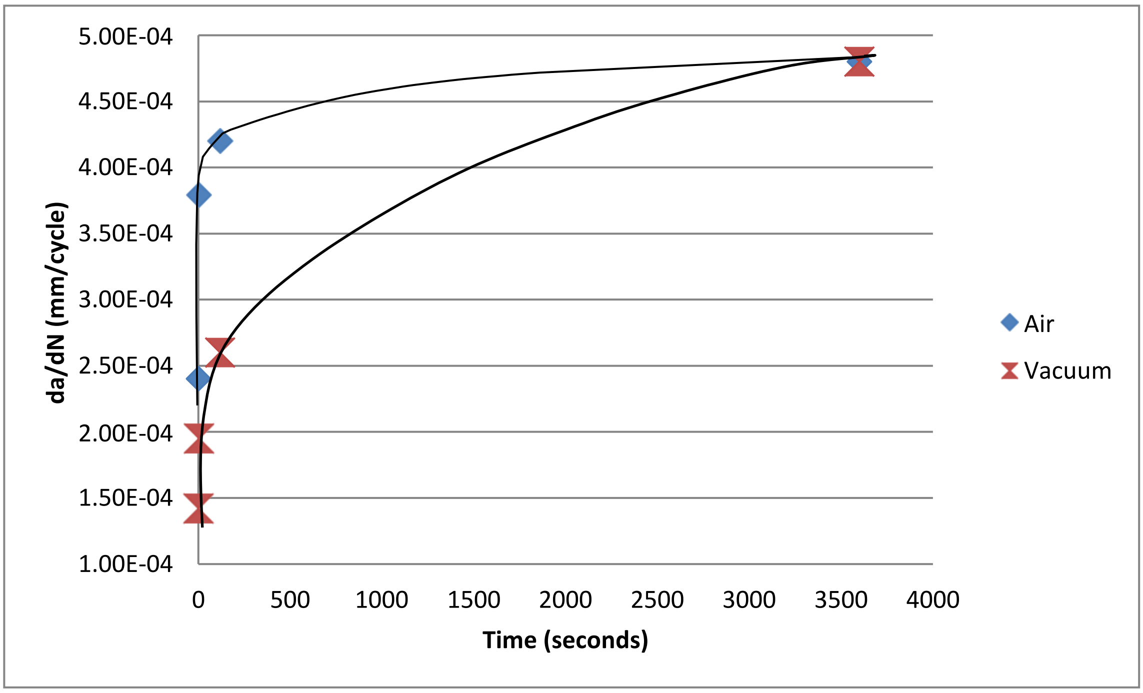

Figure 9.15: Crack growth rates at different times for air and vacuum conditions at a ΔK of 20 MPa√m. As time increases, crack growth rates become similar thought to be due to time spent growing oxides ahead of the crack tip.

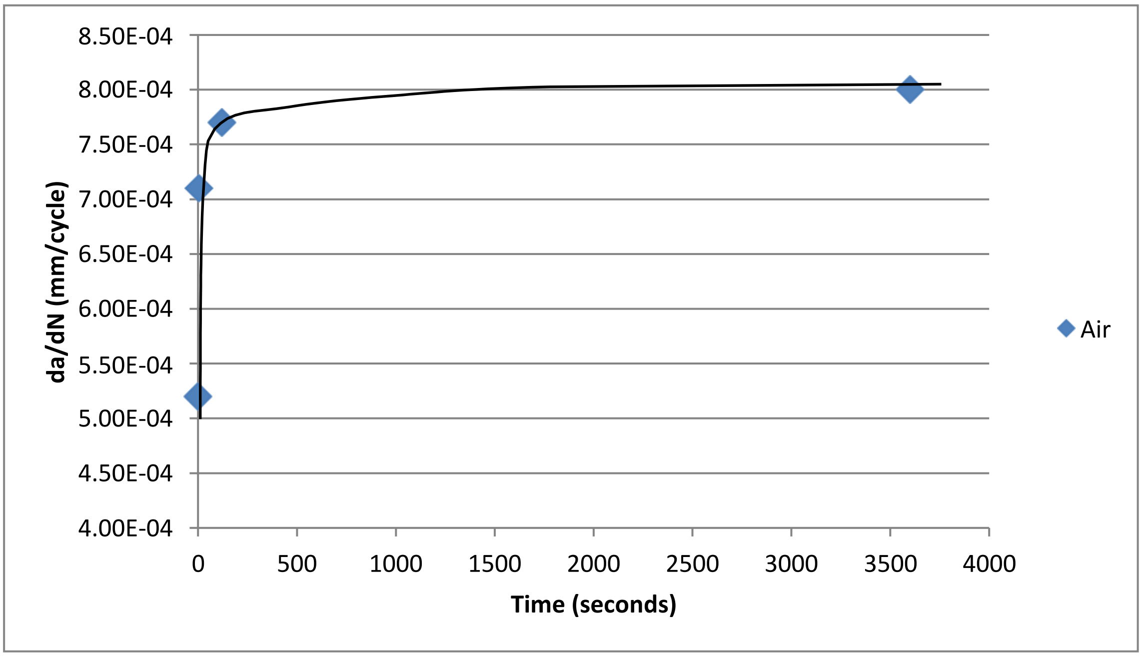

Figure 9.16: Crack growth rates at different frequencies for air conditions at a ΔK of 28 MPa√m. The difference in crack growth rates for 120 and 3600 seconds has decreased at this ΔK compared to a ΔK of 20 MPa√m.

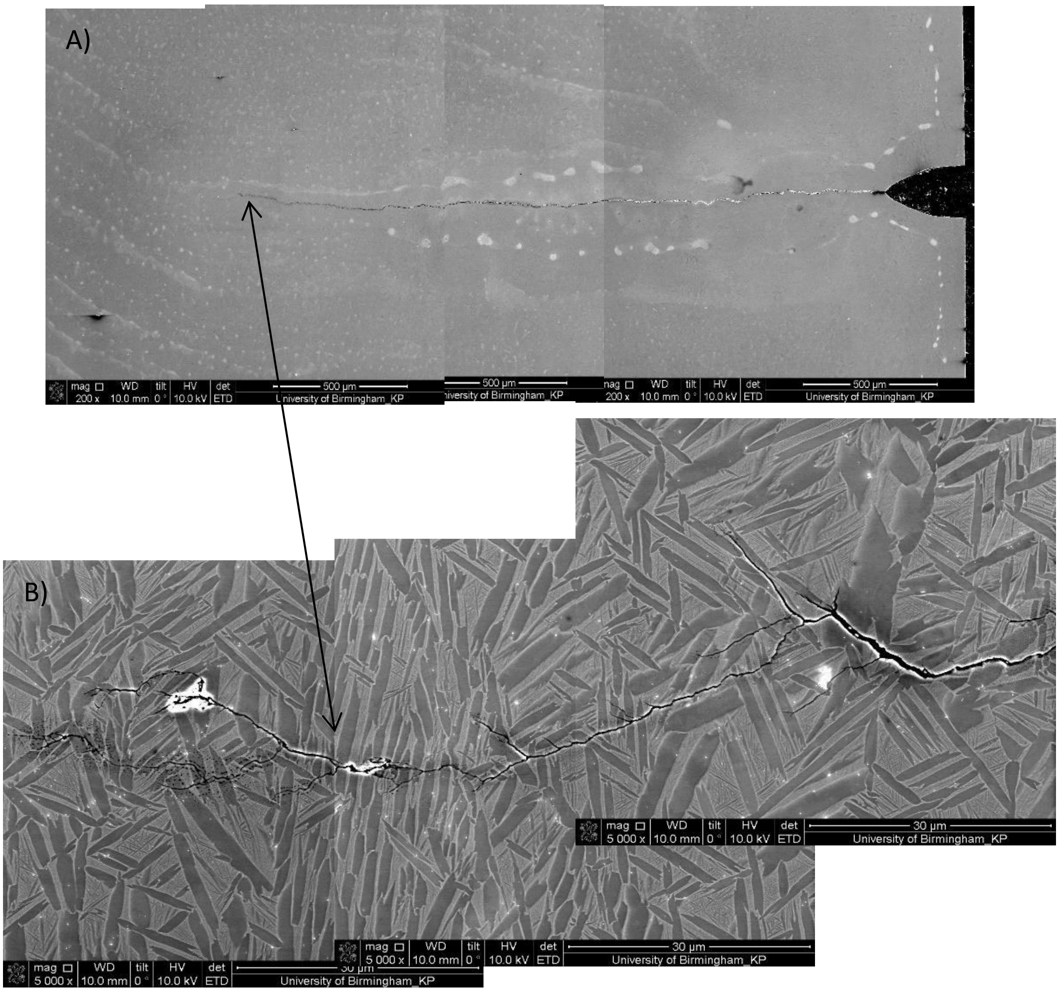

Figure 9.17: SEM images taken of the interrupted test in air at 500^{o}C. A) Shows an overview of the entire crack. B) Shows a magnified image the end of the crack showing secondary cracking and branching along the crack.

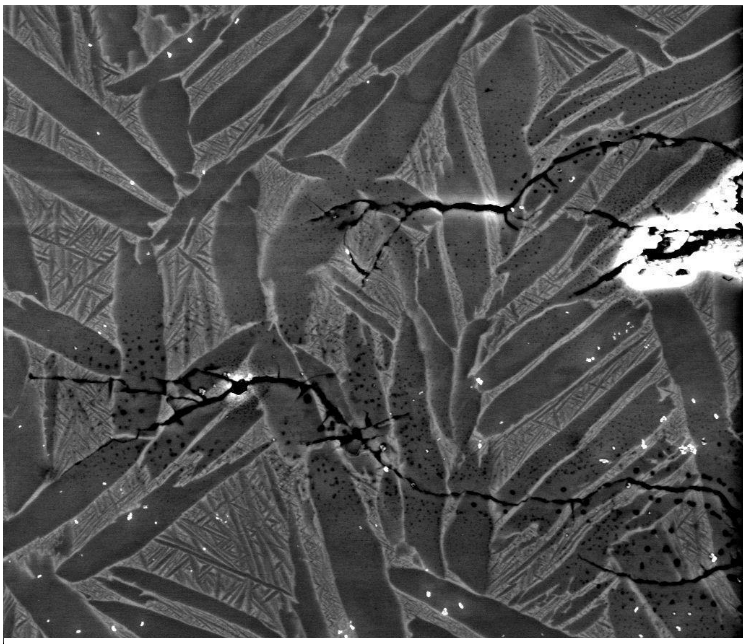

Figure 9.18: Magnified image of the crack tip from the air test at 500^{o}C. Secondary cracking is visible.

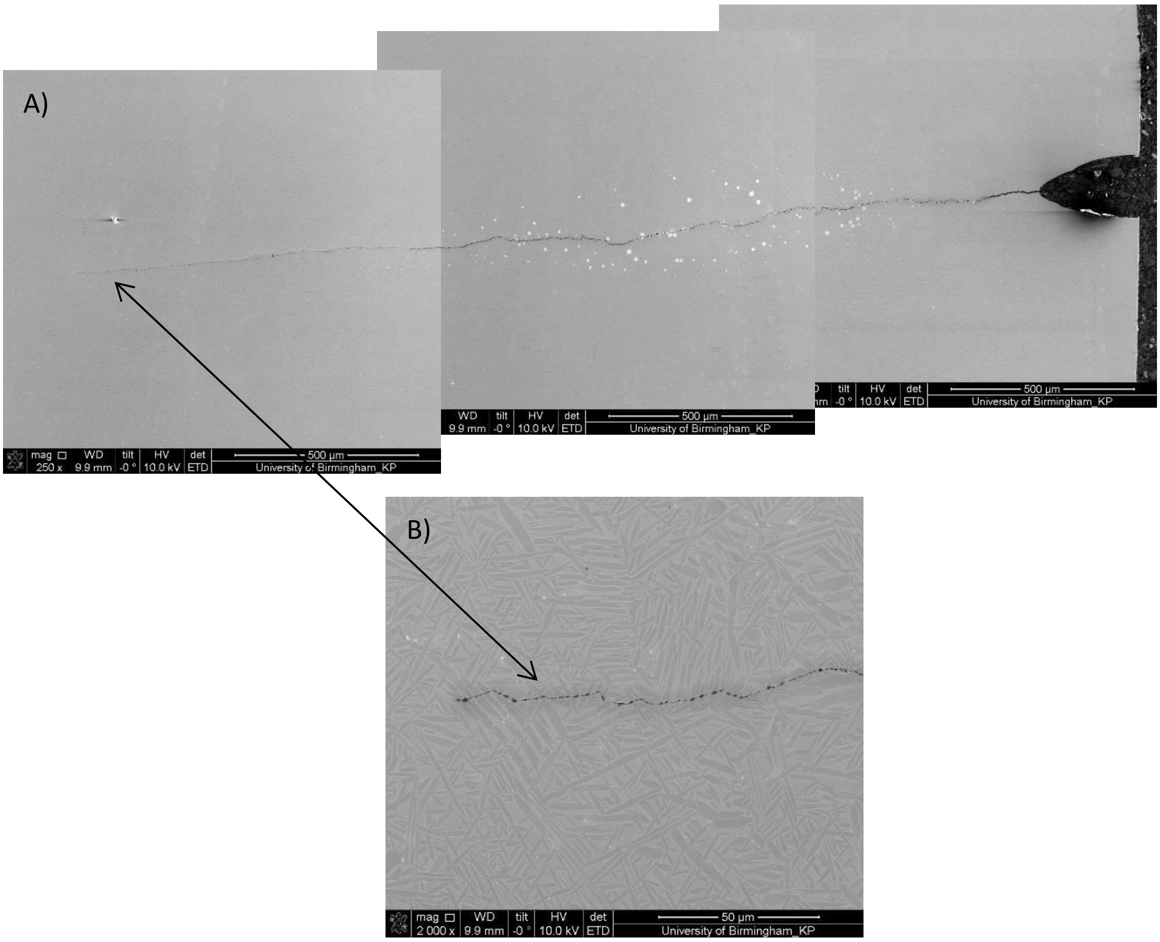

Figure 9.19: SEM images taken of the interrupted test under vacuum at 500^{o}C. A) Shows an overview of the entire crack. B) Shows a magnified image the end of the crack showing a single clear crack tip with no secondary cracking or branching.

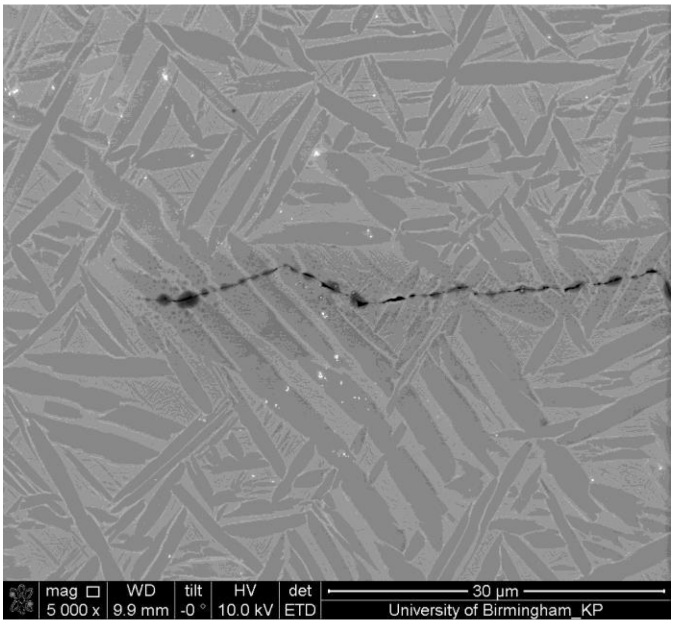

Figure 9.20: Magnified image of the crack tip from the vacuum test at 500^{o}C showing one clear crack tip.

Figure 9.21: Measurements taken of the oxide length ahead of the crack tip for the air test at 500^{o}C.

Figure 9.22: Measurements taken of the oxide length ahead of the crack tip for the vacuum test at 500°C.

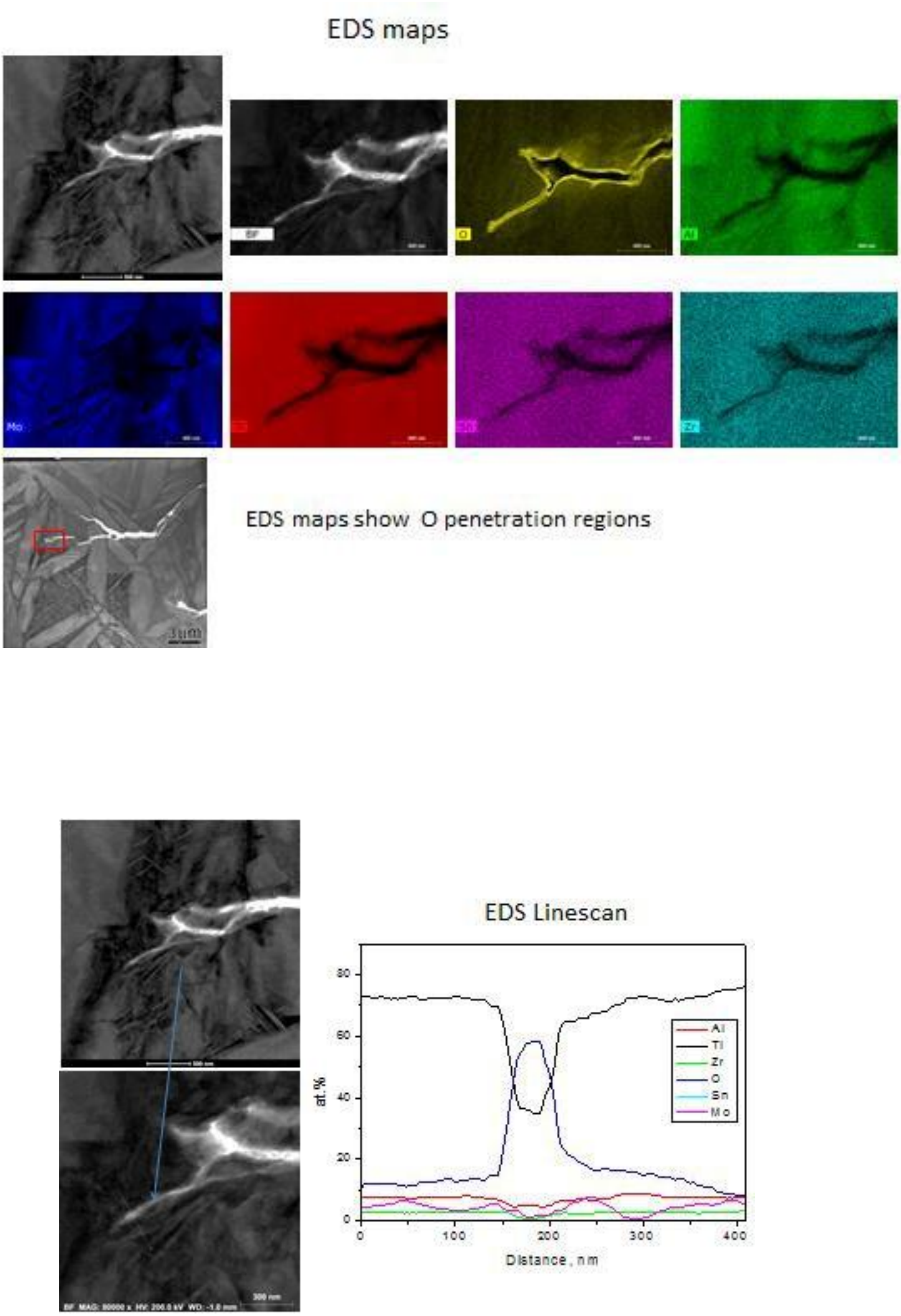

Figure 9.23: EDS map of the primary crack tip for the air test at 500°C.

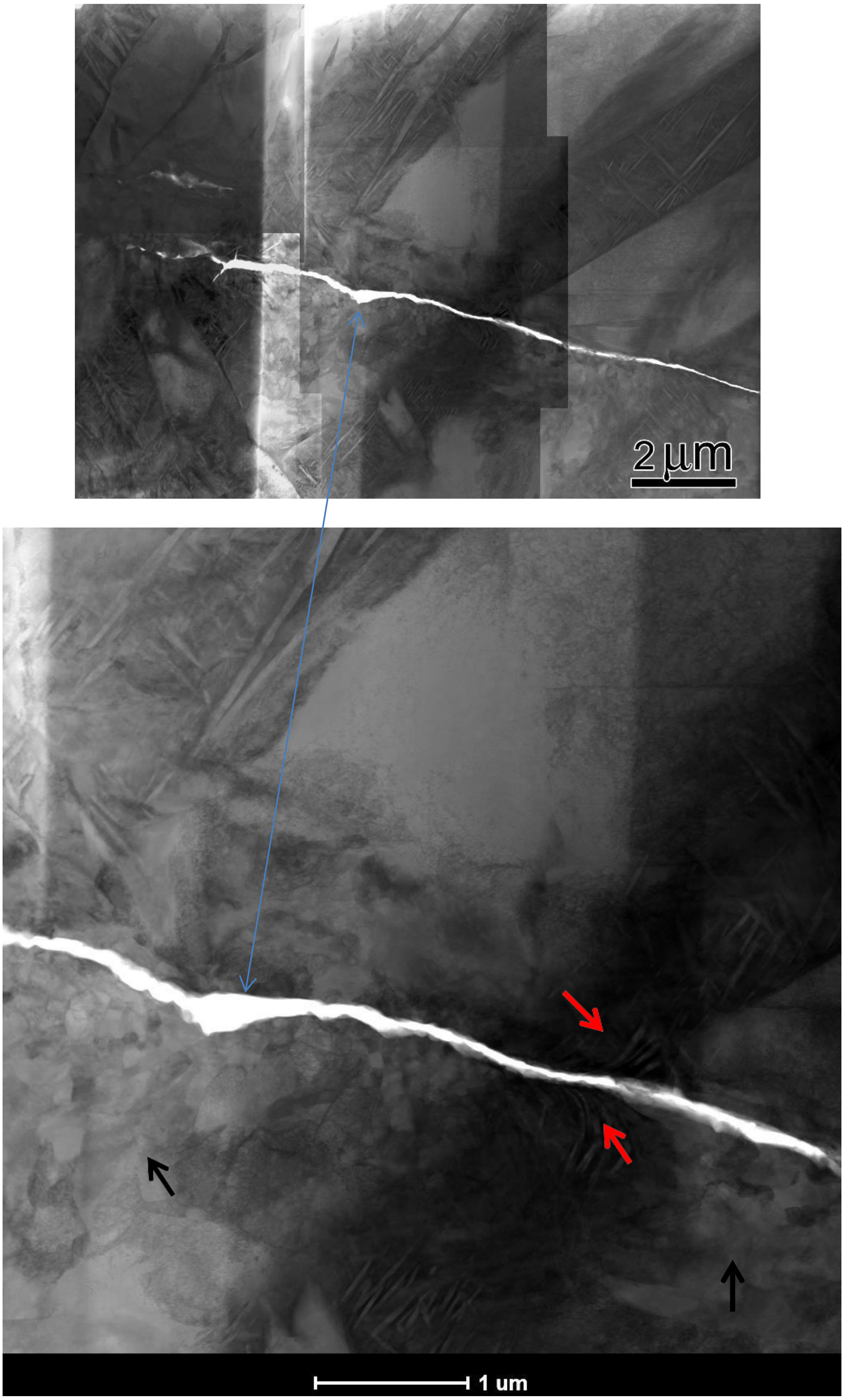

Figure 9.24: Vacuum test at 500^{o}C showing bent α laths (red arrows) and regions of recrystallization (black arrows).

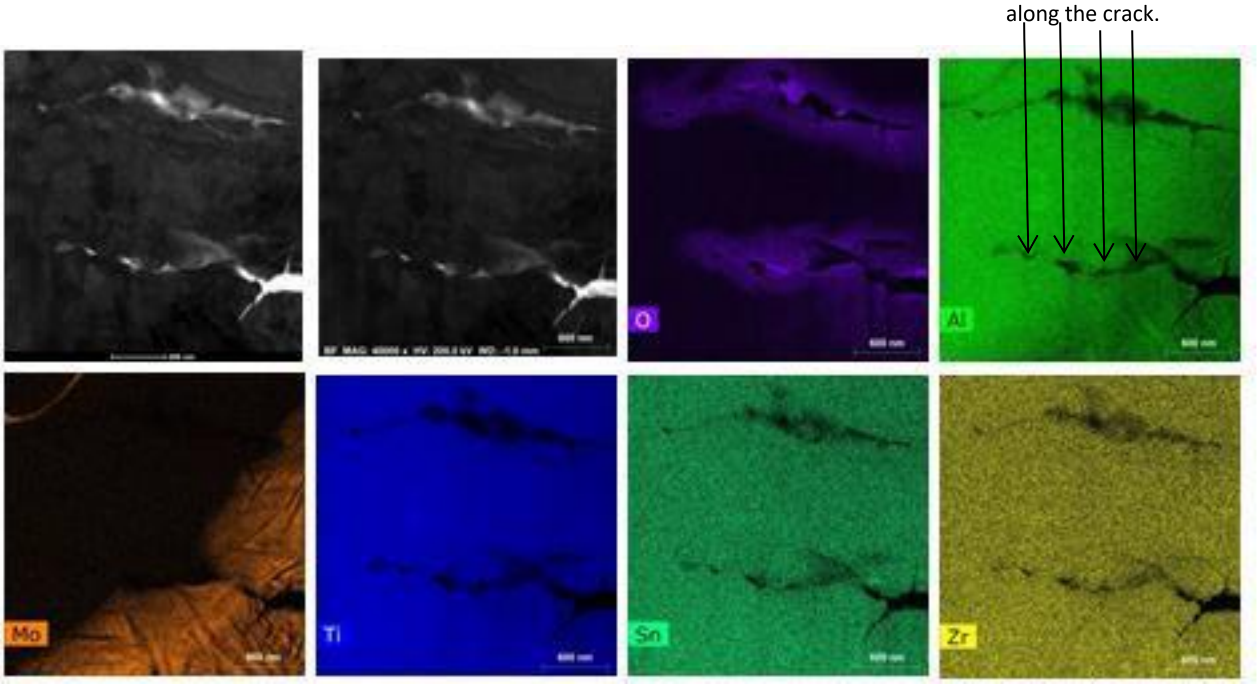

Four black “voids” visible along the crack.

Spot EDS spectra

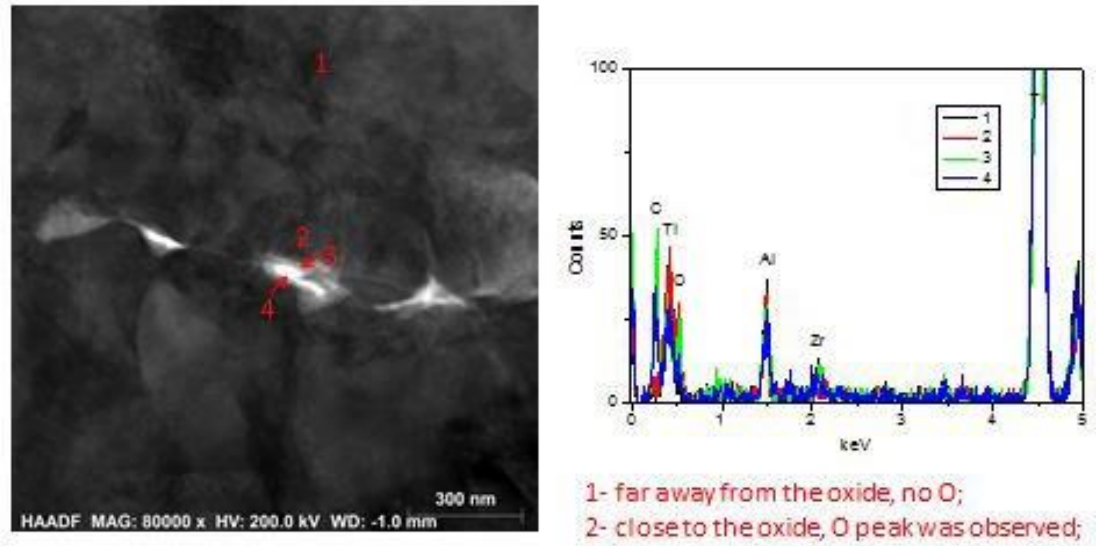

1- far away from the oxide, no O;
2- close to the oxide, O peak was observed;
3,4 – oxide with C.

Figure 9.25: EDS map created of the crack tip for the vacuum 500^{o}C test. Four black “voids” are highlighted along the crack.